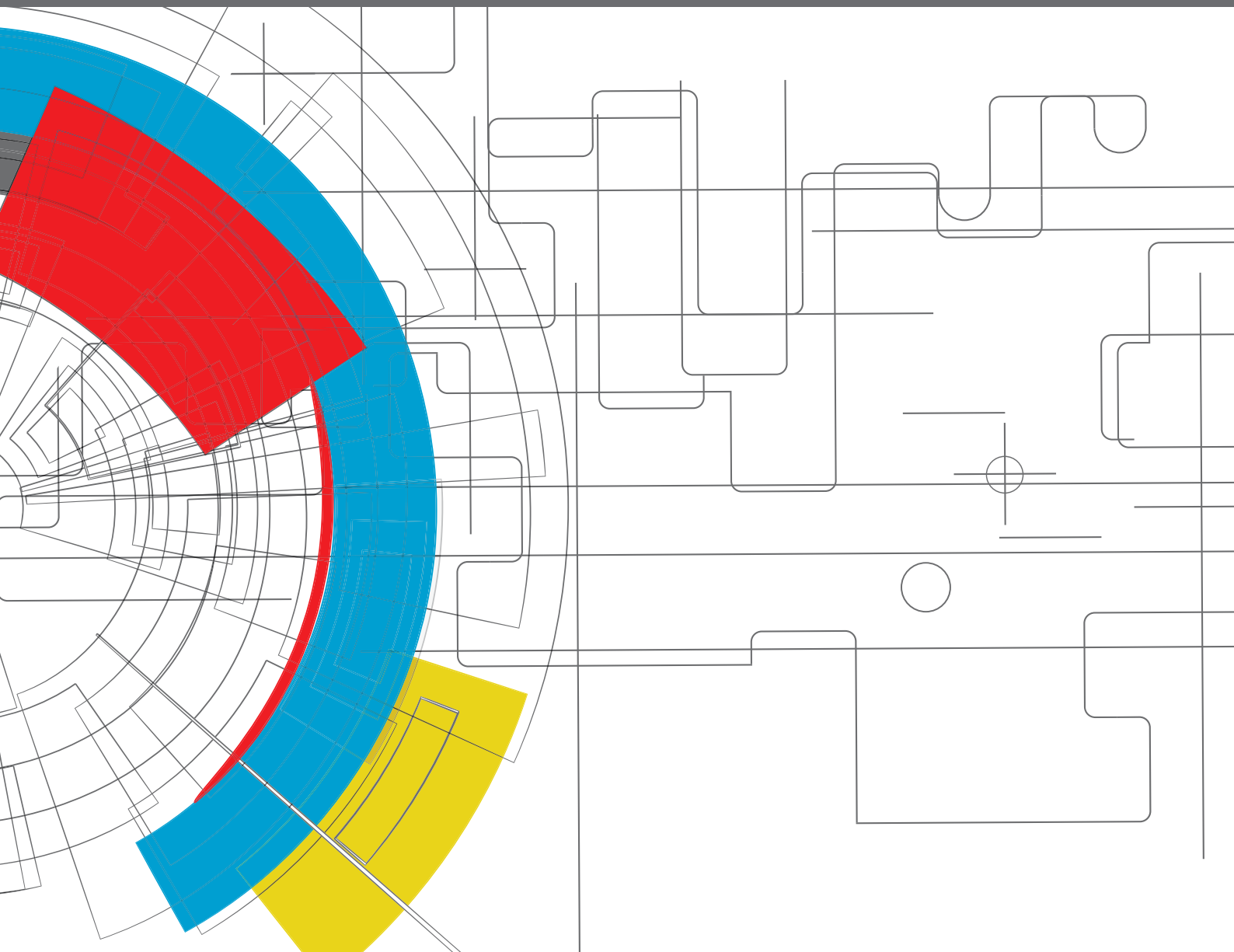


FRICTION AND WEAR: FROM ELEMENTARY MECHANISMS TO MACROSCOPIC BEHAVIOR

EDITED BY: Valentin L. Popov and Roman Pohrt
PUBLISHED IN: Frontiers in Mechanical Engineering





frontiers

Frontiers Copyright Statement

© Copyright 2007-2019 Frontiers Media SA. All rights reserved.

All content included on this site, such as text, graphics, logos, button icons, images, video/audio clips, downloads, data compilations and software, is the property of or is licensed to Frontiers Media SA ("Frontiers") or its licensees and/or subcontractors. The copyright in the text of individual articles is the property of their respective authors, subject to a license granted to Frontiers.

The compilation of articles constituting this e-book, wherever published, as well as the compilation of all other content on this site, is the exclusive property of Frontiers. For the conditions for downloading and copying of e-books from Frontiers' website, please see the Terms for Website Use. If purchasing Frontiers e-books from other websites or sources, the conditions of the website concerned apply.

Images and graphics not forming part of user-contributed materials may not be downloaded or copied without permission.

Individual articles may be downloaded and reproduced in accordance with the principles of the CC-BY licence subject to any copyright or other notices. They may not be re-sold as an e-book.

As author or other contributor you grant a CC-BY licence to others to reproduce your articles, including any graphics and third-party materials supplied by you, in accordance with the Conditions for Website Use and subject to any copyright notices which you include in connection with your articles and materials.

All copyright, and all rights therein, are protected by national and international copyright laws.

The above represents a summary only. For the full conditions see the Conditions for Authors and the Conditions for Website Use.

ISSN 1664-8714

ISBN 978-2-88963-074-5

DOI 10.3389/978-2-88963-074-5

About Frontiers

Frontiers is more than just an open-access publisher of scholarly articles: it is a pioneering approach to the world of academia, radically improving the way scholarly research is managed. The grand vision of Frontiers is a world where all people have an equal opportunity to seek, share and generate knowledge. Frontiers provides immediate and permanent online open access to all its publications, but this alone is not enough to realize our grand goals.

Frontiers Journal Series

The Frontiers Journal Series is a multi-tier and interdisciplinary set of open-access, online journals, promising a paradigm shift from the current review, selection and dissemination processes in academic publishing. All Frontiers journals are driven by researchers for researchers; therefore, they constitute a service to the scholarly community. At the same time, the Frontiers Journal Series operates on a revolutionary invention, the tiered publishing system, initially addressing specific communities of scholars, and gradually climbing up to broader public understanding, thus serving the interests of the lay society, too.

Dedication to Quality

Each Frontiers article is a landmark of the highest quality, thanks to genuinely collaborative interactions between authors and review editors, who include some of the world's best academicians. Research must be certified by peers before entering a stream of knowledge that may eventually reach the public - and shape society; therefore, Frontiers only applies the most rigorous and unbiased reviews.

Frontiers revolutionizes research publishing by freely delivering the most outstanding research, evaluated with no bias from both the academic and social point of view. By applying the most advanced information technologies, Frontiers is catapulting scholarly publishing into a new generation.

What are Frontiers Research Topics?

Frontiers Research Topics are very popular trademarks of the Frontiers Journals Series: they are collections of at least ten articles, all centered on a particular subject. With their unique mix of varied contributions from Original Research to Review Articles, Frontiers Research Topics unify the most influential researchers, the latest key findings and historical advances in a hot research area! Find out more on how to host your own Frontiers Research Topic or contribute to one as an author by contacting the Frontiers Editorial Office: researchtopics@frontiersin.org

FRICTION AND WEAR: FROM ELEMENTARY MECHANISMS TO MACROSCOPIC BEHAVIOR

Topic Editors:

Valentin L. Popov, Technische Universität Berlin, Germany

Roman Pohrt, Technische Universität Berlin, Germany

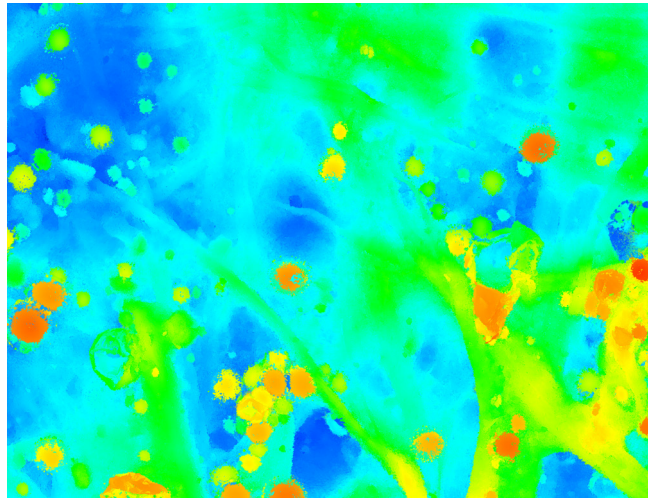


Image: Microscopic topology map of commercial paper with high friction coating for coefficient of friction up to 1.6.

Copyright 2019 @ Jasminka Starcevic, Technische Universität Berlin

Friction and the interaction of surfaces can usually be felt at the scale of the contacting bodies. Indeed, phenomena such as the frictional resistance or the occurrence of wear can be observable with plain eye, but to characterize them and in order to make a prediction, a more detailed understanding at smaller scales is often required. These can include individual roughness peaks or single molecule interactions.

In this Research Topic, we have gathered a collection of articles representing the state of the art in tribology's endeavor to bridge the gap between nano scale elementary research and the macroscopic behavior of contacting bodies. These articles showcase the breadth of questions related to the interaction of micro and macro scale and give examples of successful transfer of insights from one to the other. We are delighted to present this Research Topic to the reader with the hope that it will further inspire and stimulate research in the field.

Citation: Popov, V. L., Pohrt, R., eds. (2019). Friction and Wear: From Elementary Mechanisms to Macroscopic Behavior. Lausanne: Frontiers Media.
doi: 10.3389/978-2-88963-074-5

Table of Contents

04	<i>Editorial: Friction and Wear: From Elementary Mechanisms to Macroscopic Behavior</i>
	Roman Pohrt and Valentin L. Popov
06	<i>Controlling Friction With External Electric or Magnetic Fields: 25 Examples</i>
	Jacqueline Krim
20	<i>Macroscale Superlubricity Achieved With Various Liquid Molecules: A Review</i>
	Xiangyu Ge, Jinjin Li and Jianbin Luo
35	<i>Are There Limits to Superlubricity of Graphene in Hard, Rough Contacts?</i>
	Martin H. Müser
43	<i>Adhesive Strength of Contacts of Rough Spheres</i>
	Qiang Li, Roman Pohrt and Valentin L. Popov
52	<i>Evolution of the True Contact Area of Laser Textured Tungsten Under Dry Sliding Conditions</i>
	Björn Lechthaler, Georg Ochs, Frank Mücklich and Martin Dienwiebel
58	<i>A Concept of the Effective Surface Profile to Predict the Roughness Parameters of Worn Surface</i>
	Alexander Kovalev, Zhang Yazhao, Cao Hui and Yonggang Meng
69	<i>Atomistic Insights Into Lubricated Tungsten/Diamond Sliding Contacts</i>
	Pedro A. Romero, Leonhard Mayrhofer, Pantcho Stoyanov, Rolf Merz, Michael Kopnarski, Martin Dienwiebel and Michael Moseler
80	<i>Role of Interfacial Water and Applied Potential on Friction at Au(111) Surfaces</i>
	Leila Pashazanusi, Kai Kristiansen, Shaowei Li, Yu Tian and Noshir S. Pesika
89	<i>Investigation on Dynamic Response of Rubber in Frictional Contact</i>
	Ken Nakano, Kai Kawaguchi, Kazuho Takeshima, Yu Shiraishi, Fabian Forsbach, Justus Benad, Mikhail Popov and Valentin L. Popov
96	<i>Hydrated Seal Lip for Live Center in Machine Tools</i>
	Tetsuya Akiyama, Yuki Yoshioka, Takuro Honda, Yuta Nakashima and Yoshitaka Nakanishi



Editorial: Friction and Wear: From Elementary Mechanisms to Macroscopic Behavior

Roman Pohrt* and Valentin L. Popov*

Department of System Dynamics and Friction Physics, Technische Universität Berlin, Berlin, Germany

Keywords: friction, wear, adhesion, viscoelasticity, superlubricity, contact area, atomistic simulations, scales

Editorial on the Research Topic

Friction and Wear: From Elementary Mechanisms to Macroscopic Behavior

In the last 25 years, the global trend toward miniaturization has raised interest in frictional processes on the micro and nanoscale, and has facilitated the appearance of nanotribology as a new branch of research. Soon it became clear that looking at tribological processes at micro- and nanoscale can be very fruitful for macroscopic systems. Researchers recognized that these processes determine the macroscopic behavior via a number of mesoscopic levels. At first, this was perceived as a “gap” between macro and micro worlds. Over time, countless attempts were undertaken to “fill the gap”—both top-down and bottom-up.

The top-down approach starts from continuous macroscopic contact mechanics. A breakthrough in the modeling of real surfaces was connected with the development of the Fast Fourier-based Boundary Element Method (Campaña and Müser, 2006; Pohrt and Li, 2014). It allowed the analyzing of surfaces with ever-increasing levels of roughness discretization, and lead to “revisiting” and a new understanding of many old tribological solutions (e.g., Yastrebov et al., 2015). The present state in this field of contact mechanics of real surfaces is documented in a much-debated paper (Müser et al., 2017) written by 35 authors, as well as in the recent review (Vakis et al., 2018) written by 27 experts in the field. The bottom-up approach is connected with the development of measurement techniques at nano-level (Robbins and Krim, 1998; Gnecco and Meyer, 2015), as well as simulation techniques at the atomic and molecular level (Robbins and Müser, 2001; Pastewka et al., 2010). This approach brought into play fundamental concepts such as structural superlubricity (Erdemir and Martin, 2007) and thin fluid layer behavior, which were essential for understanding boundary lubrication (Erdemir, 2005).

The present Article Collection is an illustration of the current state of attempts to bring micro and macro together. It is opened by a review “Controlling Friction With External Electric or Magnetic Fields: 25 Examples” by Krim. Both the title and the author are symbolic for the topic. In the late 1990s, her experimental works on interfacial energy dissipation made an important contribution to the emerging field of nanotribology, and generally the physical understanding of interfacial processes. The review presents 25 examples of active control of friction from recent literature, thus reminding us of the huge complexity of tribological phenomena. At the same time, it clearly shows that they can be understood and well-controlled.

One of the most fundamental concepts discovered and analyzed in the last 25 years is the concept of superlubricity. It is classified in solid (or structural) superlubricity and liquid superlubricity, both of which are addressed in this article collection. In their paper “Macroscale Superlubricity Achieved With Various Liquid Molecules: A Review,” Ge et al. discuss the advancements in liquid superlubricity at the macroscale.

Müser combines the fundamental understanding of structural superlubricity with the advances of the contact mechanics of rough surfaces. He successfully links the scales and answers the question “Are There Limits to Superlubricity of Graphene in Hard, Rough Contacts?”

OPEN ACCESS

Edited and reviewed by:

Emile Van Der Heide,
Faculty of Engineering Technology,
University of Twente, Netherlands

*Correspondence:

Roman Pohrt
roman.pohrt@tu-berlin.de
Valentin L. Popov
v.popov@tu-berlin.de

Specialty section:

This article was submitted to
Tribology,
a section of the journal
Frontiers in Mechanical Engineering

Received: 19 June 2019

Accepted: 18 July 2019

Published: 02 August 2019

Citation:

Pohrt R and Popov VL (2019) Editorial:
Friction and Wear: From Elementary
Mechanisms to Macroscopic
Behavior. *Front. Mech. Eng.* 5:47.
doi: 10.3389/fmech.2019.00047

Any mechanism of friction considered at the atomic scale can be seen as the formation and destruction of intermolecular bonds, or small scale “adhesive contacts.” Therefore, it is not surprising that the adhesive interaction of rough surfaces has long been of interest to friction physicists (Fuller and Tabor, 1975). Li et al. employ a recent numerical technique to analyze both spreading and detaching of rough surfaces. Their paper, “Adhesive Strength of Contacts of Rough Spheres,” gives important implications: It is found that the short range adhesion is dependent only on one single parameter introduced by Johnson (1995)!

Surface roughness is the key factor leading to a scale-dependency of the “real contact area.” One of the central problems and challenges here is to not only determine the surface profile at one moment in time, but to also follow its development during the relative sliding of bodies (Popov, 2018). The paper “Evolution of the True Contact Area of Laser Textured Tungsten Under Dry Sliding Conditions” by Lechthaler et al. is devoted to an experimental investigation of the true contact area. In their work, a combination of methods was used to estimate the development of the real contact surface, and the results were compared with the evolution of the coefficient of friction.

Kovalev et al. present an efficient way of predicting wear evolution. They devote their paper “A concept of the effective surface profile to predict the roughness parameters of worn surface” to a theoretical study of the development of surface topography.

The paper “Atomistic Insights Into Lubricated Tungsten/Diamond Sliding Contacts” by Romero et al. is an excellent illustration of the possibilities of both contemporary atomistic modeling and experimental analysis at the atomic scale. The authors reveal the chemical roots of the very low friction resistance in that system. It is the formation of a

hydrocarbon film, preventing the partners from cold welding!

An intermediate scale between atomic and macroscopic is the scale of single asperities. Atomic force microscopy is the method of choice for experimental research at this scale. The authors of the paper “Role of Interfacial Water and Applied Potential on Friction at Au(111) surfaces” investigate how, in the presence of interfacial water, friction can be controlled by an electric field (Pashazanusi et al.).

Friction in soft matter, including elastomers, can be directly linked to rheological properties, but such understanding is not extensive. The experimental study in the paper “Investigation on Dynamic Response of Rubber in Frictional Contact” shows that we are still far from understanding how the dynamic response in frictional contacts should be described (Nakano et al.).

A practical example in the form of a seal in machining tools is given in the last paper by researchers from Kumamoto University (Akiyama et al.).

Tribologists will continue their quest to “bridge the gap” between nano and macro scale and the current article collection is a representative landmark in this endeavor. We hope you will find it inspiring.

AUTHOR CONTRIBUTIONS

All authors listed have made a substantial, direct and intellectual contribution to the work, and approved it for publication.

ACKNOWLEDGMENTS

The authors acknowledge financial support of the German Research Society (DFG), Project numbers PO 810/55-1, PO 810/53-1, PO 810/48-1.

REFERENCES

- Campaná, C., and Müser, M. H. (2006). Practical Green's function approach to the simulation of elastic semi-infinite solids. *Phys. Rev. B* 74:7. doi: 10.1103/physrevb.74.075420
- Erdemir, A. (2005). Review of engineered tribological interfaces for improved boundary lubrication. *Tribol. Int.* 38, 249–256. doi: 10.1016/j.triboint.2004.08.008
- Erdemir, A., and Martin, J.-M. (eds.). (2007). *Superlubricity*. Elsevier. doi: 10.1016/B978-0-444-52772-1.X5029-X
- Fuller, K. N. G., and Tabor, D. (1975). The effect of surface roughness on the adhesion of elastic solids. *Proc. R. Soc. A Math. Phys. Eng. Sci.* 345, 327–342. doi: 10.1098/rspa.1975.0138
- Gnecco, E., and Meyer, E. (eds.). (2015). *Fundamentals of Friction and Wear on the Nanoscale*. NanoScience and Technology. doi: 10.1007/978-3-319-10560-4
- Johnson, K. L. (1995). The adhesion of two elastic bodies with slightly wavy surfaces. *Int. J. Solids Struct.* 32, 423–430. doi: 10.1016/0020-7683(94)00111-9
- Müser, M. H., Dapp, W. B., Bugnicourt, R., Sainsot, P., Lesaffre, N., Lubrecht, T. A., et al. (2017). Meeting the contact-mechanics challenge. *Tribol. Lett.* 65:4. doi: 10.1007/s11249-017-0900-2
- Pastewka, L., Moser, S., Gumbsch, P., and Moseler, M. (2010). Anisotropic mechanical amorphization drives wear in diamond. *Nat. Mater.* 10, 34–38. doi: 10.1038/nmat2902
- Pohrt, R., and Li, Q. (2014). Complete boundary element formulation for normal and tangential contact problems. *Phys. Mesomech.* 17, 334–340. doi: 10.1134/s1029959914040109
- Popov, V. L. (2018). Is tribology approaching its golden age? Grand challenges in engineering education and tribological research. *Front. Mech. Eng.* 4:16. doi: 10.3389/fmech.2018.00016
- Robbins, M. O., and Krim, J. (1998). Energy dissipation in interfacial friction. *MRS Bull.* 23, 23–26. doi: 10.1557/s088376940003058x
- Robbins, M. O., and Müser, M. H. (2001). “Computer simulations of friction, lubrication and wear,” in *Handbook of Modern Tribology* Chapter 20, ed B. Bhushan (Boca Roca: CRC Press).
- Vakis, A. I., Yastrebov, V. A., Scheibert, J., Nicola, L., Dini, D., Minfray, C., et al. (2018). Modeling and simulation in tribology across scales: an overview. *Tribol. Int.* 125, 169–199. doi: 10.1016/j.triboint.2018.02.005
- Yastrebov, V. A., Anciaux, G., and Molinari, J.-F. (2015). From infinitesimal to full contact between rough surfaces: evolution of the contact area. *Int. J. Solids Struct.* 52, 83–102. doi: 10.1016/j.ijsolstr.2014.09.019

Conflict of Interest Statement: The authors declare that the research was conducted in the absence of any commercial or financial relationships that could be construed as a potential conflict of interest.

Copyright © 2019 Pohrt and Popov. This is an open-access article distributed under the terms of the Creative Commons Attribution License (CC BY). The use, distribution or reproduction in other forums is permitted, provided the original author(s) and the copyright owner(s) are credited and that the original publication in this journal is cited, in accordance with accepted academic practice. No use, distribution or reproduction is permitted which does not comply with these terms.



Controlling Friction With External Electric or Magnetic Fields: 25 Examples

Jacqueline Krim*

Physics Department, North Carolina State University, Raleigh, NC, United States

OPEN ACCESS

Edited by:

Roman Pohrt,
Technische Universität Berlin,
Germany

Reviewed by:

Martin H. Müser,
Saarland University, Germany
Valentin L. Popov,
Technische Universität Berlin,
Germany
Alexander Filippov,
Donetsk Institute for Physics and
Engineering, Ukraine

*Correspondence:

Jacqueline Krim
jkrim@ncsu.edu

Specialty section:

This article was submitted to
Tribology,
a section of the journal
Frontiers in Mechanical Engineering

Received: 07 December 2018

Accepted: 10 April 2019

Published: 21 May 2019

Citation:

Krim J (2019) Controlling Friction With
External Electric or Magnetic Fields:
25 Examples. *Front. Mech. Eng.* 5:22.
doi: 10.3389/fmech.2019.00022

Studies of the fundamental origins of friction have progressed rapidly in recent years, yielding valuable information on the relative contributions of electronic, magnetic, electrostatic, and phononic dissipative mechanisms. The field is now moving toward design of active control method for nano and/or meso scale friction, including the use of magnetic and electric fields external to the contact. These methods constitute an area of rapidly growing interest, as they address one of tribology's present day grand challenges: achieving *in situ* control of friction levels without removing and replacing lubricant materials situated within inaccessible confines of a contact. In this review, 25 examples of electromagnetic tuning of friction are overviewed, with examples spanning atomic to macro scale systems to demonstrate the variety and versatility of approaches that have been reported in the literature. Applications include, but are not limited to triboelectric generators, geological drilling, automotive braking and efficiency, spacecraft systems, biological systems, and magnetic spintronics. Experimental methods for measuring the impact of electric or magnetic fields on friction include AFM, SFA, QCM, pin-on-disk, hard disk head-on-substrate, MEMS and NEMS based tribometers, and optical spectroscopies. Computational and theoretical approaches include analytic, equilibrium and non-equilibrium Monte Carlo simulations.

Keywords: tribotronics, magnetorheology, nanoparticles, electrotuning friction, nanotribology, ionic liquids

INTRODUCTION AND OVERVIEW

Studies of how friction originates at the atomic scale have advanced rapidly in recent years, (Krim, 2012) from passive investigations of model systems (Müser et al., 2001) to active control and custom design of adaptive lubricant systems (Wu et al., 2015; Berman et al., 2018). Control and manipulation of adhesion and friction at a sliding contact is essential for progress in a wide variety of applications spanning nanoscale to macroscale applications. Achieving *in situ* control of friction levels without removing and replacing lubricant materials situated within inaccessible confines of a contact constitutes a current grand challenge in the field of nanotribology. The overarching goal is to successfully switch and/or adjust materials at the molecular level so as to reversibly and non-invasively tune friction levels. Externally applied electric or magnetic fields constitute a particularly promising, and rapidly growing, means to achieve to such “active” or “smart” control of friction at a molecular level in a field that has come to be known as “tribotronics” (Glavatskih and Höglund, 2008).

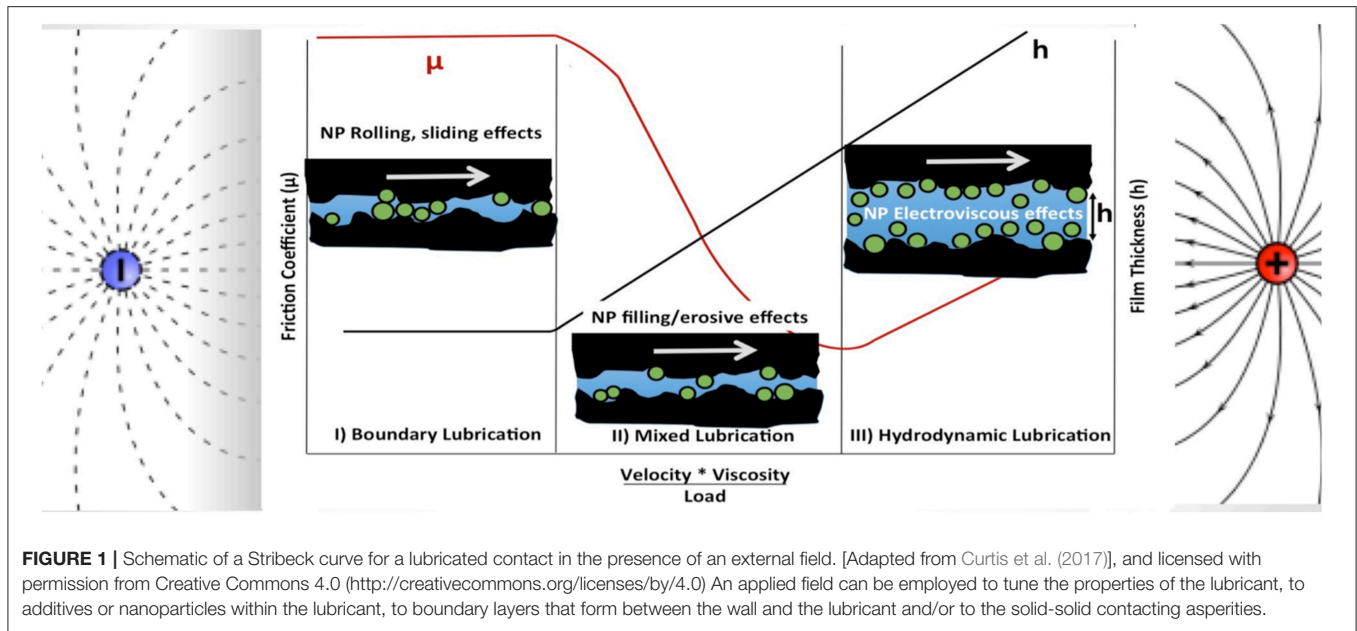


Figure 1 depicts a molecular level schematic, including possible nanoparticle or molecular additives to the bulk lubricant, of the Stribeck curve (Lu et al., 2006), which is a plot of a lubricated contact's friction coefficient $\mu = F_f/N$ vs. the quantity $\eta v/N$. The friction force F_f is defined as the force that resists sliding, and the quantities η , v and N are, respectively, the lubricant viscosity, the sliding speed and the applied load. The friction coefficient is a non-linear function of the load, lubricant viscosity and lubricant entrainment speed and the curve is divided into three regions: full solid on solid contact (boundary lubrication), partial contact (mixed lubrication), and zero contact (hydrodynamic lubrication). For fixed viscosity and load, the friction coefficient is notably independent of velocity in the boundary lubrication regime where it is comparable to "Coulomb," or dry-contact, friction. This is because the contacting asperities in the boundary lubrication regime support the full load of the solids pressed into contact. As the velocity increases, there is a progressive transition to a "Stokes" regime of hydrodynamic lubrication characterized by linear dependence of friction on velocity, with the solid surfaces fully separated by the intervening lubricant.

Active control of friction can be achieved by field-induced changes to lubricants, to lubricant additives, to boundary layers and/or to the contacting solids themselves. In this review, 25 examples of tuning of friction by means of an external electric or magnetic field are overviewed, with examples spanning atomic to macroscale systems. The goal is not to present a comprehensive list of all publications in this rapidly growing area, but rather to demonstrate the variety and versatility of approaches reported on in the literature. Examples are divided into 4 sections: (I) Field induced changes to bulk lubricants (Boulware et al., 2010a,b; Démery and Dean, 2010; De Vicente et al., 2011; Tusch et al., 2014; Ashtiani et al., 2015; Kabeel et al., 2015; Rodriguez-López et al., 2015; Vlachová et al., 2015; Zhao et al., 2017; Pardue et al., 2018; Acharya et al., 2019) (II) Field induced changes to solid

contacts (Gabureac et al., 2004; Highland and Krim, 2006; Park et al., 2006, 2007; Socoliuc et al., 2006; Qi et al., 2008; Pierno et al., 2010; Kisiel et al., 2011; Krim et al., 2011; Altfeder and Krim, 2012; Benassi et al., 2014; Mao et al., 2017; Popov et al., 2017; Benad et al., 2018; Popov and Li, 2018; Rajauria et al., 2018; Wolloch et al., 2018); (III) Field induced changes to surface boundary layers (Zhu et al., 1994; Coffey and Krim, 2005; Ismail et al., 2009; Drummond, 2012; Wolter et al., 2012; Wei et al., 2013; de Wijn et al., 2014, 2016; Kreer, 2016; Zeng et al., 2017; Fredricks et al., 2019); and (IV) Ionic liquid systems (Wanless et al., 1994; Sweeney et al., 2012; Hausen et al., 2013; Fedorov and Kornyshev, 2014; Li et al., 2014; Fajardo et al., 2015; Kong et al., 2016; David et al., 2017; Zhou and Qu, 2017; Pilkington et al., 2018; Pivnic et al., 2018).

The majority of the examples presented here parameterize friction in terms of either the friction coefficient $\mu = F_f/N$ or shear stress $\tau = F_f/A$, where A is the true area of contact between the opposing surfaces. Fluid viscosity and diffusion coefficients are also in some cases utilized as parameters to document friction levels. The latter quantity is closely linked to frictional drag forces of an object through that material. Friction coefficients are generally employed for cases of dry contact measurements performed in the boundary lubrication regime of lubricated contacts. In the hydrodynamic lubrication regime it is meanwhile more common to parameterize friction in terms of the shear stress, which for contacts separated by an average distance h , is linear in the velocity gradient as $\tau = F_f/A = \eta v/h$.

Experimental methods employed in the various examples include Atomic Force Microscopy (AFM), Surface Forces Apparatus (SFA), Quartz Crystal Microbalance (QCM), optical spectroscopies and wide range of tribometer systems comprised of macroscale, microscale and/or nanoscale components. In practice, magnetic fields are applied by either positioning samples directly within the interior regions of a solenoid or within the uniform field regions of Helmholtz coils, which consist of

two electromagnets aligned on the same axis. Electric fields are meanwhile applied through direct application of a bias voltage across the sliding contacts, or alternatively by positioning working, counter, and quasireference electrodes close to the contacts. The experimental literature therefore generally reports magnetic fields in units of Tesla while electric field control of friction is generally reported in terms of potential difference in Volts applied at or near the contact.

Computational and theoretical methods employed analytic, finite element, and both equilibrium and non-equilibrium Monte Carlo approaches. External fields are modeled either by performing the study within a force field or by adjusting materials' properties to reflect the presence of an external field.

Section I. Field Induced Changes to Bulk Lubricants and Lubricant Additives

Example 1: Improved Tribological Performance of Magnetorheological Fluids Comprised of Magnetic Particles in Oil Associated With Nanodiamond Additives (Zhao et al., 2017)

Magnetorheological fluids are liquids whose viscosity increases significantly in the presence of an applied magnetic field (De Vicente et al., 2011; Ashtiani et al., 2015). In their most common form, they are comprised of magnetizable microparticles dispersed into a carrier fluid and held in suspension with the aid of stabilizing additives. When an external field is applied, the particles transform from random individual particles into chains aligned along the field direction and, within milliseconds, become semisolid materials. The transformation is fast, reversible and continuously adjustable. The actively controllable nature of the fluid, as well as its low energy consumption, has given rise to a wide range of applications in machinery manufacturing, auto parts, precision machining, aerospace, biomedical, and other applications. Magnetorheological brakes and tunable clutches are commonplace in automotive industry applications, where applying the field substantially increases the friction.

Despite widespread commercial availability, settlement of the particles, instabilities in the friction, and insufficiently high shear stresses remain problematic for some applications. Of these, a weak response to the applied field, as well as instabilities in the friction and shear stress levels are the greatest challenges that inhibit widespread and broader commercial use of these materials. To address these challenges, Zhao et al. (2017) performed a study of the impact of dispersing nanodiamonds on the performance of a conventional magnetorheological fluid. In particular, the researchers compared the shear stress and viscosity of fluids in fields ranging from 0 to 0.76 T in the presence and absence of 2% suspensions of 90 nm diameter nanodiamonds. The carrier fluid consisted of a 75% slurry of 2.75 μm carbonyl iron powder $\text{Fe}(\text{CO})_5$ and stabilizers dispersed in a synthetic mineral oil carrier fluid. The external magnetic field was applied by positioning the sample within a solenoid coil.

In zero magnetic field, the nanodiamonds were reported to have no significant effects. However, when magnetic fields were applied, the nanodiamonds were reported to abrade the surfaces, enhancing the ability of the metallic particles to lock to the walls. This in turn increased the shear stress values by up to

a factor of 5, from several hundred Pa in the absence of a field to nearly 10^5 Pa at the highest field strengths studied. The nanodiamonds were also reported to assist in preventing settlement of the magnetic particles. It was therefore concluded that nanodiamonds as additives provide a straightforward and low cost approach to improved settling stability along with significant improvements in shear strength. The results are depicted schematically in **Figure 2**.

Example 2: Experimental Studies of Magnetic Field Dependent Friction for Two Particles in Water, Enabling an Analysis Method for Treating More Complex Systems (Tusch et al., 2014)

Fundamental studies of the underlying mechanisms of magnetorheological fluids require a detailed understanding of the response of individual particles in the suspension to the applied magnetic field. Single particle treatments are relatively straightforward. However, they are insufficient to capture the more complex behavior of actual suspensions of many particles. Tusch et al. (2014) reported an experimental study of magnetic field manipulation of a two-particle system, along with an analysis that provides a simplified approach that is extendable to more complex systems. The study consisted of two 2.8 μm beads suspended in water in a periodic time dependent external magnetic field that varied between 0.15 and 0.45 mT. Diffusion coefficients of the particles, which are a measure of the hydrodynamic friction, were measured by analyzing the time response to the applied field. The analysis was performed within a framework of stochastic thermodynamics using a hydrodynamic model.

Two different estimation methods for the system's dissipation were performed. The first was referred to as "energy based" and was based on interaction potentials measured for the two particle system. The second was referred to as "information based" and relied exclusively on the positions and trajectories of the particles. The latter was obtained by video microscopy of projections of the Brownian motion of the two beads onto their container's bottom wall. The authors found the latter approach to be simpler to implement and also, and more importantly, of general applicability to more complex systems. The energy-based approach was found to be too cumbersome and/or prohibitive difficulty to be extended to complex systems. Overall, the authors concluded that information-based estimates "*are attractive since they are simple to implement and do not require any knowledge of the dynamics of the system, a definitive advantage for many experimental applications.*" They also suggested that the approach could be useful for microrheology studies of biological systems and for analysis of small chemical or biochemical reactors.

Example 3: Liquid Oxygen as a Magnetorheological Fluid for Cryogenic and Space Applications and Mechanical Systems With no Moving Parts (Boulware et al., 2010a,b; Kabeel et al., 2015)

Commercial magnetorheological fluids, such as those reported on in Examples 1 and 2, perform well in many industrial applications. But they cannot be used in cryogenic applications where the carrier fluids are solid and the colloidal suspensions are immobile. Moreover, in space applications there are many

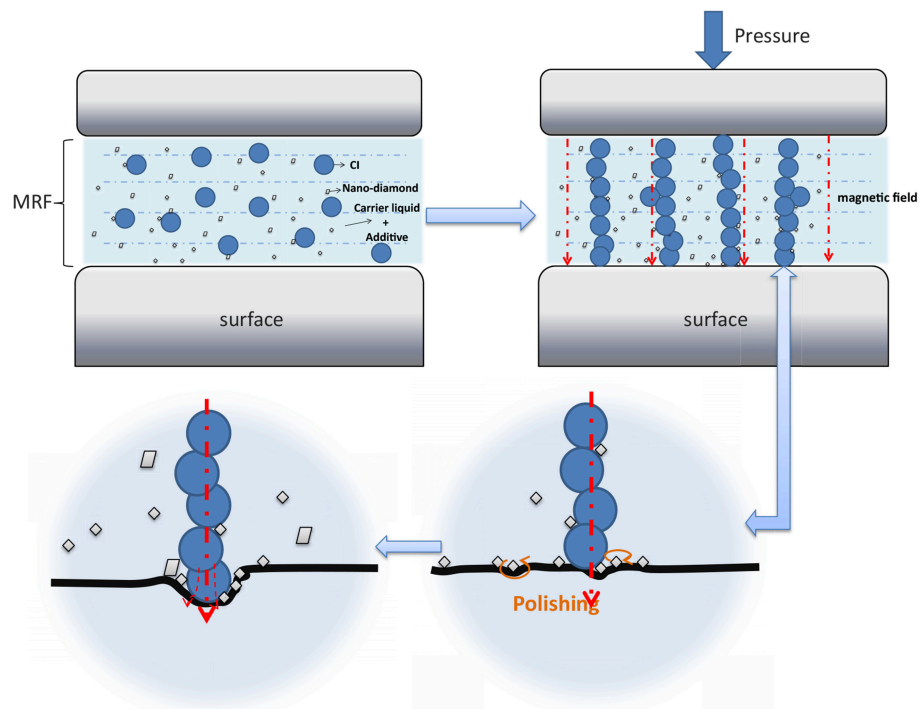


FIGURE 2 | Schematic of the underlying mechanism explaining nanodiamond enhancement of magnetorheological performance. Polishing mechanisms in the presence of the field enable higher wall friction levels, giving rise to higher shear strengths when the field is applied. Reprinted with permission from Zhao et al. (2017).

components whose lifetime is limited by wear associated with moving parts in rubbing contact. This challenge is particularly inhibiting for applications such as satellites since testing on earth only approximates the extreme mechanical conditions during launch and the extreme environmental conditions in space. Repair after launch is generally not feasible. One proposed solution to this technical need is the development of liquid oxygen as working magnetorheological fluid. Unlike the vast majority of magnetorheological fluids, which freeze at cryogenic temperatures, oxygen remains liquid. Since it is already used extensively for life support systems and propellants in space systems, it is an ideal candidate for use as a magnetic fluid in such systems for magnetorheological purposes. Since liquid oxygen exhibits strong paramagnetic susceptibility, it can be used as the working fluid in a cryogenic magnetic fluid system designed so as to have no mechanically moving parts, and thus no wear.

Boulware et al. have reported a number of experimental and theoretical studies to develop a basic understanding of the dynamics of liquid oxygen subjected to external magnetic fields of up to 1.1T (Boulware et al., 2010a,b). Its paramagnetic susceptibility increases as temperature decreases associated with a reduction in thermal energy that allows polar molecules to more readily align with an externally applied magnetic field. Since it is a paramagnetic fluid, it is however far weaker than the common ferrofluids employed for room temperature applications. Theoretical treatments are however more straightforward from the point of view that the system is comprised of only one component.

The researchers performed both experimental and theoretical studies of the dynamics of a slug liquid oxygen within a solenoid when subjected to an external magnetic field. The dynamics were monitored by recording pressure changes in a closed volume on both sides of the slug as oxygen molecules, which are oblong in shape, reoriented in response to the applied field. The researchers modeled the system by incorporating viscous, magnetic, and pressure forces into an equation of motion. They next employed a one-dimensional discretized algorithm to solve coupled Navier-Stokes and Maxwell's equations for the equation of motion. Overall, their combined experimental and theoretical approach successfully established liquid oxygen as a viable candidate for a moving part free magnetorheological system in cryogenic applications.

Example 4: Colloidal Stability and Magnetic Field-Induced Ordering of Iron Particles in *silicon* Oil and Hydrocarbons Studied With a Quartz Crystal Microbalance (Rodriguez-López et al., 2015)

Real time monitoring of the rheological properties of a magnetorheological fluid are of particular importance for advancing both applied and fundamental knowledge. QCM is a technique that provides such real time measurements, yielding nanoscale results that have been routinely linked to macroscale friction coefficients (Vlachová et al., 2015; Pardue et al., 2018). Rodriguez-López et al. employed the technique for *in situ* and real time measurements of fluid shear stress as a function of applied magnetic fields ranging from 0 to 0.02T. The researchers

studied silicon oil and hydrocarbon carrier fluids with 5 and 32% respective volume fractions of 5–10 μm iron microparticles, and were the first to successfully use a QCM for measures of shear stress in a magnetorheological slurry.

QCM studies were reported for both particle sedimentation under gravity and the impact of externally applied magnetic fields on the shifts of resonance frequency and dissipation factor. As expected, interactions among particles and also interactions between the iron particles and the resonator surface increased when magnetic fields were applied. The increase was attributed to increased contact stiffness between the particles and the surface. QCM data are also reflective of a lubricant's shear loss modulus G'' and shear storage modulus G' , providing a means for the researchers to compare the results with theoretical predictions of system behavior.

In particular, they performed a finite element modeling study examining both cases of free settling of particles and particle alignment under the action of the magnetic field. The modeling was performed by utilizing realistic materials values for the QCM, and high shear loss values for the viscous fluid ($G'' = 25 \text{ MPa}$). The particles were modeled as viscoelastic structures ($G' = G'' = 5 \text{ MPa}$ for settling particles; $G' = 50 \text{ MPa}$, $G'' = 5 \text{ MPa}$ for the particles in a magnetic field) forming within the fluid and acting in combination with the fluid itself. The basic model was in agreement with the trends observed in the frequency and dissipation QCM data.

Example 5: Tuning Friction Through Electric Field Manipulation of Charged Silica and Alumina Nanoparticles in Aqueous Lubricant Suspensions (Acharya et al., 2019)

Magnetorheological fluids require at least one of the constituents of a lubricant to be magnetic, so as to respond to an externally applied magnetic field. In an analogous fashion, electrically charged constituents of a lubricant will respond to externally applied electric fields. Nanoparticles in suspension are often electrically charged either intrinsically or by design. The study of their motion through active external control by electrical fields is rapidly growing, and active colloids are emerging as an area of widespread applications. In separate studies, nanoparticles have been demonstrated as lubricant additives capable of producing significant reductions or increases in the friction coefficients of the materials that they are added to.

Acharya et al. have recently reported the first use of active colloids for tuning friction at material-nanoparticle-liquid interfaces. Static, and also low frequency (0.6–50 mHz), electric fields of magnitude 100 N/C were applied to suspensions of either negatively charged TiO_2 (40 nm diameter; -33 mV zeta potential) or positively charged Al_2O_3 (30 nm diameter; $+61 \text{ mV}$ zeta potential) nanoparticles suspended in water. The fields resulted in electrophoretic forces, which were employed to reposition the particles relative to a planar platinum surface of a quartz crystal microbalance, which was then used to monitor friction levels. Friction levels were reported in terms of the damping levels of the surrounding suspension on the oscillatory motion of the QCM electrode. The field was produced by biasing the sensing electrode of the QCM with respect to a grounded Pt

electrode positioned nearby within the surrounding suspension. The authors report successful active electrotunable control of friction, and studied the response as a function of the applied field's frequency. Kinetic effects corresponding to nanoparticle repositioning at the interface were reported to occur at glasslike time scales and the studies also reported that nanoparticles manipulated by electric fields can act as “cantilever-free” atomic force probes capable of “tapping mode” exploration of interfacial properties in addition to being manipulated purely for the purpose of adjusting interfacial friction. In particular, features attributed to field-induced reorientation of water layers were identified in the friction data.

Example 6: Monte Carlo Simulation of Drag Forces in Classical Fields (Démery and Dean, 2010)

Démery and Dean (2010) performed Monte Carlo simulations of inclusions (point defects and or small objects that are otherwise recognizably distinct from the substance they are embedded in) moving at constant velocity in the presence of an external field. They found, as anticipated, that the defects experienced frictional drag forces that depended on both the field dynamics and how the inclusion coupled to the field. Changes in friction were manifested by changes in the diffusion constants of the inclusion moving within a surrounding material. The authors used their results to predict frictional drag levels exerted on the inclusions such as proteins in lipid membranes associated with protein interactions with membrane height and composition fluctuations. The forces on a point-like magnetic field moving within an Ising ferromagnet were also investigated, and were well-explained by these results. The theory is potentially applicable to soft materials such as those described in Example 5.

The authors argue that a rich phenomenology can arise from their relatively straightforward analysis because a wide range of field theories is available to describe soft materials. They also suggested directions for future investigations, including interacting fields, extensions to more realistic dynamics and possible experiments where their predictions could be tested. In particular, they suggested using optical tweezers to pull an inclusion, such as a colloid, through a binary fluid mixture close to the critical point.

Section II. Field Induced Changes to Solid Contacts.

Example 7: Control of Friction at an AFM Contact With a Semiconductor by Tuning Bias Levels and Charge Density Levels (Park et al., 2006, 2007; Qi et al., 2008)

Park et al. successfully controlled charge carrier densities to tune friction levels, utilizing semiconducting contacts, by applying external bias voltages to vary doping levels, and thus the mobile charge concentrations of the systems studied (Park et al., 2006, 2007; Qi et al., 2008) (Figure 3). In a first study, the researchers demonstrated electronic control of friction by employing a friction force microscope with a conductive titanium nitride coated tip in sliding contact with an oxygen passivated Si(100) wafer. The wafer was patterned with arrays of 2 μm -wide highly

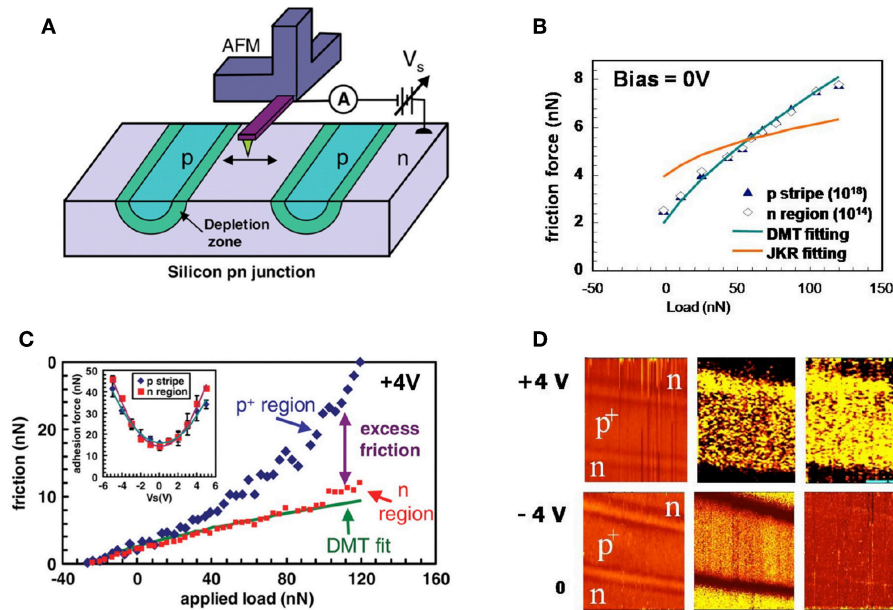


FIGURE 3 | (A) Schematic of AFM measurements on a silicon pn junction device. (B) In the absence of an external bias voltage the friction force vs. load curve for p-type and n-type regions of the surface are indistinguishable. Application of positive (C) or negative (C,D) bias voltages allows the friction to be tuned. The excess friction in the presence of an external bias is attributed to static charge and triboelectric effects. Reprinted with permission from Park et al. (2006) (A,C); and Park et al. (2007).

doped p-type strips with a period of $30\ \mu\text{m}$ in a nearly intrinsic n-type substrate. Increased friction levels were observed only in the highly doped p regions and were observed to increase with tip-sample bias voltage, contact strain, and velocity. The increases in friction levels could not be attributed to wear or surface damage.

The researchers also later investigated electronic contributions to friction at a semiconducting n-type GaAs surface covered by an approximately 1 nm thick oxide layer (Qi et al., 2008). The friction force microscope tip in this case had a 50 nm radius and was coated with Pt. Charge accumulation or depletion was induced by the application of forward or reverse bias voltages and substantial changes in friction levels were observed. The friction levels could be quantitatively explained by modeling the forces exerted by the trapped charges on the surfaces that were triboelectrically generated.

Example 8: Control of Friction Through Magnetic Levitation and Surface Charge Densities at a Contact Between a Magnetic AFM Tip and a Superconducting YBCO Sample (Altfeder and Krim, 2012)

As demonstrated by Example 7, and confirmed by recent theory (Woloch et al., 2018), surface charge distributions are known to play a major and dominant role in friction and adhesion and can be highly dynamic in nature in the presence of an external field. For insulating surfaces, tribo-generated static electricity moreover can be the dominant contribution to friction. An example of this is reported in Altfeder et al. who performed a magnetic probe microscopy study of levitation and atomic-scale friction for an Fe film coated AFM tip sliding on YBCO

between 65 and 293 K. The study was therefore performed in a temperature range that passed through the superconducting transition temperature $T_c = 92.5\ \text{K}$ of the YBCO sample. The friction coefficient was observed to be constant at $\mu_k = 0.19$ when the sample was in a superconducting state and exhibited no correlation with the strength of superconducting levitation forces. The friction coefficient abruptly began to increase with temperature as the sample passed into the normal phase, progressively increasing and nearly doubling, to $\mu_k = 0.33$ at room temperature. The results were attributed to contact electrification and static electricity giving rise to increased friction levels in the non-superconducting phase, which for the sample studied was believed to be semiconducting in nature. As such, friction measurements provide a means to test theories of superconductivity that predict thin superconducting or semiconducting surface regions above T_c .

Example 9: Magnetic Field Dependence of Friction of Adsorbed Layers on Superconductors (Highland and Krim, 2006)

The density of charge carriers in a superconducting material can be varied by applying an external magnetic field to the material so as to drive the material from a superconducting into a normal state.

Highland and Krim employed this approach to study sliding friction levels in nitrogen, water, and superheated helium films adsorbed on Pb(111) substrates with a quartz crystal microbalance by positioning the sample chamber within a solenoid coil and applying a weak magnetic field close to the

superconducting transition to, respectively, drive the system in and out of the superconducting state. Reductions in friction upon entry into the superconducting state were reported to be larger for nitrogen than helium, consistent with theory based on polarizability of the adsorbed layers and were successfully interpreted in terms of conduction electron contributions to friction. The Highland and Krim studies were performed in conditions that suppressed competing mechanisms for friction, allowing electronic effects to be resolved. In general, however, such effects are quite small relative to alternate mechanisms (phononic, static electricity, etc.). Independent efforts to observe conduction electron friction have variously encountered high background levels of phonon friction which prevented them from being resolved (Pierro et al., 2010), or required non-contact conditions to minimize contributions from competing mechanisms (Kisiel et al., 2011).

In addition to reporting friction levels in the presence and absence of the external magnetic field, the researchers also observed that the repetitive cycling of an externally applied magnetic field in and of itself impacted friction levels as compared to measurements performed in static field conditions. This phenomenon remains unexplained, but is potentially attributed to either “noise” induced by abrupt changes in field (Examples 11, 12) and/or molecular film reorientations associated with the changing field (Examples 18,19).

Example 10: Tuning Friction Through Magnetic Field Induced Changes to Contact Geometry: Magnetostriction of Nanoscale Ni-Ni Contacts (Gabureac et al., 2004)

Gabureac et al. report studies of nickel nanocontacts in the presence of an applied magnetic field.

They observed significant changes in resistance depending on the angle between the applied field and the contact direction. The changes are consistent with modifications of the contact geometry induced by magnetostriction, which is a property of ferromagnetic materials whereby they change their shape or dimensions during the process of magnetization. The studies were performed at field strengths ranging from 0 to 1T for Ni-Ni nanocontacts in close proximity.

The authors point out that a small 100 μm diameter Ni magnet shrinks in the direction of magnetization by 5 nm, which is a very large effect when considering atomic scale nanocontacts. While they do not specifically report friction levels associated with the varying contact levels resulting from the applied magnetic fields, they point out that such effects are likely to be ubiquitous in systems employing externally applied fields, and must be accounted for to properly design and control mechanical systems via electronic methods.

They conclude by emphasizing the importance of magnetomechanical effects in measuring magnetoresistance in nanocontacts and argue that the effects are extremely difficult to avoid. This in turn impacts studies of the electrical resistance of nanocontacts. The same would therefore be applicable to nanoscale studies of the impact of magnetic fields on tribocontacts.

Example 11: Microscale Motion Control With Magnetic Fields Applied to Ferromagnetic Films (Benassi et al., 2014)

Benassi et al. report a theoretical study of actuation and control that is applicable to motion and friction control in micromechanical systems. The work is motivated by the fact that recent progress in friction reduction associated with lowering commensurability of contacting crystal lattices lacks versatility in terms of modifying and/or controlling friction. To circumvent this lack of versatility, they propose to tune the material properties with external control parameters, and note that the example of an external field applied to an ionic liquid is a promising example of such control.

In particular, they propose a non-contact motion control technique based on the introduction of a tunable magnetic interaction. As a specific example, they suggest coating two non-contacting bodies with ferromagnetic films.

The researchers demonstrate that wear-free motion control in these systems can be achieved by means of interacting magnetic domains arising at the surface below the Curie temperature. Their hypothesis is that the size, shape, and ordering of such domains is easily controlled with an external magnetic field, allowing a flexible and reversible means to tune system tribological properties. Given that typical domain sizes are on the order of nm to tens of μm , the approach is well-suited for integration into micron scale devices, and the domain behavior could be tailored through proper design and preparation of the ferromagnetic coatings, external magnetic fields and the distance between the plates.

Example 12: Electrostatically Tunable Adhesion Via Oscillation Induced Reductions in Contact Hysteresis at a Head-Disk Interface (Rajauria et al., 2018)

Rajauria et al. have recently studied the impact of vibrations induced by an external field on a high speed sliding interface, namely a recording head-disk contact moving in close proximity at high speeds on the order of 5–40 m/s. Contact hysteresis between sliding interfaces is a common phenomenon that has a major impact on the tribological performance of a head-disk system. The majority of studies of contact hysteresis have been performed with AFM at very slow speeds on the order of $\mu\text{m/s}$. Additional methods that perform measurements at higher speed are therefore of interest.

The researchers employed commercially available hard disk drives to perform the studies. Such systems are of particular interest, since the sliding speeds are high, while the gap sizes between the contacts are of nm extent. The primary result was to demonstrate that out-of-plane oscillations induced by AC voltages applied between the head and the disk are able to completely suppress contact hysteresis, and thus tune the friction and adhesion levels. They noted that this is a dynamic effect associated with the time for contacts to grow and adhere, since the electrostatic force arising from the applied DC or AC voltage is attractive.

It should also be noted here that a large number of studies have examined active control of friction through externally applied vibrations (Socoliuc et al., 2006; Krim et al., 2011; Mao et al., 2017;

Popov et al., 2017; Benad et al., 2018; Popov and Li, 2018), and in many cases the vibrations were induced by electromagnetic fields (Socoliuc et al., 2006; Krim et al., 2011). The two approaches to tuning friction therefore have some overlap.

Section III. Field Induced Changes to Surface Boundary Layers

Example 13: Influence of Electrochemical Potentials on the Friction and Wear of Iron and Iron Oxides in Aqueous Systems. A Microscopic Study of Macroscale Rubbing Contacts (Zhu et al., 1994)

Bias potential dependence of friction is a common phenomenon in the literature for rubbing contacts that contain iron, particularly in the presence of water. In a 1994 study, Zhu et al. explored the chemical nature of the boundary layer films that form under such conditions, which in turn have a strong impact on friction levels. They studied the influence of electrochemical potentials on both friction and wear, for iron/iron, and iron oxide/alumina oxide rubbing contacts that were lubricated with aqueous fluids. They employed impedance spectroscopy and Fourier transform infrared micro spectroscopy to explore friction and wear of the rubbing contacts in well-defined conditions as a function of the applied bias voltage. The researchers measured friction coefficients with a macroscale tribometer comprised of a reciprocating hemispherical pin with stroke length 0.3 mm at a frequency of 10 Hz. The pin was pressed into contact with a flat surface that was fully immersed in a cell filled with an aqueous electrolyte employed as the lubricant. The pin and flat were both connected to an external potentiostat and otherwise electrically grounded. A reference electrode and Pt counterelectrode were also immersed in the cell within close proximity to the contact, to facilitate potential control in cases where both the pin and flat were conducting.

The researchers concluded that the observed changes in friction and wear were attributable to two primary mechanisms: (1) Changes in electrostatic repulsion associated with changes to the double layer charge and (2) surface redox reactions. They also modeled the electric double layer effect and found a significant dependence of the friction coefficient on surface bias potential for ratios of the applied contact pressure to inter-surface pressure falling below an approximate factor of 10. In addition, they also observed that the decreased friction levels at positive electrode potentials were attributable to the formation of FeOOH on the metal surfaces. Positive electrode potentials also produced iron (II) carboxylate on the surfaces when octanoic acid was present, causing a significant reduction in friction.

Example 14: Switching on a Lubricant at Sliding Contact Lubricated by Aqueous Solutions: A Pin on Disc Study (Ismail et al., 2009)

Ismail et al. (2009) reviewed the bias voltage dependence of a number of macroscale systems comprised of steel contacts lubricated by water, and found a general trend for systems containing octanoate. In particular, friction coefficients were collectively reported to drop from approximately 0.4 to 0.15 for bias voltages, respectively, tuned between -1.0 and $+1.0$ V.

The authors then reported their own investigation of alkaline aqueous-based solutions, employing a macroscale pin-on-disk setup with a bias voltage that spanned ± 1 V. They observed that friction was reduced in octanoate solutions under negative electrochemical bias due to a production of a low friction tribochemical layer (iron octanoate). They noted the usefulness for industrial applications of mastering the capability of switching friction between two known values by varying the bias voltage, namely high and low values for cathodic and anodic potentials. They also reported that the tribochemical layer reduced wear of both pin and disk and that in general NaOH tests yielded much higher friction coefficients and more corrosion for the same applied potentials.

Example 15: Tuning Macroscale Friction Employing Polyelectrolyte Brushes and Fluid Counterions (Wei et al., 2013)

Some of the lowest known friction coefficients, $\mu < 0.001$, occur in aqueous systems at biological interfaces. These include the vitreous body of eyes and synovial joints such as hip, knees, and fingers. The exceptional tribological performance of such systems is associated with the presence of phospholipids, hyaluronan, lubricins, and bottle-brush-like glycoproteins in synovial fluids. Hyaluronan and glycoproteins are biopolyelectrolytes whose side chains contain large amounts of sulfonic and carboxylic groups. The charged nature of these biomacromolecules and their brush-like structures are thought to underlie their superior lubricating properties (Kreer, 2016). In particular, they respond to electrostatic interactions via swelling-collapse transitions of end-tethered polymer chains and osmotic pressures within the brushes. Polyelectrolyte brushes are fully stretched when they are immersed in pure water, allowing water molecules to fully penetrate them. But when they are immersed in an electrolyte solution, strong electrostatic screening occurs causing the water to be expelled and the brushes to collapse (**Figure 4**). The various configurations are associated with significantly different friction levels, and have been the topic of much interest in the nanotribology community.

Wei et al. for example reported significant tuning of friction levels in polymer brushes linked to swelling and collapse of the polymers (Wei et al., 2013). Friction coefficients were measured in macroscale setups, employing a pin-on-disk configuration (**Figure 4**). The pin, which was not coated with a polymer brush, was prepared from a commercial silicon elastomer kit mixture poured into a mold to produce an elastomeric poly-(dimethylsiloxane) (PDMS) hemisphere. The disks were comprised of silicon and were prepared with surface treatments that initiated growth and attachment of the polyelectrolyte brushes. The conformation of the brushes was characterized by both AFM and measurements with a QCM positions *in situ* to monitor liquid dynamic response. Superior lubrication with friction coefficients $\mu < 0.001$ was associated with the fully extended swollen polymers, while completely collapsed configurations exhibited high friction coefficients close to $\mu = 1$. Intermediate configurations with intermediate friction coefficients were also achieved for partially collapsed configurations.

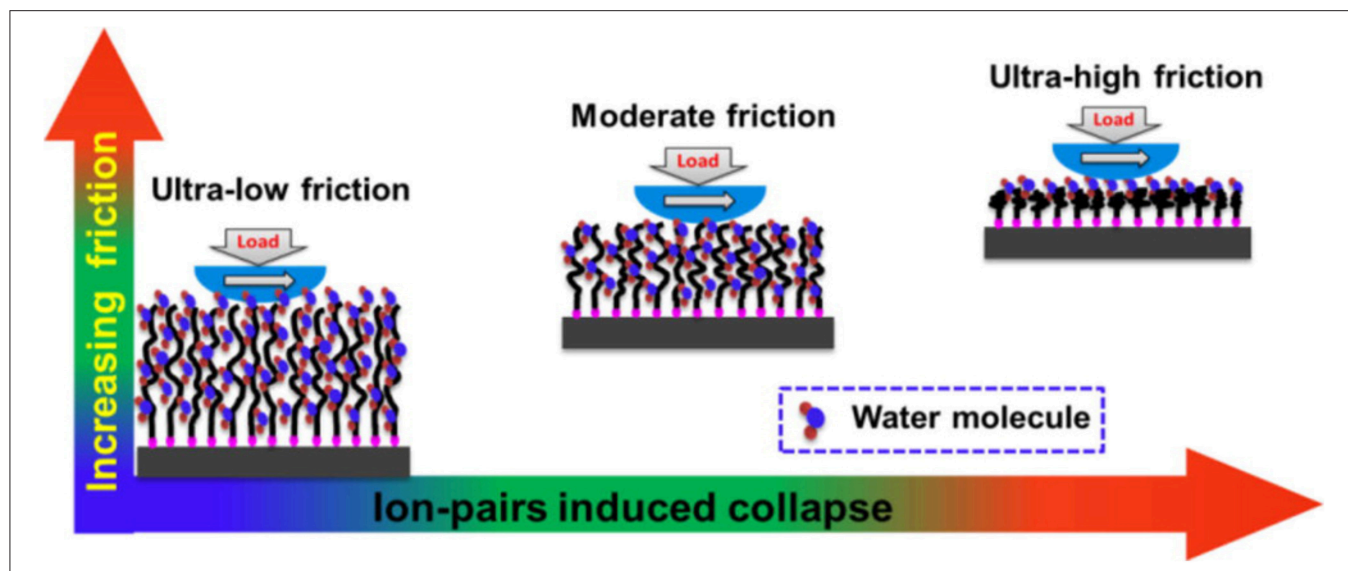


FIGURE 4 | Schematic of the dependence of friction on the stretching of polyelectrolyte brushes. Reprinted with permission from Wei et al. (2013). Copyright 2013 American Chemical Society. Externally applied fields and/or changes in the electrolyte counterions or pH can modify the brush configuration because the brushes are electrically charged. Water molecules fully penetrate the brushes when they are fully stretched and friction coefficients are ultra-low, of order $\mu = 10^{-3}$. Water molecules are completely expelled from the brushes when they are fully compressed and friction levels are high, of order $\mu = 1$.

The authors achieved the dramatic range of friction levels by exchanging counterions in the surrounding liquid, which tuned the system's electrochemical properties. For the case of cationic brushes with quaternary ammonium groups, they successfully tuned friction coefficients in a progressive manner between approximately 0.001 and 1 by exchanging the counterions in the surrounding liquid progressively in series, as $\text{Cl}^- < \text{ClO}_4^- < \text{PF}_6^- < \text{TFSI}^-$. For the case of anionic brushes they achieved tuning of the friction levels by employing oppositely charged surfactants (tetraalkylammonium) with varying hydrophobic tail lengths, multivalent metal ions, and protons. The increases in friction observed for cationic brushes were successfully explained to result from a collapse configuration induced by ion-pairing interactions. The increases in friction observed for anionic brushes were linked to the length of hydrophobic tails of surfactants, and the associated hydrophobicity induced by electrostatic interactions between the surfactants and polymer chains.

Example 16: Surface Forces Apparatus Study of Electric Field Induced Reductions to Friction in Polyelectrolyte Coatings (Drummond, 2012)

Drummond reported in 2012 a careful investigation of the impact of an external electric field applied to polymer brush materials attached to both contacts in a crossed-mica surface configuration of a Surface Forces Apparatus (Drummond, 2012). Drummond hypothesized that external electric fields would produce far more rapid changes in molecular configuration than methods that alter the properties of the surrounding electrolyte solution, for example the counterion exchange method described in Example 15. Drummond further hypothesized that coating both surfaces with a polyelectrolyte brush could result in lower friction levels than coating just one surface.

Samples were prepared by attaching polymer brushed to the surfaces of atomically uniform cleaved mica substrates. In particular, the mica surfaces were coated by self-assembly of amphiphilic diblock polystyrene-polyacrylic acid co- polymers ($\text{PS}_{36}\text{-b-PAA}_{125}$) from aqueous solution at pH 10, and both atomic force microscopy and quartz crystal microbalance methods were employed to monitor the degree of adsorption and structure. The mica surfaces themselves were curved and attached to the front surfaces of the two crossed cylinder silica disks pressed into sliding contact by a SFA. The posterior surfaces of such disks are commonly coated with silver films in a SFA, allowing a means to apply a bias voltage across the sliding contacts.

Drummond applied AC electric fields by applying bias voltages in the form of square waves with frequencies ranging between 200 and 1,000 Hz and amplitudes of up to 20 V peak to peak. The intensity of the applied field was proposed to determine the degree of interpenetration between polymer brushes in contact, and explored the speed of the dynamical responses of the polymer by examining the friction reduction vs. applied frequency. Friction levels were observed to drop by several orders of magnitude, to below the detection level of the instrument, when fields were applied. The response was fast and reversible for externally applied fields up to 450 Hz, and the electrically extended brushed were observed to resist collapse under application of a normal load.

Example 17: A Reversibly Electrocontrollable Polymer Brush for Electroswitchable Friction (Zeng et al., 2017)

Zeng et al. (2017), reported success at developing electrically switchable friction, defined as friction that can be reversibly manipulated by an external electric

field, via an electro-controllable polymer branched brush. They grafted the electro-controllable polymer branched brush, poly-sodium allyloxy hydroxypropyl sulfonate (poly-AHPS), onto an electrically conductive indium tin oxide (ITO) glass, and observed two friction states: (1) stretched polymer brush arrays when negatively charged and (2) rolled polymer knolls when positively charged and two substantially different friction levels. The range of the change in friction, although modest, could be tuned by sandwiching polar, or non-polar molecules between the brushes. The authors proposed that the system is useful for automatic control of friction, and could find wide application in automatization, intelligent manipulation and actuators, and micro-electro-mechanical systems.

Example 18: Theoretical Model of Electrochemical Control of Nanoscopic Friction and Effects of Molecule Anchoring (de Wijn et al., 2014, 2016)

The majority of published studies of electrotuning of friction are experimental in nature, and there is a great need for detailed theoretical understanding of the mechanisms. In one such study, de Wijn et al. reported a theoretical model of nanoscopic friction under electrochemical conditions that models an AFM tip sliding along an adsorbed layers of polar molecules. The system is representative of systems such as water on platinum, where electric fields control the orientation of the molecules with respect to the substrate (see also Example 5, where flipping of water by an external field is observed to impact friction levels.). They concluded that the dependence of the friction force on the electric field was determined by the interplay of two dissipative mechanisms (1) the rotation of the dipoles and (2) slipping motion of the tip over potential barriers presented by the molecular surface. They moreover developed a strategy for custom design of how friction depends on the external field. The strategy was based on the competition between long-range electrostatic interactions and short-range chemical interactions that are present between the polar molecules adsorbed on the surface and the AFM tip.

In a follow-up publication they explored the effects of anchoring the molecules, and how it impacts friction levels near bias voltages that are sufficiently large to cause them to reorient, employing the same strategy involving the long-range electrostatic interactions and short-range chemical interactions. The authors also derived a dispersion relation for phononic vibrations of the surface molecules and showed how it could be used to understand important features of the frictional response. Both molecules that rotate about their center of mass and molecules anchored on one side were considered. As might be expected, the variation of friction with external electrical fields was strongly influenced by how the adsorbed molecules were anchored to the surface. The work thus revealed unique theoretical insights into how molecular anchoring can be used for custom design of electrolyte-based lubricants with specific responses to external electric fields.

Example 19: Tuning Nanoscale Friction by Applying Weak Magnetic Fields to Reorient Adsorbed Oxygen Molecules (Fredricks et al., 2019)

In a manner analogous to polar surface molecules being reoriented by an external field, magnetic molecular adlayers can be reoriented by an external magnetic field. Fredricks et al. employed a QCM to study sliding friction levels of thin (1–2 monolayers) and thick (~10 monolayers) oxygen films adsorbed on nickel and gold at 47.5 K. The magnetic fields were applied by positioning the sample chamber and its surrounding within the uniform field regions of Helmholtz coils. The measurements were performed at a temperature close to that where oxygen adlayers lying flat on the surface are readily reoriented to a more compressed and upright position. Weak fields, in combination with the ferromagnetic nature of nickel, are therefore sufficient to reorient the adlayers. As is the case for Example 18, changes in orientation and corrugation are known to have a great impact on phononic friction levels (Coffey and Krim, 2005; Krim, 2012). Friction levels are therefore tuned in association with reorientation of the molecules.

The researchers observed experimentally that friction levels for the thin (thick) films in the presence of a weak magnetic field were observed to be approximately 30% (50%) lower than those recorded in the absence of the external field for films adsorbed on nickel, but increased for adsorbed layers on gold. Magnetically induced structural reorientation (magnetostriction) and/or realignment of adlayer spins, which, respectively, reduced structural phononic mechanisms and magnetic interfacial corrugation and commensurability, were suggested as the most likely mechanisms underlying the observed field-induced reductions in friction. The work demonstrated the role of magnetic effects in a model system that is highly amenable to future theoretical studies (Wolter et al., 2012).

Section IV. Ionic Liquid Systems

In 2008, when Glavatskih and Höglund first suggested the expression “tribotronics,” (Glavatskih and Höglund, 2008) they envisioned one approach to active control of friction could be through the possible use of electrorheological fluids. Electrical bias of the surfaces in tribological contact lubricated by polar liquids would in this case allow the composition, structure and boundary film formation attributes to be varied. Ideally this would be performed in a tunable and reversible manner. Experiments performed under electrochemical conditions using molten salts or electrolyte solutions constitute physical realizations of this approach (Figure 5). Ionic liquids are molten salts whose melting points below room temperature (Fedorov and Kornyshev, 2014). Their low melting points are the results of weak electrostatic interactions between the ions, which also hinders their ordering into a crystalline solid lattice. Weakened electrostatic forces are achieved by incorporating at least one large and organic ionic species, which increases the distance between neighboring charged centers. Studies of ILs as lubricants have been rapidly increasing in recent years. This section presents a selection of results from the current literature.

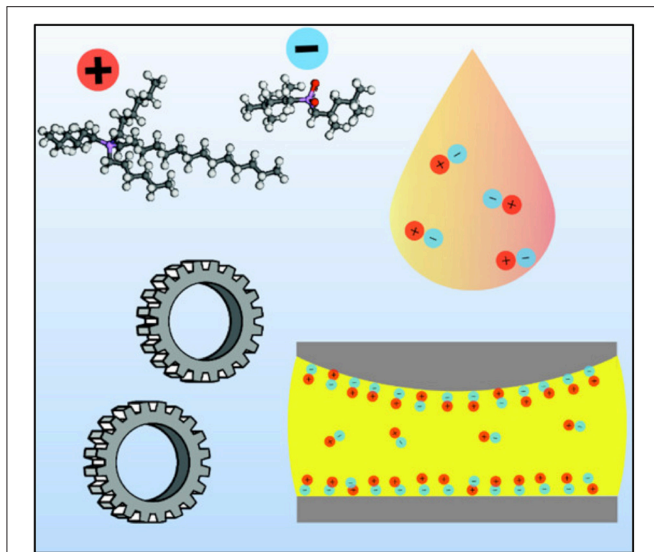


FIGURE 5 | Schematic of ionic liquid as a lubricant additive. Externally applied electric fields reposition the charged constituents within the confines of a contact. Reprinted with permission from Zhou and Qu (2017).

Example 20: Ball on Disk Studies of Ionic Liquid Lubrication at Electrified Interfaces (Kong et al., 2016)

Kong et al. (2016) have reported on the tribological performance of ionic liquids at electrified interfaces with a macroscale stainless steel ball on stainless steel disk reciprocating tribometer. They varied the bias voltage from 0 to 10V, and measured friction coefficients as a function of the applied bias. Three ionic liquids were studied: 1-Ethyl-3-methylimidazolium tetrafluoroborate ([C2MIM][BF₄]), 1-Butyl-3-methylimidazolium tetrafluoroborate ([C4MIM][BF₄]), and 1-Hexyl-3-methylimidazolium tetrafluoroborate ([C6MIM][BF₄]) (Purity: 99%). These were characterized by a fixed anionic structure and cationic backbone with different alkyl side chain lengths.

They observed the friction coefficient to increase by almost a factor of two under the applied bias voltage, from about 0.08 to 0.014 for the shortest side chain length studied. The effect was less pronounced for the longer chain lengths. They attributed the difference in response to either the greater flexibility of the longer side chains or possibly differences in electrical conductivity. The latter could potentially impact the strength of the response to the applied field.

Example 21: Control of Nanoscale Friction on Gold Surfaces in Ionic Liquids and Electrolytes via Electric Potential-Induced Changes to the Surface Chemistry, Structure, and/or Lubricant Layers (Wanless et al., 1994; Sweeney et al., 2012; Hausen et al., 2013)

Sweeney et al. and also Hausen et al. have measured friction coefficients for nanoscale contacts on gold surfaces in an AFM lubricated by an ionic liquid or electrolyte under an applied bias voltage (Sweeney et al., 2012; Hausen et al., 2013). The AFM instruments in these studies employed tips and contacts that were

immersed directly in a surrounding liquid, and electric fields were applied to the contacts by positioning working, counter and quasireference electrodes close to the contacts (Wanless et al., 1994). While both groups studied gold surfaces, Hausen et al. focused on changes to the surface structure and chemistry of the gold surface as well as changes to the electrolyte induced by the external field. Sweeney et al. focused on how changes to an ionic liquid surrounding the contact impacted friction levels.

Hausen et al. utilized a Au(100) surface and a silicon AFM tip immersed in perchloric acid, and the potential was varied between 0 and +1.45 V. Reversible surface oxidation occurs at 1.2V, with a corresponding increase in friction coefficient. The researchers also succeeded to reversibly induce surface reconstruction and oxidation by varying the bias between -0.12V and +0.5V for contacts immersed in 0.05 M H₂SO₄. The friction coefficients in the latter study varied between 0.02 and 0.04, respectively for the reconstructed and oxidized surfaces.

Sweeney et al. studied an ionic liquid system consisted of 1-butyl-1-methylpyrrolidinium tris(pentafluoroethyl)trifluorophosphate (1/2Py_{1,4}FAP) confined between silica colloid probes or sharp silica tips and a Au(111) substrate (Sweeney et al., 2012). The bias voltage was varied between -2 and +1.5V, and friction coefficients varied, respectively, in the range of approximately 0.15 to 0.7. The researchers explained the results as evidence for the confined ion layer between the two surfaces changing from cation-enriched (at negative potentials) to anion-enriched (at positive potentials) when the bias was varied. Tuning frictional forces reversibly at the molecular level was therefore achieved without changing the substrates and employing a self-replenishing boundary lubricant of low vapor pressure.

Example 22: AFM and Neutron Reflectance Studies of an Ionic Liquid Lubricant Enabling Superlubricity to be Switched on and off *in situ* Using an Electrical Potential (Li et al., 2014; Pilkington et al., 2018)

Li et al. (2014) have reported on the tribological performance of ionic liquid lubrication of a silica tip sliding on a graphite surface, and report friction coefficients falling below 0.01 in the low friction state (Li et al., 2014).

The researchers applied a +1.5V potential to the graphite surface, which changed the ion composition of the boundary layer and thus the lubricity. At positive potentials, when the interfacial ion layer was anion rich, and the friction fell below the detection limits of the instrument, thus the term superlubricity. The ionic liquid used for these studies was 1-hexyl-3-methylimidazolium tris(pentafluoroethyl)trifluorophosphate ([HMIm] FAP), a material that is chemically stable to both air and water. Later studies by (Pilkington et al., 2018) have directly detected the response of ionic liquids to applied fields by means of a neutron reflectance technique (Pilkington et al., 2018).

Example 23: Molecular Dynamics Simulations of Friction Force Microscopy of Ionic Liquid Lubricated Contacts (Fajardo et al., 2015; Pivnic et al., 2018)

Fajardo et al. employed molecular dynamics simulations and a coarse-grained model of ionic liquids, to study mechanisms

of electro-tunable friction for ionic liquids confined between planar substrates. Their model employed parameters to simulate the ionic liquid 1-butyl-3-methylimidazolium hexafluorophosphate, BMIM+PF₆⁻ confined between mica surfaces. Their modeling effort focussed on the shape and the intramolecular charge distribution of the ions, and how it impacted frictional drag forces. As expected, externally applied electric fields were found to induce significant structural changes in the film, which in turn gave rise to modification of friction forces.

A major conclusion of the study was the authors' finding that although only a specific system was modeled, the results were applicable to a wide range of ionic system lubricants. In particular, they found that an electric-field-induced shift of the slippage plane from the solid-liquid interface to the interior of the film was common. Quoting their summary, two generic trends were in evidence: (Fajardo et al., 2015)

- (1) *"The friction force reaches a maximum as a function of surface charge. This maximum corresponds to the charge at which the slippage plane shifts one layer away from the solid-liquid interface to the boundary between the counterion- and co-ion-rich layers."*
- (2) *"The nanoscale film will exhibit the electrostriction/electroswelling effect, which will be asymmetric with respect to the sign of the surface charge, as long as the cations and anions have different molecular shapes, chemical structures, and intramolecular charge distributions."*

Pivnic et al. (2018) also employed molecular dynamics simulations and a coarse-grained model to examine a tip-substrate geometry lubricated by one layer of an ionic liquid (Pivnic et al., 2018). Their work revealed the dependence of the friction force on the electrode surface charge density to be dependent on the motion of the confined liquid relative to the substrate and tip. This in turn was found to be dependent on two primary factors: (1) the strengths of the ion-substrate and ion-tip interactions, and (2) the degree of commensurability between characteristic ion dimensions and that of the substrate and tip surface lattices.

Example 24: Impact of Surface Roughness on Ionic Lubricant Tribological Performance (David et al., 2017)

David et al. (2017) studied the impact of surface roughness on electro-tuning by means of ionic liquids, noting that most prior studies examined atomically smooth surfaces while in

practice most contacting surfaces were rough. Their studies were performed by means of non-equilibrium molecular dynamics for a range of increasingly rough surfaces. Surface roughness was introduced in the form of a periodic array of parallel troughs with rectangular cross sections. The dimensions of the troughs were varied in order to change the degree of roughness.

The researchers found friction to depend on both the direction of shear (parallel or perpendicular to the troughs) as well as the roughness, and increased with roughness for the specific systems studied. The friction force was observed to display a maximum at a specific surface charge density. Strengthening of the substrate-liquid dispersion interactions acted to shift this maximum toward lower surface charge levels. The authors also noted that surface roughness has also been reported in the literature to decrease friction in systems that exhibit roughness profiles distinct from that which they modeled. The sensitive dependence on roughness therefore presents both a challenge and opportunity for custom atomic scale design of ionic lubricant systems.

Example 25: Ionic Liquids as Lubricant Additives: A Review (Zhou and Qu, 2017)

The majority of studies of ionic liquids as lubricants have studied pure (neat) fluids or as base fluids for lubricants. The lubricating features nonetheless have been commonly attributed to boundary layer formation of adlayers whose structures are controlled by the external field. The use of ionic fluids as an additive is increasingly growing as an area of research since a breakthrough in achieving miscibility in non-polar hydrocarbon oils was achieved in the past few years. Small quantities of ionic liquids added to a base fluid appear to be equally effective as lubrication by the pure ionic liquid. Zhou and Qu (2017) provide a review of how ionic liquids have recently been used as additives, including an effort to correlate lubricity with cationic and anionic structures, oil-solubility, and other relevant physicochemical properties.

AUTHOR CONTRIBUTIONS

The author confirms being the sole contributor of this work and has approved it for publication.

FUNDING

This work was supported by National Science Foundation Award Number DMR1535082.

REFERENCES

- Acharya, B., Seed, C. M., Brenner, D. W., Smirnov, A. I., and Krim, J. (2019). Tuning friction at material-nanoparticle-liquid interfaces with an external electric field. arXiv:1901.10512.
- Altfeder, I., and Krim, J. (2012). Temperature dependence of nanoscale friction for Fe on YBCO. *J. Appl. Phys.* 111:094916. doi: 10.1063/1.4717983
- Ashtiani, M., Hashemabadi, S. H., and Ghaffari, A. (2015). A review on the magnetorheological fluid preparation and stabilization. *J. Mag. Mater.* 374, 716–730. doi: 10.1016/j.jmmm.2014.09.020
- Benad, J., Nakano, K., Popov, V. L., and Popov, M. (2018). Active control of friction by transverse oscillations. *Friction*. 7, 74–85 doi: 10.1007/s40544-018-0202-1
- Benassi, A., Schwenk, J., Marioni, M. A., Hug, H. J., and Passerone, D. (2014). Microscale motion control through ferromagnetic films. *Adv. Mater. Interfaces* 1:1400023. doi: 10.1002/admi.201400023
- Berman, D., Erdemir, A., and Sumant, A. V. (2018). Approaches for achieving superlubricity in two-dimensional materials. *ACS Nano* 12, 2122–2137. doi: 10.1021/acsnano.7b09046
- Boulware, J. C., Ban, H., Jensen, S., and Wassom, S. (2010a). Experimental studies of the pressures generated by a liquid oxygen slug in a magnetic field. *J. Mag. Mater.* 322, 1752–1757. doi: 10.1016/j.jmmm.2009.12.022

- Boulware, J. C., Wassom, S., Jensen, S., and Ban, H. (2010b). "The magnetohydrodynamic response of liquid oxygen: experimentation and simulation," in AIP Conference Proceedings (Tuscon, AZ), 1554–1561. doi: 10.1063/1.3422336
- Coffey, T., and Krim, J. (2005). Impact of substrate corrugation on the sliding friction levels of adsorbed films. *Phys. Rev. Lett.* 95:076101. doi: 10.1103/PhysRevLett.95.076101
- Curtis, C. K., Marek, A., Smirnov, A. I., and Krim, J. (2017). A comparative study of the nanoscale and macroscale tribological attributes of alumina and stainless steel surfaces immersed in aqueous suspensions of positively or negatively charged nanodiamonds. *Beilstein J. Nanotechnol.* 8, 2045–2059. doi: 10.3762/bjnano.8.205
- David, A., Fajardo, O. Y., Kornyshev, A. A., Urbakh, M., and Bresme, F. (2017). Electrotunable lubricity with ionic liquids: the influence of nanoscale roughness. *Faraday Discuss.* 199, 279–297. doi: 10.1039/C6FD00244G
- De Vicente, J., Klingenberg, D. J., and Hidalgo-Alvarez, R. (2011). Magnetorheological fluids: a review. *Soft Matt.* 7, 3701–3710. doi: 10.1039/c0sm01221a
- de Wijn, A. S., Fasolino, A., Filippov, A. E., and Urbakh, M. (2014). Nanoscopic friction under electrochemical control. *Phys. Rev. Lett.* 112:055502. doi: 10.1103/PhysRevLett.112.055502
- de Wijn, A. S., Fasolino, A., Filippov, A. E., and Urbakh, M. (2016). Effects of molecule anchoring and dispersion on nanoscopic friction under electrochemical control. *J. Phys.* 112:055502. doi: 10.1088/0953-8984/28/10/105001
- Démery, V., and Dean, D. S. (2010). Drag forces in classical fields. *Phys. Rev. Lett.* 104:080601. doi: 10.1103/PhysRevLett.104.080601
- Drummond, C. (2012). Electric-field-induced friction reduction and control. *Phys. Rev. Lett.* 109:154302. doi: 10.1103/PhysRevLett.109.154302
- Fajardo, O. Y., Bresme, F., Kornyshev, A. A., and Urbakh, M. (2015). Electrotunable friction with ionic liquid lubricants: how important is the molecular structure of the ions? *J. Phys. Chem. Lett.* 6:3998–4004. doi: 10.1021/acs.jpclett.5b01802
- Fedorov, M. V., and Kornyshev, A. A. (2014). Ionic liquids at electrified interfaces. *Chem. Rev.* 114, 2978–3036. doi: 10.1021/cr400374x
- Fredricks, Z. B., Stevens, K. M., Kenny, S., Acharya, B., and Krim, J. (2019). Tuning nanoscale friction by applying weak magnetic fields to reorient adsorbed oxygen molecules. *Condensed Matt.* 4:1. doi: 10.3390/condmat4010001
- Gabureac, M., Viret, M., Ott, F., and Fermon, C. (2004). Magnetoresistance in nanocontacts induced by magnetostrictive effects. *Phys. Rev. B.* 69:100401. doi: 10.1103/PhysRevB.69.100401
- Glavatskih, S., and Höglund, E. (2008). Tribotronics—towards active tribology. *Tribol. Int.* 41, 934–939. doi: 10.1016/j.triboint.2007.03.001
- Hausen, F., Zimmet, J. A., and Bennewitz, R. (2013). Surface structures and frictional properties of Au (100) in an electrochemical environment. *Surface Sci.* 607, 20–24. doi: 10.1016/j.susc.2012.08.009
- Highland, M., and Krim, J. (2006). Superconductivity dependent friction of water, nitrogen, and superheated He films adsorbed on Pb (111). *Phys. Rev. Lett.* 96:226107. doi: 10.1103/PhysRevLett.96.226107
- Ismail, M. N., Harvey, T. J., Wharton, J. A., Wood, R. J., and Humphreys, A. (2009). Surface potential effects on friction and abrasion of sliding contacts lubricated by aqueous solutions. *Wear* 267, 1978–1986. doi: 10.1016/j.wear.2009.06.007
- Kabeel, A. E., El-Said, E. M., and Dafea, S. A. (2015). A review of magnetic field effects on flow and heat transfer in liquids: present status and future potential for studies and applications. *Renew. Sustain. Energy Rev.* 45:830–837. doi: 10.1016/j.rser.2015.02.029
- Kisiel, M., Gnecco, E., Gysin, U., Marot, L., Rast, S., and Meyer, E. (2011). Suppression of electronic friction on Nb films in the superconducting state. *Nat. Mater.* 10:119. doi: 10.1038/nmat2936
- Kong, L., Huang, W., and Wang, X. (2016). Ionic liquid lubrication at electrified interfaces. *J. Phys.* 49:225301. doi: 10.1088/0022-3727/49/22/225301
- Kreer, T. (2016). Polymer-brush lubrication: a review of recent theoretical advances. *Soft Matt.* 12, 3479–3501. doi: 10.1039/C5SM02919H
- Krim, J. (2012). Friction and energy dissipation mechanisms in adsorbed molecules and molecularly thin films. *Adv. Phys.* 61, 155–323. doi: 10.1080/00018732.2012.70640
- Krim, J., Yu, P., and Behringer, R. P. (2011). Stick-slip and the transition to steady sliding in a 2d granular medium and a fixed particle lattice. *Pure Appl. Geophys.* 168:2259–2275. doi: 10.1007/s00024-011-0364-5
- Li, H., Wood, R. J., Rutland, M. W., and Atkin, R. (2014). An ionic liquid lubricant enables superlubricity to be "switched on" *in situ* using an electrical potential. *Chem. Commun.* 50, 4368–4370. doi: 10.1039/c4cc00979g
- Lu, X., Khonsari, M. M., and Gelinck, E. R. (2006). The Stribeck curve: experimental results and theoretical prediction. *J. Tribol.* 128, 789–794. doi: 10.1115/1.2345406
- Mao, X., Popov, V. L., Starcevic, J., Popov, M. (2017). Reduction of friction by normal oscillations. II. In-plane system dynamics. *Friction* 5, 194–206. doi: 10.1007/s40544-017-0146-x
- Müser, M. H., Wenning, L., and Robbins, M. O. (2001). Simple microscopic theory of amontons's laws for static friction. *Phys. Rev. Lett.* 86:1295. doi: 10.1103/PhysRevLett.86.1295
- Pardue, T. N., Acharya, B., Curtis, C. K., and Krim, J. (2018). A tribological study of γ -Fe₂O₃ nanoparticles in aqueous suspension. *Tribol. Lett.* 66:130. doi: 10.1007/s11249-018-1083-1
- Park, J. Y., Ogletree, D. F., Thiel, P. A., and Salmeron, M. (2006). Electronic control of friction in silicon pn junctions. *Science* 313:186. doi: 10.1126/science.1125017
- Park, J. Y., Qi, Y., Ogletree, D. F., Thiel, P. A., and Meron, S. (2007). Influence of carrier density on the friction properties of silicon pn junctions. *Phys. Rev. B.* 76:064108. doi: 10.1103/PhysRevB.76.064108
- Pierro, M., Bruschi, L., Fois, G., Mistura, G., Boragno, C., de Mongeot, F. B., et al. (2010). Nanofriction of neon films on superconducting lead. *Phys. Rev. Lett.* 105:016102. doi: 10.1103/PhysRevLett.105.016102
- Pilkington, G. A., Harris, K., Bergendal, E., Reddy, A. B., Palsson, G. K., Vorobiev, A., et al. (2018). Electro-responsivity of ionic liquid boundary layers in a polar solvent revealed by neutron reflectance. *J. Chem. Phys.* 148:193806. doi: 10.1063/1.5001551
- Pivnic, K., Fajardo, O. Y., Bresme, F., Kornyshev, A. A., and Urbakh, M. (2018). Mechanisms of electrotunable friction in friction force microscopy experiments with ionic liquids. *J. Phys. Chem.* 122, 5004–5012. doi: 10.1021/acs.jpcc.8b00516
- Popov, M., and Li, Q. (2018). Multimode active control of friction, dynamic ratchets and actuators. *Phys. Mesomech.* 21, 24–31. doi: 10.1134/s1029959918010046
- Popov, M., Popov, V. L., and Popov, N. V. (2017). Reduction of friction by normal oscillations. I. Influence of contact stiffness. *Friction* 5, 45–55. doi: 10.1007/s40544-016-0136-4
- Qi, Y., Park, J. Y., Hendriksen, B. L., Ogletree, D. F., and Salmeron, M. (2008). Electronic contribution to friction on GaAs: an atomic force microscope study. *Phys. Rev. B.* 77:184105. doi: 10.1103/PhysRevB.77.184105
- Rajauria, S., Ruiz, O., Canchi, S. V., Schreck, E., and Dai, Q. (2018). Electrostatically tunable adhesion in a high speed sliding interface. *Phys. Rev. Lett.* 120:026101. doi: 10.1103/PhysRevLett.120.026101
- Rodriguez-López, J., Castro, P., de Vicente, J., Johannsmann, D., Elvira, L., Morillas, J. R., et al. (2015). Colloidal stability and magnetic field-induced ordering of magnetorheological fluids studied with a quartz crystal microbalance. *Sensors* 15, 30443–30456. doi: 10.3390/s151229808
- Socoliuc, A., Gnecco, E., Maier, S., Pfeiffer, O., Barattoff, A., Bennewitz, R., et al. (2006). Atomic-scale control of friction by actuation of nanometer-sized contacts. *Science* 313, 207–210. doi: 10.1126/science.1125874
- Sweeney, J., Hausen, F., Hayes, R., Webber, G. B., Endres, F., Rutland, M. W., et al. (2012). Control of nanoscale friction on gold in an ionic liquid by a potential-dependent ionic lubricant layer. *Phys. Rev. Lett.* 109:155502. doi: 10.1103/PhysRevLett.109.155502
- Tusch, S., Kundu, A., Verley, G., Blondel, T., Miralles, V., Démoulin, D., et al. (2014). Energy versus information based estimations of dissipation using a pair of magnetic colloidal particles. *Phys. Rev. Lett.* 9:112. doi: 10.1103/PhysRevLett.112.180604
- Vlachová, J., König, R., and Johannsmann, D. (2015). Stiffness of sphere-plate contacts at MHz frequencies: dependence on normal load, oscillation amplitude, and ambient medium. *Beilstein J. Nanotechnol.* 6:845. doi: 10.3762/bjnano.6.87
- Wanless, E. J., Senden, T. J., Hyde, A. M., Sawkins, T. J., and Heath, G. A. (1994). A new electrochemical cell for atomic force microscopy. *Rev. Sci. Instrum.* 65, 1019–1020. doi: 10.1063/1.1145108

- Wei, Q., Cai, M., Zhou, F., and Liu, W. (2013). Dramatically tuning friction using responsive polyelectrolyte brushes. *Macromolecules* 46, 9368–9379. doi: 10.1021/ma401537j
- Wolloch, M., Levita, G., Restuccia, P., and Righi, M. C. (2018). Interfacial charge density and its connection to adhesion and frictional forces. *Phys. Rev. Lett.* 121:026804. doi: 10.1103/PhysRevLett.121.026804
- Wolter, B., Yoshida, Y., Kubetzka, A., Hla, S. W., von Bergmann, K., and Wiesendanger, R. (2012). Spin friction observed on the atomic scale. *Phys. Rev. Lett.* 109:116102. doi: 10.1103/PhysRevLett.109.116102
- Wu, Y., Wei, Q., Cai, M., and Zhou, F. (2015). Interfacial friction control. *Adv. Mater. Interfaces* 2:1400392. doi: 10.1002/admi.201400392
- Zeng, H., Zhang, Y., Mao, S., Nakajima, H., and Uchiyama, K. (2017). A reversibly electro-controllable polymer brush for electro-switchable friction. *J. Mater. Chem.* 5, 5877–5881. doi: 10.1039/C7TC01624G
- Zhao, M., Zhang, J., Yao, J., and Peng, Z. (2017). Effects of nano-diamond on magnetorheological fluid properties. *Nano* 12:1750119. doi: 10.1142/S1793292017501193
- Zhou, Y., and Qu, J. (2017). Ionic liquids as lubricant additives: a review. *ACS Appl. Mater. Interface* 9, 3209–3222. doi: 10.1021/acsami.6b12489
- Zhu, Y. Y., Kelsall, G. H., and Spikes, H. A. (1994). The influence of electrochemical potentials on the friction and wear of iron and iron oxides in aqueous systems. *Tribol. Trans.* 37, 811–819. doi: 10.1080/10402009408983363
- Conflict of Interest Statement:** The author declares that the research was conducted in the absence of any commercial or financial relationships that could be construed as a potential conflict of interest.
- Copyright © 2019 Krim. This is an open-access article distributed under the terms of the Creative Commons Attribution License (CC BY). The use, distribution or reproduction in other forums is permitted, provided the original author(s) and the copyright owner(s) are credited and that the original publication in this journal is cited, in accordance with accepted academic practice. No use, distribution or reproduction is permitted which does not comply with these terms.



Macroscale Superlubricity Achieved With Various Liquid Molecules: A Review

Xiangyu Ge, Jinjin Li* and Jianbin Luo*

State Key Laboratory of Tribology, Tsinghua University, Beijing, China

OPEN ACCESS

Edited by:

Valentin L. Popov,
Technische Universität Berlin,
Germany

Reviewed by:

Wenling Zhang,
University of Alberta, Canada
Ali Erdemir,
Argonne National Laboratory (DOE),
United States

*Correspondence:

Jinjin Li
lijinjin@mail.tsinghua.edu.cn
Jianbin Luo
luojb@tsinghua.edu.cn

Specialty section:

This article was submitted to
Tribology,
a section of the journal
Frontiers in Mechanical Engineering

Received: 17 December 2018

Accepted: 17 January 2019

Published: 05 February 2019

Citation:

Ge X, Li J and Luo J (2019)
Macroscale Superlubricity Achieved
With Various Liquid Molecules: A
Review. *Front. Mech. Eng.* 5:2.
doi: 10.3389/fmech.2019.00002

Superlubricity is generally classified as solid superlubricity and liquid superlubricity according to the lubricants involved at the interfaces, and is a popular research topic in tribology, which is closely linked to energy dissipation. Significant advancements in both experimental studies and theoretical analysis have been made regarding superlubricity in the past two decades. Compared with solid superlubricity, liquid superlubricity has many advantages; e.g., it is more easily achieved at the macroscale and less sensitive to the surface smoothness and atmospheric conditions. In the present study, the advancements in liquid superlubricity at the macroscale are reviewed, and the corresponding mechanisms for various types of liquid lubricants are discussed. This investigation is important for engineering traditional mechanical lubricating systems. Finally, the issues regarding the liquid superlubricity mechanism and the future development of liquid superlubricity are addressed.

Keywords: macroscale superlubricity, liquid lubricants, polymers, acid-based lubricants, room-temperature ionic liquids, oil-based lubricants, nanomaterial-based lubricants

INTRODUCTION

Because the energy consumption and material losses derived from friction and wear in mechanical systems place large economic and environmental burdens on all nations (Erdemir and Eryilmaz, 2014), studies on lubrication technology and mechanisms are very important for energy conservation and emission reduction. Since it was invented in the early 1990s (Shinjo and Hirano, 1993), superlubricity has attracted extensive concentration from researchers in many fields (Tisza, 1938; Meyer and Gnecco, 2014; Baykara et al., 2018; Li et al., 2018a,b). It describes a phenomenon where the friction force between two sliding surfaces nearly vanishes ideally (Hirano, 2014) or a state in which the sliding coefficient of friction (COF) is <0.01 in actual mechanical lubricating systems (Erdemir et al., 2007).

Superlubricity is generally classified as solid superlubricity and liquid superlubricity according to the lubricants involved at the interfaces (Baykara et al., 2018; Berman et al., 2018; Sinclair et al., 2018). Solid superlubricity at the nanoscale or microscale is easily achieved with two-dimensional materials, such as molybdenum disulfide (Martin et al., 1994), graphite flakes (Liu et al., 2012), boron nitride (BN) (Song et al., 2018), and graphene (Feng et al., 2013). It has also been achieved at dissimilar interfaces, including the crystalline gold/graphite interface (Cihan et al., 2016), graphene nanoribbons/gold interface (Kawai et al., 2016), and silica/graphite interface

(Li et al., 2018a). However, solid superlubricity at the macroscale is rarely achieved (Li et al., 2018b), owing to the strict requirement of atomically smooth contact in these materials. In contrast to solid superlubricity, many liquid lubricants have been found to possess a macroscale superlubricity property, such as water (Xu and Kato, 2000; Zhou et al., 2005), oils (Bouchet et al., 2007; Matta et al., 2008), and polymers (Muller et al., 2003; Zhang et al., 2017). The superlubricity mechanism of these lubricants accounts for the formation of a hydrogen-bond network, a tribofilm, a hydration layer, or a molecular brush, depending on the properties of the lubricants. Recently, our group found that a phosphoric acid aqueous solution ($\text{H}_3\text{PO}_{4(\text{aq})}$) as a liquid lubricant could achieve superlubricity at the $\text{Si}_3\text{N}_4/\text{SiO}_2$ interface with an extremely low COF of 0.004 under maximum initial contact pressures of 700 MPa (Li et al., 2011, 2012, 2013a). According to the superlubricity mechanism of $\text{H}_3\text{PO}_{4(\text{aq})}$, a series of acid-based lubricants composed of different polyhydroxy alcohols and acids were established (Li et al., 2013b,c). Among these acid-based lubricants, the one composed of polyethylene glycol (PEG) and boric acid (BA) allows superlubricity to be achieved under neutral conditions, avoiding acid corrosion (Ge et al., 2018a). Room-temperature ionic liquids (RTILs) are well-known as eco-friendly lubricants and lubricating additives (Ge et al., 2015; Jiang et al., 2018). Research into the superlubricity property of RTILs has been performed by experts recently (Espinosa et al., 2014). Because RTILs can be designed by combining a variety of cations and anions, it is possible to develop RTILs possessing not only the superlubricity property but also special properties for different operating conditions. One of the issues for liquid lubricants is that the wear is severe during the wearing-in period. To alleviate this defect, a mixture of short-chain dihydric alcohol and graphene-oxide nanoflakes (GONFs) is explored, making it possible to achieve macroscale superlubricity and super-low wear simultaneously.

To better illustrate the differences of the superlubricity materials and their corresponding superlubricity mechanisms, these superlubricity materials are classified into 6 main types based on the main functioning materials during superlubricity period. The “Water” section describes the first discovery of superlubricity at a ceramic interface. The “Polymers” section reviews the superlubricity property of polymers. The “Acid-Based Aqueous Lubricants” section presents the development of a single phosphoric acid into a series of acid-based lubricants composed of acids and polyhydroxy alcohols. The “RTIL Lubricants” section outlines recent advances in RTILs, focusing on their superlubricity mechanism. The “Oil-Based Lubricants” section describes the superlubricity achieved with oils and oil-like liquids. The “Nanomaterial-Based Lubricants” section focuses primarily on the feasibility of macroscale superlubricity achieved with nanomaterials (like GONFs, BN, NaOH-modified black phosphorus (BP-OH), layered double hydroxide nanoplatelets (LDH), and nanodiamonds) as additives. The “Conclusions and Outlook” section concludes the paper, offering perspectives and suggestions for future research on macroscale liquid superlubricity.

WATER

The first liquid superlubricity phenomenon was discovered by Tisza with helium II in 1938 (Tisza, 1938); it was called superfluidity at that time. In 1987, water was found to provide superlubricity at the $\text{Si}_3\text{N}_4/\text{Si}_3\text{N}_4$ interface, and an extremely low COF—even <0.002 —was achieved after a wearing-in period (Tomizawa and Fischer, 1987). The wearing-in process provides ultra-smooth surfaces and a very low contact pressure. The smooth surfaces make the lubrication enter the elastohydrodynamic lubrication (EHL) regime, in which a thin water film exists at the interface and provides low viscous friction. In addition to smooth surfaces, tribochemical reactions contribute to the superlubricity. Induced by shear, a tribochemical film is formed on the surfaces via tribochemical reactions, as indicated by Equations (1, 2) (Spikes and Tysoe, 2015; Khajeh et al., 2018). This film has extremely low shear resistance and can be maintained on the surfaces during the rubbing process. Analysis shows that this tribofilm is composed of colloidal silica, which can produce the electrical double layer, leading to very low friction in boundary lubrication (BL). Therefore, an extremely low friction is achieved in the mixed lubrication (ML) regime (EHL + BL) under a low contact pressure. Later, several studies on ceramic lubrication, e.g., using SiC, were performed under water lubrication (Chen et al., 2001, 2002). These studies report that the COFs under water lubrication can decrease to 0.01 or even less, but the wearing-in period is significantly longer than that for a $\text{Si}_3\text{N}_4/\text{Si}_3\text{N}_4$ tribopair, as depicted in **Figure 1**. Their superlubricity mechanism is similar to that of $\text{Si}_3\text{N}_4/\text{Si}_3\text{N}_4$ tribopairs: the large friction reduction results from the decrease of the contact pressure and the formation of the colloidal silica tribofilm as indicated by Equations (2, 3).

However, there are two issues for ceramic tribopairs under water lubrication. First, the wear on ceramic surfaces is too large. To solve this issue, amorphous carbon nitride coatings (a-CN_x) are deposited on the surface of a Si_3N_4 disc. For an $\text{a-CN}_x/\text{Si}_3\text{N}_4$ tribopair, after a wearing-in period under water lubrication, an average stable COF of ~ 0.007 is achieved at a sliding speed of 160 mm/s and a normal load of 5 N (Zhou et al., 2007). Moreover, the wear rate of the Si_3N_4 ball in an $\text{a-CN}_x/\text{Si}_3\text{N}_4$ tribopair is only 1/35 of that in a $\text{Si}_3\text{N}_4/\text{Si}_3\text{N}_4$ tribopair under water lubrication. The wear mechanism of $\text{a-CN}_x/\text{Si}_3\text{N}_4$ is the formation of a carbonaceous transfer film on the a-CN_x coatings via a tribochemical reaction between the a-CN_x coatings and water induced by friction. The second issue is that the superlubricity of ceramic tribopairs under water lubrication can hardly be achieved under a high contact pressure; thus, laser texturing technology is applied to SiC/SiC tribopairs to improve the load-carrying capacity of their surfaces (Wang et al., 2001). The critical load, under which the COF suddenly increases, is used to evaluate the effect of the surface texture, and a high critical load indicates that the load-carrying capacity is high. The authors conclude that the optimum pore area ratio (the ratio of the area occupied by pores to the area of the end surface) is 2.8% for SiC for providing the highest critical load, which is 20% higher

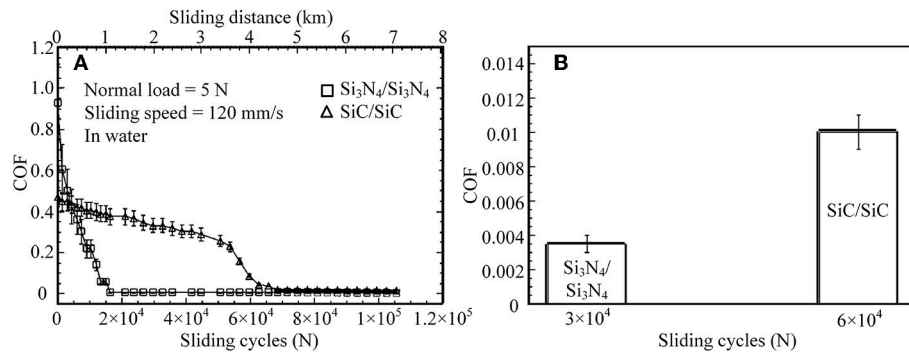


FIGURE 1 | (A) COFs for various sliding cycles and sliding distance, (B) average COFs for various sliding cycles. Si₃N₄/Si₃N₄ and SiC/SiC tribopairs under water lubrication: the normal load is 5 N, the sliding speed is 120 mm/s. Chen et al. (2001) Copyright 2001, Springer.

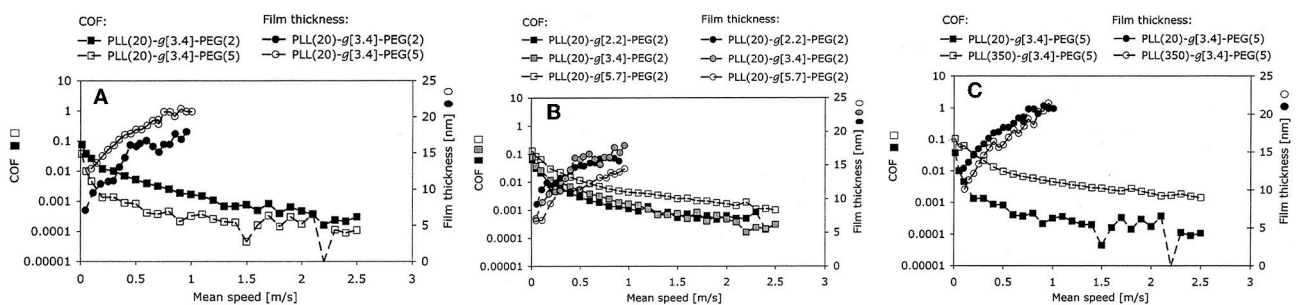
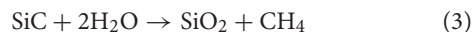
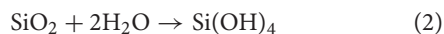
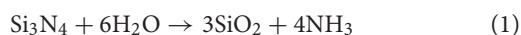


FIGURE 2 | Effects of (A) the molecular weight of the PEG side chains, (B) the Lys/PEG grafting ratio, and (C) the molecular weight of the PLL backbone on the COF. The lubricant film thickness was measured with respect to the speed using an MTM and ultrathin-film interferometry. Muller et al. (2003) Copyright 2003, Springer.

than that of the untextured SiC surface (Wang et al., 2001).

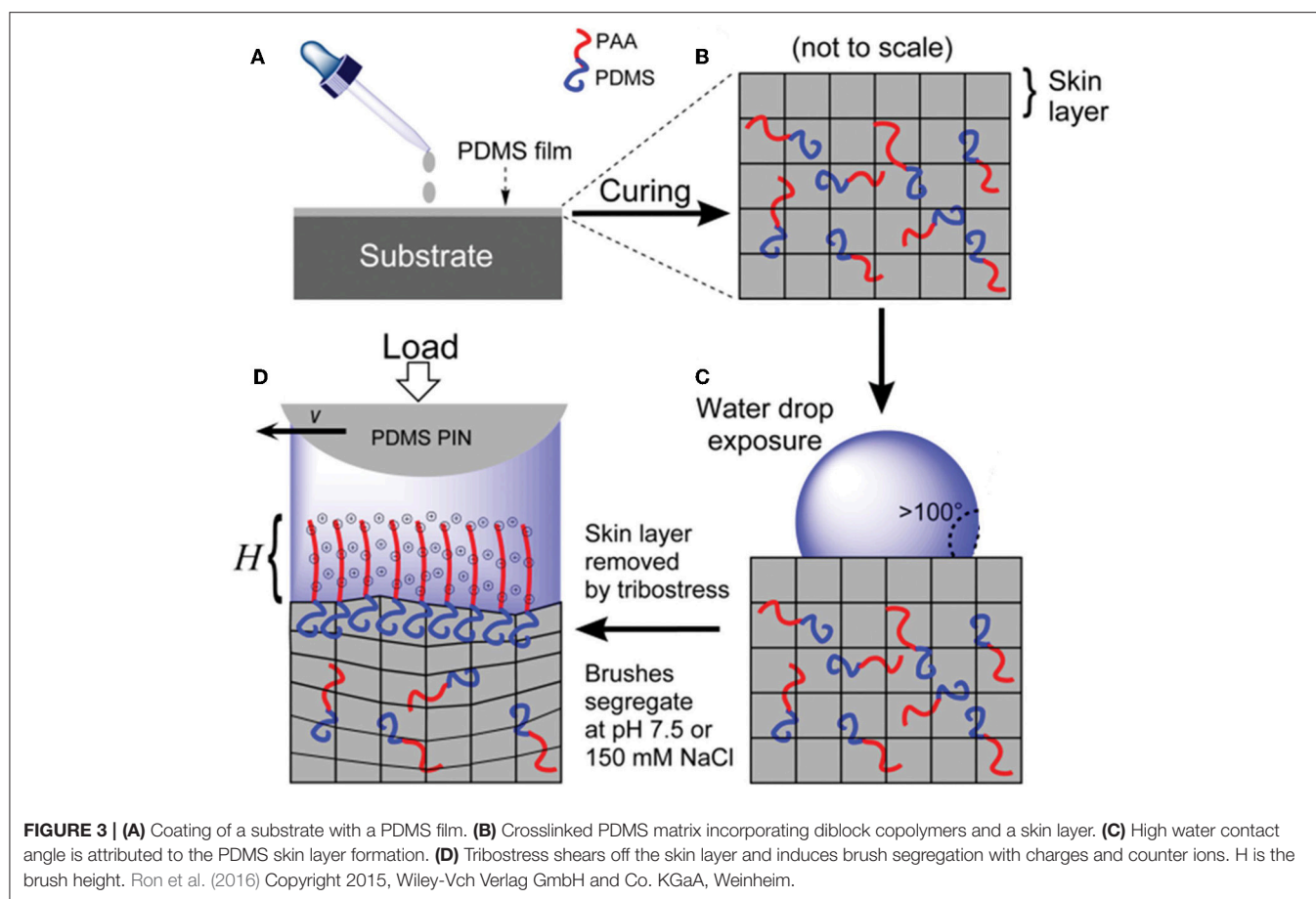


POLYMERS

Because they can be both solid-like to sustain a normal load and liquid-like to shear easily (Baykara et al., 2018), polymers are usually grafted onto contact surfaces to form polymer brushes, which can be adsorbed on the charged surfaces via electrostatic adsorption, and are accompanied by good solvents for achieving superlubricity. For instance, the copolymer poly(L-lysine)-g-poly(ethylene glycol) (PLL-g-PEG) can be synthesized by grafting PEG onto poly(L-lysine) (PLL) and has proven to be an effective biomimetic BL additive in aqueous lubrication (Lee et al., 2003). An extremely low COF of 0.0001 was achieved on a mini-traction machine (MTM), which allows rolling friction testing; thus the hydrodynamic effect is very strong (Muller et al., 2003). The influence of the chemical architecture on the lubricity performance has been studied in detail, including the side-chain (PEG) length, Lys/PEG grafting ratio, and backbone chain (PLL) length, as depicted in Figure 2. The authors demonstrate that both the increase of the molecular weight of PEG and the

reduction of the grafting ratio enhance the lubricity properties of the aqueous PLL-g-PEG solution at low sliding velocities, and the increase of the molecular weight of the PLL leads to an increase of the COF. The superlubricity mechanism for a neutral brush is as follows: the permeation pressure of the solvent makes the PEG chains spread throughout the aqueous solution, leading to the formation of molecular brushes and the separation of the contact surfaces, which can greatly reduce the friction (Raviv et al., 2003). A solvent layer with low shear resistance between the brush layers helps to achieve superlubricity (Klein, 2013). The superlubricity mechanism of a charged brush is similar to that of a neutral brush at low pressures. However, at high pressures, the permeation pressure of the trapped counter-ions provides extra load support, while the hydration layer formed between the two polymer surfaces provides low friction (Raviv et al., 2003; Inutsuka et al., 2013; Klein, 2013; Ron et al., 2016), thereby improving the performance of the charged brush compared with a neutral brush.

Recently, researchers reported a new grafting method for acquiring hydrophilic polymer brushes on poly(dimethyl siloxane) (PDMS) surfaces (Ron et al., 2016). This method is based on the selective separation of the hydrophilic chain in an amphiphilic diblock copolymer under water conditions, as depicted in Figure 3. The amphiphilic diblock copolymers can be formed by charged hydrophilic poly(acrylic acid) (PAA) and PDMS or by neutral PEG and PDMS and are denoted



as PDMS-b-PAA and PDMS-b-PEG, respectively. This grafting strategy causes the polymer brushes to be regenerated *in situ*. For instance, when the brush layer is damaged under harsh operating conditions, it can be readily self-restored without any external supports. This self-restoring feature makes it very useful for lubricating systems, because the stability and durability of lubricants are very important for a steady lubricating performance. Friction test results show that under different conditions, including the substrate, load, counter surface, pH, and salinity, the COFs of these two polymer brushes are between 0.001 and 0.05 for soft contacts. Moreover, charged PAA exhibits far better lubricity than neutral PEG, which is explained by the significantly lower free energy of the PAA chains upon hydration.

Recently, poly(vinylphosphonic acid) (PVPA) with salt ions was found to achieve superlubricity on a $\text{Ti}_6\text{Al}_4\text{V}$ /polytetrafluoroethylene tribopair. Research into the superlubricity mechanism reveals that the cations and anions function together to achieve the superlubricity even under harsh conditions (Zhang et al., 2017). This finding makes PVPA-modified $\text{Ti}_6\text{Al}_4\text{V}$ a potential material for artificial implants. It is concluded that when used as lubricants, polymers must be accompanied by a good solvent. In this way, solvent molecules can improve the stretching of polymer brushes for inducing a permeation pressure to sustain a normal load and provide low friction.

Similar to polymers, macroscale superlubricity could be achieved with hydrated alkali metal ions (Li^+ , Na^+ , K^+) based on hydration effect (Han et al., 2018). This superlubricity is attributed to the hydration layer formed by alkali metal ions, providing hydration repulsive force and having a liquid-like response to shear. This work paves the way to the macroscale superlubricity induced by hydration effect and therefore to the wide application of hydration lubrication.

ACID-BASED AQUEOUS LUBRICANTS

Phosphoric acid as a lubricant was first found to achieve superlubricity at the Si_3N_4 /glass interface in 2011 (Li et al., 2011). Thereafter, acid-based lubricants as a new series of lubricants were investigated by the authors in detail at various tribopairs, such as Si_3N_4 /glass, Si_3N_4 / SiO_2 , Si_3N_4 /sapphire, and ruby/sapphire (Deng et al., 2014; Li et al., 2014). As depicted in **Figure 4a**, when a Si_3N_4 ball slides on a glass disc under the lubrication of $\text{H}_3\text{PO}_4(\text{aq})$, the COF decreases from 0.45 to 0.004 after a wearing-in period of 600 s. The wearing-in period is vital to the achievement of superlubricity and can be divided into two stages according to the evolution of the COF with time. In each wearing-in stage, a different mechanism accounts for the friction reduction.

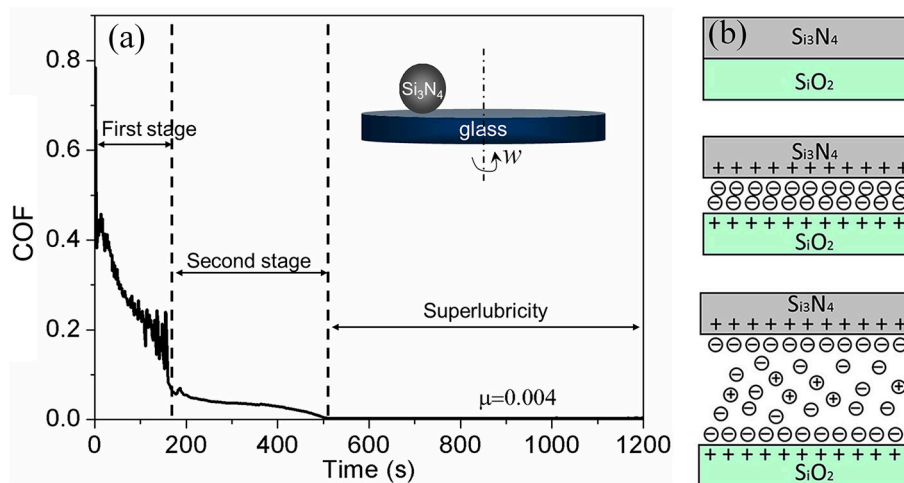


FIGURE 4 | (a) Evolution of the COF with time under lubrication with an H_3PO_4 aqueous solution ($\text{pH} = 1.5$). Inset is the ball-on-disk model for friction testing. The tribopair is Si_3N_4 /glass, the load is 3 N, and the sliding velocity is 75 mm/s. (Li et al., 2013a) Copyright 2013, AIP Publishing LLC. (b) Schematic of the lubrication model, including three kinds of contacts. Li et al. (2012) Copyright 2012, American Chemical Society.

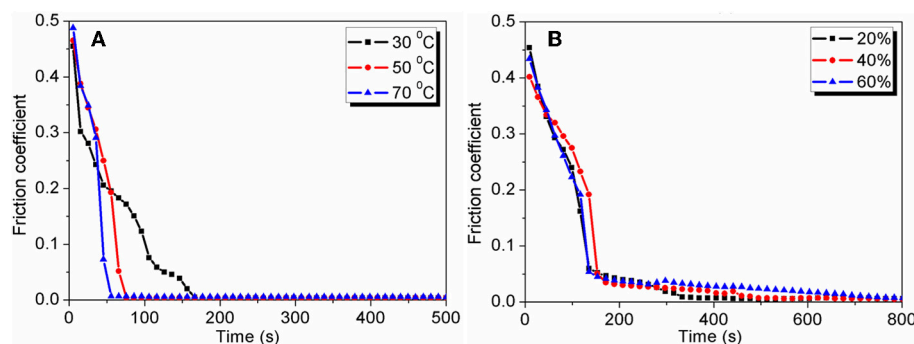
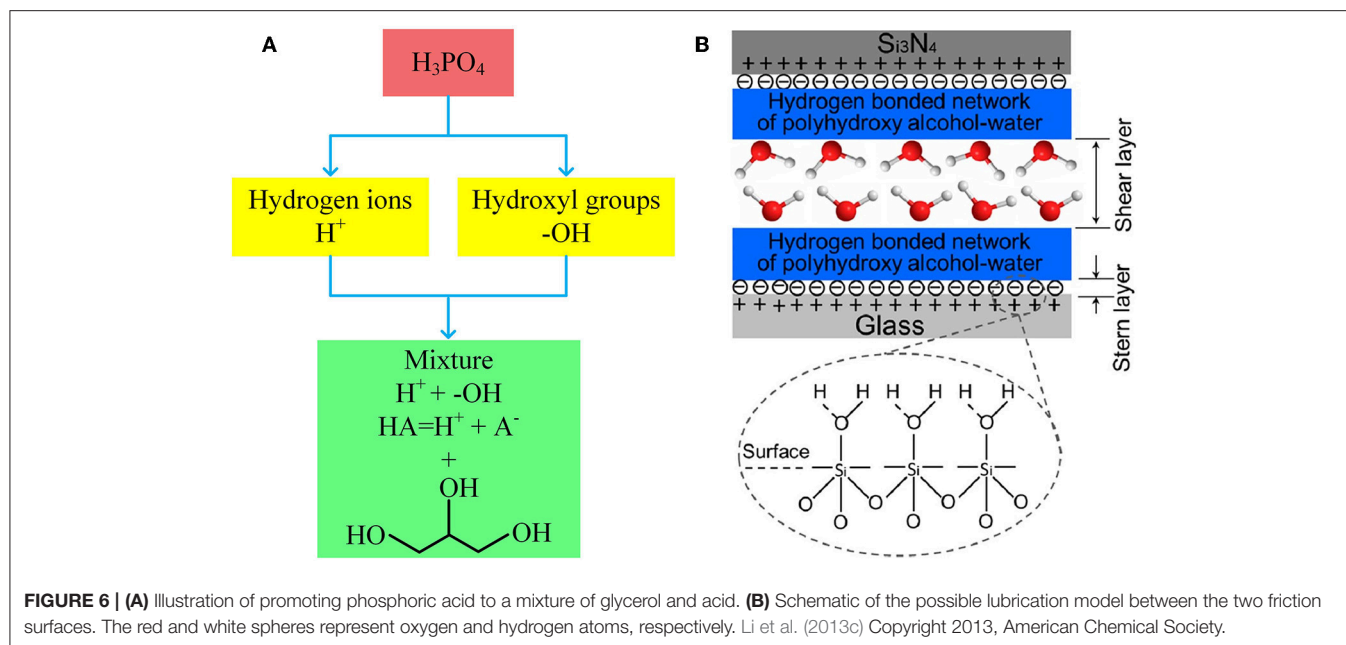


FIGURE 5 | Effects of the temperature and humidity. (A) Evolution of the COF with time under lubrication with H_3PO_4 ($\text{pH} = 1.5$) at different temperatures, at a humidity of 25%. (B) Evolution of the COF with time under lubrication with H_3PO_4 ($\text{pH} = 1.5$) at different humidity values, at a temperature of 25°C. The tribopair is Si_3N_4 /glass, the load is 3 N, and the sliding velocity is 75 mm/s.

In the first wearing-in stage, H^+ ions play a key role in the rapid reduction of the COF from 0.45 to 0.05. Because there are $\equiv \text{SiOH}$ bonds on the surfaces of glass and Si_3N_4 , the H^+ ions in H_3PO_4 can be adsorbed on the contact surfaces via the protonation reaction (Sjoberg, 1996; Sahai, 2002), making the contact surfaces become positively charged after the first wearing-in stage. The surface charge is balanced by H_2PO_4^- anions; therefore, a stern layer and diffuse double layer form between the two charged surfaces (Figure 4b), which provide a repulsive force and a hydration force, respectively. With the increase of the contact area, which is caused by wear, the contact pressure decreases. After the first wearing-in stage, the contact pressure, hydration force, and repulsive force are in an equilibrium state, leading to significant friction reduction.

Although H^+ ions strongly affect the friction reduction in the first wearing-in stage, they cannot realize superlubricity directly. Among the acids, only H_3PO_4 is found to realize superlubricity

after the second wearing-in stage; the COF decreases from 0.05 to 0.004 gradually. For other acids, there is no second wearing-in stage, and the COF remains larger than 0.01 (Li et al., 2012), indicating that the second wearing-in stage is unique to H_3PO_4 . H_3PO_4 is in a liquid state before the end of second wearing-in stage, when only a solid-like layer is observed on the wear track. This is because the free water evaporates completely from the lubricant at the end of the second wearing-in stage, resulting in only hydrated water molecules remaining in the solid-like layer. Thus, the second wearing-in stage is closely related to the water evaporation, which has been experimentally proven at different temperatures and humidities, as depicted in Figure 5. At a lower temperature or a higher humidity, a longer wearing-in period is needed to vaporize the water completely. The chemical composition of the solid-like layer is investigated using Raman spectroscopy, which shows that the solid-like layer is composed of the hydrogen-bond network of H_3PO_4 and



hydrated water molecules (Li et al., 2013a). If the hydrogen-bond network is destroyed by adding 2 μL of pure water to the wear track, the superlubricity state is destroyed immediately (Li et al., 2011), indicating that the superlubricity is closely related to the hydrogen-bond network. Moreover, the low friction state of phosphoric acid was simulated by reactive molecular dynamics (Yue et al., 2013). The simulation result at a temperature between 300 and 600 K shows no tribochemical reaction occurred, and the COF reduced due to the acceleration in both rotational- and translational-motions of lubricant molecules and the weakened hydrogen-bond network.

Based on the foregoing analysis, the superlubricity model of H_3PO_4 is proposed. In the first wearing-in stage, H^+ and H_2PO_4^- ions are adsorbed on the contact surfaces, forming the stern layer. After the second wearing-in stage, the hydrogen-bond network is adsorbed above the stern layer and plays a key role in sustaining load. In addition to providing load support, an important function of the hydrogen-bond network is locking water molecules in the contact region. It is inferred that a thin hydrated water layer is adsorbed on the surface of the hydrogen-bond network because of the strong hydrogen-bond effect of the H_3PO_4 molecules, similar to a water layer adsorbed on the top of surface of ice (Dash et al., 1995). During sliding, shearing occurs in the hydrated water layer because of its good fluidity under a high pressure (Klein, 2013).

The superlubricity model of H_3PO_4 indicates that this type of superlubricity is dominated by two factors: the positively charged surfaces formed by the adsorption of H^+ ions and the hydrogen-bond network of H_3PO_4 and water molecules. Accordingly, it is possible to achieve superlubricity with a mixture of acid and polyhydroxy alcohol, because the H^+ ions from the acid can satisfy the first factor and the hydroxyl groups from the polyhydroxy alcohol can satisfy the second factor, as depicted in Figure 6A.

TABLE 1 | Lowest COF under lubrication with four kinds of polyhydroxy alcohols and their mixtures with four kinds of acid lubricants (H_2SO_4 , HCl , $\text{H}_2\text{C}_2\text{O}_4$, and $\text{H}_3\text{NO}_3\text{S}$, $\text{pH} = 1$).

	No acid	H_2SO_4	HCl	$\text{H}_2\text{C}_2\text{O}_4$	$\text{H}_3\text{NO}_3\text{S}$
1,2-ethanediol	0.05	0.004	0.004	0.004	0.003
1,3-propanediol	0.07	0.004	0.003	0.003	0.003
1,4-butanediol	0.06	0.004	0.005	0.005	0.004
1,5-pentanediol	0.06	0.004	0.006	0.004	0.003

The tribo pair is $\text{Si}_3\text{N}_4/\text{glass}$, the load is 3 N, and the sliding velocity is 75 mm/s. Data are obtained from Li et al. (2013c), Copyright 2013, American Chemical Society.

To prove this hypothesis, mixtures of acids (H_2SO_4 , HCl , $\text{H}_2\text{C}_2\text{O}_4$, and $\text{H}_3\text{NO}_3\text{S}$, $\text{pH} = 1$) and polyhydroxy alcohols (glycerol, 1,2-ethanediol, 1,3-propanediol, 1,4-butanediol, and 1,5-pentanediol) were prepared and tested. If the tests are performed with these polyhydroxy alcohols only, the minimum COF would be larger than 0.05. If the tests are performed with the mixtures, the friction behavior of the mixtures is similar to that of H_3PO_4 : the COF decreases to ~ 0.05 during the wearing-in period and then gradually decreases to < 0.01 (Li et al., 2013b,c). The minimum COFs of these mixtures are listed in Table 1, indicating that superlubricity can be achieved by the mixtures of acids and polyhydroxy alcohols.

The superlubricity of these mixtures is affected by the concentration of polyhydroxy alcohol in the mixture. Superlubricity can be achieved if the concentration of polyhydroxy alcohols is less than a critical value, which is 40, 50, 40, and 30% for 1,2-ethanediol, 1,3-propanediol, 1,4-butanediol, and 1,5-pentanediol, respectively. The superlubricity mechanism of these acid-based mixtures is as follows: the hydrogen-bond network formed by polyhydroxy alcohols and water molecules is adsorbed onto the surface of the stern layer (induced by H^+ ions) during the wearing-in period; thus,

a hydrated water layer is formed, yielding superlubricity, as depicted in **Figure 6B** (Li et al., 2013c).

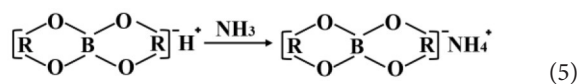
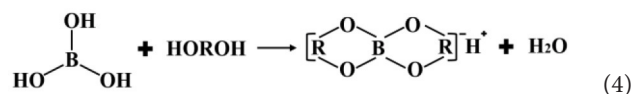
To check whether all the alcohols can be mixed with acid to achieve superlubricity, three key characteristics of alcohols that affect their physicochemical properties are investigated: the number of hydroxyl groups, the position of the hydroxyl groups on the C-C skeletal chain, and the length of the C-C skeletal chain (Li et al., 2013c). **Figure 7A** shows the friction results for lubrication with four mixtures of alcohols (1-propanol, 2-propanol, 1,2-propanediol, and 1,3-propanediol) and H_2SO_4 (pH = 1). Clearly, the mixtures formulated with 1-propanol and 2-propanol cannot achieve superlubricity. Because there is only one hydroxyl group in 1-propanol and 2-propanol and there are two or three hydroxyl groups in the other three kinds of alcohols, there should be at least two hydroxyl groups in the structure for achieving superlubricity. Moreover, comparing the result for 1,2-propanediol with that for 1,3-propanediol reveals that the position of the hydroxyl groups hardly affects the superlubricity. The effect of the length of the carbon chain is tested with mixtures of H_2SO_4 and five other polyhydroxy alcohols: ethylene glycol, diethylene glycol, triethylene glycol, tetraethylene glycol, and pentaethylene glycol, which have 2, 4, 6, 8, and 10 carbon atoms in the C-C skeletal chain, respectively. The results in **Figure 7B** indicate that superlubricity can be achieved by all five mixtures and that the length of the C-C skeletal chain has no obvious effect on the superlubricity (Li et al., 2013c).

As mentioned previously, the two factors for superlubricity are the H^+ ions and the hydrogen-bond network. The first factor can be satisfied for all mixtures because of the existence of acid, but if the alcohol has only one hydroxyl group in its molecular structure, it cannot form a hydrogen-bond network with water molecules and thus cannot satisfy the second factor for superlubricity. If the alcohol has more than one hydroxyl group in its molecular structure, it can form the hydrogen-bond network with water molecules, yielding superlubricity. The position of the hydroxyl groups and the number of carbon atoms in the C-C skeletal chain have no effect on the hydrogen-bond network formation and thus have no obvious effect on the superlubricity.

Analysis of the superlubricity behavior of H_3PO_4 and the mixtures of polyhydroxy alcohols and acids reveals that their superlubricity mechanism is the same and that the two critical factors for superlubricity are the H^+ ions and the hydrogen-bond network. The H^+ ions help to form the stern layer on the surfaces via the protonation reaction, which requires the pH of the lubricant to be <2. The hydrogen-bond network provides load support and locks water molecules in the contact region, which requires the existence of at least two hydroxyl groups in the lubricant molecular structure. The authors proved that these two factors are required for achieving superlubricity. The steady COF achieved with only H^+ ions (e.g., acid, except for H_3PO_4) is >0.03, and that achieved with only the hydrogen-bond network (e.g., glycerol only) is >0.02. The superlubricity mechanism of the acid-based lubricants is attributed to both the formation of the hydrogen-bond network and the stern layer. The friction results and mechanism indicate that if a liquid lubricant satisfies two criteria—possessing H^+ ions (pH ≤ 2) and at least two hydroxyl groups in its molecule—liquid superlubricity can

be achieved. Therefore, a novel system of liquid superlubricity based on H^+ ions and hydroxyl groups is established, and this study offers a new method for achieving liquid superlubricity.

However, the strong acidity of these acid-based lubricants limits their applications in a practical mechanical system. Recently, a new type of acid-based lubricant, which is a mixture of BA and a PEG aqueous solution ($\text{PEG}_{(\text{aq})}$), was synthesized and found to provide superlubricity (COF ≈ 0.004) in neutral conditions (pH ≈ 6.4) at $\text{Si}_3\text{N}_4/\text{SiO}_2$ interfaces, as depicted in **Figure 8** (Ge et al., 2018a). The mechanism of this superlubricity achieved in neutral conditions is similar to that of acid-based lubricants discussed previously. The neutral condition is attributed to the tribochemical reactions (Equation 4) between PEG (denoted as HOROH, where R is the alkyl chain) and BA (Shteinberg, 2011), which can provide sufficient H^+ to form the stern layer and to reduce the friction during the wearing-in period. The H^+ then can be consumed by further reaction (Equation 5) with NH_3 from the reaction of Equation (1) to maintain a neutral condition (Shteinberg, 2009). Furthermore, a tribochemical layer is formed on the contact surfaces to provide low friction. Such liquid superlubricity achieved in neutral conditions is of immense importance to both scientific understanding and industrial technology implementation.



RTIL LUBRICANTS

RTILs are a series of well-known lubricants and lubricant additives in surface science and engineering (Ye et al., 2001; Qu et al., 2012, 2015) because they can improve the lifetime of mechanical systems by reducing the friction and providing wear protection (Holmberg et al., 2012). The tribological properties of RTILs, such as the friction reduction, anti-wear, and anti-corrosion properties, have been well explored (Somers et al., 2013; Fan et al., 2014; Saurin et al., 2016; Li et al., 2017). However, studies of the superlubricity of RTILs have only been performed under a very low normal load (0.02 N) in combination with carbon quantum dots (Ma et al., 2017), or at the microscale between a SiO_2 /graphite tribopair (Li et al., 2014). Therefore, the macroscale superlubricity of RTILs under high normal loads must be investigated.

Recently, as depicted in **Figure 9**, researchers explored the robust superlubricity of a 1-ethyl-3-methylimidazolium trifluoromethanesulfonate ([EMIM]TFS) aqueous solution between a $\text{Si}_3\text{N}_4/\text{SiO}_2$ tribopair (Ge et al., 2018b). A COF as low as 0.002 was achieved under neutral conditions (pH ≈ 6.9 ± 0.1). Surface analysis shows that a tribochemical layer is deposited on the contact surfaces and provides low friction. This tribochemical layer is formed by tribochemical reactions and

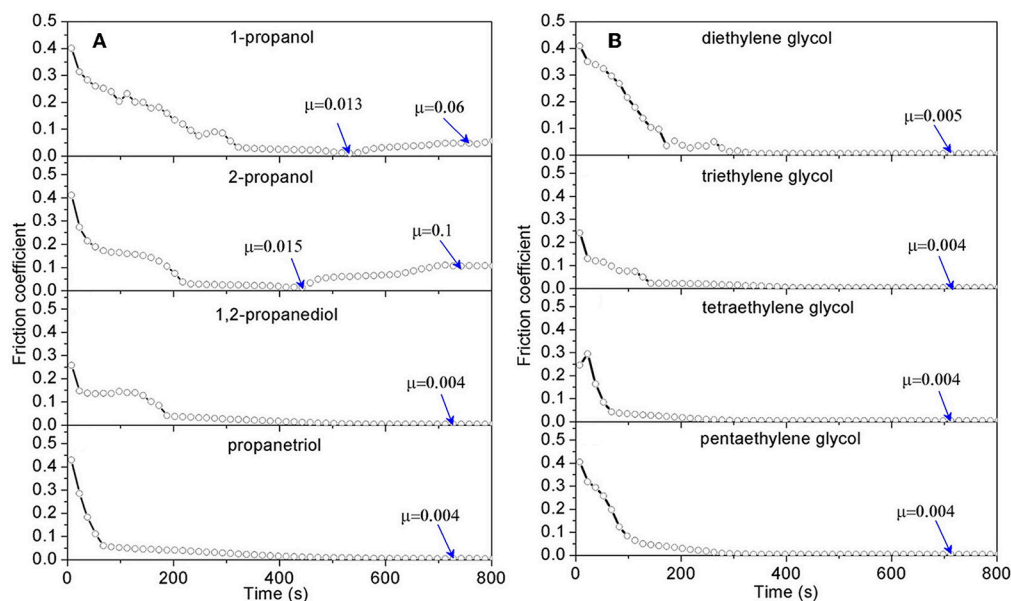


FIGURE 7 | COF under lubrication with mixtures of H_2SO_4 solution and polyhydroxy alcohols (A) with 3 carbon atoms in its carbon chain; (B) with various carbon chain length. The volume ratio of the polyhydroxy alcohols to the H_2SO_4 solution (pH 1) is 10:1. Li et al. (2013c) Copyright 2013, American Chemical Society.

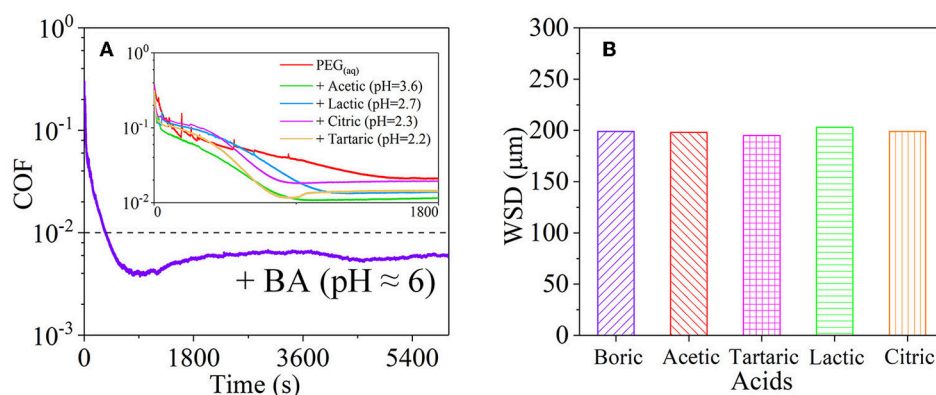


FIGURE 8 | (A) COFs and (B) wear scar diameter (WSD) of the mixtures of PEG and several acids: BA, acetic acid, tartaric acid, lactic acid, and citric acid. Ge et al. (2018a) Copyright 2018, American Chemical Society.

comprises [EMIM]TFS, colloidal silica, ammonia-containing compounds, and sulfides. Moreover, a fluid layer between the contact surfaces provides a low shear resistance. Because it has the superlubricity property under neutral conditions, [EMIM]TFS has great potential in engineering applications. Notably, RTILs can be designed by combining various cations and anions, giving rise to numerous potential RTILs with the superlubricity property. Nevertheless, the search for RTILs with the superlubricity property is in an initial stage, and additional research on the physicochemical and superlubricity properties is required.

OIL-BASED LUBRICANTS

In general, friction for liquid lubrication depends on the lubrication regime, which transitions from BL to ML and then

to EHL. Moreover, the liquid friction is generally the lowest during the transition to EHL, where the thickness of the fluid film is perfect for separating the surfaces completely and providing extremely low viscous friction (Baykara et al., 2018). However, for viscous lubricants, such as oils and polyhydroxy alcohols, the COFs during EHL are ~ 0.05 , which is higher than the maximum value for superlubricity (0.01). Therefore, surface modification of the tribopair is performed to make the surface interact with the viscous lubricants. One of the effective methods for modifying the contact surfaces is surface coating. Superlubricity has been observed for the tetrahedral amorphous carbon (ta-C) coating [a type of hydrogen-free diamond-like carbon (DLC)] under lubrication with poly- α -olefin (PAO), glycerol mono-oleate (GMO), and glycerol under BL (Kano, 2006a,b). The ta-C/steel tribopair shows an extremely low COF of 0.006 under lubrication with PAO + GMO at a sliding velocity of 100 mm/s, while

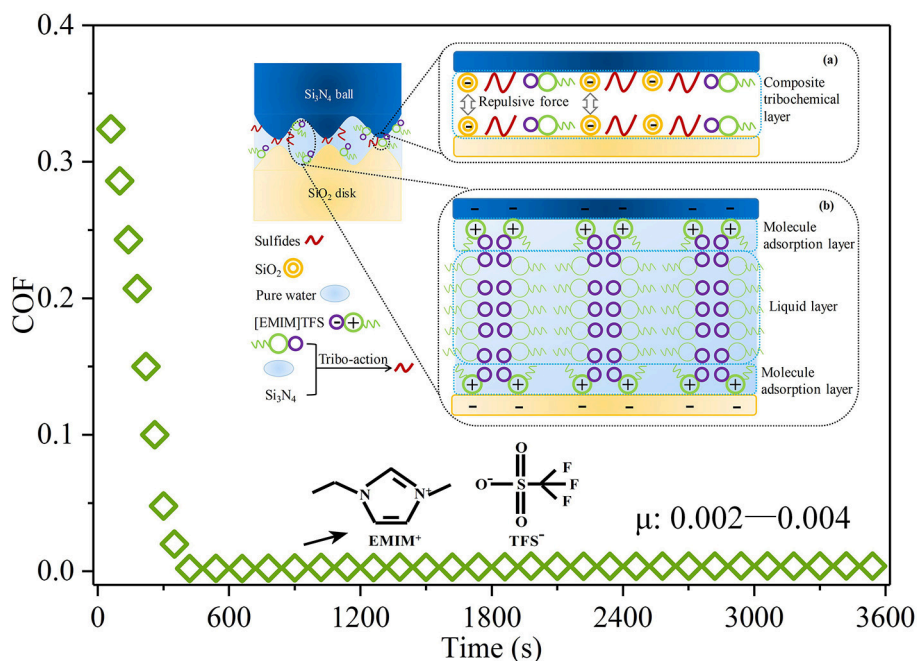


FIGURE 9 | COF of the [EMIM]TFS aqueous solution. The inset shows the proposed superlubricity model. Ge et al. (2018b) Copyright 2018, American Chemical Society.

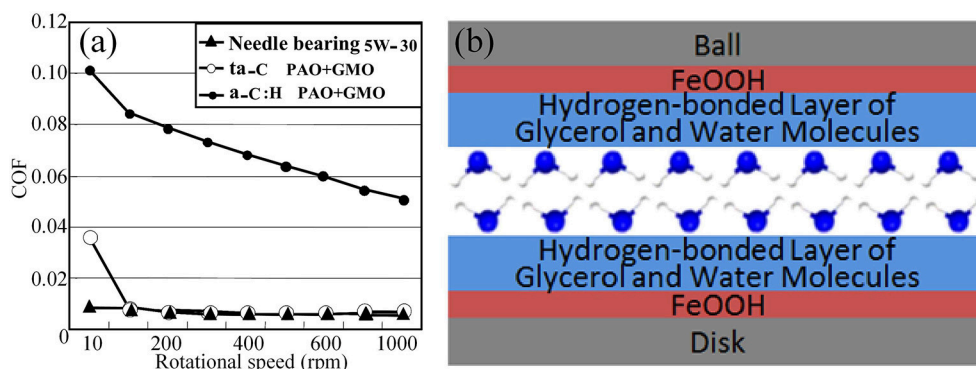
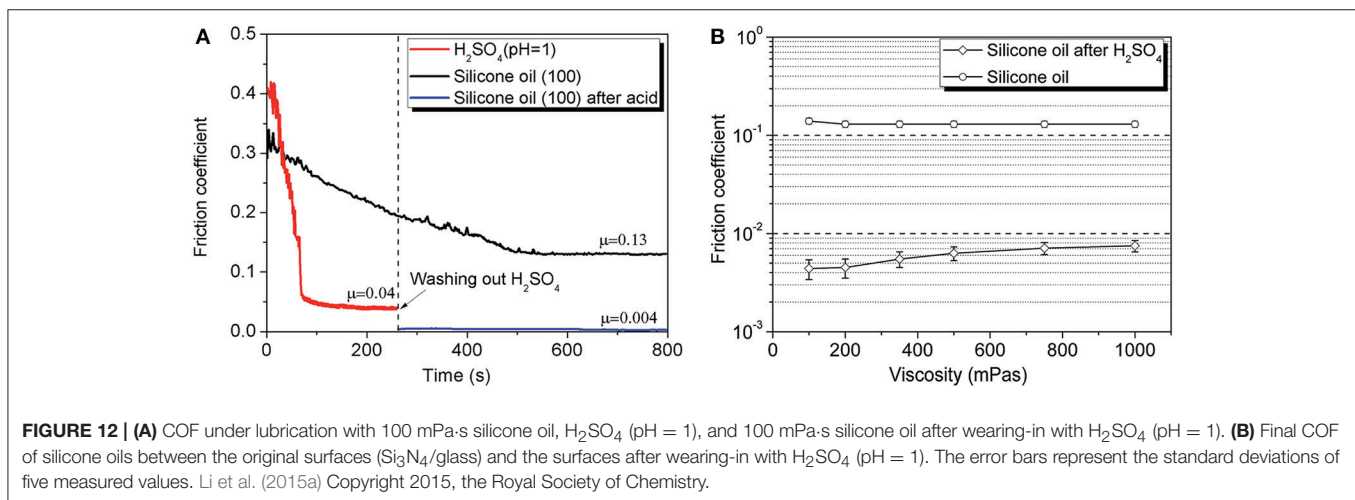
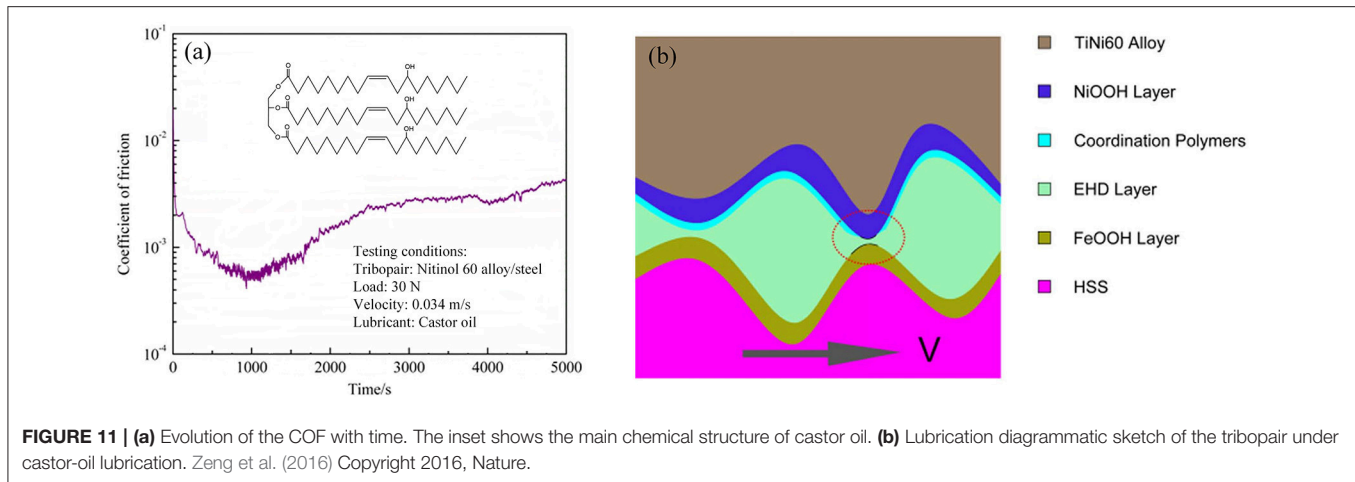


FIGURE 10 | (a) Relationship between the COF and the rotational speed. Bouchet et al. (2007) Copyright 2007, IOP Publishing Ltd. (b) Schematic of the lubrication model and molecular schematic presentation of the hydrogen-bond layer of glycerol and water. Chen et al. (2013) Copyright 2013, American Chemical Society.

the COF of a hydrogen-containing DLC/steel tribopair is >0.05 , as depicted in **Figure 10a**. The superlubricity of the ta-C/ta-C tribopair is also achieved under lubrication with glycerol at 80°C (Bouchet et al., 2007; Matta et al., 2008). The computer simulation results show that OH atoms are nearly all bound to surface sp¹ atoms, resulting in the easy sliding property of this triboformed OH-terminated surfaces (Bouchet et al., 2007). At a low temperature, the superlubricity is also associated with the decomposition of glycerol, which generates a thin layer of organic acids and water, and the formation of a hydrogen-bond network (Matta et al., 2008). A similar mechanism applies for the superlubricity of the steel/steel tribopair under lubrication with a mixture of glycerol and *myo*-inositol (Matta et al., 2008), as well

as aqueous glycerol (Chen et al., 2013), as depicted in **Figure 10b**. Notably, the lubrication with glycerol + *myo*-inositol yielded the first achievement of superlubricity in the absence of long-chain polar molecules under BL.

In addition to surface coating, alloys are typically used in mechanical engineering applications for different conditions. Some alloy tribopairs, such as Nitinol 60 alloy/steel tribopairs, are also used to study superlubricity. Superlubricity can be achieved under lubrication with castor oil in the boundary regime. Researchers examined the influence of the sliding speeds and normal loads on the friction in detail (Zeng and Dong, 2013). The results showed that the influence of the sliding speed on the lubricity is greater than that of the load owing to the



chemical structure of castor oil, which is not suitable at high sliding speeds, because of its poor oxidation stability. Therefore, maintaining the sliding speed in an appropriate range is very important for achieving the superlubricity of the Nitinol 60 alloy. The same researchers compared castor oil, turbine oil, seed oil, and paraffin oil, and the results showed that only castor oil can achieve superlubricity for a Nitinol 60 alloy/steel tribopair (Zeng and Dong, 2014). Therefore, the hydroxyl groups branched on the acid chain may be necessary for superlubricity. The main chemical structure of castor oil has three long-chain fatty acids with an alkyl ester group, as depicted in the inset of **Figure 11a**. Thus, castor oil has the ability to form a thin film as an intermolecular layer and reduces the friction between the interfaces (Zeng and Dong, 2013). Analysis shows that tribochemical reactions occur during rubbing motion, including the decomposition of castor oil, the formation of iron oxy-hydroxide, and the triboformed OH-terminated surface with iron oxy-hydroxide. The authors propose a new superlubricity model, as depicted in **Figure 11b**. Here, a lamellar structure is formed by the intercalation of hexanoic acid molecules between Ni and iron oxy-hydroxide, which can provide strong

repulsive electrostatic forces, contributing to the achievement of the superlubricity state (Zeng et al., 2016). As a good vegetable oil, castor oil is an eco-friendly lubricant owing to its excellent properties, such as its high biodegradability, renewability, and superlubricity performance. Therefore, the superlubricity achieved with castor oil makes it suitable for practical engineering applications in many fields, including biotechnology.

Researchers also achieved superlubricity with silicone oil between a Si_3N_4 /glass tribopair by pre-treating the interface with H_2SO_4 (Li et al., 2015a). The COF of silicone oils can decrease to as low as 0.004, which is only 1/30 of its original value (0.13), as depicted in **Figure 12**. The acid helps to form a plane on the ball and a micro-slope on the disc, leading to the reduction of the contact pressure during the wearing-in period. The silicone oil helps to form a hydrodynamic layer between the contact surfaces. The tribochemical reaction between Si_3N_4 and water provides a low friction in ML but hardly affects the friction in EHL. The liquid superlubricity achieved with silicone oil accounts for the formation of ML and EHL between the plane on the ball and the micro-slope on the disc, which are formed

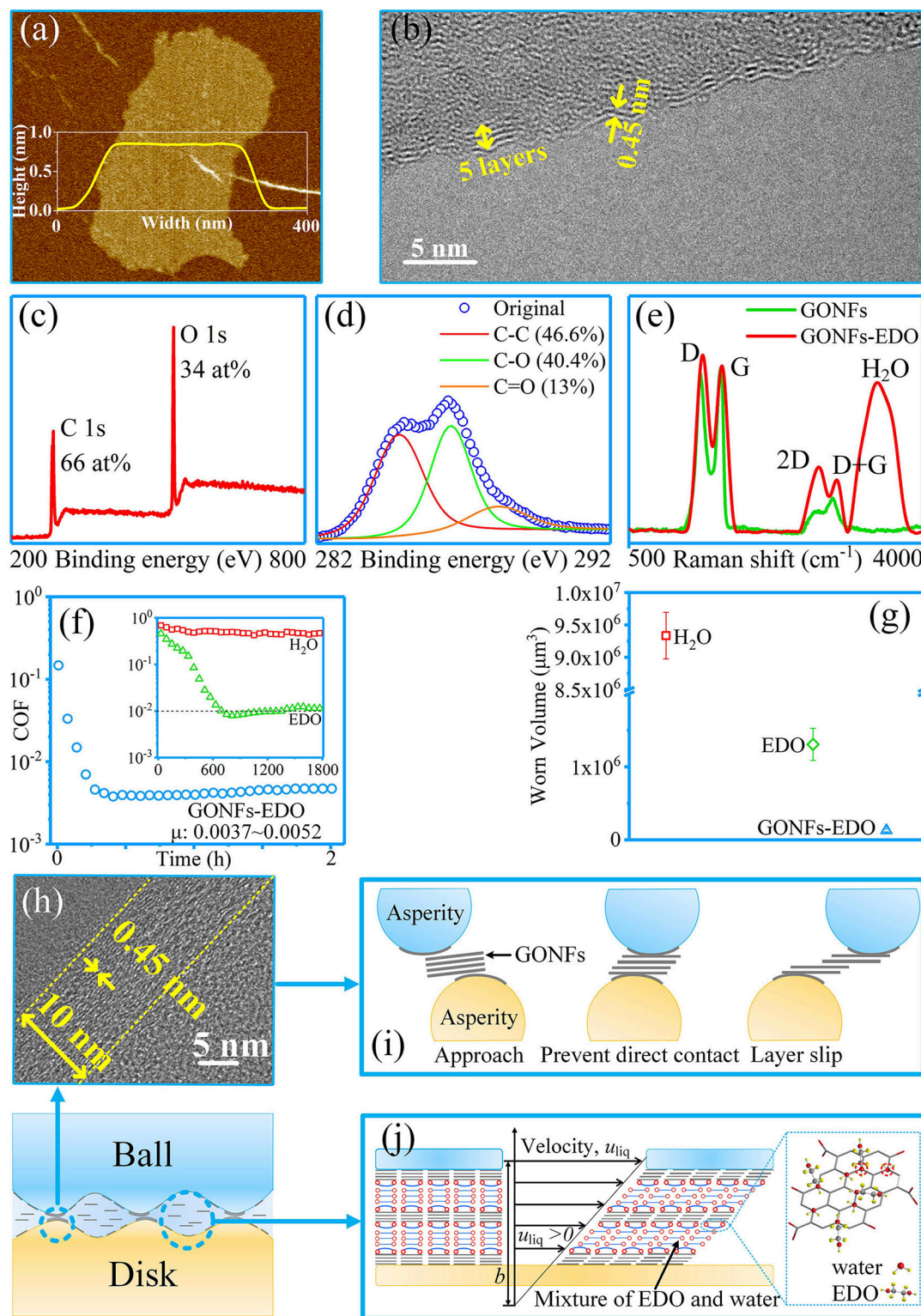


FIGURE 13 | Characterization of GONFs: **(a)** atomic force microscopy image; **(b)** high-resolution transmission electron microscopy (HRTEM) image; **(c,d)** XPS spectra; **(e)** Raman spectra. **(f,g)** Friction and wear testing results for GONFs-EDO. **(h)** HRTEM image of the cross-sectional area of the worn surface. **(i,j)** Proposed superlubricity and anti-wear mechanism of GONFs-EDO. Ge et al. (2018d) Copyright 2018, American Chemical Society.

during the wearing-in period with acid. Later, the same authors found that this kind of superlubricity cannot be achieved at a sapphire/sapphire tribopair when the average contact pressure is >50 MPa (Li et al., 2015b). The authors demonstrated via calculation that this kind of liquid superlubricity is related to both the contact pressure between the contact surfaces and the pressure–viscosity coefficient (PVC) of the lubricant. Their calculation results show that under a high contact pressure, the PVC must be as small as possible to achieve superlubricity, whereas under a low contact pressure, superlubricity can be achieved in a wide range of PVCs. Most recently, our group achieved superlubricity with both polar (polyalkylene glycols (PAG) and non-polar (PAO) oils between a steel/steel tribopair by pre-treating the interface with PEG_(aq) (Ge et al., 2018c). The superlubricity was found to achieve at thin film lubrication regime (Gao et al., 2018; Qiao et al., 2018), which is composed of a tribochemical layer (formed by the tribochemical reaction between PEG and steel surfaces), an ordered layer (formed by the PAG or PAO molecules), and a liquid film of the lubricants.

NANOMATERIAL-BASED LUBRICANTS

One common feature of liquid superlubricity is that a wearing-in process is required before the achievement of superlubricity, which usually leads to severe wear. It has been proven that graphene-oxide (GO) materials can provide wear protection. Through the generation of a GO-adsorption film on the contact surfaces, GO can separate the contact surfaces and reduce the wear (Wu et al., 2018; Zhao et al., 2018). However, the macroscale COFs of GO are generally in the range of 0.02–0.1 (Meng et al., 2015; Jaiswal et al., 2016; Fan et al., 2018; Wu et al., 2018; Zhang et al., 2018; Zhao et al., 2018), indicating a near-superlubricity state or traditional lubrication state.

Our group achieved a macroscale superlubricity state through the synergy effect of GONFs and ethanediol (EDO) at ceramic tribopairs including Si₃N₄/SiO₂, Si₃N₄/Si₃N₄, and Si₃N₄/Sapphire (Ge et al., 2018d). The used GONFs were prepared via a modified Hummers method. They were 0.8 nm thick, had an interlayer spacing of 0.45 nm, and had an oxygen content of 30–40%, as depicted in **Figures 13a–e**. The results for the friction and wear of GONFs-EDO are depicted in **Figures 13f,g**. The COF of GONFs-EDO decreased to <0.01 after the wearing-in period of 600 s; thereafter, the COF further decreased to 0.0037 and remained stable for 2 h. Furthermore, the wear results show that the wear volume of the ball under lubrication with GONFs-EDO ($5.1 \times 10^4 \mu\text{m}^3$) was only 5% of that of the ball under lubrication with EDO ($1.3 \times 10^6 \mu\text{m}^3$). These results indicate the excellent superlubricity and anti-wear performances of GONFs-EDO. GONFs were adsorbed on the surfaces of the tribopair (**Figure 13h**), preventing direct contact between asperities. The super-low shear stresses between the GONFs interfaces contributed to the superlubricity and super-low wear, as depicted in **Figure 13i**. Moreover, the formation of the GONFs-EDO

hydrated network and the partial-slip boundary condition at the GONFs-EDO interface contributed to the super-low shear stresses of the liquid layer, leading to superlubricity, as depicted in **Figure 13j**.

Other nanomaterials like BP-OH, BN, LDH, and nanodiamonds were also found to help the base lubricants achieve superlubricity. The superlubricity mechanism for BP-OH aqueous solution is attributed to the effective lubricating layer formed by the attachment of water molecules on BP-OH nanosheets in the silica-gel (Wang et al., 2018). The superlubricity mechanism for BN-containing PAO at Si₃N₄/DLC interface is the contact area reduction because of BN as nanoscale ball bearings lead to the point-like contact, and the weak van der Waals interaction force between BN molecules (Zeng et al., 2013). The superlubricity mechanism for LDH is regarded as its small size and good dispersion in water make LDH enter the contact area and form an effective lubricating layer, and therefore protect the asperity peaks from direct collision (Wang et al., 2016). Additionally, nanodiamonds glycerol colloidal solution was found to achieve superlubricity and low wear, which are due to the hydrodynamic effect, hydrogen bond layer, and rolling effect of nanodiamonds (Chen et al., 2016).

CONCLUSIONS AND OUTLOOKS

Studies on liquid superlubricity at the macroscale are focused on the mechanism, which differs for different lubricants and is usually attributed to multiple factors, such as the silica layers and hydrodynamic lubrication for water, the tribochemical layer, and hydrogen-bond network for viscous lubricants, and the stern layer and hydrogen-bond network for acid-based lubricants. The mechanism of liquid superlubricity is very complicated and should be further investigated. Because of the limitation of the present technology, the structure, and arrangement of liquid molecules in the contact region, which play the dominate role on the superlubricity, are still not clear. In addition, the kinds of materials for liquid superlubricity are limited; only a few materials exhibit superlubricity behavior. The possibility of other liquid materials with superlubricity properties remains to be investigated. Furthermore, there are many factors that limit the application of liquid superlubricity, such as the severe wear, acidic conditions, and complexity of manufacturing ideal surfaces. However, the prospects for liquid superlubricity in industrial applications are excellent. For instance, hydrophilic polymer brushes may be suitable for silicone rubbers in microfluidics, marine paints (antifouling), biomedical devices, etc. Acid-based lubricants and ionic liquids may be suitable for Si₃N₄ bearings, who have strong resistance to acidic corrosion. Oil-based lubricants may be suitable for the mechanical parts like gears and bearings, who are made of steels and alloys. PVPA-modified Ti₆Al₄V is a potential material for artificial implants. Therefore, research in the near future should focus on the development of new liquid lubricants to offer lubricating performance with extremely low friction and wear, as well as be associated with practical operating conditions in mechanical systems.

AUTHOR CONTRIBUTIONS

JLu and JLi gave the guidance on the structure and content of this review. XGe completed this review.

ACKNOWLEDGMENTS

The work is financially supported by the National Natural Science Foundation of China (51775295, 51527901, and 51335005).

REFERENCES

- Baykara, M., Vazirisereshk, M., and Martini, A. (2018). Emerging superlubricity: a review of the state of the art and perspectives on future research. *Appl. Phys. Rev.* 5:041102. doi: 10.1063/1.5051445
- Berman, D., Erdemir, A., and Sumant, A. (2018). Approaches for achieving superlubricity in two-dimensional materials. *ACS Nano* 12, 2122–2137. doi: 10.1021/Acsnano.7b09046
- Bouchet, M., Matta, C., Le-Mogne, T., Martin, J., Zhang, Q., Goddard, W., et al. (2007). Superlubricity mechanism of diamond-like carbon with glycerol. Coupling of experimental and simulation studies. *J. Phys. Confer. Ser.* 89:012003. doi: 10.1088/1742-6596/89/1/012003
- Chen, M., Kato, K., and Adachi, K. (2001). The difference in running-in period and friction coefficient between self-mated Si₃N₄ and SiC under water lubrication. *Tribol. Lett.* 11, 23–28. doi: 10.1023/A:1016621929078
- Chen, M., Kato, K., and Adachi, K. (2002). The comparisons of sliding speed and normal load effect on friction coefficients of self-mated Si₃N₄ and SiC under water lubrication. *Tribol. Int.* 35, 129–135. doi: 10.1016/S0301-679X(01)00105-0
- Chen, Z., Liu, Y., and Luo, J. (2016). Superlubricity of nanodiamonds glycerol colloidal solution between steel surfaces. *Colloids Surf. A* 489, 400–406. doi: 10.1016/j.colsurfa.2015.10.062
- Chen, Z., Liu, Y., Zhang, S., and Luo, J. (2013). Controllable super lubricity of glycerol solution via environment humidity. *Langmuir* 29, 11924–11930. doi: 10.1021/La402422h
- Cihan, E., Ipek, S., Durgun, E., and Baykara, M. (2016). Structural lubricity under ambient conditions. *Nat. Commun.* 7:12055. doi: 10.1038/Ncomms12055
- Dash, J., Fu, H., and Wettlaufer, J. (1995). The premelting of ice and its environmental consequences. *Rep. Prog. Phys.* 58, 115–167. doi: 10.1088/0034-4885/58/1/003
- Deng, M., Zhang, C., Li, J., Ma, L., and Luo, J. (2014). Hydrodynamic effect on the superlubricity of phosphoric acid between ceramic and sapphire. *Friction* 2, 173–181. doi: 10.1007/S40544-014-0053-3
- Erdemir, A., and Eryilmaz, O. (2014). Achieving superlubricity in DLC films by controlling bulk, surf ace, and tribochemistry. *Friction* 2, 140–155. doi: 10.1007/S40544-014-0055-1
- Erdemir, A., and Martin, J., (eds.). (2007). *Superlubricity*. New York, NY: Elsevier. doi: 10.1016/B978-0-444-52772-1.X5029-X
- Espinosa, T., Jimenez, M., Sanes, J., Jimenez, A., Iglesias, M., and Bermudez, M. (2014). Ultra-low friction with a protic ionic liquid boundary film at the water-lubricated sapphire-stainless steel interface. *Tribol. Lett.* 53, 1–9. doi: 10.1007/S11249-013-0238-3
- Fan, K., Liu, J., Wang, X., Liu, Y., Lai, W., Gao, S., et al. (2018). Towards enhanced tribological performance as water-based lubricant additive: selective fluorination of graphene oxide at mild temperature. *J. Colloid Interf. Sci.* 531, 138–147. doi: 10.1016/j.jcis.2018.07.059
- Fan, M., Song, Z., Liang, Y., Zhou, F., and Liu, W. (2014). Laxative inspired ionic liquid lubricants with good detergency and no corrosion. *ACS Appl. Mater. Interfaces* 6, 3233–3241. doi: 10.1021/Am4049332
- Feng, X., Kwon, S., Park, J., and Salmeron, M. (2013). Superlubric sliding of graphene nanoflakes on graphene. *ACS Nano* 7, 1718–1724. doi: 10.1021/Nn305722d
- Gao, M., Li, H., Ma, L., Gao, Y., Ma, L., and Luo, J. (2018). “Molecular behaviors in thin film lubrication, part two: direct observation of the molecular orientation near the solid surface,” in *Friction Accepted*, ed J. Luo (Beijing: Tsinghua University Press).
- Ge, X., Halmans, T., Li, J., and Luo, J. (2018c). “Molecular behaviors in thin film lubrication, part three: superlubricity attained by polar and nonpolar molecules” *Friction Online*, ed J. Luo (Beijing: Tsinghua University Press). doi: 10.1007/S40544-018-0254-2
- Ge, X., Li, J., Luo, R., Zhang, C., and Luo, J. (2018d). Macroscale superlubricity enabled by synergy effect of graphene-oxide nanoflakes and ethanediol. *ACS Appl. Mater. Interfaces* 10, 40863–40870. doi: 10.1021/Acsami.8b14791
- Ge, X., Li, J., Zhang, C., and Luo, J. (2018a). Liquid superlubricity of polyethylene glycol aqueous solution achieved with boric acid additive. *Langmuir* 34, 3578–3587. doi: 10.1021/acs.Langmuir.7b04113
- Ge, X., Li, J., Zhang, C., Wang, Z., and Luo, J. (2018b). Superlubricity of 1-ethyl-3-methylimidazolium trifluoromethanesulfonate ionic liquid induced by tribochemical reactions. *Langmuir* 34, 5245–5252. doi: 10.1021/acs.Langmuir.8b00867
- Ge, X., Xia, Y., and Shu, Z. (2015). Conductive and tribological properties of lithium-based ionic liquids as grease base oil. *J. Tribol. Trans. ASME* 58, 686–690. doi: 10.1080/10402004.2015.1012772
- Han, T., Zhang, C., and Luo, J. (2018). Macroscale superlubricity enabled by hydrated alkali metal ions. *Langmuir* 34, 11281–11291. doi: 10.1021/acs.Langmuir.8b01722
- Hirano, M. (2014). Atomistics of superlubricity. *Friction* 2, 95–105. doi: 10.1007/S40544-014-0049-Z
- Holmberg, K., Andersson, P., and Erdemir, A. (2012). Global energy consumption due to friction in passenger cars. *Tribol. Int.* 47, 221–234. doi: 10.1016/j.triboint.2011.11.022
- Inutsuka, M., Yamada, N., Ito, K., and Yokoyama, H. (2013). High density polymer brush spontaneously formed by the segregation of amphiphilic diblock copolymers to the polymer/water interface. *ACS Macro Lett.* 2, 265–268. doi: 10.1021/Mz300669q
- Jaiswal, V., Kalyani, Umrao, S., Rastogi, R., Kumar, R., and Srivastava, A. (2016). Synthesis, characterization, and tribological evaluation of TiO₂-reinforced boron and nitrogen co-doped reduced graphene oxide based hybrid nanomaterials as efficient antiwear lubricant additives. *ACS Appl. Mater. Interfaces* 8, 11698–11710. doi: 10.1021/Acsami.6b01876
- Jiang, C., Li, W., Nian, J., Lou, W., and Wang, X. (2018). Tribological evaluation of environmentally friendly ionic liquids derived from renewable biomaterials. *Friction* 6, 208–218. doi: 10.1007/S40544-017-0170-X
- Kano, M. (2006a). DLC coating technology applied to sliding parts of automotive engine. *New Diamond Front. Carbon Technol.* 16, 201–210.
- Kano, M. (2006b). Super low friction of DLC applied to engine cam follower lubricated with ester-containing oil. *Tribol. Int.* 39, 1682–1685. doi: 10.1016/j.triboint.2006.02.068
- Kawai, S., Benassi, A., Gnecco, E., Söde, H., Pawlak, R., Feng, X., et al. (2016). Superlubricity of graphene nanoribbons on gold surfaces. *Science* 351, 957–961. doi: 10.1126/Science.Aad3569
- Khajeh, A., He, X., Yeon, J., Kim, S., and Martini, S. (2018). Mechanochemical association reaction of interfacial molecules driven by shear. *Langmuir* 34, 5971–5977. doi: 10.1021/acs.Langmuir.8b00315
- Klein, J. (2013). Hydration lubrication. *Friction* 1, 1–23. doi: 10.1007/S40544-013-0001-7
- Lee, S., Muller, M., Ratoi-Salagean, M., Voros, J., Pasche, S., De Paul, S., et al. (2003). Boundary lubrication of oxide surfaces by Poly(L-Lysine)-G-Poly(Ethylene Glycol) (PLL-G-PEG) in aqueous media. *Tribol. Lett.* 15, 231–239. doi: 10.1023/A:1024861119372
- Li, H., Wood, R., Rutland, M., and Atkin, R. (2014). An ionic liquid lubricant enables superlubricity to be “Switched on” *in situ* using an electrical potential. *Chem. Commun.* 50, 4368–4370. doi: 10.1039/C4cc00979g
- Li, J., Gao, T., and Luo, J. (2018a). Superlubricity of graphite induced by multiple transferred graphene nanoflakes. *Adv. Sci.* 5:1700616. doi: 10.1002/Adv.201700616
- Li, J., Ge, X., and Luo, J. (2018b). Random occurrence of macroscale superlubricity of graphite enabled by tribo-transfer of multilayer graphene nanoflakes. *Carbon* 138, 154–160. doi: 10.1016/j.carbon.2018.06.001

- Li, J., Ma, L., Zhang, S., Zhang, C., Liu, Y., and Luo, J. (2013a). Investigations on the mechanism of superlubricity achieved with phosphoric acid solution by direct observation. *J. Appl. Phys.* 114:114901. doi: 10.1063/1.4821063
- Li, J., Zhang, C., Deng, M., and Luo, J. (2014). Investigations of the superlubricity of sapphire against ruby under phosphoric acid lubrication. *Friction* 2, 164–172. doi: 10.1007/S40544-014-0050-6
- Li, J., Zhang, C., Deng, M., and Luo, J. (2015a). Superlubricity of silicone oil achieved between two surfaces by running-in with acid solution. *RSC Adv.* 5, 30861–30868. doi: 10.1039/C5ra00323g
- Li, J., Zhang, C., Deng, M., and Luo, J. (2015b). Investigation of the difference in liquid superlubricity between water- and oil-based lubricants. *RSC Adv.* 5, 63827–63833. doi: 10.1039/C5ra10834a
- Li, J., Zhang, C., and Luo, J. (2011). Superlubricity behavior with phosphoric acid-water network induced by rubbing. *Langmuir* 27, 9413–9417. doi: 10.1021/La201535x
- Li, J., Zhang, C., and Luo, J. (2013c). Superlubricity achieved with mixtures of polyhydroxy alcohols and acids. *Langmuir* 29, 5239–5245. doi: 10.1021/La400810c
- Li, J., Zhang, C., Ma, L., Liu, Y., and Luo, J. (2013b). Superlubricity achieved with mixtures of acids and glycerol. *Langmuir* 29, 271–275. doi: 10.1021/La3046115
- Li, J., Zhang, C., Sun, L., Lu, X., and Luo, J. (2012). Tribochemistry and superlubricity induced by hydrogen ions. *Langmuir* 28, 15816–15823. doi: 10.1021/La303897x
- Li, Y., Zhang, S., Ding, Q., Feng, D., Qin, B., and Hu, L. (2017). The corrosion and lubrication properties of 2-mercaptopbenzothiazole functionalized ionic liquids for bronze. *Tribol. Int.* 114, 121–131. doi: 10.1016/j.Triboint.2017.04.022
- Liu, Z., Yang, J., Grey, F., Liu, J., Liu, Y., Wang, Y., et al. (2012). Observation of microscale superlubricity in graphite. *Phys. Rev. Lett.* 108:205503. doi: 10.1103/PhysRevLett.108.205503
- Ma, W., Gong, Z., Gao, K., Qiang, L., Zhang, J., and Yu, S. (2017). Superlubricity achieved by carbon quantum dots in ionic liquid. *Mater. Lett.* 195, 220–223. doi: 10.1016/j.Matlet.2017.02.135
- Martin, J., Pascal, H., Donnet, C., Le Mogne, T., Loubet, J., and Epicier, T. (1994). Superlubricity of MoS₂: crystal orientation mechanisms. *Surf. Coat. Technol.* 68–69, 427–432. doi: 10.1016/0257-8972(94)90197-X
- Matta, C., Joly-Pottuz, L., Bouchet, M., and Martin, J. (2008). Superlubricity and tribochemistry of polyhydric alcohols. *Phys. Rev. B* 78:085436. doi: 10.1103/PhysRevB.78.085436
- Meng, Y., Su, F., and Chen, Y. (2015). A novel nanomaterial of graphene oxide dotted with Ni nanoparticles produced by supercritical CO₂-assisted deposition for reducing friction and wear. *ACS Appl. Mater. Interfaces* 7, 11604–11612. doi: 10.1021/Acsami.5b02650
- Meyer, E., and Gnecco, E. (2014). Superlubricity on the nanometer scale. *Friction* 2, 106–113. doi: 10.1007/S40544-014-0052-4
- Muller, M., Lee, S., Spikes, H., and Spencer, N. (2003). The influence of molecular architecture on the macroscopic lubrication properties of the brush-like co-polyelectrolyte poly(L-Lysine)-G-poly(Ethylene Glycol) (PLL-G-PEG) adsorbed on oxide surfaces. *Tribol. Lett.* 15, 395–405. doi: 10.1023/B:TRIL.0000003063.98583.bb
- Qiao, Y., Zhang, S., Liu, Y., Ma, L., and Luo, J. (2018). “Molecular behaviors in thin film lubrication, part one: film formation for different polarities of molecules,” in *Friction Submitted*, ed J. Luo (Beijing: Tsinghua University Press).
- Qu, J., Bansal, D., Yu, B., Howe, J. Y., Luo, H., Dai, S., et al. (2012). Antiwear performance and mechanism of an oil-miscible ionic liquid as a lubricant additive. *ACS Appl. Mater. Interfaces* 4, 997–1002. doi: 10.1021/Am201646k
- Qu, J., Barnhill, W., Luo, H., Meyer, H., Leonard, D., Landauer, A., et al. (2015). Synergistic effects between phosphonium-alkylphosphate ionic liquids and zinc dialkyldithiophosphate (ZDDP) as lubricant additives. *Adv. Mater.* 27, 4767–4774. doi: 10.1002/Adma.201502037
- Raviv, U., Giasson, S., Kampf, N., Gohy, J., Jerome, R., and Klein, J. (2003). Lubrication by charged polymers. *Nature* 425, 163–165. doi: 10.1038/Nature01970
- Ron, T., Javakhishvili, I., Hvilsted, S., Jankova, K., and Lee, S. (2016). Ultralow friction with hydrophilic polymer brushes in water as segregated from silicone matrix. *Adv. Mater. Interfaces* 3:1500472. doi: 10.1002/Admi.201500472
- Sahai, N. (2002). Is silica really an anomalous oxide? Surface acidity and aqueous hydrolysis revisited. *Environ. Sci. Technol.* 36, 445–452. doi: 10.1021/Es010850u
- Saurin, N., Sanes, J., Carrion, F., and Bermudez, M. (2016). Self-healing of abrasion damage on epoxy resin controlled by ionic liquid. *RSC Adv.* 6, 37258–37264. doi: 10.1039/C6ra05503f
- Shinjo, K., and Hirano, M. (1993). Dynamics of friction-superlubric state. *Surf. Sci.* 283, 473–478. doi: 10.1016/0039-6028(93)91022-H
- Shteinberg, L. (2009). Effect of boric acid concentration on the catalysis of the reaction of 4-nitrobenzoic acid with ammonia. *Russ. J. Appl. Chem.* 82, 613–617. doi: 10.1134/S1070427209040156
- Shteinberg, L. (2011). A study of the kinetics and mechanism of amidation of 4-nitrobenzoic acid with ammonia, catalyzed by boric acid in the presence of polyethylene glycol PEG-400. *Russ. J. Appl. Chem.* 84, 815–819. doi: 10.1134/S1070427211050132
- Sinclair, R. C., Suter, J. L., and Coveney, P. V. (2018). Graphene-graphene interactions: friction, superlubricity, and exfoliation. *Adv. Mater.* 30:1705791. doi: 10.1002/Adma.201705791
- Sjoberg, S. (1996). Silica in aqueous environments. *J. Non-Cryst. Solids* 196, 51–57. doi: 10.1016/0022-3093(95)00562-5
- Somers, A., Khemchandani, B., Howlett, P., Sun, J., MacFarlane, D., and Forsyth, M. (2013). Ionic liquids as antiwear additives in base oils: influence of structure on miscibility and antiwear performance for steel on aluminum. *ACS Appl. Mater. Interfaces* 5, 11544–11553. doi: 10.1021/Am4037614
- Song, Y., Mandelli, D., Hod, O., Urbakh, M., Ma, M., and Zheng, Q. (2018). Robust microscale superlubricity in graphite/hexagonal boron nitride layered heterojunctions. *Nat Mater.* 17, 894–899. doi: 10.1038/S41563-018-0144-Z
- Spikes, H., and Tysoe, W. (2015). On the commonality between theoretical models for fluid and solid friction, wear and tribochemistry. *Tribol. Lett.* 59:21. doi: 10.1007/S11249-015-0544-Z
- Tisza, L. (1938). On the thermal supraconductibility of liquid helium II and the bose-einstein statistics. *Comptes Rendus Hebdomadaires Des Seances De L'Academie Des Sci.* 207, 1035–1037.
- Tomizawa, H., and Fischer, T. (1987). Friction and wear of silicon-nitride and silicon-carbide in water: hydrodynamic lubrication at low sliding speed obtained by tribochemical wear. *ASLE Trans.* 30, 41–46. doi: 10.1080/05698198708981728
- Wang, H., Liu, Y., Chen, Z., Wu, B., Xu, S., and Luo, J. (2016). Layered double hydroxide nanoplatelets with excellent tribological properties under high contact pressure as water-based lubricant additives. *Sci. Rep.* 6:22748. doi: 10.1038/Srep22748
- Wang, W., Xie, G., and Luo, J. (2018). Superlubricity of black phosphorus as lubricant additive. *ACS Appl. Mater. Interfaces* 10, 43203–43210. doi: 10.1021/Acsami.8b14730
- Wang, X., Kato, K., Adachi, K., and Aizawa, K. (2001). The effect of laser texturing of SiC surface on the critical load for transition of water lubrication mode from hydrodynamic to mixed. *Tribol. Int.* 34, 703–711. doi: 10.1016/S0301-679X(01)00063-9
- Wu, L., Xie, Z., Gu, L., Song, B., and Wang, L. (2018). Investigation of the tribological behavior of graphene oxide nanoplates as lubricant additives for ceramic/steel contact. *Tribol. Int.* 128, 113–120. doi: 10.1016/j.Triboint.2018.07.027
- Xu, J., and Kato, K. (2000). Formation of tribochemical layer of ceramics sliding in water and its role for low friction. *Wear* 245, 61–75. doi: 10.1016/S0043-1648(00)00466-X
- Ye, C., Liu, W., Chen, Y., and Yu, L. (2001). Room-temperature ionic liquids: a novel versatile lubricant. *Chem. Commun.* 2001, 2244–2245. doi: 10.1039/B106935g
- Yue, D., Ma, T., Hu, Y., Yeon, J., van Duin, A., Wang, H., et al. (2013). Tribochemistry of phosphoric acid sheared between quartz surfaces: a reactive molecular dynamics study. *J. Phys. Chem. C* 117, 25604–25614. doi: 10.1021/Jp406360u
- Zeng, Q., and Dong, G. (2013). Influence of load and sliding speed on super-low friction of nitinol 60 alloy under castor oil lubrication. *Tribol. Lett.* 52, 47–55. doi: 10.1007/S11249-013-0191-1
- Zeng, Q., and Dong, G. (2014). Superlubricity behaviors of nitinol 60 alloy under oil lubrication. *Trans. Nonferrous Met. Soc. China* 24:354359. doi: 10.1016/S1003-6326(14)63068-5
- Zeng, Q., Dong, G., and Martin, J. (2016). Green superlubricity of nitinol 60 alloy against steel in presence of castor oil. *Sci. Rep.* 6:29992. doi: 10.1038/Srep29992

- Zeng, Q., Yu, F., and Dong, G. (2013). Superlubricity behaviors of Si₃N₄/DLC films under PAO oil with nano boron nitride additive lubrication. *Surf. Interface Anal.* 45, 1283–1290. doi: 10.1002/sia.5269
- Zhang, C., Liu, Y., Liu, Z., Zhang, H., Cheng, Q., and Yang, C. (2017). Regulation mechanism of salt ions for superlubricity of hydrophilic polymer cross-linked networks on Ti6Al4V. *Langmuir* 33, 2133–2140. doi: 10.1021/acs.Langmuir.6b04429
- Zhang, G., Xu, Y., Xiang, X., Zheng, G., Zeng, X., Li, Z., et al. (2018). Tribological performances of highly dispersed graphene oxide derivatives in vegetable oil. *Tribol. Int.* 126, 39–48. doi: 10.1016/j.Triboint.2018.05.004
- Zhao, F., Zhang, L., Li, G., Guo, Y., Qi, M., and Zhang, G. (2018). Significantly enhancing tribological performance of epoxy by filling with ionic liquid functionalized graphene oxide. *Carbon* 136, 309–319. doi: 10.1016/j.Carbon.2018.05.002
- Zhou, F., Adachi, K., and Kato, K. (2005). Friction and wear property of a-CNx coatings sliding against ceramic and steel balls in water. *Diam. Relat. Mater.* 14, 1711–1720. doi: 10.1016/j.Diamond.2005.06.025
- Zhou, F., Wang, X., Kato, K., and Dai, Z. (2007). Friction and wear property of a-CNx coatings sliding against Si₃N₄ balls in water. *Wear* 263, 1253–1258. doi: 10.1016/j.Wear.2006.11.048

Conflict of Interest Statement: The authors declare that the research was conducted in the absence of any commercial or financial relationships that could be construed as a potential conflict of interest.

Copyright © 2019 Ge, Li and Luo. This is an open-access article distributed under the terms of the Creative Commons Attribution License (CC BY). The use, distribution or reproduction in other forums is permitted, provided the original author(s) and the copyright owner(s) are credited and that the original publication in this journal is cited, in accordance with accepted academic practice. No use, distribution or reproduction is permitted which does not comply with these terms.



Are There Limits to Superlubricity of Graphene in Hard, Rough Contacts?

Martin H. Müser*

Lehrstuhl für Materialsimulation, Department of Materials Science and Engineering, Saarland University, Saarbrücken, Germany

OPEN ACCESS

Edited by:

Roman Pohrt,
Technische Universität Berlin,
Germany

Reviewed by:

Qunyang Li,
Tsinghua University, China
Yoshitaka Nakanishi,
Kumamoto University, Japan
Wenling Zhang,
University of Alberta, Canada
Mehmet Z. Baykara,
University of California, Merced,
United States

*Correspondence:

Martin H. Müser
martin.mueser@mx.uni-saarland.de

Specialty section:

This article was submitted to
Tribology,
a section of the journal
Frontiers in Mechanical Engineering

Received: 06 November 2018

Accepted: 08 May 2019

Published: 22 May 2019

Citation:

Müser MH (2019) Are There Limits to
Superlubricity of Graphene in Hard,
Rough Contacts?
Front. Mech. Eng. 5:28.
doi: 10.3389/fmech.2019.00028

Yes, there are. They result from the splitting of a large correlated contact into many small patches. When the lubricant consists of thin solid sheets, like graphene, the patches are expected to act independently from each other. Crude estimates for the friction forces between hard, stiff solids with randomly rough surfaces are given, which apply to surfaces with Hurst roughness exponents $H > 0.5$. The estimates are obtained by combining realistic contact-patch-size distributions with friction-load relations deduced for isolated contact patches. The analysis reveals that load is carried predominantly by large patches, while most frictional forces stem from small contact patches. Low friction is favored when the root-mean-square height gradients are small, while a large roll-off wavelength and thus large root-mean-square roughness is predicted to lead to small friction. Moreover, friction is found to increase sublinearly with load in a nominally flat, structurally lubric contact.

Keywords: friction, superlubricity, contact mechanics, theory, graphene

1. INTRODUCTION

When two solids are pressed against each other, surface atoms experience large normal and lateral forces from the counterbody in the true contact points. While normal forces on atoms in the top layer are, for the most part, unidirectional with minor relative fluctuations, lateral forces are expected to quickly change sign on small scales (Hirano and Shinjo, 1990; Shinjo and Hirano, 1993), because atoms are (statistically) pushed as many times to the left as to the right. If this expectation were generally true, solid friction would be generally super small. However, plastic deformation, e.g., in the form of dislocations that are nucleated by corner-stress concentrations (Sørensen et al., 1996; Sharp et al., 2016) or by strong interfacial interactions (Dietzel et al., 2017) but also the presence of loosely bonded atoms (lubricant, airborne contamination, etc.) (He et al., 1999; Dietzel et al., 2008) can lead to a systematic interlocking of solids and thereby to significant interfacial shear stresses and thus noticeable friction during sliding. Significant friction can also arise when two solids with identical lattice spacings are perfectly aligned with each other or when the solids happen to be one-dimensional (Aubry, 1983), or, in some other exotic situation that may interest some physicists (Müser et al., 2003) but does not relate to applications.

Real solids happen to be three-dimensional and their surfaces tend to be chemically passivated. Under these circumstances, simulations of flat, clean, crystalline, and amorphous model systems (Hirano and Shinjo, 1990; Müser et al., 2001; Verhoeven et al., 2004; Dietzel et al., 2018), scaling arguments (Müser et al., 2001) and even experiments on small antimony particles adsorbed on graphite (Dietzel et al., 2008, 2013, 2017) show that friction can be a sublinear function of the contact area. In this case, the ratio of the (static) shear force and the normal force would disappear in the thermodynamic or macroscopic limit. The effect has been called structural

lubricity (Müser, 2004). It is revealed most prominently by graphite flakes rotated against a graphite substrate (Dienwiebel et al., 2004) but also by misoriented MoS₂ transfer films (Martin et al., 1993).

Structural lubricity is a special form of superlubricity (Baykara et al., 2018). The latter term only implies friction coefficients below 0.01, irrespective of its molecular origin (Martin and Erdemir, 2018). Soft-matter systems, in which a liquid lubricant remains in the contact, such as in hydrogels or solvated polymer brushes, may have tiny friction coefficients (Lee and Spencer, 2008; Martin and Erdemir, 2018) but are not addressed in this work.

The critical question to be addressed for flat, clean interfaces is whether—or more precisely to what contact length (Sharp et al., 2016)—do elastic restoring forces dominate the interfacial deformation forces so that multistability is avoided? Multistability means that different microscopic equilibrium configurations are possible for identical macroscopic set-ups. It is a necessary condition for hysteresis at small velocities and thus for Coulomb friction (no or weak dependence of friction on the sliding velocity) to occur, as explained so beautifully in Prandtl's work on the origin of friction (Prandtl, 1928; Popov and Gray, 2012). Simple scaling arguments (on static friction) suggest that elastic restoring forces should keep the upper hand in contacts between three-dimensional crystals and that there is a tie when one or both solids are amorphous (Müser, 2004). Even if corrections to these simple scaling laws might always turn the interfacial interactions into the winner (Sharp et al., 2016), friction forces should remain extremely small, because the domains moving as a correlated, effectively rigid unit would supposedly be extremely large. In fact, Sharp et al. (2016) found that the (kinetic) friction between a circular disk with a flat surface and an essentially infinite substrate dropped exponentially with the ratio of the shear modulus G and the local maximum traction τ_{\max} . Whenever G is given by relatively strong covalent or metallic bonds but τ_{\max} results from weak van-der-Waals interactions, friction forces can remain extremely small.

The situation is sensitive to the dimension of the objects (Shinjo and Hirano, 1993; Müser, 2004), because one-dimensional solids become effectively softer at large scales, while three-dimensional objects become stiffer. This is ultimately at the root for elasticity to “outperform” interfacial interactions up to large scales and thereby to allow for superlubricity of three-dimensional solids. In contrast, one-dimensional chains are rather prone to elastic instabilities (Aubry, 1983), while the onset of (local) elastic instabilities in more highly-dimensional objects should almost unavoidably induce non-elastic deformations (Hammerberg et al., 1998; Müser, 2001). This conclusion is inline with the observation that wearless (Coulomb) friction with atomic-force microscope tips can generally only be observed with soft cantilevers (Socoliuc et al., 2004).

The symmetry of solids (amorphous vs. crystalline) in direct contact matters for static friction, because it determines how systematic lateral forces add up or cancel each other (Müser et al., 2001; Müser, 2004). Even the shape of contact patches and their

orientation to a substrate can affect the static friction in this regard (de Wijn, 2012, 2014).

When assessing the effect of interfacial symmetry on structural lubricity, kinetic friction is more difficult to address than static friction, as a better geometric interlocking (and thus higher static friction) does not automatically lead to more or more intense instabilities (Müser et al., 2003). In fact, when a thin layer of weakly adsorbed molecules mediates the locking between solids, kinetic friction is expected to turn out substantially smaller for commensurate than for incommensurate surfaces, while the opposite is true for their static friction (Müser, 2002). Interestingly, the symmetry of the surfaces appears to be surprisingly irrelevant for kinetic friction when interlocking is due to the contact-induced generation of dislocations (Sharp et al., 2016).

Thus, if chemically passivated solids are hard enough to not deform plastically during contact, the only possible mechanism mediating a significant friction stress between solids across the interface is related to the presence of mobile atoms or molecules in the interface. Contaminants may induce a linear scaling of shear forces with contact area (He et al., 1999; Müser and Robbins, 2000; He and Robbins, 2001; Dietzel et al., 2008) and in fact, super low friction forces have first been reported to necessitate ultra-high vacuum (Martin et al., 1993; Dietzel et al., 2008). However, it recently turned out that contaminants (e.g., airborne molecules) do not have to act that way and that the concept of structural lubricity may persist even under ambient conditions (Cihan et al., 2016; Özoğul et al., 2017), for example, when the contaminants can easily glide past a smooth surface, as is the case for graphite.

Given the analysis of friction between flat solids, friction coefficients appear possible that might be even smaller than so far reported experimental values near 10^{-3} for molybdenum disulfide (MoS₂) (Martin et al., 1993) or hydrogen-enriched diamond-like carbon coatings (Erdemir and Eryilmaz, 2014). However, the multi-scale roughness on almost any natural or technical surface induces interfacial stress distributions that are much more heterogeneous than those encountered in model systems (Persson, 2001, 2008; Campañá et al., 2008), such as graphene and flat antimony islands moving past graphite, or the plane-parallel walls that are routinely studied with molecular dynamics. Superlubricity is then suppressed even more strongly than in the case of circular disks (Sharp et al., 2016). Individual contact patches could act independently, so that the static friction force rather than the kinetic friction force of individual patches would need to be considered.

In this paper, an attempt is made to estimate the friction coefficient for situations, in which individual contact patches are too small for dislocations to be nucleated, while the separation between them is large enough so that they can act essentially independently. Solids separated by thin, solid lubricants should match this category. Within a contact patch, the lubricant's large in-plane stiffness makes it act like a rigid sheet. However, a lubricant sheet can bend rather easily outside contact patches (Lee et al., 2010). This allows it to minimize its energy in a given contact patch without being much constrained by the energy minimization in an adjacent contact patch, if the given

sheet happens to extend over more than one contact patch. While in-plane, intra-bulk deformation might also add to the ability of graphite flakes to locally minimize their free energy, the pertinent transverse deflections of asperities are assumed to be negligibly small in comparison.

2. THEORY

The following set-up, which is sketched in **Figure 1**, is considered in the theory: the substrate is treated as an infinitely stiff solid composed of discrete atoms. It is supposed to adhere weakly to a solid, two-dimensional lubricant, which is going to be called graphene, because graphene is the most appropriate material for the theoretical considerations pursued here. We will be predominantly concerned with estimating the maximum possible lateral forces between the stiff substrate and graphene. The layer separates the substrate from a rough, but elastically deformable counterface. Due to its compliance, the top layer is assumed to be able to accommodate the corrugation of graphene much better than the more rigid substrate, such that slip occurs between the substrate and graphene. None of the results identified hereafter would be affected if compliance or elasticity were divided up more evenly between the two solids in contact. However, the treatment would become rather cumbersome and thereby its simplicity be hidden.

Three main assumptions are made, which the author of this paper believes to be reasonable even if they are uncontrolled approximations. (i) The graphene sheets are so large that in general not more than one sheet resides within a connected contact patch. (ii) A given sheet can accommodate each microscale contact patch to essentially the best of its abilities without being affected by the geometry of adjacent patches, i.e., it can move back and forth small distances within a patch without having to pay significant elastic or surface energy for the associated deformation (in particular bending) between the patches. (iii) Within a contact patch, the in-plane bonds of graphene are too stiff to allow for elastic multistability. Free bending of the sheet is suppressed by the relatively large normal stresses within a patch, but possible, for example in-between the two stress bumps in the double asperity contact of **Figure 1**.

Last but not least, a model for the relation between local normal and lateral forces needs to be identified. Two extreme points of view can be taken toward this end. One extreme would be to claim that in contact, the lateral force of a substrate on a

graphene atom can only depend on an atom's lateral position relative to the substrate irrespective of the normal force squeezing it against the substrate. This would automatically lead to a shear force independent of the normal force and perhaps be a model assumption favored by those who believe that microscopic shear stresses are independent of the microscopic normal stresses. This viewpoint indeed makes sense if adhesive forces exceed the external forces, e.g., in soft-matter systems or potentially also for flat solids moving under their own adhesive force over a surface. The other extreme view would be to treat the interactions between chemically passivated solids in zones of high pressures within a hard-disk picture. In this case the determination of the relation between normal and shear forces reduces to a geometrical exercise, whose result is that the tangential force is the tangent of an effective slope times the normal force. The same relation is obtained in the case of short-range repulsion and large contact pressures (Müser, 2008).

To incorporate the two just-discussed limits, the following (interfacial) lateral force component f_{nx} of atom n is assumed

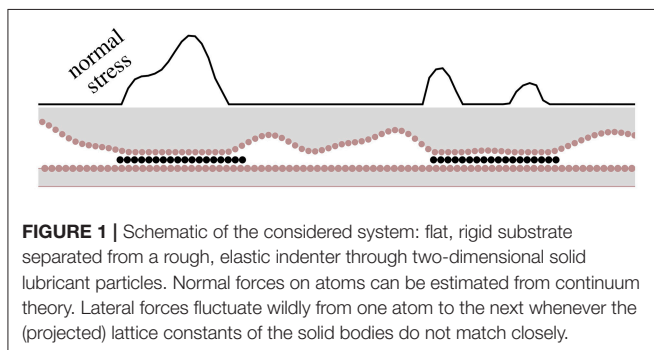
$$f_{nx} = u_n \cdot \mu_m \cdot (f_{nz} + f_z^{\text{off}}), \quad (1)$$

when the atom is squeezed at a random lateral position with a normal force f_{nz} against a rigid substrate, while f_z^{off} invokes an additional offset to the lateral force, which can be due to adhesion. Here μ_m can be interpreted as a microscopic friction coefficient (which would be the static friction coefficient for commensurate surfaces), while u_n can be treated as a random number of zero mean distributed on $(-1,1)$ for non-commensurate surfaces. In a first approximation, u_n can be treated as uniformly distributed. In section 2.2, we show that a more realistic distribution does not lead to relevant changes of the presented treatment.

Determining a reasonable value for μ_m is certainly more important than reflecting the correct distribution function of u_n . The classical hard-sphere value for μ_m is close to 0.3, which is also obtained for Lennard-Jones atoms moving past Lennard-Jones systems. The graphene bond, however, is relative strong while the bond length is relatively short. This leads to a reduction of μ_m , which is estimated to be 0.1 from a set of small simulation runs of various atoms sliding over graphite.

Estimating a net friction force from Equation (1) can be broken up into three steps. First, the distribution of contact patch size needs to be identified. Second, an expression for the rms-lateral force in a contact patch of size A carrying a load L needs to be found. Third, the results from the first two steps need to be merged and ballpark estimates for materials coefficient be made.

Since the main target of this paper is the analysis of rough, stiff contacts, adhesion is assumed to be small enough to barely affect the contact-patch statistics, i.e., adhesion should be small enough so that in the relevant load range the proportionality coefficient between true contact area and load is not increased by more than order 10% compared to the adhesion-free case. However, adhesion will be included in as far as that adhesive effects can increase the rms lateral force of a patch of a given size A . Moreover, it will be assumed that the normal pressure is small enough for the relative contact area to be much less than unity but sufficiently large for more than two or three meso-scale asperities



to be in contact so that a linear dependence of the real contact area on load is a good approximation (Pastewka et al., 2013).

2.1. Contact-Patch Statistics

Many surfaces in nature and technology can be described as being randomly rough. The most common characterization is in terms of their height spectrum $C(q)$ (Persson, 2014), which is essentially defined with four numbers, that is, the Hurst roughness exponent H , the short wavelength cutoff λ_s , the roll-off wavelength λ_r , and the spectrum at either one of the two wavelengths, or, alternatively, the root-mean-square height gradient \bar{g} . The part of the spectrum, which is the most relevant to this work, is the so-called self-affine branch, on which $C(q)$ is proportional to $q^{-2(1+H)}$, i.e., for $\lambda_s < 2\pi/q \leq \lambda_r$, where q denotes the magnitude of a given wavevector.

In addition to the four numbers needed to define $C(q)$, it also matters to some degree if the transition from self-affine scaling to the roll-off regime is smooth or abrupt. The findings for the contact-patch size distribution $n(A)$ summarized in this section are predominantly based on computer simulations (Müser and Wang, 2018) using the more realistic smooth transition (Palasantzas, 1993; Jacobs et al., 2017).

Computer simulations of continuum models for surfaces reveal three scaling regimes for the $n(A)$ dependence. At small A , $n(A)$ is approximately constant (Campaña, 2008), up to a small-scale cross-over area of Müser and Wang (2018)

$$A_s \approx \frac{3\pi(2-H)}{16\kappa^2(1-H)} \lambda_s^2, \quad (2)$$

where κ is the proportionality coefficient relating the true relative contact area a_r and the mean macroscopic pressure p_0 via

$$a_r = \frac{\kappa p_0}{E^* \bar{g}}. \quad (3)$$

The value of κ turns out close to two for typical values of Hurst exponents. Thus, if the generic value of $H = 0.8$ is used, A_s turns out close to λ_s .

Individual contact patches of size $A < A_s$ show a relation between contact area and load similar to that of Hertzian contacts. Note, however, that the identification of this scaling regime necessitates the contact mechanics treatment to use discretizations that are much finer than λ_s . Real surfaces appear to show self-affine scaling of the height topography almost down to the smallest measurable scales, i.e., even down to the nanometer scale (Jacobs et al., 2017). It could be argued that λ_s was only introduced as a means to have a well-defined continuum model for contact mechanics, in which contact patches are true areas rather than isolated points. Because of the self-affine branch extending almost to atomic scales, it is doubtful that the small- A scaling regime exists in reality. In fact, when the self-affine scaling was taken down to (twice) the discretization length, a Hertzian scaling regime was not identified (Hyun et al., 2004). For this reason, but also because the net load carried by the (hypothetical) quasi-Hertzian patches is minuscule and even more importantly because thermal activation most certainly assists the sliding

motion in sub-nanometer scale contacts, the effect of these ultra-small patches on both friction and normal force will be ignored. Instead, it will be assumed that a contact area of $A > A_{\min}$ is needed to convey a (quasi-) static shear force in a given contact patch, where A_{\min} should be larger but not much larger than atomic dimensions. In the following, A_{\min} will be set equal to the (hypothetical) A_s and estimated to be of order 1 nm^2 .

The distribution of medium- and large patches was observed to obey (Müser and Wang, 2018)

$$n(A) = n(A_{\text{ref}}) \left(\frac{A_{\text{ref}}}{A} \right)^{2-H/2} e^{-(A-A_{\text{ref}})/A_{\text{max}}}, \quad (4)$$

where A_{ref} is a reference patch size on the self-affine scaling branch and A_{max} is a characteristic (maximum) patch size. Thus, the probability for patch areas exceeding A_{max} is suppressed exponentially. To keep the closed-form mathematical description simple, the exponential factor in Equation (4) will therefore be replaced with a Heaviside step function $\Theta(A_{\text{max}} - A)$. A numerical analysis of the relative errors of this approximation on the final friction coefficient shows that this approximation only leads to effects of the order of 10%.

A central question to address is, how large is A_{max} ? For $H = 0.8$, A_{max} was found to depend on the ratio $\epsilon_f \equiv \lambda_s/\lambda_r$ with a rather steep power law of $A_{\text{max}} \propto \epsilon_f^\beta$, where $\beta(H = 0.8) = 1.5 \pm 0.1$, and a more moderate power law on the normal stress through $A_{\text{max}} \propto p_0^\gamma$ with $\gamma(H = 0.8) = 0.55 \pm 0.05$ for normal pressures well below the pressure, at which contact percolates. Combining these two laws results in

$$A_{\text{max}} = g(H) \cdot \epsilon_f^{\beta(H)} \cdot \left(\frac{\kappa p_0}{E^* \bar{g}} \right)^{\gamma(H)} \cdot \lambda_s^2 \quad (5)$$

The simulation data presented in reference Müser and Wang (2018) is consistent with a numerical value of $g(H = 0.8) \approx 0.023$. When p_0 is so small and/or ϵ_f so large that A_{max} does not turn out at least ten times A_s , the conditions for the derivation of Equation (5) are obviously violated. Likewise, A_{max} should not be anywhere near λ_r^2 . Sensitivity by the reader regarding the used parameters and range of applicability is required.

Similar relations as that in Equation (5) are expected to hold for other Hurst exponents >0.5 , however, with changed numerical values for $g(H)$, $\beta(H)$, and $\gamma(H)$. The reason why interfaces with a Hurst exponent less than one half should behave differently than those above it is that the elastic energy in full contact stems predominantly from the long- (short-) wavelength roughness above (below) $H = 0.5$. Indeed, A_{max} reveals a power law dependence neither on ϵ_f nor on p_0 for $H = 0.3$ (Müser and Wang, 2018).

2.2. Relation Between Load and Friction Force in a Meso-Scale Patch

This section is concerned with the question of how the mean-square force within a contact patch increases with its area under the assumption that the area is small enough to prevent the nucleation of a dislocation. To facilitate the treatment, the adhesion-free case is considered first.

2.2.1. Adhesion-Free Case

In the hard-disk, adhesion-free limit, the effective normal offset force f_z^{off} is neglected. Given Equation (1), the square of the lateral force that the substrate exerts onto a randomly placed graphene sheet in contact patch p then reads

$$F_{lp}^2 = \mu_m^2 \left(\sum_{n \in \text{patch } p} u_{nz} f_{nz} \right)^2. \quad (6)$$

To calculate the expectation value of that expression, we neglect correlation of the lateral forces acting on adjacent graphene atoms. This assumption is ultimately justified when the substrate has significant elements of randomness, as it occurs in disordered systems. [Commensurate contacts are not considered here, also because the lubricant patches and the two (single-crystal, but randomly rough) confining walls would have to have identical in-plane elementary cells and all three would have to be perfectly oriented—a situation that appears to be rather irrelevant]. Equation (6) then simplifies to

$$\langle F_{lp}^2 \rangle = \mu_m^2 \left\langle \sum_{n \in \text{patch } p} u_{nz}^2 f_{nz}^2 \right\rangle. \quad (7)$$

$$\approx \mu_m^2 N_p \langle u_n^2 \rangle \langle f_{nz}^2 \rangle_{\text{patch } p}, \quad (8)$$

$$= \mu_m^2 N_p \Delta A^2 \langle u_n^2 \rangle \langle \sigma^2 \rangle_{\text{patch } p}. \quad (9)$$

By going from Equations (7, 8), it was assumed that the relative lateral position of graphene atoms to substrate atoms is independent of pressure, which can be motivated by the strong in-plane bonds of graphene. In Equation (9), the average over the normal stress is taken over the contact patch area in the continuum approximation and a constant area ΔA is assigned to each graphene atom. Moreover σ refers by default (that is, when no indices are added) to the normal stress, while $\langle \dots \rangle_{\text{patch } p}$ indicates an average over patch p .

Thus, to evaluate typical lateral forces, we need to evaluate the second moment of the lateral numbers u_n and the second moment of the stress in individual patches. The second moment of a uniform random number on $(-1, 1)$ is $1/3$. If we had distributed u_n according to $u_n = \cos(\varphi_n)$, where φ_n is a uniform random number on $(0, 2\pi)$ the result would have been $1/2$. If instead, it had been chosen as $u_n = \cos(\varphi_n^{(x)}) \cos(\varphi_n^{(y)})$, it would have been $1/4$. Both numbers results in a negligible difference for the final friction coefficient in the semi-quantitative analysis presented here.

The second moment of the stress in a patch as a function of its patch size A_p needs to be determined next. The overwhelming part of contact points resides in patches belonging to the $\text{Pr}(A) \propto A^{-(2-H/2)}$ scaling regime. Campana observed a linear relation between load and contact area on that branch with rather small scatter in the proportionality constant from one patch to the next (Campaña, 2008). Our own simulations supported his finding (Müser and Wang, 2018). It is therefore meaningful to approximate the distribution of normal stresses with the function that describes the full stress distribution.

Stress distributions in elastic contacts are well-described by Persson (2001) and Campaña and Müser (2007)

$$\text{Pr}(\sigma) \propto e^{-2(\sigma-p_0)^2/(E^*\bar{g})^2} - e^{-2(\sigma+p_0)^2/(E^*\bar{g})^2}. \quad (10)$$

Evaluating the second moment of σ over the ideal distribution and normalizing it to the true contact area, which satisfies $a_r \approx 2p_0/E^*\bar{g}$ (assuming that $p_0 \ll E^*\bar{g}$),

$$\langle \sigma^2 \rangle \approx \frac{1}{\sqrt{2\pi}} (E^*\bar{g})^2 \quad (11)$$

is obtained while the first moment of the normal stress reads $\langle \sigma \rangle \approx E^*\bar{g}/2$.

Putting all things together and forming the ratio $\mu \equiv \sqrt{\langle F_{lp}^2 \rangle}/L_p$, where L_p is the load carried by the meso-scale patch, yields

$$\begin{aligned} \frac{\mu}{\mu_m} &= \sqrt{\frac{2}{3 \cdot \sqrt{2\pi}}} \sqrt{N_p} \\ &\approx 0.5 \cdot \sqrt{N_p}. \end{aligned} \quad (12)$$

Except for a slightly reduced pre-factor of ≈ 0.5 , this relation is identical to that obtained for a delta-distributed normal force. A similar result is obtained for any other stress distribution that does not change with contact area and that is not too broad. Thus, corrections to the normal stress distribution used here can scarcely matter.

2.2.2. General Case

The calculation starting from Equation (6) can be repeated for the general case by replacing f_{nz} with $f_{nz} + f_z^{\text{off}}$. The mean-square lateral force in patch p is readily obtained as

$$\langle F_{lp}^2 \rangle = \mu_m^2 \cdot \langle u_n^2 \rangle \cdot \left(\langle f_{nz}^2 \rangle + 2\langle f_{nz} \rangle \cdot f_z^{\text{off}} + (f_z^{\text{off}})^2 \right) \cdot N_p \quad (13)$$

Results for $\langle u_n^2 \rangle$ or $\langle f_{nz}^2 \rangle$ can then be taken from the above treatment of the adhesionless case.

2.2.3. Sanity Check

It is certainly not possible to compute high-precision lateral forces from models that are as simple as the one pursued here. It might yet be useful to check if the correct order of magnitude of experimental results is reproduced. Toward this end, the model is now applied to estimate the friction between a disordered cluster sitting under its own adhesive load on a graphite substrate.

In order to conduct a comparison, an adhesive stress needs to be ascertained first. Assuming 12-6 Lennard Jones interactions between atoms residing in opposite solids, the surface energy between two planes (after integrating over the volume of the counterbody and the line below a material point at the surface) is obtained to

$$\gamma(z) = \frac{4 \cdot 2^{2/3}}{3} \cdot \gamma_0 \cdot \left\{ \left(\frac{\zeta}{z} \right)^8 - \left(\frac{\zeta}{z} \right)^2 \right\}, \quad (14)$$

where γ_0 is the true cleavage energy and σ can be gauged to be $\zeta = \sqrt[3]{2}z_{\text{eq}}$ so that a realistic interlayer spacing ($z_{\text{eq}} = 3.4 \text{ \AA}$ for graphite) is obtained. $\gamma_0 = 0.37 \text{ J/m}^2$ is taken for the cleavage energy of graphite (Wang et al., 2015).

After differentiation of the second summand on the r.h.s. of Equation (14) with respect to z , the magnitude of the adhesive pressure per unit area at the equilibrium distance thus turns out to be

$$p_a = \frac{16 \cdot 2^{1/3}}{3} \cdot \frac{\gamma_0}{z_{\text{eq}}} \quad (15)$$

The numerical value for the case study conducted here is about 1 GPa. It is obtained for graphite interacting with graphite, but a similar order of magnitude should be obtained, for example, for antimony on graphite. Both fall in-between a clear classification of being insulators or metals and thus have a similar electronic polarizability, which determines the magnitude of dispersive interactions.

Using the result from Equation (13), the (maximum) shear stress in the absence of an external normal force is then simply estimated to be

$$\tau = \mu_m \cdot p_a \cdot \sqrt{\frac{\Delta A}{2 \cdot A}}, \quad (16)$$

where ΔA is the surface area per graphite atom.

Using an atomic friction coefficient of $\mu_m = 0.1$, the correct value of $\Delta A = 2 \cdot a_{\text{ip}}^2 / \sqrt{3}$, where $a_{\text{ip}} = 1.4 \text{ \AA}$ is taken as the in-plane distance between two graphite atoms, the relation $\tau = (0.1/\sqrt{A}) \text{ J/m}^2$ is obtained. This ballpark estimate fits experimental results extremely well, see, e.g., the structural-lubricity branches shown in Figure 2 of reference Dietzel et al. (2017). While difficult to prove, the author wishes to state that none of the (many) *ad-hoc* numbers used in this ballpark estimate had been adjusted to achieve this level of agreement with the experimental data. The level of agreement certainly benefits from some fortuitous error cancelation, also because the repulsion in the 12-6 Lennard Jones interaction law (the starting point for the $p_a = 1 \text{ GPa}$ -estimate) is significantly less accurate than the exponential repulsion in a Buckingham potential, provided the $1/R^6$ singularity is screened in the Buckingham potential at small R .

2.3. Merging Single-Patch Friction Laws With Patch-Area Statistics

The results from sections 2.1, 2.2 remain to be combined. In the limit of weak coupling between adjacent patches, each isolated patch is supposed to contribute to the maximum of its ability so that the total friction force and total load need to be summed up over the various patch-size scaling regimes. In other words, each graphite sheet is assumed to resist the sliding motion with the maximum of its abilities, or more precisely, with the rms of the lateral force. When replacing a sum over discrete patches with a continuous integral, net force components of

$$\langle F_\alpha \rangle = \int dA n(A) F_\alpha(A), \quad (17)$$

are obtained.

As argued in section 2.1, the dominant contribution for both normal and lateral force stems from the self-affine scaling branch of $n(A)$. The central difference between normal and lateral force is that the normal load grows linearly with A while the lateral force only scales with \sqrt{A} . As a consequence, the load is carried predominantly by the large patches for the $n(A) = c \cdot A^{-2+H/2}$ relation:

$$F_z = \frac{2 \cdot c \cdot F_z^{\text{char}}}{H} \cdot \left\{ \left(\frac{A_{\text{max}}}{\Delta A} \right)^{H/2} - \left(\frac{A_s}{\Delta A} \right)^{H/2} \right\} \quad (18)$$

where c is a normalization constant and F_z^{char} a characteristic normal force per (surface) atom, i.e.,

$$F_z^{\text{char}} = E^* \bar{g} \Delta A / \kappa \quad (19)$$

for a randomly rough surface.

In contrast, the lateral force turns out to be dominated by the small patches for $H < 1$:

$$F_x = \frac{2 \cdot c \cdot F_x^{\text{char}}}{1-H} \cdot \left\{ \left(\frac{\Delta A}{A_s} \right)^{\frac{1-H}{2}} - \left(\frac{\Delta A}{A_{\text{max}}} \right)^{\frac{1-H}{2}} \right\}, \quad (20)$$

where the characteristic atomic lateral force can be deduced to be

$$F_x^{\text{char}} = \frac{\mu_m}{\sqrt{2}} \sqrt{(F_z^{\text{char}})^2 + 2F_z^{\text{char}} p_a + p_a^2}. \quad (21)$$

When H is very close to unity, Equation (20) is well approximated by

$$F_x(H \rightarrow 1) = c \cdot F_x^{\text{char}} \cdot \ln(A_{\text{max}}/A_s). \quad (22)$$

Defining the friction coefficient as the ratio of lateral and normal force gives

$$\mu \approx \frac{F_x^{\text{char}}}{F_z^{\text{char}}} \cdot \frac{H}{1-H} \sqrt{\frac{\Delta A}{A_s}} \cdot \left(\frac{A_s}{A_{\text{max}}} \right)^{H/2} \quad (23)$$

for Hurst exponents that do not approach $H = 1$ too closely from below,

At this point, elaborate guesses could be inserted for the various quotients that arise in Equation (23). However, a quick estimate might be more instructive. The ratio $F_x^{\text{char}}/F_z^{\text{char}}$ will be in the order of 0.1. For $H = 0.8$, the ratio $H/(1-H)$ is equal to 5. The minimum size of a contact patch that does not move in a thermally activated matter is of order $A_s = \pi \cdot 1 \text{ nm}^2$, while the surface area associated with a single (graphite) atom is roughly $\Delta A = \pi \cdot 3 \text{ \AA}^2$ (bond length of 1.4 \AA and a packing fraction of the honeycomb lattice of 0.68). The crucial number is the value for A_{max} . According to a review on solid friction and contact aging (Baumberger and Caroli, 2006), it usually lies in the micrometric range, so let us call a typical radius $1 \text{ }\mu\text{m}$. This turns the last factor of the r.h.s. of Equation (23) into $1/1,000^H$. Combining all these factors yields $\mu = 3.5 \cdot 10^{-4}$. This

value should be clearly below the detection limit for macroscopic friction experiments. At the same time, it only applies to the friction between two nominally flat surfaces and not to a pin-on-disk geometry. For the latter, friction coefficients should turn out distinctly larger, because many small contact patches should exist near the macroscopic contact line.

It is interesting to note that the precise estimate for the size A_s is not particularly relevant. It almost enters only in a logarithmic fashion into Equation (23). For $H = 0.8$, μ_s is predicted to decrease only by 25% if A_s is increased by a factor of ten. The only truly critical variable in Equation (23) is A_{\max} .

Rather than taking a potentially arbitrary number from experiment, results for A_{\max} obtained from contact-mechanics simulations can be used, i.e., those summarized in section 2.1. However, the author fears that the resulting formula might be over-interpreted even if it is labeled with clear caution signs. Mathematically literate readers, however, are invited to insert the pertinent expression for A_{\max} into Equation (23). They will find that the friction coefficient in the model is predicted to decrease with a weak power law of the nominal contact pressure squeezing the surfaces together. At the same time, μ_s is found to decrease quite quickly with the ϵ_f , i.e., for $H = 0.8$ roughly according to $\epsilon_f^{0.78}$. This leads to the counterintuitive result that more roughness (on large wavelength) leads to less friction. Yet, roughness at small wavelengths increases friction—unless adhesive effects start to contribute significantly. The important restriction for these results to be borne out experimentally is that the dominant source of friction is a structural interlocking in the absence of dislocations and contaminants on the surfaces.

3. DISCUSSION AND CONCLUSIONS

In this work, a theory for structural lubricity of hard randomly rough surfaces that are lubricated with thin lamellar solids (graphene) was developed. The main assumptions entering the theory was that each individual contact patch is structurally lubric and that non-connected contact patches could act independently from each other. This is because different patches are lubricated by different sheets and/or thin sheets can buckle in-between two patches so that they are able to accommodate the local interface to the best of their abilities and as if there were no constraints on the sheet locally from other patches.

This study also included a back-of-the-envelope type calculation for the friction of flat, amorphous antimony particles moving in ultra-high vacuum on graphite (Dietzel et al., 2017). Results turned out rather promising thereby giving credibility to the possibility of structural lubricity.

The theory finds the friction coefficient to quickly decrease with the characteristic contact patch size, which itself increases

with load. Thus, if none of the usual friction mechanisms matters significantly, the ratio of lateral and normal force should decrease with increasing load, up to the point where the externally imposed stress induces dislocations. Assuming that maximum or characteristic contact patches are micrometer sized, a minimum friction coefficient of order $5 \cdot 10^{-4}$ is identified for nominally flat surfaces. For larger maximum contact patches, plastic deformation might be difficult to avoid.

A potentially counter-intuitive result of the theory is that increasing the roll-off wavelength λ_r and thus the rms-roughness is predicted to reduce friction, at least until plasticity sets in. The reason is that larger values of λ_r (while keeping the surface height spectrum at smaller wavelengths unchanged—whereby the rms-gradient would remain essentially unaltered) increases the typical distance between meso-scale contact patches. As a consequence, individual contact patches tend to carry more load, whereby the characteristic size of individual small-scale patches within the meso-scale patch increases. Finally, large individual contact patches have a small ratio of (maximum) shear forces and load.

For pin-on-disk type experiments, the microscopic scaling theory would have to be folded with the macroscopic Hertzian stress profile of the tip, as done, for example, in reference Müser (2016). It seems clear that this procedure leads to many more small patches near the (macroscopic) contact line and thereby to a substantial increase of the estimated friction coefficient. In addition, the predicted power law dependence of μ on the load would become (even) weaker.

Obviously, the results presented in this paper should be taken as crude order-of-magnitude guesses, even if much effort was made to provide reasonable pre-factors. In fact, most of the effort was made to provide reasonable pre-factors, which hopefully did not hide the simplicity of the scaling arguments. It would yet be interesting to apply the theory to a well-characterized contact, in which height spectra—or even better height topographies—of both surfaces are provided. In the case of a surface whose profile violates the random-phase approximation and/or for the regular pin-on-disk measurement, a full contact-mechanics analysis might have to be conducted first so that contact-patch statistics are accurate.

AUTHOR CONTRIBUTIONS

The author confirms being the sole contributor of this work and has approved it for publication.

ACKNOWLEDGMENTS

MM acknowledges helpful discussions with Sergej Sukhomlinov.

REFERENCES

- Aubry, S. (1983). The twist map, the extended Frenkel-Kontorova model and the devil's staircase. *Phys. D Nonlinear Phenomena* 7, 240–258. doi: 10.1016/0167-2789(83)90129-X
- Baumberger, T. and Caroli, C. (2006). Solid friction from stick-slip down to pinning and aging. *Adv. Phys.* 55, 279–348. doi: 10.1080/00018730600732186
- Baykara, M. Z., Vazirisereshk, M. R., and Martini, A. (2018). Emerging superlubricity: a review of the state of the art and perspectives

- on future research. *Appl. Phys. Rev.* 5:041102. doi: 10.1063/1.5015445
- Campaña, C. (2008). Using green's function molecular dynamics to rationalize the success of asperity models when describing the contact between self-affine surfaces. *Phys. Rev. E* 78:026110. doi: 10.1103/PhysRevE.78.026110
- Campaña, C. and Müser, M. H. (2007). Contact mechanics of real vs. randomly rough surfaces: A Green's function molecular dynamics study. *Europhys. Lett.* 77:38005. doi: 10.1209/0295-5075/77/38005
- Campaña, C., Müser, M. H., and Robbins, M. O. (2008). Elastic contact between self-affine surfaces: comparison of numerical stress and contact correlation functions with analytic predictions. *J. Phys. Condensed Matter* 20:354013. doi: 10.1088/0953-8984/20/35/354013
- Cihan, E., İpek, S., Durgun, E., and Baykara, M. Z. (2016). Structural lubricity under ambient conditions. *Nat. Commun.* 7:12055. doi: 10.1038/ncomms12055
- de Wijn, A. S. (2012). (In)commensurability, scaling, and multiplicity of friction in nanocrystals and application to gold nanocrystals on graphite. *Phys. Rev. B* 86:085429. doi: 10.1103/PhysRevB.86.085429
- de Wijn, A. S. (2014). Erratum: (in)commensurability, scaling, and multiplicity of friction in nanocrystals and application to gold nanocrystals on graphite [phys. rev. b86, 085429 (2012)]. *Phys. Rev. B* 90:039906. doi: 10.1103/PhysRevB.90.039906
- Dienwiebel, M., Verhoeven, G. S., Pradeep, N., Frenken, J. W. M., Heimberg, J. A., and Zandbergen, H. W. (2004). Superlubricity of graphite. *Phys. Rev. Lett.* 92:126101. doi: 10.1103/PhysRevLett.92.126101
- Dietzel, D., Brndiar, J., Štich, I., and Schirmeisen, A. (2017). Limitations of structural superlubricity: Chemical bonds versus contact size. *ACS Nano* 11, 7642–7647. doi: 10.1021/acsnano.7b02240
- Dietzel, D., de Wijn, A. S., Vorholzer, M., and Schirmeisen, A. (2018). Friction fluctuations of gold nanoparticles in the superlubric regime. *Nanotechnology* 29:155702. doi: 10.1088/1361-6528/aaac21
- Dietzel, D., Feldmann, M., Schwarz, U. D., Fuchs, H., and Schirmeisen, A. (2013). Scaling laws of structural lubricity. *Phys. Rev. Lett.* 111:235502. doi: 10.1103/PhysRevLett.111.235502
- Dietzel, D., Ritter, C., Mönninghoff, T., Fuchs, H., Schirmeisen, A., and Schwarz, U. D. (2008). Frictional duality observed during nanoparticle sliding. *Phys. Rev. Lett.* 101:125505. doi: 10.1103/PhysRevLett.101.125505
- Erdemir, A. and Eryilmaz, O. (2014). Achieving superlubricity in DLC films by controlling bulk, surface, and tribochemistry. *Friction* 2, 140–155. doi: 10.1007/s40544-014-0055-1
- Hammerberg, J., Holian, B., Röder, J., Bishop, A., and Zhou, S. (1998). Nonlinear dynamics and the problem of slip at material interfaces. *Phys. D Nonlinear Phenomena* 123, 330–340. doi: 10.1016/S0167-2789(98)00132-8
- He, G., Müser, M. H., and Robbins, M. O. (1999). Adsorbed layers and the origin of static friction. *Science* 284, 1650–1652.
- He, G. and Robbins, M. O. (2001). Simulations of the kinetic friction due to adsorbed surface layers. *Tribol. Lett.* 10, 7–14. doi: 10.1023/A:1009030413641
- Hirano, M. and Shinjo, K. (1990). Atomistic locking and friction. *Phys. Rev. B* 41, 11837–11851.
- Hyun, S., Pei, L., Molinari, J.-F., and Robbins, M. O. (2004). Finite-element analysis of contact between elastic self-affine surfaces. *Phys. Rev. E* 70:026117. doi: 10.1103/PhysRevE.70.026117
- Jacobs, T. D. B., Junge, T., and Pastewka, L. (2017). Quantitative characterization of surface topography using spectral analysis. *Surf. Topogr. Metrol. Prop.* 5:013001. doi: 10.1088/2051-672X/aa51f8
- Lee, C., Li, Q., Kalb, W., Liu, X. Z., Berger, H., Carpick, R. W., et al. (2010). Frictional characteristics of atomically thin sheets. *Science* 328, 76–80. doi: 10.1126/science.1184167
- Lee, S. and Spencer, N. D. (2008). Sweet, hairy, soft, and slippery. *Science* 319, 575–576. doi: 10.1126/science.1153273
- Martin, J. M., Donnet, C., Mogné, T. L., and Epicier, T. (1993). Superlubricity of molybdenum disulphide. *Phys. Rev. B* 48, 10583–10586. doi: 10.1103/PhysRevB.48.10583
- Martin, J. M. and Erdemir, A. (2018). Superlubricity: friction's vanishing act. *Phys. Today* 71, 40–46. doi: 10.1063/PT.3.3897
- Müser, M. (2001). Dry friction between flat surfaces: multistable elasticity vs. material transfer and plastic deformation. *Tribol. Lett.* 10, 15–22. doi: 10.1023/A:1009086631388
- Müser, M. H. (2002). Nature of mechanical instabilities and their effect on kinetic friction. *Phys. Rev. Lett.* 89:224301. doi: 10.1103/PhysRevLett.89.224301
- Müser, M. H. (2004). Structural lubricity: role of dimension and symmetry. *Europhys. Lett.* 66, 97–103. doi: 10.1209/epl/i2003-10139-6
- Müser, M. H. (2008). Rigorous field-theoretical approach to the contact mechanics of rough elastic solids. *Phys. Rev. Lett.* 100:055504. doi: 10.1103/PhysRevLett.100.055504
- Müser, M. H. (2016). On the contact area of nominally flat hertzian contacts. *Tribol. Lett.* 64:14. doi: 10.1007/s11249-016-0750-3
- Müser, M. H. and Robbins, M. O. (2000). Conditions for static friction between flat crystalline surfaces. *Phys. Rev. B* 61, 2335–2342. doi: 10.1103/PhysRevB.61.2335
- Müser, M. H., Urbakh, M., and Robbins, M. O. (2003). "Statistical mechanics of static and low-velocity kinetic friction," in *Advances in Chemical Physics*, eds I. Prigogine and S. A. Rice (New York, NY: John Wiley & Sons), 187–272.
- Müser, M. H. and Wang, A. (2018). Contact-patch-size distribution and limits of self-affinity in contacts between randomly rough surfaces. *Lubricants* 6:85. doi: 10.3390/lubricants6040085
- Müser, M. H., Wenning, L., and Robbins, M. O. (2001). Simple microscopic theory of amontons's laws for static friction. *Phys. Rev. Lett.* 86, 1295–1298. doi: 10.1103/PhysRevLett.86.1295
- Özoğul, A., İpek, S., Durgun, E., and Baykara, M. Z. (2017). Structural superlubricity of platinum on graphite under ambient conditions: the effects of chemistry and geometry. *Appl. Phys. Lett.* 111:211602. doi: 10.1063/1.5008529
- Palasantzas, G. (1993). Roughness spectrum and surface width of self-affine fractal surfaces via the k-correlation model. *Phys. Rev. B* 48, 14472–14478.
- Pastewka, L., Prodanov, N., Lorenz, B., Müser, M. H., Robbins, M. O., and Persson, B. N. J. (2013). Finite-size scaling in the interfacial stiffness of rough elastic contacts. *Phys. Rev. E* 87:062809. doi: 10.1103/PhysRevE.87.062809
- Persson, B. N. J. (2001). Theory of rubber friction and contact mechanics. *J. Chem. Phys.* 115:3840. doi: 10.1063/1.1388626
- Persson, B. N. J. (2008). On the elastic energy and stress correlation in the contact between elastic solids with randomly rough surfaces. *J. Phys. Condensed Matter* 20:312001. doi: 10.1088/0953-8984/20/31/312001
- Persson, B. N. J. (2014). On the fractal dimension of rough surfaces. *Tribol. Lett.* 54, 99–106. doi: 10.1007/s11249-014-0313-4
- Popov, V. and Gray, J. (2012). Prandtl-Tomlinson model: history and applications in friction, plasticity, and nanotechnologies. *ZAMM J. Appl. Math. Mech.* 92, 683–708. doi: 10.1002/zamm.201200097
- Prandtl, L. (1928). Ein Gedankenmodell zur kinetischen Theorie der festen Körper. *Z. Angew. Math. Mech.* 8:85.
- Sharp, T. A., Pastewka, L., and Robbins, M. O. (2016). Elasticity limits structural superlubricity in large contacts. *Phys. Rev. B* 93:121402. doi: 10.1103/PhysRevB.93.121402
- Shinjo, K. and Hirano, M. (1993). Dynamics of friction: superlubric state. *Surf. Sci.* 283, 473–478.
- Socoliuc, A., Bennewitz, R., Gnecco, E., and Meyer, E. (2004). Transition from stick-slip to continuous sliding in atomic friction: entering a new regime of ultralow friction. *Phys. Rev. Lett.* 92:134301. doi: 10.1103/PhysRevLett.92.134301
- Sørensen, M. R., Jacobsen, K. W., and Stoltz, P. (1996). Simulations of atomic-scale sliding friction. *Phys. Rev. B* 53, 2101–2113.
- Verhoeven, G. S., Dienwiebel, M., and Frenken, J. W. M. (2004). Model calculations of superlubricity of graphite. *Phys. Rev. B* 70:165418. doi: 10.1103/PhysRevB.70.165418
- Wang, W., Dai, S., Li, X., Yang, J., Srolovitz, D. J., and Zheng, Q. (2015). Measurement of the cleavage energy of graphite. *Nat. Commun.* 6:8853. doi: 10.1038/ncomms8853

Conflict of Interest Statement: The author declares that the research was conducted in the absence of any commercial or financial relationships that could be construed as a potential conflict of interest.

Copyright © 2019 Müser. This is an open-access article distributed under the terms of the Creative Commons Attribution License (CC BY). The use, distribution or reproduction in other forums is permitted, provided the original author(s) and the copyright owner(s) are credited and that the original publication in this journal is cited, in accordance with accepted academic practice. No use, distribution or reproduction is permitted which does not comply with these terms.



Adhesive Strength of Contacts of Rough Spheres

Qiang Li^{1*}, Roman Pohrt^{1*} and Valentin L. Popov^{1,2*}

¹ Institute of Mechanics, Berlin University of Technology, Berlin, Germany, ² National Research Tomsk State University, Tomsk, Russia

The adhesive contact between a parabolic indenter with superimposed roughness and an elastic half space is studied in the JKR-limit (infinitely small range of action of adhesive forces) using the boundary element method with mesh-dependent detachment criterion suggested in 2015. Three types of superimposed roughness are considered: one- and two-dimensional waviness and randomly rough roughness. It is shown that in the case of regular waviness, the character of adhesion is governed by the Johnson adhesion parameter. For our randomly rough surfaces a new adhesion parameter has been identified numerically, which uniquely determines the adhesive strength of the contact.

OPEN ACCESS

Keywords: adhesion, roughness, wavy surface, rough surface, boundary element method

Edited by:

Irina Georgievna Goryacheva,
Institute for Problems in Mechanics
(RAS), Russia

Reviewed by:

Feodor M. Borodich,
Cardiff University, United Kingdom
Luciano Afferrante,
Politecnico di Bari, Italy

*Correspondence:

Qiang Li
qiang.li@tu-berlin.de
Roman Pohrt
roman.pohrt@tu-berlin.de
Valentin L. Popov
v.popov@tu-berlin.de

Specialty section:

This article was submitted to
Tribology,
a section of the journal
Frontiers in Mechanical Engineering

Received: 05 December 2018

Accepted: 01 March 2019

Published: 26 March 2019

Citation:

Li Q, Pohrt R and Popov VL (2019)
Adhesive Strength of Contacts of
Rough Spheres.
Front. Mech. Eng. 5:7.
doi: 10.3389/fmech.2019.00007

INTRODUCTION

It is well-known that neutral bodies attract each other by van der Waals forces. However, adhesive forces in macroscopic systems often are negligible. Kendall expressed this with his famous statement “solids are expected to adhere; the question is to explain why they do not, rather than why they do!” (Kendall, 2001). The reason for the weakness of adhesion in macroscopic contacts is the roughness of surfaces. It is the roughness which prevents intimate contact on the atomic scale (Fuller and Tabor, 1975; Luan and Robbins, 2005; Ciavarella, 2017). However, it was shown both theoretically and experimentally that roughness sometimes can even enhance adhesion. Briggs and Briscoe have observed that a small roughness increases the adhesion energy compared to the smooth surface in the pull-off experiment of smooth rubber against a Perspex cylinder, but large roughness can reduce the adhesion significantly (Briggs and Briscoe, 1977). The analysis of a sphere with axially-symmetrical waviness studied by Guduru and numerically by Wu also shows an increase in the adhesive force (Guduru, 2007; Wu, 2012).

The influence of simplified roughness in form of regular waviness on adhesion in the whole range of roughness amplitudes from “very rough” to “practically smooth” was studied by Johnson in 1995. He introduced a dimensionless parameter governing the adhesion behavior. He found that above a critical value of this “Johnson parameter,” surfaces jump into complete contact even at zero load (Johnson, 1995). This study was based on the solution of non-adhesive contact given by Westergaard (1939) and the Griffith idea of energy balance as used in the original Johnson-Kendall-Robert (JKR) theory for parabolic contacts (Johnson et al., 1971). In recent years a few attempts have been undertaken to generalize this work of Johnson. Afferrante et al. proposed an analytical solution for rough surfaces containing a series of superposed sinewaves defined by the Weierstrass function (Afferrante et al., 2015). Persson and Scaraggi used a DMT-type model (Derjaguin-Muller-Toporov) to study the effect of roughness on adhesion in DMT-limit (Persson and Scaraggi, 2014). Ciavarella proposed a simple approach for rough adhesive contact, the so-called bearing-area model (BAM) (Ciavarella, 2018a) and also an approximation in the JKR regime (Ciavarella, 2018b). Numerically, the adhesion of rough surfaces has been studied using molecular

dynamics (Pastewka and Robbins, 2014, 2016), finite element method based on molecular dynamics (Eid et al., 2011), Boundary Element Method (BEM) (Carbone et al., 2009; Joe et al., 2017; Rey et al., 2017) and the method of non-linear boundary integral equations (Galanov, 2011).

In the present paper we numerically study contacts of parabolic bodies with superimposed roughness either in form of a regular waviness or multi-scale roughness. We restrict ourselves to the limiting case of very short ranged adhesive forces which we will call the JKR-limit, because the JKR theory uses exactly the same assumption. Application of the Boundary Element Method for simulation of adhesive contacts in the JKR limit was made possible in 2015 by means of a mesh-size dependent detachment criterion proposed by Pohrt and Popov (Pohrt and Popov, 2015). This numerical approach has been validated by comparison with existing analytical solutions including axisymmetric contacts (Popov et al., 2017), elliptic contacts (Li et al., 2018) and toroidal contacts (Argatov et al., 2016). The method was applied to solve a number of contact problems, such as brush-like structures (Li and Popov, 2018a,b) and flat-ended indenters with complicated face shapes (Popov et al., 2017). Recently this method was developed further to include functionally graded material and layered material (Li and Popov, 2017; Li et al., 2018). The present paper closes the gap in the classes of systems considered so far by considering adhesion of curved contacts with superimposed roughness—the problem which in some sense can be considered as the generic case of any real adhesive contact.

The structure of this paper is the following. In section Adhesive Contact of One- and Two-Dimensional Wavy Surface With Periodic Boundary Conditions we recapitulate the known analytical results for adhesive contact between a wavy surface (one- and two-dimensional waviness) and an elastic half space and reproduce them by numerical simulation. In section Adhesive Contact of a Sphere With a Two-Dimensional Wavy Roughness the adhesive contact of a curved surface with superimposed waviness is considered. We show that the character of adhesion in this case is essentially governed by the Johnson parameter. In section Adhesive Contact of a Parabolic Indenter With a Random Roughness contacts of curved surfaces with superimposed random roughness are investigated. It is noted that the numerical simulation in sections Adhesive Contact of a Sphere With a Two-Dimensional Wavy Roughness and Adhesive Contact of a Parabolic Indenter With a Random Roughness are carried out only for the pull-off (unloading). Section Conclusion gives conclusions on the above cases.

ADHESIVE CONTACT OF ONE- AND TWO-DIMENSIONAL WAVY SURFACE WITH PERIODIC BOUNDARY CONDITIONS

One-Dimensional Waviness

Basic understanding of the role of roughness on adhesion has been achieved by Johnson (Johnson, 1995). He considered adhesion between a regular slightly wavy surface with amplitude h and wavelength λ :

$$f(x) = h[1 - \cos(2\pi x/\lambda)] \quad (1)$$

and an elastic half space with effective elastic modulus $E^* = E/(1 - \nu^2)$, where E is elastic modulus and ν is Poisson's ratio. The relation between the mean pressure p and the contact half-width a (within one wavelength λ) in a dimensionless form is given by

$$p/p_{1D}^* = \sin^2 \psi_a - \alpha (\tan \psi_a)^{1/2}, \quad (2)$$

where $p_{1D}^* = \pi E^* h / \lambda$ is the pressure needed for complete contact in the corresponding non-adhesive problem and $\psi_a = \pi a / \lambda$. The dimensionless parameter α is defined as

$$\alpha = \left(\frac{2\lambda\gamma}{\pi^2 h^2 E^*} \right)^{1/2}, \quad (3)$$

where γ is the work of adhesion per unit area. In the following, we will refer to α as the “Johnson parameter.”

The relation is shown in **Figure 1** for different values of Johnson parameter α (solid lines). Numerically we simulated the same contact using the Boundary Element Method with periodic boundary conditions. Dependences of the normalized average pressure on the normalized half-width of the contact are represented with symbols. The subplot shows a 3D representation of a sample contact configuration. Numerical simulations were carried out under controlled approach of surfaces. This allows us to reach steady states which are not obtained in force-control. The reason is that when the force is controlled and increased from zero for $\alpha < 0.57$, small values of $\pi a / \lambda$ are not reached. Instead, the first touch of the surfaces leads to a sudden jump into the contact configuration corresponding to the intersection of the corresponding curve and the axis $p = 0$. Further increase of pressure leads to increase of the contact area until the maximum of the force is achieved. At further approach, the system jumps into complete contact. At the values of Johnson parameter $\alpha > 0.57$ the maximum of the force is negative; this means that the system jumps into complete contact immediately at first touch.

Two-Dimensional Waviness

In the paper by Johnson (1995) contacts with two-dimensional waviness of the form

$$f(x, y) = h[1 - \cos(2\pi x/\lambda) \cos(2\pi y/\lambda)] \quad (4)$$

were also briefly discussed. An analytical solution was given only for the extreme case of large load (approaching the complete contact) based on the asymptotic solution of non-adhesive contact (Johnson et al., 1985) while the non-contact area was assumed to be circular. This solution is also governed by the same Johnson parameter α as given in equation (3):

$$p/p_{2D}^* = 1 - 4/3 \cdot \psi_b^2 - \pi/(2\sqrt{2}) \alpha \cdot (1/\psi_b)^{1/2}. \quad (5)$$

Here $p_{2D}^* = \sqrt{2}\pi E^* h / \lambda$ is the pressure needed for achieving complete contact in the non-adhesive problem and $\psi_b = \pi b / \lambda$. Note that here b is the radius of the non-contact area.

Dependencies of the average pressure on the normalized contact radius obtained by BEM are shown in **Figure 2**. The

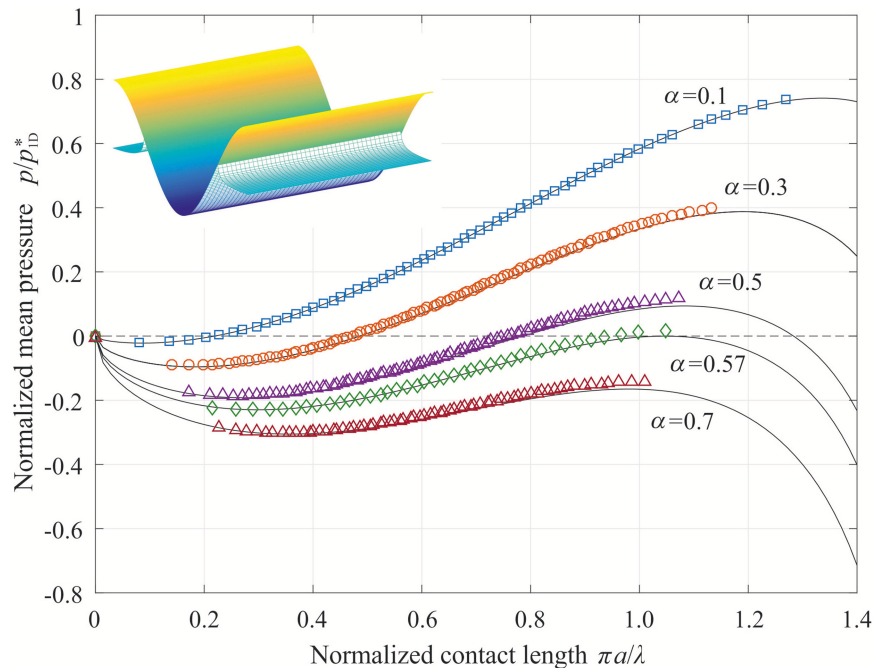


FIGURE 1 | Dependence of the mean pressure on the contact half-width in “one-dimensional” adhesive contact. Solid lines show analytical solution and symbols present results of numerical simulation with BEM.

“contact radius” is formally defined as $a^* = \sqrt{A_{\text{con}}/\pi}$. At the full contact we have $a^* = \sqrt{\lambda^2/\pi}$ or $\pi a^*/\lambda = \sqrt{\pi} \approx 1.77$, so the value of 1.77 in x-axis of **Figure 2** indicates the complete contact. The relation between load and contact radius for different parameter α is presented in **Figure 2A**. More details can be seen in **Figure 2B**, where the force-radius dependence and the contact configurations are shown for the case of a moderate value $\alpha = 0.4$. As already pointed out by Johnson, adhesive contact with a two dimensional waviness is similar to that of one-dimensional waviness but has also some differences. One can see that there are two contact stages during detachment: From point A to C, adjacent contact areas are connected and the shape of the non-contact region resembles a square with rounded corners. The transition from point C to point D is not continuous. Instead, the contact drops from the connected state to the multi-area contact. The amplitude of the discontinuity depends on the value of α . For very small values of α , the curve is more connected (see **Figure 2A** at $\alpha = 0.1$). In the opposite case of α larger than a critical value of ~ 0.57 , a stable multi-contact configuration cannot be reached during detachment. Instead the contact is lost entirely. Please note that this value of 0.57 has different interpretation from that in one-dimensional contact.

ADHESIVE CONTACT OF A SPHERE WITH A TWO-DIMENSIONAL WAVY ROUGHNESS

Consider a parabolic shape with a superimposed waviness:

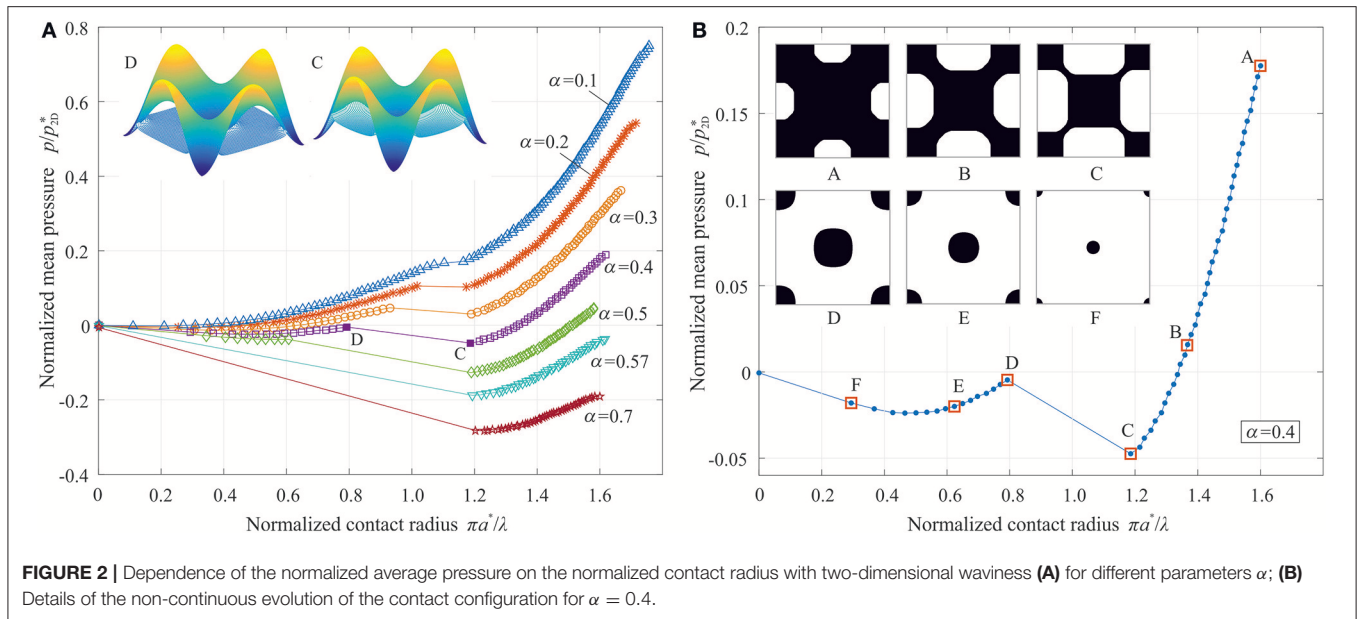
$$f(x, y) = \frac{x^2 + y^2}{2R} + h \left[1 - \cos \frac{2\pi x}{\lambda} \cos \frac{2\pi y}{\lambda} \right] \quad (6)$$

where R is the radius of curvature of the parabolic profile and other parameters are the same as defined in section Adhesive Contact of One- and Two-Dimensional Wavy Surface With Periodic Boundary Conditions. An example of such a surface is illustrated in **Figure 3A**. For a smooth sphere, the well-known analytical solution (JKR theory) for the load-displacement dependence is plotted in **Figure 4A** with solid line. Normal force and displacement are normalized by the critical values

$$F_{\text{JKR}} = -\frac{3}{2}\pi\gamma R, \quad (7)$$

$$d_{\text{JKR}} = -\left(\frac{3\pi^2\gamma^2 R}{64E^*2}\right)^{1/3}. \quad (8)$$

Numerical simulation of the pull-off was again carried out using the BEM under the displacement-controlled condition. In this series of simulations we did not use periodic boundary conditions but free boundaries like in Hertz-theory. Due to the macroscopic curvature, a new dimensionless parameter λ/R appears in the present problem. We begin our consideration with an illustration of the influence of waviness on adhesion in the special case $\lambda/R = 0.05$, with the amplitudes of waviness h/λ varying from 0.2 to 1. The mesh size was chosen in such a way that one period of waviness has at least 42×42 grid points. The dependencies of the normal force on the displacement are shown in **Figure 4A**. To compare the results with the JKR solution, we focus on the adhesive force F_{ad} defined as the greatest tensile force corresponding to the minimum of the force-displacement relation. The absolute values of this force for different amplitudes of waviness are shown in **Figure 4B**. One can see that the



adhesive force first increases with the amplitude of waviness and then drops to a very low value for amplitudes exceeding some threshold value.

Figure 4C shows a series of typical contact configurations during the pull-off for four increasing wave amplitudes, corresponding to the curves *b*, *d*, *e*, *f* in **Figure 4A**. The last picture always corresponds to the last stable configuration before complete detachment. For small enough roughness amplitude, as represented by the case *b*, the contact area represents basically a complete circle with a rough border. The maximum adhesive force is in this case larger than for the smooth sphere (JKR). From **Figure 4B** it can be seen that maximum enhancement is by the factor 1.7 for such situation. The case *d* is similar to *b*, but here the contact area is not continuous: there are some isolated points at the border around the rough circle. With increasing the amplitude of waviness, this effect becomes more pronounced, as exemplified with the case *e*: a circular area at the center is surrounded by a ring of separated points around the border. The pictures A and B in case *e* illustrate a transition between a state having a compact center contact to a cloud of point contacts. The two configurations are marked in **Figure 4A**: one can see the jump in the force from A to B. In case *f*, the contact always consists of unconnected points. The adhesive force in such a configuration is very small and further decreases when the amplitude of the waviness is increased (**Figure 4B**). There is an intuitive explanation of the described behavior. When the Johnson parameter for the chosen waviness is much larger than the critical one, the macroscopic profile can be considered as smooth. Only at the border there will be some perturbation as in the case *b*. In the opposite case of very small Johnson parameter, the contact occurs only at the summits of the waviness. Our hypothesis is thus that the Johnson parameter determines which one of the two scenarios will be realized.

To prove this hypothesis, we replotted **Figure 4B** to show the dependence of the adhesive force on the Johnson parameter. For different values of the elastic modulus, surface energy, radius of the sphere and the wave length, the adhesive detachment shows a universal behavior: the maximum pull-off force expressed in terms of the JKR value indeed depends strongly on the Johnson parameter and only very weak on the normalized wavelength λ/R . At the critical value of the Johnson parameter $\alpha \approx 0.24$, the transition from the “compact area” to the “point cloud” solution occurs and the adhesive force drops drastically. For smaller Johnson parameter ($\alpha < 0.24$), the adhesive force is very small and approximately proportional to the Johnson parameter, as shown in **Figure 5B** the encircled part corresponding to the area in **Figure 5A**.

The dependence of adhesive force on the Johnson parameter can be approximated as

$$\frac{F_{ad}}{F_{JKR}} \approx \Lambda(\alpha) = \begin{cases} \frac{0.27}{\alpha^2} \cdot \exp\left(-\frac{0.14}{\alpha^2}\right) + 1, & \text{for } \alpha > 0.24 \\ 0.65 \cdot \alpha - 0.025, & \text{for } \alpha < 0.24 \end{cases} \quad (9)$$

The maximum tensile force during adhesive detachment of a sphere with superposed regular waviness can thus be expressed as

$$F_{ad} \approx -\frac{3}{2} R \pi \gamma \Lambda(\alpha). \quad (10)$$

ADHESIVE CONTACT OF A PARABOLIC INDENTER WITH A RANDOM ROUGHNESS

In this section we consider the adhesion of a rough sphere. On the one hand, it is widely accepted that roughness can significantly reduce adhesion. In Fuller and Tabor (1975), this was shown for a contact between a smooth sphere and a rough flat surface having asperities with Gaussian height distribution. In some cases,

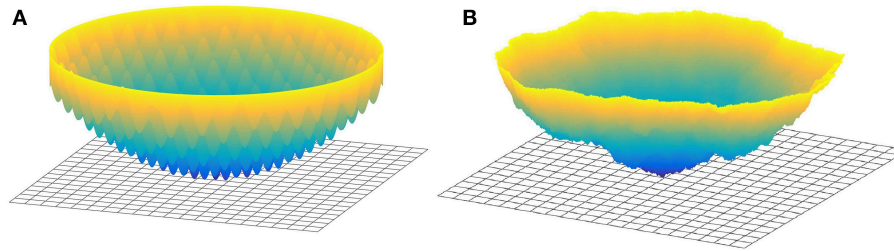


FIGURE 3 | Illustration of a regularly (A) and randomly (B) rough sphere in contact with an elastic half-space.

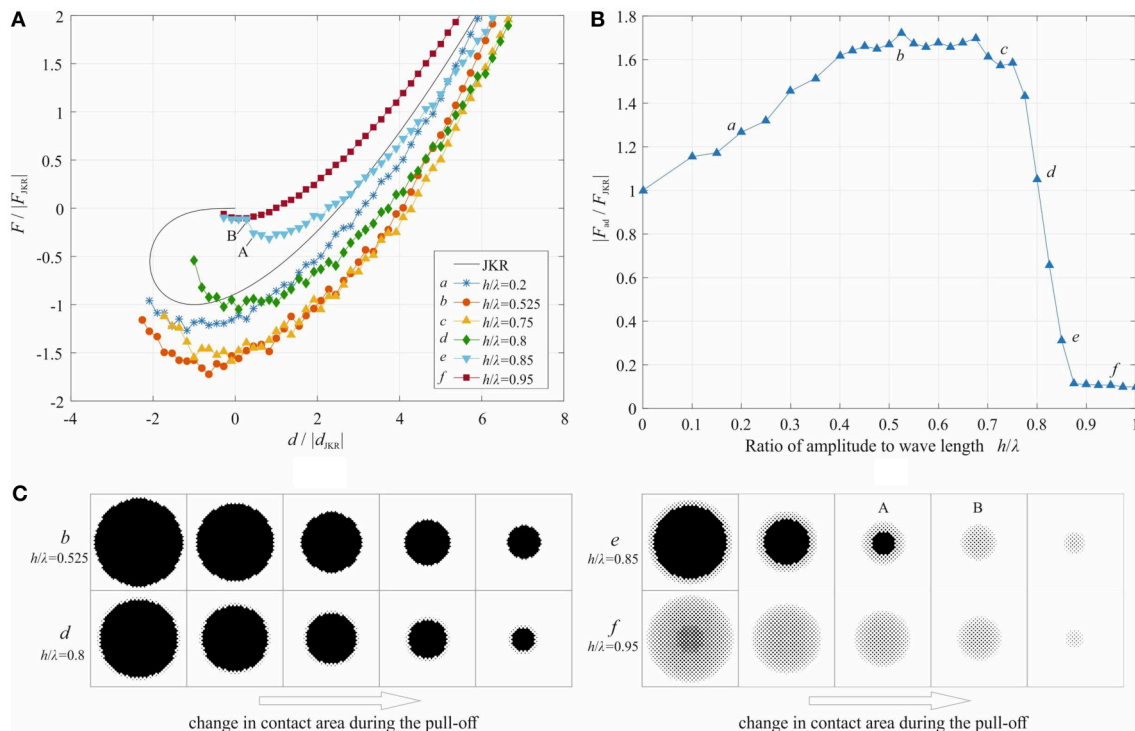
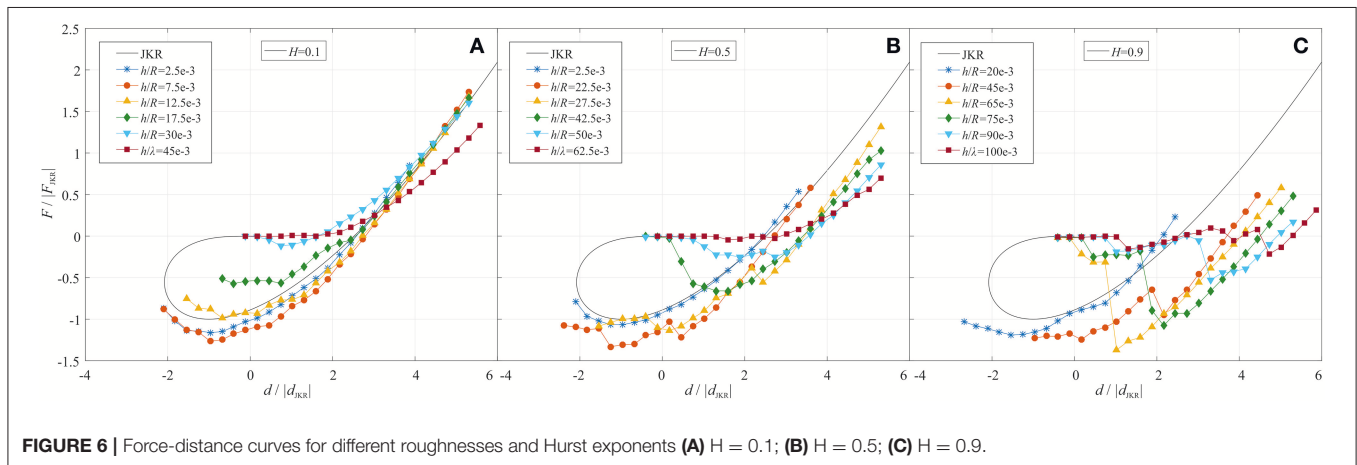
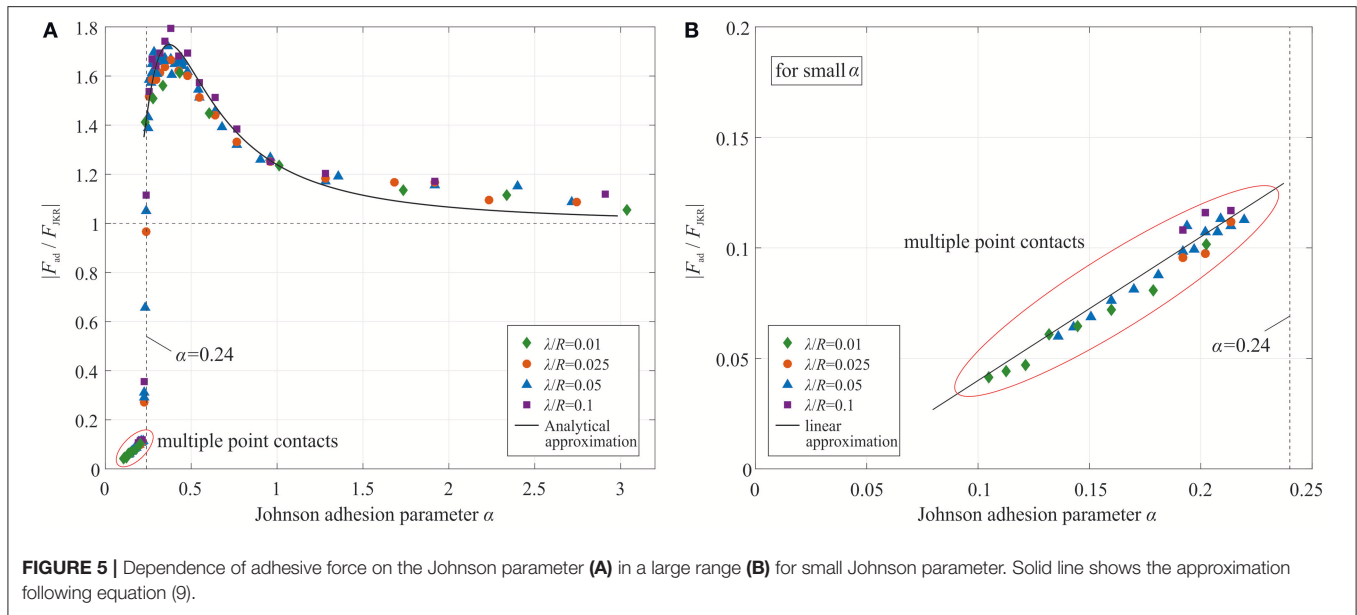


FIGURE 4 | Adhesive contact of a rough sphere. (A) Load-displacement dependence for different amplitudes of waviness; (B) dependence of adhesive force on the amplitude of the waviness; (C) four exemplary evolutions of the contact area during pull-off.

however, roughness can enhance adhesion. Early in 1977 the experimental investigation of a smooth rubber against a Perspex cylinder has shown that some small roughness can enhance the adhesion but the opposite is true for larger roughness (Briggs and Briscoe, 1977). The theoretical and numerical study of a sphere covered with only one regular waviness also showed an increase of adhesive force (Guduru, 2007; Wu, 2012). In Fuller (2011) it was found experimentally that adhesion in the rolling contact of a cylinder on an elastomer could substantially increase if the surfaces were rough. This enhancement was only observed when the elastomer was soft enough. The enhancement of adhesion was associated with the bulk viscoelastic effects of materials. Kesari et al. found that the surface roughness increases the energy hysteresis in the adhesion experiment of depth-dependent hysteresis using both AFM and nanoindentation apparatus and it

was stated that the hysteresis is contributed by several factors and surface roughness could be an important one (Kesari et al., 2010). Medina and Dini found a similar increase of the adhesive pull-off force at low roughness for large values of Tabor parameter (≈ 5) in a numerical study. They used the Lennard-Jones potential for calculating van der Waals forces between elements (Medina and Dini, 2014). Recently an indentation test of spheres with micro-force tester showed that the highest pull-off force was found not on the smooth sample but that with micro roughness (Pepelyshev et al., 2018). It was argued that the increase of the contact area is the main cause for the increase pull-off force. In our numerical simulation, we also find the same behavior in the adhesive contact of rough spheres.

Consider a parabolic profile with curvature radius R superposed with a random roughness (Figure 3B). In the present



paper, we use a roughness generator described in Pohrt and Li (2014). It produces a randomly rough surface by using the back Fourier transformation from a Fourier-density with a power-law dependency of its absolute value on the absolute value of the wave-vector, q , as well as vectors q_0 , q_1 and the rms roughness h . The minimum and maximum random phases, while integration is performed between two “cut-off” wave vectors q_0 , q_1 . The exponent of the power-law dependency, H , (ranging from 0 to 1), is sometimes called the “Hurst exponent.” The roughness generated by the above mentioned procedure is unambiguously determined by the exponent H , the cut-off wave vectors which can be realized in a finite discrete system are given by $q_{\min} = 2\pi/L$ and $q_{\max} = \pi/\Delta x$, where L is the length of simulation area and Δx is the mesh size. In the simulation, we assume $L = R$ and put $q_0 = q_{\min}$ and $q_1 = q_{\max}$. Note that the roughness produced in the described way does not necessarily represent real surfaces, which normally show strong phase correlation (Borodich et al., 2016). However, we consider

the described generator as a way for producing well-defined comparable rough topography. We avoid calling these surfaces “fractal” but will further use for H the notation “Hurst exponent”

The pull-off was simulated for a number of increasing amplitudes of roughness and for different Hurst exponents. A few examples of force-distance curve are shown in **Figure 6**. One can see that, similarly to the case in section Adhesive Contact of a Sphere With a Two-Dimensional Wavy Roughness, small roughness leads to an increase of the adhesive force. Further increase of roughness reduces the force of adhesion. This behavior can be observed more clearly in **Figure 7A**, where the average values of pull-off force for 15 realizations of rough surfaces are shown as well as the corresponding standard deviations. The phenomenon of enhanced adhesion is observed for small Hurst exponents from 0.1 to 0.5, but not always for large Hurst exponent 0.7 and 0.9: the pull-off force for some rough surfaces with $H = 0.7$ or 0.9 decreases with roughness. In direct comparison it can be seen that surfaces with higher Hurst

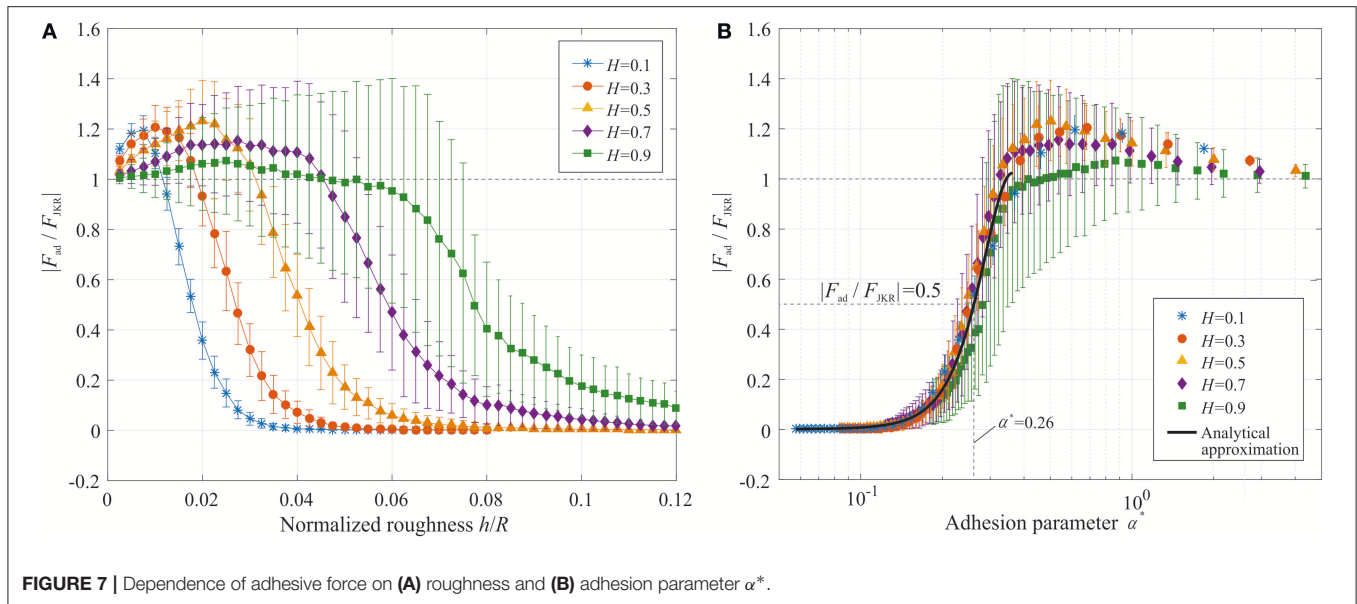


FIGURE 7 | Dependence of adhesive force on (A) roughness and (B) adhesion parameter α^* .

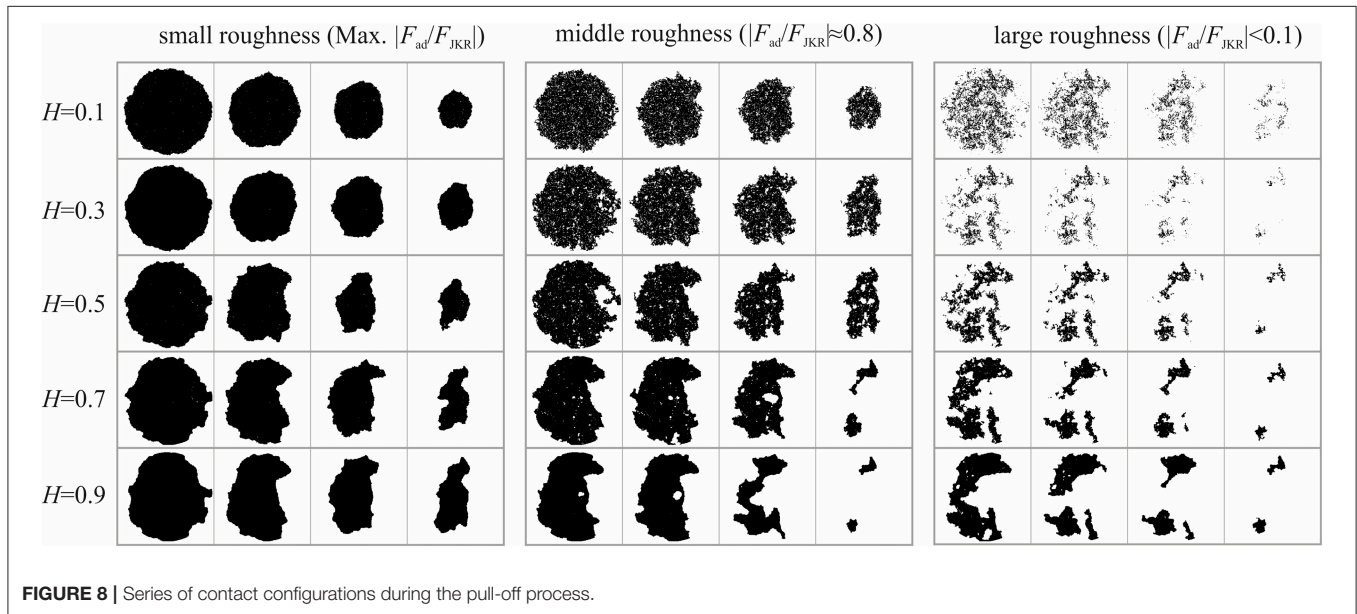


FIGURE 8 | Series of contact configurations during the pull-off process.

exponent have generally a wider range of roughness for which the adhesive force is enhanced. Results presented in **Figure 7A** suggest that there is no critical value of the Hurst exponent.

As we have seen in sections Adhesive Contact of One- and Two-Dimensional Wavy Surface With Periodic Boundary Conditions and Adhesive Contact of a Sphere With a Two-Dimensional Wavy Roughness, the main governing parameter for adhesion of wavy surfaces is the Johnson parameter. In the case of randomly rough surfaces, this parameter cannot be determined from the waviness because the roughness is a superposition of a large number of waves with various amplitudes. If any, a series of Johnson parameters for different scales would have to be defined. If a single governing parameter similar to the Johnson parameter does exist in this case, it

may depend on all material and geometric parameters of the contact problem: elastic modulus E^* , surface energy γ , surface roughness h , Hurst exponent H and cutoff wave vectors q_0 and q_1 . Based on the results presented in **Figure 7A** we suggest the following definition for an “adhesion parameter” of this kind of rough surfaces:

$$\alpha^* = \left(\frac{4\gamma q_1^{0.8H-1}}{\pi E^* h^2 q_0^{0.8H}} \right)^{1/2}. \quad (11)$$

Note that if there is only one wave vector $q_0 = q_1$, equation (11) reduces to the original Johnson parameter equation (3). When the force of adhesion is plotted as function of α^* , all results collapse to a single dependency shown in **Figure 7B**.

Different from the case of regular waviness in section Adhesive Contact of a Sphere With a Two-Dimensional Wavy Roughness, the pull-off force here doesn't drop dramatically at some critical value apparently, so we give an analysis of the relation of pull-off force and the adhesion parameter in this transition region. It is found that the following Gaussian-type expression gives a good approximation:

$$\left| \frac{F_{ad}}{F_{JKR}} \right| \approx \Lambda^*(\alpha^*) = 1.023 \cdot \exp \left(-\frac{(\alpha^* - 0.3619)^2}{0.1188^2} \right). \quad (12)$$

It covers the range from very low force $|F_{ad}/F_{JKR}| \approx 0$ transiting to the value $|F_{ad}/F_{JKR}| \approx 1$ for $\alpha^* = 0.344$. In the range for larger α^* , enhanced adhesion is not always observed for large Hurst exponents, so an analytical approximation is not given in this study. Furthermore, there is not a clear critical value of α^* as in the case of regular waviness, therefore we give here only a value of adhesion parameter $\alpha^* = 0.26$ for $|F_{ad}/F_{JKR}| \approx 0.5$.

Figure 8 presents details of contact configurations corresponding to numerical results presented in **Figure 6** and **Figure 7**. For each Hurst exponent, three values of h are shown, related to their effect on the obtained adhesive force: In the left column of **Figure 8**, the amplitude of roughness is small and corresponds to the maximum of the adhesive force (see **Figure 7**), the second column represents intermediate roughness with $|F_{ad}/F_{JKR}| \approx 0.8$. In the third column, a large roughness value is chosen with $|F_{ad}/F_{JKR}| < 0.1$. If the roughness is small enough, the contact area is almost compact. This is particularly pronounced for large H and small h .

CONCLUSION

The adhesive detachment of curved surfaces with two-dimensional waviness from an elastic half space was numerically

simulated using the boundary element method. We found that waviness can both increase and decrease the adhesive force compared to the smooth JKR solution. The deviation from JKR behavior depends mainly on the unmodified Johnson adhesion parameter α . At some critical value $a \approx 0.24$, a transition occurs from a compact contact with rough boundary to a contact consisting of multiple separated contact spots and the obtained tensile force is reduced significantly.

In the case of added random roughness, the simulation was carried out for different Hurst exponents and amplitudes of roughness. In all cases we observed that the adhesive force at small roughness amplitudes is increased. For roughness amplitudes above some critical value, the adhesion is decreased significantly. This observation is in agreement with experiments, such as those conducted by Briggs and Briscoe (1977). For the investigated class of randomly rough surfaces, we identified an adhesive parameter determining the force of adhesion.

AUTHOR CONTRIBUTIONS

VP and RP conceived the study. VP carried out analytical analysis. QL carried out numerical simulations. All authors drafted and reviewed the manuscript.

FUNDING

Authors acknowledge financial support of the Deutsche Forschungsgemeinschaft (DFG PO 810-55-1) and the German ministry for research and education BMBF, grant No. 13NKE011A. This research was also partially supported by the Tomsk State University competitiveness improvement program.

REFERENCES

- Afferrante, L., Clavarella, M., and Demelio, G. (2015). Adhesive contact of the weierstrassprofile. *Proc. R. Soc. A Math. Phys. Eng. Sci.* 471, 387–405. doi: 10.1098/rspa.2015.0248
- Argatov, I., Li, Q., Pohrt, R., and Popov, V. L. (2016). Johnson-kendall-roberts adhesive contact for a toroidal indenter. *Proc. R. Soc. London A Math. Phys. Eng. Sci.* 472:20160218. doi: 10.1098/rspa.2016.0218
- Borodich, F. M., Pepelyshev, A., and Savencu, O. (2016). Statistical approaches to description of rough engineering surfaces at nano and microscales. *Tribol. Int.* 103, 197–207. doi: 10.1016/j.triboint.2016.06.043
- Briggs, G. A. D., and Briscoe, B. J. (1977). The effect of surface topography on the adhesion of elastic solids. *J. Phys. D Appl. Phys.* 10, 2453–2466. doi: 10.1088/0022-3727/10/18/010
- Carbone, G., Scaraggi, M., and Tartaglino, U. (2009). Adhesive contact of rough surfaces: Comparison between numerical calculations and analytical theories. *Eur. Phys. J. E* 30, 65–74. doi: 10.1140/epje/i2009-10508-5
- Ciavarella, M. (2017). On pastewka and robbins' criterion for macroscopic adhesion of rough surfaces. *J. Tribol.* 139:031404. doi: 10.1115/1.4034530
- Ciavarella, M. (2018a). A very simple estimate of adhesion of hard solids with rough surfaces based on a bearing area model. *Meccanica* 53, 241–250. doi: 10.1007/s11012-017-0701-6
- Ciavarella, M. (2018b). An approximate JKR solution for a general contact, including rough contacts. *J. Mech. Phys. Solids* 114, 209–218. doi: 10.1016/j.jmps.2018.03.005
- Eid, H., Adams, G. G., Mcgruer, N. E., Fortini, A., Buldyrev, S., and Srolovitz, D. (2011). A combined molecular dynamics and finite element analysis of contact and adhesion of a rough sphere and a flat surface. *Tribol. Trans.* 54, 920–928. doi: 10.1080/10402004.2011.615638
- Fuller, K. (2011). Effect of surface roughness on the adhesion of elastomers to hard surfaces. *Mater. Sci. Forum* 662, 39–51. doi: 10.4028/www.scientific.net/MSF.662.39
- Fuller, K. N. G., and Tabor, D. (1975). The effect of surface roughness on the adhesion of elastic solids. *Proc. R. Soc. A Math. Phys. Eng. Sci.* 345, 327–342. doi: 10.1098/rspa.1975.0138
- Galanov, B. A. (2011). Models of adhesive contact between rough elastic bodies. *Int. J. Mech. Sci.* 53, 968–977. doi: 10.1016/j.jmecs.2011.07.010
- Guduru, P. R. (2007). Detachment of a rigid solid from an elastic wavy surface: theory. *J. Mech. Phys. Solids* 55, 445–472. doi: 10.1016/j.jmps.2006.09.004
- Joe, J., Scaraggi, M., and Barber, J. R. (2017). Effect of fine-scale roughness on the tractions between contacting bodies. *Tribol. Int.* 111, 52–56. doi: 10.1016/j.triboint.2017.03.001
- Johnson, K. L. (1995). The adhesion of two elastic bodies with slightly wavy surfaces. *Int. J. Solids Struct.* 32, 423–430. doi: 10.1016/0020-7683(94)00111-9

- Johnson, K. L., Greenwood, J. A., and Higginson, J. G. (1985). The contact of elastic regular wavy surfaces. *Int. J. Mech. Sci.* 27, 383–396. doi: 10.1016/0020-7403(85)90029-3
- Johnson, K. L., Kendall, K., and Roberts, A. D. (1971). Surface energy and the contact of elastic solids. *Proc. R. Soc. London A.* 324, 301–313. doi: 10.1098/rspa.1971.0141
- Kendall, K. (2001). *Molecular Adhesion and Its Applications*. New York, NY: Springer US.
- Kesari, H., Doll, J. C., Pruitt, B. L., Cai, W., and Lew, A. J. (2010). Role of surface roughness in hysteresis during adhesive elastic contact. *Philos. Mag. Lett.* 90, 891–902. doi: 10.1080/09500839.2010.521204
- Li, Q., and Argatov, I., Popov, V. L. (2018). Onset of detachment in adhesive contact of an elastic half-space and flat-ended punches with non-circular shape: analytic estimates and comparison with numeric analysis. *J. Phys. D: Appl. Phys.* 51:145601. doi: 10.1088/1361-6463/aab28b
- Li, Q., Pohrt, R., Lyashenko, I. A., and Popov, V. L. (2018). Boundary element method for non-adhesive and adhesive contacts of a coated elastic half-space. *arXiv:1807.01885*.
- Li, Q., and Popov, V. L. (2017). Boundary element method for normal non-adhesive and adhesive contacts of power-law graded elastic materials. *Comput. Mech.* 61, 319–329. doi: 10.1007/s00466-017-1461-9
- Li, Q., and Popov, V. L. (2018a). Adhesive force of flat indenters with brush-structure. *Facta Univ. Ser. Mech. Eng.* 16, 1–8. doi: 10.22190/FUME171220005L
- Li, Q., and Popov, V. L. (2018b). Adhesive contact of rough brushes. *Beilstein J. Nanotechnol.* 9, 2405–2412. doi: 10.3762/bjnano.9.225
- Luan, B., and Robbins, M. O. (2005). The breakdown of continuum models for mechanical contacts. *Nature* 435, 929–932. doi: 10.1038/nature03700
- Medina, S., and Dini, D. (2014). A numerical model for the deterministic analysis of adhesive rough contacts down to the nano-scale. *Int. J. Solids Struct.* 51, 2620–2632. doi: 10.1016/j.ijsolstr.2014.03.033
- Pastewka, L., and Robbins, M. O. (2014). Contact between rough surfaces and a criterion for macroscopic adhesion. *Proc. Natl. Acad. Sci. U.S.A.* 111, 3298–3303. doi: 10.1073/pnas.1320846111
- Pastewka, L., and Robbins, M. O. (2016). Contact area of rough spheres: large scale simulations and simple scaling laws. *Appl. Phys. Lett.* 108:221601. doi: 10.1063/1.4950802
- Pepelyshev, A., Borodich, F. M., Galanov, B. A., Gorb, E. V., and Gorb, S. N. (2018). Adhesion of soft materials to rough surfaces: experimental studies, statistical analysis and modelling. *Coatings* 8:350. doi: 10.3390/coatings8100350
- Persson, B. N., and Scaraggi, M. (2014). Theory of adhesion: role of surface roughness. *J. Chem. Phys.* 141:124701. doi: 10.1063/1.4895789
- Pohrt, R., and Li, Q. (2014). Complete boundary element formulation for normal and tangential contact problems. *Phys. Mesomechan.* 17, 334–340. doi: 10.1134/s1029959914040109
- Pohrt, R., and Popov, V. L. (2015). Adhesive contact simulation of elastic solids using local mesh-dependent detachment criterion in boundary elements method. *Facta Univ. Ser. Mech. Eng.* 13, 3–10.
- Popov, V. L., Pohrt, R., and Li, Q. (2017). Strength of adhesive contacts: influence of contact geometry and material gradients. *Friction* 5, 308–325. doi: 10.1007/s40544-017-0177-3
- Rey, V., Anciaux, G., and Molinari, J. F. (2017). Normal adhesive contact on rough surfaces: efficient algorithm for FFT-based BEM resolution. *Comput. Mech.* 60, 69–81. doi: 10.1007/s00466-017-1392-5
- Westergaard, H. M. W. (1939). Bearing pressures and cracks. *J. Appl. Mech.* 6, 49–53.
- Wu, J. J. (2012). Numerical simulation of the adhesive contact between a slightly wavy surface and a half-space. *J. Adhes. Sci. Technol.* 26, 331–351. doi: 10.1163/016942411X576527

Conflict of Interest Statement: The authors declare that the research was conducted in the absence of any commercial or financial relationships that could be construed as a potential conflict of interest.

Copyright © 2019 Li, Pohrt and Popov. This is an open-access article distributed under the terms of the Creative Commons Attribution License (CC BY). The use, distribution or reproduction in other forums is permitted, provided the original author(s) and the copyright owner(s) are credited and that the original publication in this journal is cited, in accordance with accepted academic practice. No use, distribution or reproduction is permitted which does not comply with these terms.



Evolution of the True Contact Area of Laser Textured Tungsten Under Dry Sliding Conditions

Björn Lechthaler^{1*}, Georg Ochs^{2,3}, Frank Mücklich¹ and Martin Dienwiebel^{2,3}

¹ Department of Materials Science and Engineering, Institute for Functional Materials, Saarland University, Saarbrücken, Germany, ² Fraunhofer Institute for Mechanics of Materials, Freiburg, Germany, ³ Microtribology Centre μ TC, Institute for Applied Materials, Karlsruhe Institute of Technology, Karlsruhe, Germany

OPEN ACCESS

Edited by:

Yu Tian,
Tsinghua University, China

Reviewed by:

Jiliang Mo,
Southwest Jiaotong University, China
Luciano Afferrante,
Politecnico di Bari, Italy
Qunyang Li,
Tsinghua University, China

*Correspondence:

Björn Lechthaler
b.lechthaler@mx.uni-saarland.de

Specialty section:

This article was submitted to
Tribology,
a section of the journal
Frontiers in Mechanical Engineering

Received: 02 November 2018

Accepted: 22 January 2019

Published: 08 February 2019

Citation:

Lechthaler B, Ochs G, Mücklich F and
Dienwiebel M (2019) Evolution of the
True Contact Area of Laser Textured
Tungsten Under Dry Sliding
Conditions. *Front. Mech. Eng.* 5:3.
doi: 10.3389/fmech.2019.00003

Despite the great importance of the real contact area, it is a parameter which, depending on the tribological system, is difficult or impossible to obtain experimentally. In this work, a combination of methods was used to estimate the development of the real contact surface, and the results were compared with the friction coefficient course. The measurements were carried out with a home-built *in situ* tribometer, which records a 3D image of the surface after each individual friction cycle. A tungsten sample was treated by laser interference with a line-like pattern to produce a deterministic surface. This allowed for more precise tracking of the real contact area when combined with the use of an inert corundum sphere as a counter-body. The real contact area was calculated numerically from the height information obtained using a contact application. Finally, the true contact surface was compared with the parallel-recorded friction values. After a short running-in phase, the friction behavior and the real contact surface showed comparable courses. This indicates that the changes in the real contact area could explain the friction behavior of the laser-patterned sample, and the methodology was proven to be suitable for experimentally estimating the real contact area.

Keywords: direct laser interference patterning, dry friction, *in-situ* tribometer, real contact area, asperity contacts

1. INTRODUCTION

The area of contact A_C has a great influence on the behavior of a tribosystem. Both the friction coefficient and wear can be influenced by changing the topography of the surface. Therefore, there are many well-known methods for modifying surfaces (Willis, 1986; Gerbig et al., 2002; Li et al., 2010).

It is important to distinguish the difference between geometric and real contact surfaces (Bowden and Tabor, 1951; Bhushan, 1998), since energy is only dissipated on the real contact surface.

One process for producing tailor-made surfaces, and thus specifically influencing the true contact area, is the direct laser interference patterning method, which allows for large-area structuring with micrometer accuracy (Mücklich et al., 2006).

Gachot et al. (2013) showed how the frictional properties of a tribosystem can be changed by laser structuring on both the base and counter-body. It was observed that the coefficient of friction initially drops rapidly and rises again continuously after a short break-in period. The results suggest that this increase is caused either by changes in the material (martensite transformation of the steel

or inhomogeneity in the laser structure) or, more possibly, by an increase in the real contact area due to flattening of the laser structures.

The question now is how to verify, in this example or for other systems, that the increase in the real contact area is the decisive factor for the behavior of the coefficient of friction? Despite the importance of this parameter, experimental access to the real contact surface is difficult. There are some methods, but they are usually restricted (Woo and Thomas, 1980). In optical methods, for example, one of the bodies must be transparent. The real contact area is then measured directly through the body using a microscope and CCD camera (Ovcharenko et al., 2006). If the experiment can be carried out completely in water or oil, the contact surface can be measured using ultrasonics (Aymerich and Pau, 2004). For a dry case, a simulation is possible, but for complex geometries, it is difficult to accurately replicate the material behavior, and the surface and the simulation can only indicate a tendency (Sayles and Thomas, 1978; Bhushan, 1998).

In this work, a different approach has been chosen. A friction experiment was performed using a home-built *in situ* tribometer with an on-line holographic microscope (Korres and Dienwiebel, 2010; Feser, 2014). Tungsten was used instead of steel to exclude the martensite transition. Furthermore, by using a new optimized laser interference method (Bieda et al., 2016), a very homogeneous, sinusoidal pattern was created to minimize the influence of uncontrolled surface defects. This type of pattern has the advantage of flattening continuously and in a defined manner, which simplifies the analysis compared to a static rough surface. The height information of the obtained topography development was then evaluated with a contact mechanics code developed by Pastewka Jacobs et al. (2016). This application made it possible to numerically calculate the real contact surface directly from the power density spectra. Finally, these data were compared with the evolution of the coefficient of friction, which allowed us to clarify whether the friction behavior can be explained by the flattening of the structures and an increase in the contact surface.

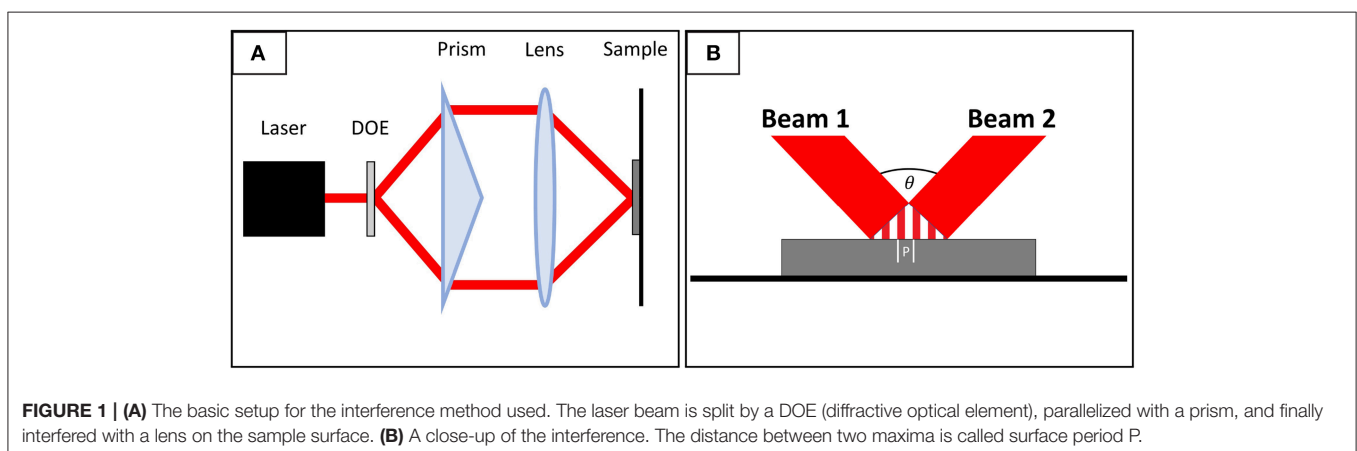
2. EXPERIMENTAL PROCEDURE

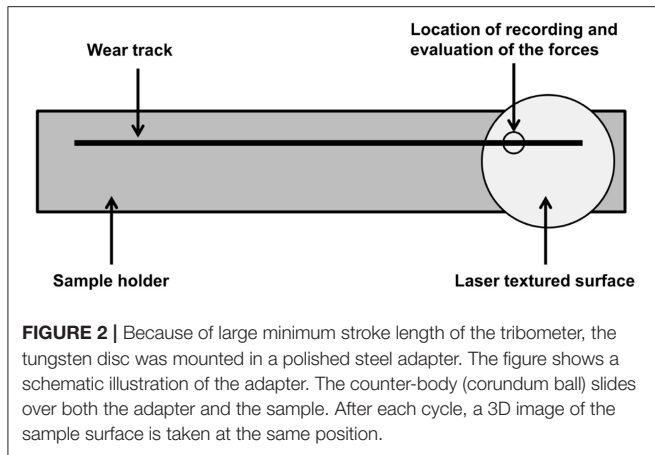
Disc-shaped samples of 20 mm in diameter and 5 mm in thickness were cut from a tungsten rod (Plansee, purity 99.95 %, Young's modulus 411 GPa and Poisson's ratio 0.28), polished to a surface roughness (R_a) of 10(2) nm, and finally patterned with a laser interference method to create a well-defined, wavy, line-like surface.

For this experiment, a picosecond interference system was used (Bieda et al., 2016). In this method, the laser beam is split by a diffractive optical element into two beams, parallelized by a prism, and finally interfered with a lens on the sample. This results in a line-shaped intensity distribution (Figure 1). After the production of the sample, the height profiles were recorded with a laser scanning microscope (LSM, OLS4100, Olympus) with a lateral resolution of 0.2 μm and a z-resolution of up to 10 nm. For this experiment, a 50 \times lens was used. Friction tests were conducted with a special *in situ* ball-on-disk tribometer in linear reciprocating sliding mode with online topography and wear measurements (Korres and Dienwiebel, 2010; Feser, 2014). As a counter-body, an alumina ball (with a diameter of 6 mm, a surface roughness (R_a) of 14(5) nm, a Young's modulus 380 GPa and a Poisson's ratio of 0.22) by Anton Paar GmbH (formerly CSM Instruments) was used.

The tests were conducted at a normal load of 0.22 N, the linear sliding speed was set to 5 mm/s, and the stroke length was 79 mm. The experiment was finished after 500 cycles. Due to the large minimum stroke length of the tribometer, the tungsten disc was mounted in a specially designed and polished steel adapter (Figure 2). During each cycle, the counter-body moved over both the steel surface and the laser-textured tungsten disc. The following surface analysis considered only the changes on the tungsten surface.

After each cycle, a 3D image was taken with a digital holographic microscope (DHM, R2100 series Lyncee Tec SA, Switzerland, Feser, 2014) with a 20 \times lens. The contact mechanics simulations were performed on the web interface of the python code PyCo by L. Pastewka (<http://contact.engineering/>). Based on the boundary element method, it employs FFT coupled to a conjugate gradient method for an efficient calculation of the inter-surface gap and pressure distribution (Pastewka and Robbins, 2016; Kling et al., 2018; Weber et al., 2018). This code outputs a diagram in which the quotient of real and geometric contact surfaces is plotted over the normalized surface pressure





σ^* . The following applies to the surface pressure:

$$\sigma = \frac{F_N}{A_{geo}} \quad (1)$$

The normalization of σ is done by the normalized modulus of elasticity E^* which is calculated from the modulus of elasticity E and Poisson's ratio ν of the two contact partners as follows:

$$\frac{1}{E^*} = \frac{1 - \nu_1}{E_1} + \frac{1 - \nu_2}{E_2} \quad (2)$$

In the version provided by Pastewka for this work, the counter-body is assumed to be smooth and even, and only elastic deformations are considered.

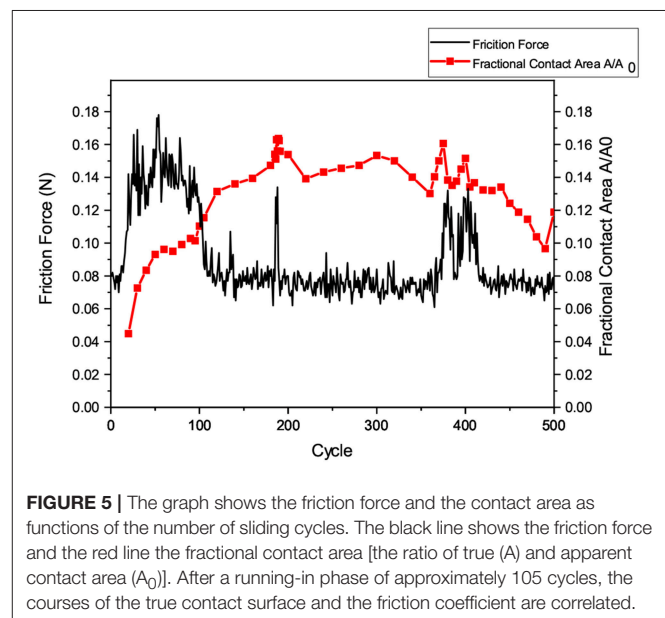
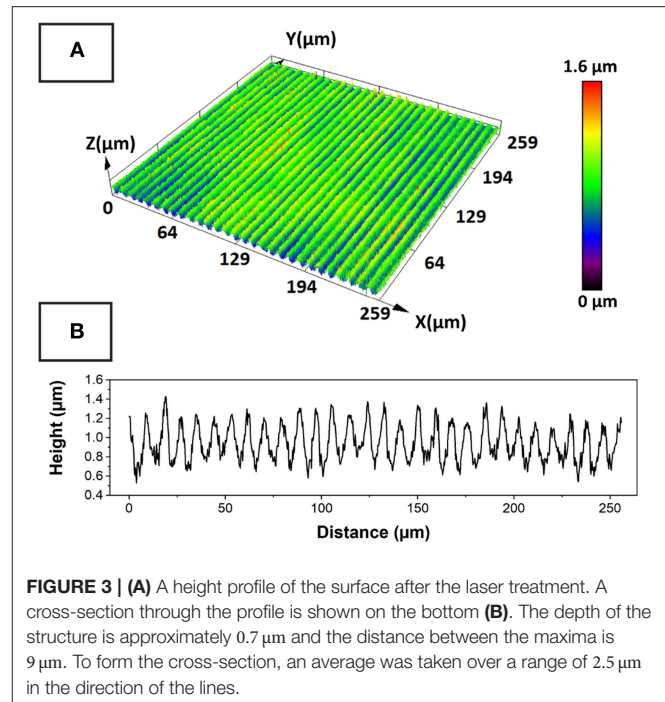
The surface morphology was imaged by scanning electron microscopy (SEM, Helios, Nanolab600). In addition, a focused ion beam (FIB) microscope (Helios, Nanolab600) was selected to prepare cross-sections to investigate the microstructure of the sample before and after the experiments (The unedited original images can be found in the **Supplementary Material**). The chemical composition of the laser-structured surface was analyzed by energy dispersive X-ray spectroscopy (EDS) with an acceleration voltage of 3 kV using an EDAX instrument detector and EDAX Genesis software.

3. RESULTS

After the laser treatment, the surface was first characterized with the LSM. The laser treatment created a sinusoidal line-like pattern on the surface of the tungsten sample. A depth of approximately $0.7 \mu\text{m}$ and a distance between the maxima of approximately $9 \mu\text{m}$ were determined (**Figure 3**).

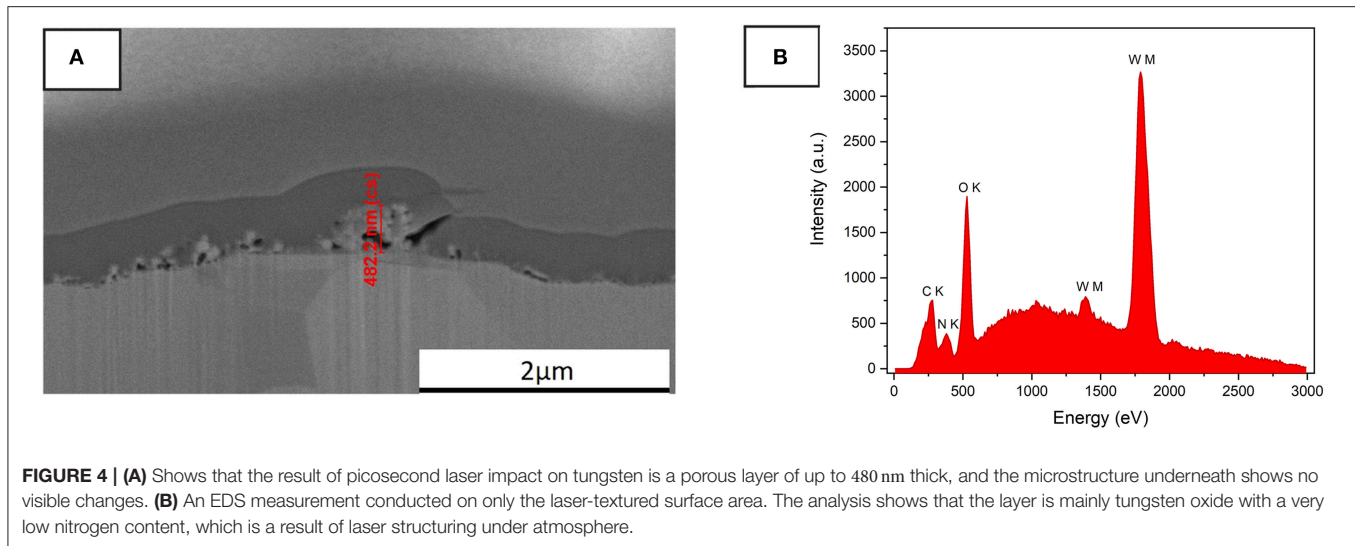
The patterning was conducted under atmosphere and a porous layer up to 480 nm thick was formed on the surface. An EDS analysis conducted on the layer showed that it was tungsten oxide (**Figure 4**). Due the use of a picosecond laser, there was a negligible influence on the microstructure.

On this laser-patterned surface, the friction force was measured under a constant normal force of 0.22 N . The



normal force was stable during the process. The friction force presented a plateau between the 15 and 105th cycles and several peaks around the 183, 386, and 405th cycles. For the remaining duration, the friction force showed a steady value of 0.08 N (**Figure 5**).

To determine the real contact area, every 20th recorded cycle was evaluated manually with the contact mechanics code. In sections where the frictional force varied significantly, the number of analyzed cycles was increased to capture the change in detail. The surface pressure was calculated for a circular contact. The width of the friction track ($26.62 \mu\text{m}$) was used as



the diameter. As an approximation, this value was assumed to be constant in the calculations.

The real contact area could only be determined from the 20th cycle onward, since no reliable friction track could be measured beforehand. Up to the 105th cycle, the contact surface increased rapidly, and afterwards, the course of the contact surface corresponded to the course of the frictional force. This behavior can be correlated to the 3 major peaks that were present in both the course of frictional force and the real contact surface. This means that, apart from the running-in phase, a correlation between friction force and real contact area was observed. An increase in the real contact area led to a corresponding increase in the coefficient of friction. The results of the real contact area calculations and the recorded friction forces are illustrated in 5.

Microstructural investigations of the laser-textured sample were carried out before and after the rubbing experiment with the FIB. For this experiment, cross-sections were prepared on a reference area and on a rubbed area. In the contact surfaces of the topography maximum, the oxide layer was completely removed, and in the underlying microstructure, significant deformation layers were obtained in the grain orientation contrast (**Figure 6**).

4. DISCUSSION

The temporal development of the fractional contact area surface correlates to but is not completely identical to the development of the friction coefficient. The most obvious deviation can be found at the beginning of the curve, where the measured real contact area is close to the zero point and the coefficient of friction rises rapidly in a short term for the first 105 cycles before dropping back down.

The increase in the real contact area at the beginning of the experiment can be explained by the continuous removal

of the oxide layer and flattening of the asperities (**Figure 4**), which increases the surface conformity. The initial height and fluctuating frictional force are a consequence of the formation and disruption of oxide particulate agglomerates. In addition, a plastic deformation of the surface, which takes place primarily at the topography maxima, can lead to a local recrystallization of the microstructure (**Figure 6**) until a state of equilibrium is formed. The sudden decrease in frictional force is mainly due to the complete removal of the oxide layer after 105 cycles, which is known to contribute to the high frictional resistance (Polcar et al., 2007). Afterwards, there is a purely metallic contact situation. It should be noted that the use of the adapter may lead to a minor contamination of the tungsten surface with steel wear particles. This could also influence the friction coefficient.

After the running-in phase, the basic course of the calculated true contact area and the measured friction forces show comparable behavior. The fact that the behavior of the frictional force depends on the contact area can be further substantiated by observing the topographical images. In **Figure 7**, there are 3 height profiles: before the friction force peak (cycle 160), at the peak (cycle 188), and after the peak (cycle 220). Notably, in cycles 160 and 220, there are considerably more areas with isolated heights (dark brown/red areas) than in cycle 188. If these heights are missing, the hard counter-body can lie on more of the surface, which leads to an increase in the contact area. This in turn would agree with the calculated course of the contact surface shown in **Figure 5**.

After the running-in phase, the real contact area was correlated to the friction force, but some deviations were observed. They were mainly related to the method of calculating the real contact area. Several approximations were used. First, the counter-body, which in reality is a ball with its own surface roughness and a diameter of 6 mm, was assumed in the calculation to be flat with a perfectly smooth surface. Additionally, the SEM images in **Figure 6** showed

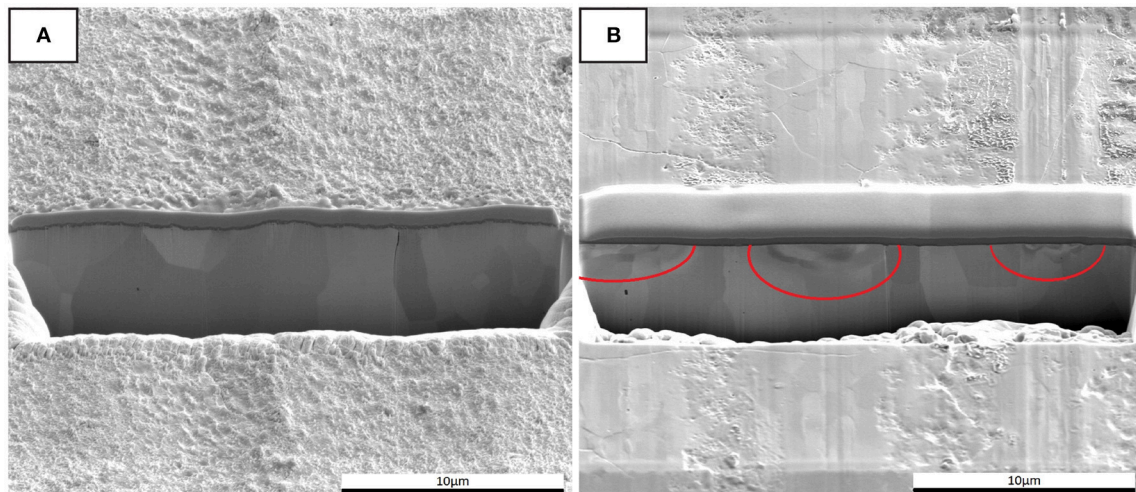


FIGURE 6 | (A) A cross-section through the surface of the laser-structured tungsten sample, where the continuous dark area is platinum applied for the cross-section. The small porous layer underneath is the oxide, for which a layer thickness of up to 480 nm was measured. The tungsten structure with the individual grains is visible below. **(B)** A cross-section in the wear track after the rubbing experiment. In the contact surfaces of the topography maximum, the oxide layer is completely removed, and in the underlying microstructure, significant deformation layers can be seen in the grain orientation contrast (marked with red circles). The normal force during the experiment was 0.22 N and the speed was 5 mm/s. As a counter-body, an alumina ball with a diameter of 6 mm was used.

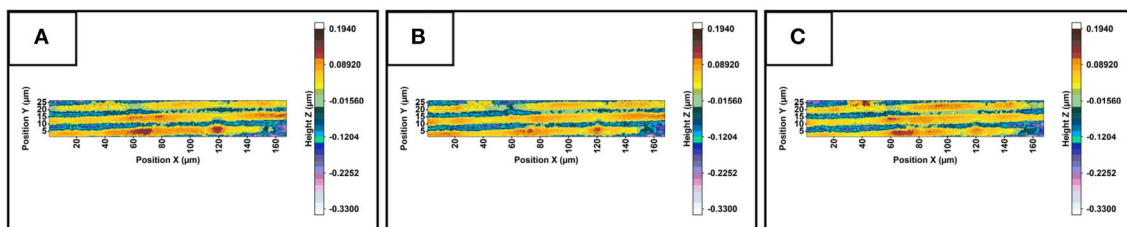


FIGURE 7 | (A) (cycle 160) and **(C)** (cycle 220) show heights (dark brown/red areas) that are almost not visible in **(B)** (cycle 188). Due to the missing heights, the counter-body in **(B)** can lie on more of the surface, which corresponds to the calculated values of the real contact area shown in **Figure 5**.

a clear plastic deformation which was not considered in the calculation.

It can be concluded that, despite the approximations, a clear trend and correlation between the real contact area and the frictional force can be observed and proved, which indicates the potential of this method.

5. CONCLUSION

It was shown that the combination of an *in situ* tribometer, contact application, and laser-textured surface allows for the estimation of the course of the real contact surface. Thus, it was demonstrated that, after a short run-in period, the course of the friction coefficient correlated directly with the development of the true contact surface. It can be concluded that the increase in the friction coefficient of laser-textured surfaces, as suggested in Gachot et al. (2013), can be attributed to an increase in the real contact area. In addition, the procedure showed much potential despite the deviations. Pastewka's contact

application is still under development. If plastic deformations and the surface properties of the counter-body are correctly considered, a very precise calculation of the contact area might be possible.

DATA AVAILABILITY STATEMENT

The Datasets for this work can be found in the **Supplementary Materials**.

AUTHOR CONTRIBUTIONS

BL designed the adapter, produced, and characterized the samples before and after the friction process and wrote the manuscript. GO conducted the friction experiment and calculated the real contact area using the contact mechanics code. BL, GO, FM, and MD discussed interpretation of results. MD and FM supervised the project.

FUNDING

The present work is supported by funding from the Deutsche Forschungsgemeinschaft (DFG, project: MU 959/30-1 and DI 1464/5-1).

ACKNOWLEDGMENTS

Special thanks go to Valentin Lang from the Chair of Large Area Laser Based Surface Structuring of Prof. Dr. Andrés

Lasagni for his help in the production of the samples. And to Dr. Lars Pastewka from Karlsruhe Institute of Technology for providing the contact application for the evaluation of the contact surface.

SUPPLEMENTARY MATERIAL

The Supplementary Material for this article can be found online at: <https://www.frontiersin.org/articles/10.3389/fmech.2019.00003/full#supplementary-material>

REFERENCES

- Aymerich, F. and Pau, M. (2004). Assessment of nominal contact area parameters by means of ultrasonic waves. *J. Tribol.* 126, 639–645. doi: 10.1115/1.1760764
- Bhushan, B. (1998). Contact mechanics of rough surfaces in tribology: multiple asperity contact. *Tribol. Lett.* 4, 1–35.
- Bieda, M., Siebold, M., and Lasagni, A. F. (2016). Fabrication of sub-micron surface structures on copper, stainless steel and titanium using picosecond laser interference patterning. *Appl. Surf. Sci.* 387, 175–182. doi: 10.1016/j.apsusc.2016.06.100
- Bowden, F. P. and Tabor, D. (1951). The friction and lubrication of solids. *Am. J. Phys.* 19:428.
- Feser, T. (2014). *Untersuchungen zum Einlaufverhalten binärer α - Messinglegierungen unter Ölschmierung in Abhängigkeit des Zinkgehaltes*. KIT Scientific Publishing. doi: 10.5445/KSP/1000041146
- Gachot, C., Rosenkranz, A., Reinert, L., Ramos-Moore, E., Souza, N., Müser, M. H., et al. (2013). Dry friction between laser-patterned surfaces: role of alignment, structural wavelength and surface chemistry. *Tribol. Lett.* 49, 193–202. doi: 10.1007/s11249-012-0057-y
- Gerbig, Y., Dumitru, G., Romano, V., Spassov, V., and Haefke, H. (2002). Effects of laser texturing on technical surfaces. *Mater. Res. Soc. Symp. Proc.* 750, 1–6. doi: 10.1557/PROC-750-Y5.37
- Jacobs, T., Junge, T., and Pastewka, L. (2016). Quantitative characterization of surface topography using spectral analysis. *arXiv* 1607.03040.
- Kling, T., Vogler, D., Pastewka, L., Amann, F., and Blum, P. (2018). Numerical simulations and validation of contact mechanics in a granodiorite fracture. *Rock Mech. Rock Eng.* 51, 2805–2824. doi: 10.1007/s00603-018-1498-x
- Korres, S. and Dienwiebel, M. (2010). Design and construction of a novel tribometer with online topography and wear measurement. *Rev. Sci. Instr.* 81:063904. doi: 10.1063/1.3449334
- Li, J., Xiong, D., Dai, J., Huang, Z., and Tyagi, R. (2010). Effect of surface laser texture on friction properties of nickel-based composite. *Tribol. Int.* 43, 1193–1199. doi: 10.1016/j.triboint.2009.12.044
- Mücklich, F., Lasagni, A. F., and Daniel, C. (2006). Laser interference metallurgy – using interference as a tool for micro / nano structuring. *Int. J. Mat. Res.* 97, 1337–1344. doi: 10.3139/146.101375
- Ovcharenko, A., Halperin, G., Etsion, I., and Varenberg, M. (2006). A novel test rig for *in situ* and real time optical measurement of the contact area evolution during pre-sliding of a spherical contact. *Trib. Lett.* 23, 55–63.
- Pastewka, L. and Robbins, M. O. (2016). Contact area of rough spheres: Large scale simulations and simple scaling laws. *Appl. Phys. Lett.* 108:221601. doi: 10.1063/1.4950802
- Polcar, T., Parreira, N. M., and Cavaleiro, A. (2007). Tungsten oxide with different oxygen contents: sliding properties. *Vacuum* 81, 1426–1429. doi: 10.1016/j.vacuum.2007.04.001
- Sayles, R. S. and Thomas, T. R. (1978). Computer simulation of the contact of rough surfaces. *Wear* 49, 273–296.
- Weber, B., Suhina, T., Junge, T., Pastewka, L., Brouwer, A. M., and Bonn, D. (2018). Molecular probes reveal deviations from Amontons' law in multi-asperity frictional contacts. *Nat. Commun.* 9:888. doi: 10.1038/s41467-018-02981-y
- Willis, E. (1986). Surface finish in relation to cylinder liners. *Wear* 109, 351–366.
- Woo, K. L. and Thomas, T. R. (1980). Contact of rough surfaces: a review of experimental work. *Wear* 58, 331–340.

Conflict of Interest Statement: The authors declare that the research was conducted in the absence of any commercial or financial relationships that could be construed as a potential conflict of interest.

Copyright © 2019 Lechthaler, Ochs, Mücklich and Dienwiebel. This is an open-access article distributed under the terms of the Creative Commons Attribution License (CC BY). The use, distribution or reproduction in other forums is permitted, provided the original author(s) and the copyright owner(s) are credited and that the original publication in this journal is cited, in accordance with accepted academic practice. No use, distribution or reproduction is permitted which does not comply with these terms.



A Concept of the Effective Surface Profile to Predict the Roughness Parameters of Worn Surface

Alexander Kovalev, Zhang Yazhao, Cao Hui and Yonggang Meng*

State Key Laboratory of Tribology, Tsinghua University, Beijing, China

OPEN ACCESS

Edited by:

Roman Pohrt,
Technische Universität
Berlin, Germany

Reviewed by:

Árpád Czifra,
Óbuda University, Hungary
Ivan Y. Tsukanov,
Institute for Problems in Mechanics
(RAS), Russia

*Correspondence:

Yonggang Meng
mengyg@tsinghua.edu.cn

Specialty section:

This article was submitted to
Tribology,
a section of the journal
Frontiers in Mechanical Engineering

Received: 11 December 2018

Accepted: 17 May 2019

Published: 06 June 2019

Citation:

Kovalev A, Yazhao Z, Hui C and
Meng Y (2019) A Concept of the
Effective Surface Profile to Predict the
Roughness Parameters of Worn
Surface. *Front. Mech. Eng.* 5:31.
doi: 10.3389/fmech.2019.00031

A new concept of the effective surface profile is proposed to facilitate the prediction of the worn surface texture at sliding friction. The effective surface profile is a 2D height characteristic that consists of the asperities of surface superimposed on a plane perpendicular both to the mean surface plane and to the direction of sliding. We hope to present a clear and compelling argument favoring the use of the effective surface profile as a versatile tool for characterization of rough surfaces at abrasive wear, calculation of contact characteristic at sliding friction, and for prediction of evolution of roughness parameters from virgin to the worn surfaces. The effective surface profile can be successfully applied for investigations of sliding abrasive wear under dry or lubricated conditions.

Keywords: sliding wear, plowing, abrasion, surface topography, surface parameters

INTRODUCTION

Prediction of wear of materials at sliding is an important but complex challenge (Zmitrowicz, 2006; Manier et al., 2008; Lu et al., 2014). General analytical models (Kato, 2002) predicting a wear mode under various conditions are complicated (Hsu et al., 1997). Wear is defined as damage to one or both surfaces involved in friction. In most of cases, a wear is characterized by the presence of tracks that have a measurable width, depth, as well as different surface roughness and texture inside of worn area. The wear profile describes the irreversible changes of a worn surface, and it is a useful measure of surface damage. Based on many experimental evidences of wear examinations (Archard, 1953; Bowden and Tabor, 1964; Glaeser, 1992), the main mechanisms of wear have been identified as asperity interlocking, plowing, and cutting of surface (Bowden and Tabor, 1964).

The objective of wear modeling depends on its application. In most of cases, the main aim of the wear modeling is to predict the volume loss depending on mechanical properties of contacting solids and the tribotesting schemes used. Perhaps, the first attempt to summarize the proposed wear models was done by Meng and Ludema (1995). They have performed classification of wear models and have distinguished three main types of wear equations: empirical, phenomenological and those based on the selected failure mechanism. The main equation allowing to calculate the loss of material is the Archard wear equation (Archard, 1953) or so called Archard's law which is a simple calculation procedure of wear volume and widely used in engineering calculations.

Another challenge is to predict the evaluation of worn surface structure and its roughness parameters occurred at abrasive wear, grinding, milling and turning processes. Study of the ground surface roughness is an important issue for tribological applications because it impacts

the performance of machine elements. The virtual reality technology was used by Gong et al. (Gong et al., 2002) to simulate the grinding process. They found that the average roughness R_a on the ground workpiece can be estimated by the arithmetic average of contour absolute values in a sampling length of workpiece. Aslan and Budak (2015) have proposed grinding model with thermo-mechanical material deformation allowing to simulate abrasive wheel topography and to obtain the final workpiece surface profile. The abrasion simulation considers three types of interactions such as rubbing, plowing, and cutting. The main point of abrasion simulation is that not all the grits are involved into the process, but some of them exceeding the certain cut-off height and these acting grits are distributed randomly within the working area. Simulating the abrasive wear by parallel scratches, da Silva and de Mello (2009) have used the load map that represents combination of position and normal load of scratches being generated and this load map closely correlates to the average profile of the reference surface used in simulation. It allows predicting the roughness parameters with good accuracy. Similar approach was proposed by Shahabi and Ratnam (2016) for determining the final surface profile of workpieces in finish turning. They have shown that final surface profile formed by the flank wear of cutting tool and the surface roughness could be predicted knowing the shape of the tool cutting edge.

In most of investigations of the contact of rough surfaces, roughness parameters are considered as characterizing the mating surfaces (Borodich and Bianchi, 0000; Borodich et al., 2016). Mainly, the analytical models consider the specific type of wear, as it was proposed by Goryacheva for fatigue wear (Goryacheva, 1998) or Popov and Pohrt for adhesive wear (Popov and Pohrt, 2018). Also, there is no simple analytical method or technique that involves the initial surface topography to allow predicting the evolution of worn surface structure or texture that occurs during the abrasive or plowing wear process.

The commonly used roughness parameters in tribology are the arithmetic average height (R_a), root mean square (R_q), skewness (R_{sk}), and kurtosis (R_{ku}). The correlation between the surface roughness and friction behavior has been recognized for a long time, however until now it is still an unsolved challenge. The variation of surface parameters during the running-in wear stage, where the mutual transition between different types of wear exists, was deeply investigated by Jeng (Jeng and Gao, 2000; Jeng et al., 2004) especially for engine bore surfaces. He has found that R_q became lower and R_{sk} got negative after sliding wear, and these results are correct for different original surface height distributions. The surface roughness evolution in sliding process has been studied by Yuan et al. (2008). The results have shown that R_a and R_q values of test samples first decreased from the running-in to steady wear stage and then increased from the steady wear to severe wear stage. However, variation of roughness parameters when initial surface undergoes the transformation during wear is still not investigated in details.

A lot of previous theoretical and experimental studies of friction and wear have formed the main basis of surface transformation during a sliding friction of rough surfaces. During sliding, the deformation of surface can be entirely elastic. In such a case the wear is absent. With an increase of external

load, the deformation mode changes to plastic one and the surface layer of material displaced by the passage of an asperity is being plowed into side ridges. Such representation was used in several models of wear (Kapoor and Johnson, 1992, 1994), where the plowing is the dominating factor (Challen et al., 1984; Xie and Williams, 1996). The steady state sliding of rough surfaces that considers the groove formation in presence of elastic and plastic “shakedown limit” was also analyzed (Kapoor et al., 1994). However, the height change of initial rough surface was taken into account based on the roughness of a surface profile only. Thus, the analysis of evolution of worn surface topography, where the initial surface structure is considered, have not been reported yet.

In this paper, a concept of effective surface profile (ESP), which is the superimposed asperities of initial hard rough surface along the direction of sliding, is presented with the aim of predicting the worn surface structure, corresponding roughness parameters, and contact characteristics under abrasive sliding conditions.

CONVENTIONAL CONTACT CHARACTERIZATION

Surface Roughness Parameters

Set of roughness parameters for a single line (profile) characterization can be divided to three main groups (Dong et al., 1992, 1993, 1994a,b; Stout, 1993; Jiang et al., 2007a,b) according to its functional properties: (1) amplitude parameters, (2) spacing parameters, and (3) hybrid parameters. According to the classification presented elsewhere (Gadellmawla et al., 2002), for roughness characterization from a profile data, total of 41 parameters, including 20 amplitude parameters, 8 spacing parameters, and 13 hybrid parameters, can be utilized. To point out which of these various parameters is the most relevant one to describe the surface transformation due to friction and wear is ambiguous and can be a pointless task.

Let us describe the main amplitude (height) parameters that commonly used for a roughness characterization. Taking into account the absence of difference of statistical meaning for equations applying for calculation of the roughness, only the capital letter “S” will be used for profile and surface parameters.

Arithmetic Average Height

The arithmetic average height parameter R_a or S_a is defined as the average deviation of the roughness irregularities from the mean line over the sampling length l , or from a mean surface over the nominal surface in case of areal characterization. The main weakness is that R_a or S_a give no information on the profile shape or texture of surface and they are not sensitive to the fine changes of asperity peaks and depths of valleys. These roughness parameters describe the average value of height deviation along the Z axis regardless how a height data was collected, along a linear profile or surface.

Root Mean Square

This parameter is the standard deviation of the distribution of profile or surface height points relating to the mean

line. Rq (Sq) parameter is more sensitive to the changes of height amplitudes.

Skewness

The skewness qualifies the symmetry of height distribution about the mean line for a profile or mean plane for a surface. For the Gaussian distribution, which has a symmetrical “bell-like” shape, the Ssk is zero. For asymmetric distribution of profile/surface heights, the Ssk may be negative or positive. Ssk is positive if a surface has many peaks and small number of valleys. The negative Ssk indicates that the quantity or deepness of valleys dominate over peaks above the mean plane.

Kurtosis

The kurtosis qualifies the flatness of the height distribution curve. The profile or surface with a Gaussian distribution of height points has a kurtosis of 3. Centrally distributed surfaces has a kurtosis value larger than 3, whereas the kurtosis of a well spread distribution is smaller than 3.

Ssk and Sku are more sensitive to the fine changes of topography than Ra and Rq , and they are used in the comparable analysis of worn surface topography (Jeng and Gao, 2000; Yuan et al., 2008).

The height roughness parameters listed above are widely used in surface characterization of worn surfaces, however, as it will be shown in this manuscript, cannot describe the evolution of surface parameters during wear.

Contact of Rough Surfaces

The basis of statistical description and corresponding classical model of contacting rough surfaces has been proposed in 1966 by Greenwood and Williamson (1966). They have shown the Gaussian distribution of heights on many surface profiles. Moreover, it was found that the distribution of asperity peaks is close to Gaussian distribution too, and both the mean value and the standard deviation of asperity peaks differ from that of heights. It should be noted here that Zhuravlev has published in 1940 the pioneering work related to the contact mechanics, where the statistical approach for describing the surface roughness was proposed. He considered a linear distribution of heights of aligned spherical asperities and yielded an almost linear relation between external load P and real contact area A_r . The translation of a historical Zhuravlev's paper has been done by Borodich (Zhuravlev, 2007) and discussed elsewhere (Borodich et al., 2016; Borodich and Savencu, 2017).

The mentioned above GW model is widely used for calculation of the bearing capacity of contacting surfaces (Bhushan, 1998, 2001). However, as it will be shown in section Contact of Rough Surfaces, GW theory describes the static contact of rough surfaces and could not correspond to the contact geometry occurred due to the repeatable sliding movements of surfaces. Here, we briefly list the main equations of GW theory and these equations will be discussed with equations derived with the help of effective surface profile in section Contact of Rough Surfaces.

The GW model was defined by three parameters: σ is the standard deviation of the asperity peak distribution; R is the radius of curvature of the asperities; n is the density of asperities

per unit area. According to the GW model, the distribution density function of peak heights is of the form:

$$\phi(z) = \frac{1}{\sqrt{2\pi}\sigma} \exp\left(-\frac{z^2}{2\sigma^2}\right), \quad (1)$$

where z is the peak height. If two surfaces are brought into contact until their nominal planes are separated by a distance d , then there will be a contact at any asperity whose height is greater than distance d . Thus, if a rough surface has N asperities, the expected number of contacting asperities is:

$$n = N \int_d^\infty \phi(z) dz \quad (2)$$

Therefore, if the surfaces come to contact with a compression of $\delta = z - d$, and all asperities undergo the elastic deformation according to the prediction of Hertzian theory, then, per unit nominal area, the real area of contact and the applied load will be:

$$A_r = \pi n R \int_d^\infty (z - d) \phi(z) dz \quad (3)$$

$$P = \left(\frac{4}{3}\right) n E^* \sqrt{R} \int_d^\infty (z - d)^{3/2} \phi(z) dz \quad (4)$$

where E^* is the composite elastic modulus of contacting rough bodies.

GW model is widely used in contact problems for predicting the normal contact of surface (Adams and Nosonovsky, 2000) and it has many variations for certain problems (Greenwood and Wu, 2001; Borodich et al., 2016). Also, GW model is often considered when the sliding friction of rough surfaces is modeled (Kapoor et al., 1994; Xie and Williams, 1996). However, the GW model is applicable for pure elastic contact only. In case of elastoplastic or pure plastic interaction typical for abrasive or plowing wear at sliding the application of GW model has to be revised.

NUMERICAL INVESTIGATIONS DETAILS

Running-in state exists at the beginning of a wear test in which the contacting surfaces experience an initial wear, resulting in the adaptation of surfaces accompanying by volume loss, after which the slope of wear curve declines reaching the steady state.

In our numerical investigation we consider an ideal case of sliding friction of rough hard surface against softer one. In fact, this corresponds to the sliding friction of hard coatings such as DLC against softer materials as metals or ceramics (Hayward et al., 1992) where the friction coefficient tends to be high, since asperities of the coating surface work as abrasives.

In numeric experiments nominally rough surface initially was shifted down according the selected vertical displacement Δz and was continuously moved over the soft surface subjected to wear. Several wear mechanisms could be involved in the groove

formation on the surface of softer material. The transformation of wear surface represents how the surface of soft material would be expected to change during the repeated sliding mainly accompanied by the plowing and cutting. However, wear mechanisms were thoroughly maintained in our computer simulation, because the main aim of our idealization is to investigate the final surface topography at given conditions of sliding, rather than the specific wear mechanism and mechanical behavior of material resulting in the topography changes.

In section Results and Discussion the conventional method to characterize a surface will be compared with the new approach allowing the prediction of surface parameters of worn surfaces and evolution of surface parameters will be discussed in detail.

RESULTS AND DISCUSSION

Any friction process begins with normal static contact. In this stage, the top of asperities of rough surface are brought into contact under high pressure, and the initial penetration to the softer material takes place. Since asperities are randomly distributed on the rough surface, discrete real contact areas are formed. When the local normal pressure exceeds a critical value, which is determined by the hardness of the asperity, the elastic deformation changes to plastic one, resulting in the plowing (Xie and Williams, 1996). Due to that, all the surface layer of material displaced by the passage of the asperity is plowed into side ridges. Such irreversible deformation of surface takes place till a balanced state governed by the interrelation between hardness, elasticity, and geometry of parallel grooves is reached. This is a steady stage of wear and it is characterized by a stable coefficient of friction and low wear (Hao and Meng, 2015). In this section the surface characterization is analyzed and new concept of prediction of worn surface evolution is presented.

Concept of Effective Surface Profile

The recent trend of tribological simulations demands the description of surface changes in wear process (Ao et al., 2002; Reizer et al., 2012; Cabanettes and Rosén, 2014). In most of wear prediction models, the surface roughness parameters are used as indicators describing sliding contact of rough surfaces (Xie and Williams, 1996; Jeng et al., 2004; Yuan et al., 2007, 2008). The changes of roughness parameters are analyzed in the range of height amplitude of initial surface topography. This is reasonable for consideration of running-in stage of wear, where the rough surface undergoes a primary transformation. However, the completed adaptation of sliding surfaces is characterized by the presence of new worn surface that provides an equilibrium state between the normal contact pressure and the elastic shakedown limit of mating surfaces. Before the steady wear stage is reached, the new friction surface is mostly generated by the plowing and abrasion by hard asperities, resulting in a set of grooves. It is evident that the roughness parameters of the “grooved” surface are different from those of the initial surface. Thus, the prediction of the structure of worn surface on the initial topography parameters is an ambiguous task and has not been proposed yet.

Here, we describe a concept of the effective surface profile (ESP) allowing prediction of worn surface profile that could be generated during wear.

Let's consider how the effective surface profile is shaped. Note that the profile shape depends on the direction of sliding. **Figure 1** shows the 3D image of a surface subjected to the study and two effective surface profiles aligned perpendicular to the direction X and Y of the surface. These profiles have been generated by means of the superimposing of all height ordinates along the selected direction to the plane, which is perpendicular to both of the selected direction and the mean surface plane. This method transforms shape of asperities, which are dominant on a surface as highest asperities, into a single profile. As a result, the ESP consists of all asperities that will contribute to the sliding wear process because they are perturbed along the selected sliding direction. As it is seen in **Figure 1**, the effective surface profiles generated from a height data of the same surface in directions X and Y are different. This is because the location of highest asperities is determined by the coordinates (x, y) on a mean surface plane and only one coordinate (or x , or y) onto the corresponding effective surface profile. In some cases, the coordinates of different asperities can be nearly the same, leading to the overlapping of asperity projection onto a profile plane. This fact has also been illustrated in **Figure 1**.

The five highest asperities, which can be distinctly identified on the effective surface profile, are labeled with A, B, C, D, E letters on the 3D surface image. The arrows are starting at a highest point of the selected asperities on the 3D surface image and they are ending on the plane of effective surface profiles to show their location on the graph. The ESP along direction Y shows all five asperities. There A, B, E present as separated asperities, meanwhile D, C have formed a single asperity with doubled peak. The ESP along X direction exhibits two asperities only. There is a doubled peak of D, C, and a single asperity E. Surface asperities A, B are not presented on the effective surface profile along X direction. This is because, first, the heights of asperities A and B are lower than the height of C or D and second, they lie exactly on the same direction as a projection has been processed.

Mentioned above facts allow us to conclude that the shape of an effective surface profile depends on the direction of sliding. If the amount of sliding asperities of the same surface depends on the sliding direction, the different energy dissipation will be occurred at the sliding in different directions. This will lead to the difference of friction coefficients regarding to the selected direction of sliding. Friction anisotropy is a well-known phenomena (Zmitrowicz, 2006), and it has been proved that surface topography plays a crucial role and nature of friction anisotropy has strong respect to topographic orientation (Yu and Wang, 2012). The analysis of shape and structure of effective surface profile allows estimating the friction anisotropy due to the discrepant force contribution to abrasion and plowing.

Real Sliding Area at the Steady Friction

One contact phenomenon that is attended for engineering interests is the real area of contact between rough surfaces. Since the topographic features of the mating surfaces are unlikely to

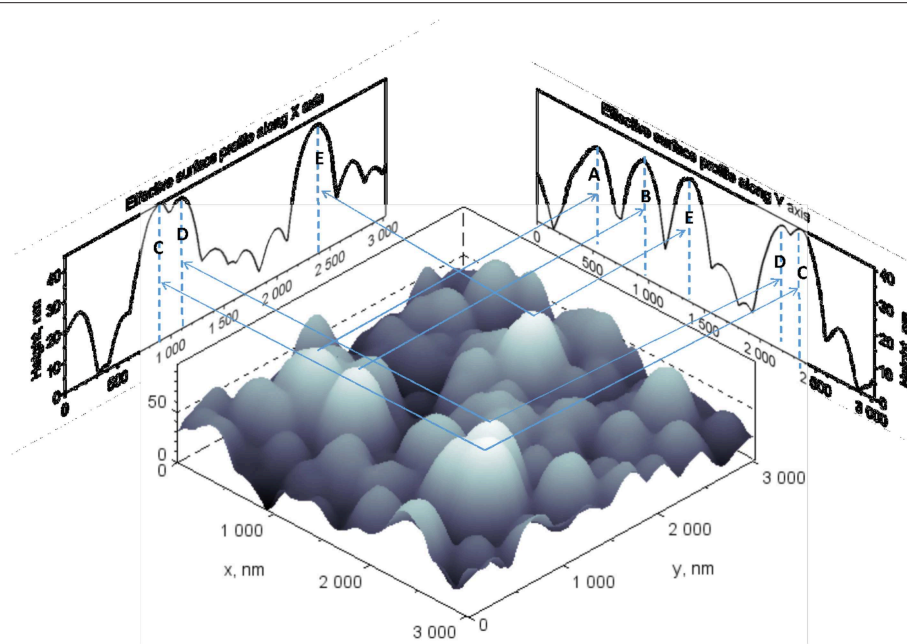


FIGURE 1 | 3D view of surface and its effective surface profiles in X and Y directions. The highest asperities of surface that contribute to the profile shape form are marked by letters A, B, C, D, E. The effective surface profile along the direction Y includes all marked surface asperities. In contrast, the effective surface profile along direction X does not include the surface asperities A and B.

be identical, only a unique distribution of spots in a contact plane will affect tribological properties at a given instant. The presence of discrete contact spots within an apparent contact area of bodies can be identified and measured with *in situ* techniques (Etsion, 2012).

If the sliding surfaces behave plastically, like most common materials do above their yield strength, then real contact area is simply the ratio of contact asperities N to the indentation hardness H , which is by definition the load per unit area under static equilibrium. If the shape of asperities is assumed to be hemisphere, each local contact spot has a circular shape (Greenwood and Williamson, 1966; Adams and Nosonovsky, 2000), as it was discussed in section Contact of Rough Surfaces. When a hard rough surface slides over a soft one, the hard asperities plow and cut the soft surface, resulting in scars generation. Such mechanical interaction of surfaces corresponds to the running-in stage of wear. The plowing and cutting end when the soft surface completely adapted to the sliding of hard one. At this steady stage of wear, the soft surface represents a set of grooves. What is the actual area of sliding contact at this stage and how it can be localized on the surface? The ESP principles allow estimation and localization of real sliding area as follows.

Let us assume that a hard rough surface, shown in **Figure 1**, can be subjected to slide in directions X or Y. ESPs that consist of surface asperities involved to friction for the selected directions have also shown in **Figure 1**. To identify the position of ESP height points on the rough surface, we mapped back the ESP height points onto the surface image. The result of localization of real sliding areas is illustrated in **Figure 2**. For better recognition

and comparison of contact areas, we marked rectangles in green color for direction Y and in red color for direction X.

There are 17 identified contact areas that contribute to friction in X direction and 14 in Y direction. The crossed and linked rectangles indicate which asperities slide in both directions will be involved to.

The geometrical shape of contact area of a single asperity on a surface with a groove during the steady stage of wear might correspond to a thin-elongated ellipse (Eldredge and Tabor, 1955). However, it should be taken into account that in most of cases (1) the penetration δ is small and incomparable to the curvature radius R_i of an asperity, (2) the arc length l of curved real groove is smaller than an aligned thin-elongated contact ellipse with aspect ratio $b_e/a_e \ll 1$ along the major axis a_e of an elliptical contact, so that the shoulder of a groove developed by one asperity will be plastically deformed by those following it. Thus, the contact area between an asperity and corresponding groove can be assumed to be a rectangular (Eldredge and Tabor, 1955), when shakedown pressure limit p_s is reached at the steady wear stage. In this case, the load of a single asperity carried by the rectangular contact in a groove (Kapoor and Johnson, 1992) is

$$P_i = a_i b_i p_s. \quad (5)$$

where $a_i b_i$ is the rectangular sliding contact area A_i of a single asperity.

In real situations, the heights of the opposite ridges of the groove are slightly different. However, this difference is negligibly

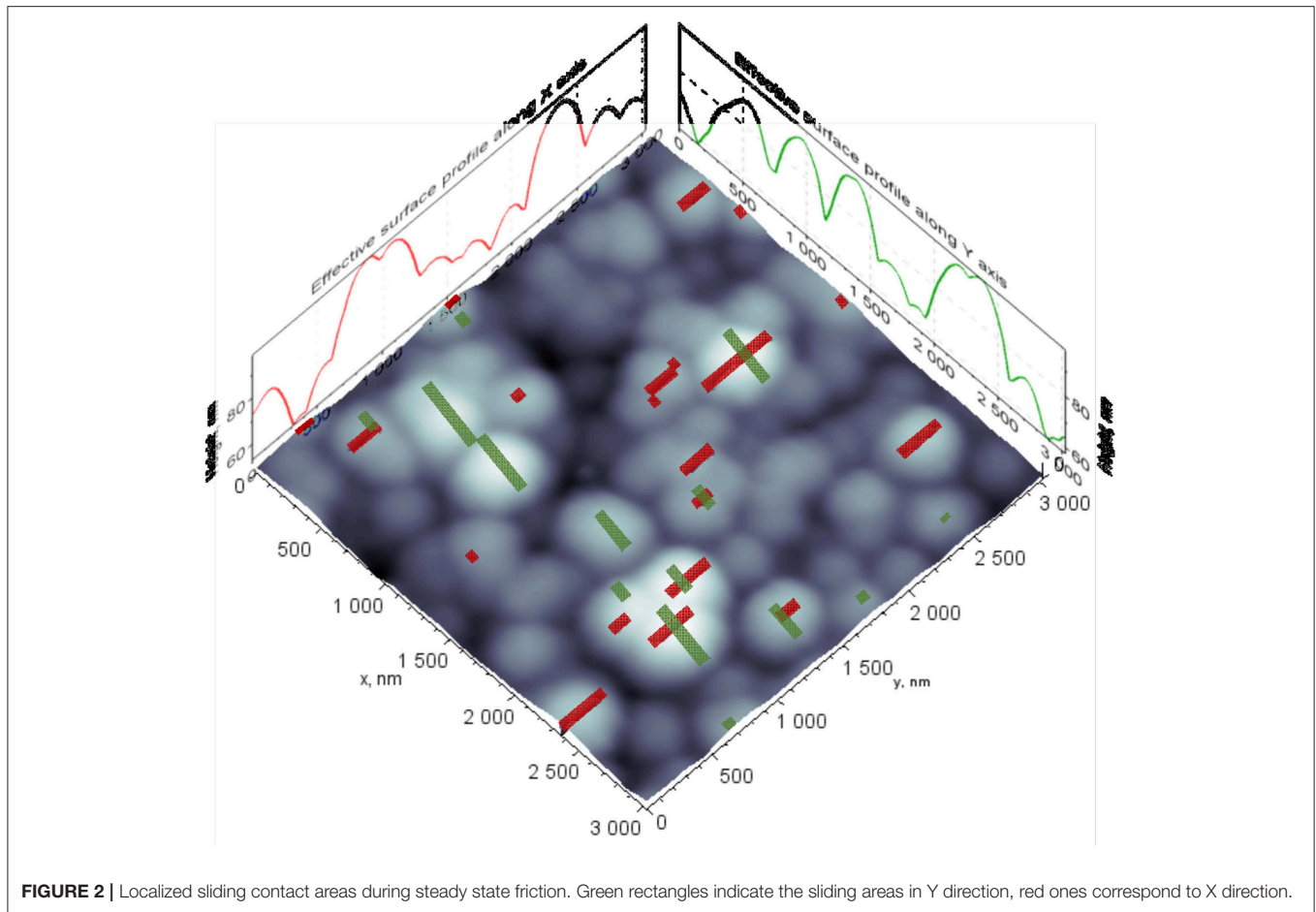


FIGURE 2 | Localized sliding contact areas during steady state friction. Green rectangles indicate the sliding areas in Y direction, red ones correspond to X direction.

small with respect to the curvature of arc l_i . Taking into account this assumption and the simple geometric relation for the arc length, the length of transverse profile of single groove might be expected to be given by

$$l_i = 2R_i \arcsin\left(\frac{a_i}{2R_i}\right). \quad (6)$$

Therefore, summing up these expressions for each asperity involved in sliding, we obtain the total length of a transverse profile of worn surface as

$$L = \sum_{i=1}^{i=N_s} 2R_i \arcsin\left(\frac{a_i}{2R_i}\right). \quad (7)$$

Hence, the total sliding contact area A_s can found by multiplying Equation (7) width b_i of an individual contact of asperity

$$A_s = \sum_{i=1}^{i=N_s} 2b_i R_i \arcsin\left(\frac{a_i}{2R_i}\right). \quad (8)$$

The transverse profile of worn surface discussed here entirely corresponds to the inverted effective surface profile considered in section Concept of Effective Surface Profile. Thus, the effective surface profile can be represented as a “band” consisting of several parts, where each part is a local contact area of sliding asperity with arc length l_i and width b_i .

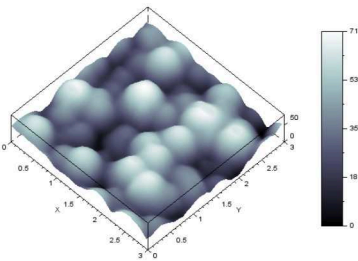
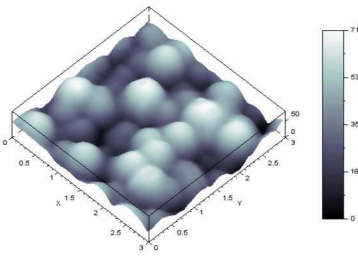
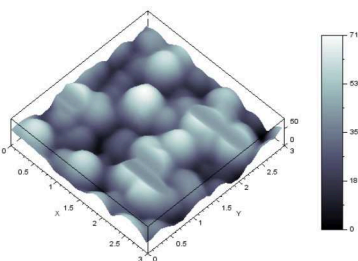
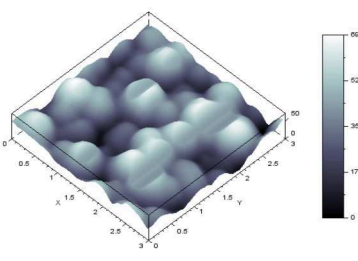
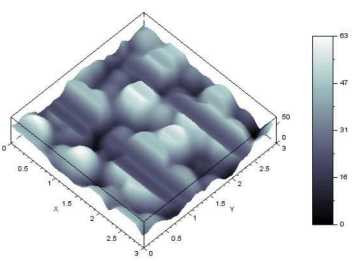
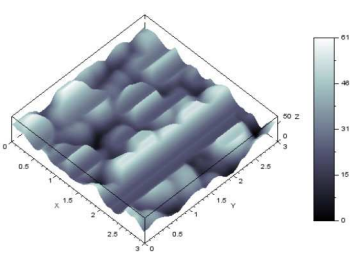
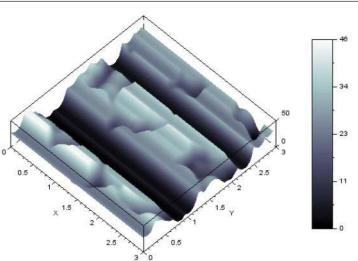
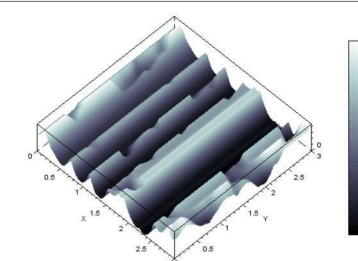
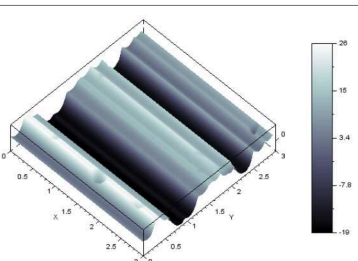
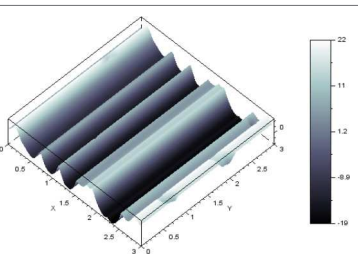
The sliding contact areas in **Figure 2** are marked as rectangles. The length of each single rectangle is equal to the projection of corresponding single arc from ESP. The width of rectangle is chosen to be a constant for a better visualization in the figure, however, in the real sliding it corresponds to b_i . Thereby, each rectangle represents a local bearing area of single asperity carried by the sliding contact according to Equation (8). The estimation of value b_i is a complicated task. In some instance, the well-known equations for an elliptical contact could be used (Greenwood, 1997; Popov, 2010), however, a concave curvature, variation in asperity radius will influence the width of selected contact rectangle.

Comparing the presented equations and equations of GW theory in section Contact of Rough Surfaces, one can see the difference between them. The distinction occurs due to the fact that GW theory describes the static contact and circular-like areas of single asperities being in contact. The proposed approach, based on the

effective surface profile definition, assumes the contact at the kinetic movement and rectangular (pseudo-elliptical) contact for a single asperity in the case of worn opposite surface.

Thus, the analysis of effective surface profile allows identifying the quantity and location of asperities contributed to friction in selected direction, and estimates the bearing area of contact and real sliding area as well.

TABLE 1 | Simulated sliding wear surfaces illustrating transition in surface texture in both perpendicular X and Y directions.

Sliding wear along X axis			Sliding wear along Y axis		
Δz	10 nm		Δz	10 nm	
Sa	37.90 nm		Sa	37.93 nm	
Sq	14.24 nm		Sq	14.26 nm	
Ssk	0.12		Ssk	0.13	
Squ	2.21		Squ	2.21	
Δz	30 nm		Δz	30 nm	
Sa	37.00 nm		Sa	36.80 nm	
Sq	13.30 nm		Sq	13.01 nm	
Ssk	0.08		Ssk	0.04	
Squ	2.40		Squ	2.39	
Δz	50 nm		Δz	50 nm	
Sa	32.77 nm		Sa	31.18 nm	
Sq	11.62 nm		Sq	10.51 nm	
Ssk	0.29		Ssk	0.41	
Squ	2.32		Squ	2.68	
Δz	70 nm		Δz	70 nm	
Sa	21.29 nm		Sa	17.95 nm	
Sq	11.46 nm		Sq	10.62 nm	
Ssk	-0.27		Ssk	0.17	
Squ	2.02		Squ	1.86	
Δz	90 nm		Δz	90 nm	
Sa	22.23 nm		Sa	18.68 nm	
Sq	12.19 nm		Sq	11.73 nm	
Ssk	-0.41		Ssk	0.05	
Squ	2.08		Squ	1.71	

The corresponding surface parameters are given at the left side of each surface image.

Modeling of Worn Surface and Its Roughness

If the transverse surface topography is perfectly correlated in sliding direction, then a set of conformal grooves will be developed in the softer material. During the repeating sliding process, when the steady state is reached, each groove corresponds to certain hard asperity on the mating surface.

However, not all hard asperities of the mating surface produce the grooves. A groove on a soft surface will be produced by an asperity which is higher than anyone else in that linear direction of groove. Moreover, worn grooved surface is not generated during one pass, surface structure undergoes the transition from an initial texture to the texture of worn surface.

The transition of surface texture always observed at finish turning (Shahabi and Ratnam, 2016), grinding (Gong et al., 2002; Cao et al., 2013; Darafon et al., 2013), abrasive wear (da Silva and de Mello, 2009; Sep et al., 2017), and proposed modeling techniques mainly based on an idea that grooves on the worn surface are produced by protuberated asperities of counterface and contour profile of grooved surfaces should correlate to the superimposing protuberated asperities.

An application of the effective surface profile to the abrasive wear process could be related to grinding or abrasive wear modeling and real experiments conducted by Gong et al. (2002) or da Silva and de Mello (2009). Both of them have been concluded that the final structure of worn surface could be represented via superimposing of set scratches generated during abrasion process, and it was stated that the rough surface could be estimated by using a computed load map and “the average profile of the reference surface.”

In our study, the simulation of abrasive wear was conducted for surfaces with similar surface structure. A surface presented in **Figure 1** was used as a counterpart assuming high hardness and its asperities work as the abrasive particles. For a surface subjected to the wear simulation, an image of surface with similar structure exhibiting the spherical-like asperities was selected. The roughness parameters of surface are $Sa = 37.94$, $Sq = 14.31$, $Ssk = 0.14$, $Sku = 2.23$.

Five subsequent stages of surface texture transformation are listed in **Table 1** in both directions X and Y. The vertical displacement Δz starts at 10 nm and following increment was set as 20 nm.

Simulation result shows that at the vertical displacement of 10 nm there are no evident damages and surface has a random granular texture. When Δz reaches the range of 30–50 nm, the partial damages of spherical-like asperities occur with a lay direction along to the direction of sliding. The grooved texture becomes manifested at Δz of 70 nm and new grooved texture is completely formed at the displacement of 90 nm.

Comparing the images at the displacement of 90 nm one can conclude that the groove widths and their heights vary and the worn surfaces do not have a uniform groove profile in directions X and Y. Thus, the selected surface, shown in **Figure 1**, generates the dissimilar worn surfaces in perpendicular sliding directions X and Y. The resulting surface profiles are inverse to the effective surface profiles in corresponding direction as it presented in **Figure 3**. The location of asperity involved in the destructive

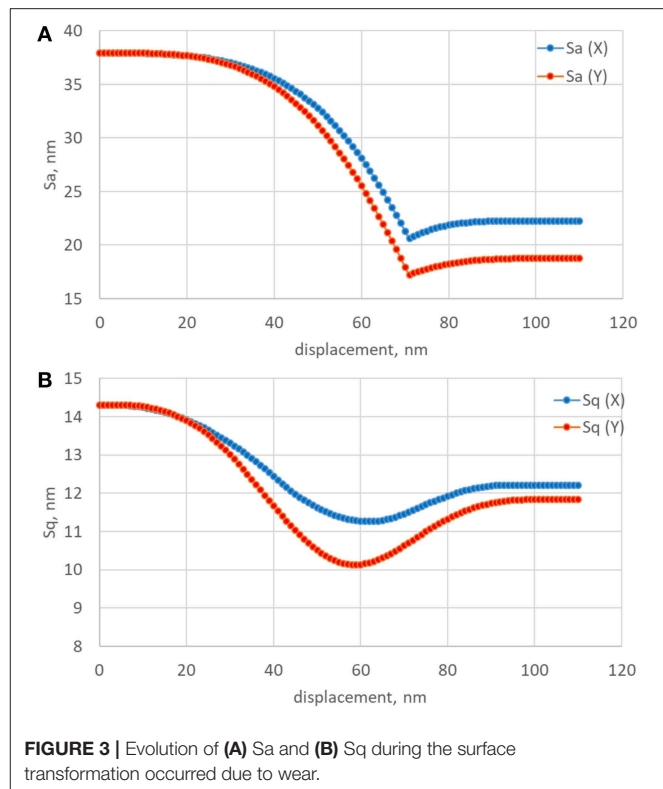


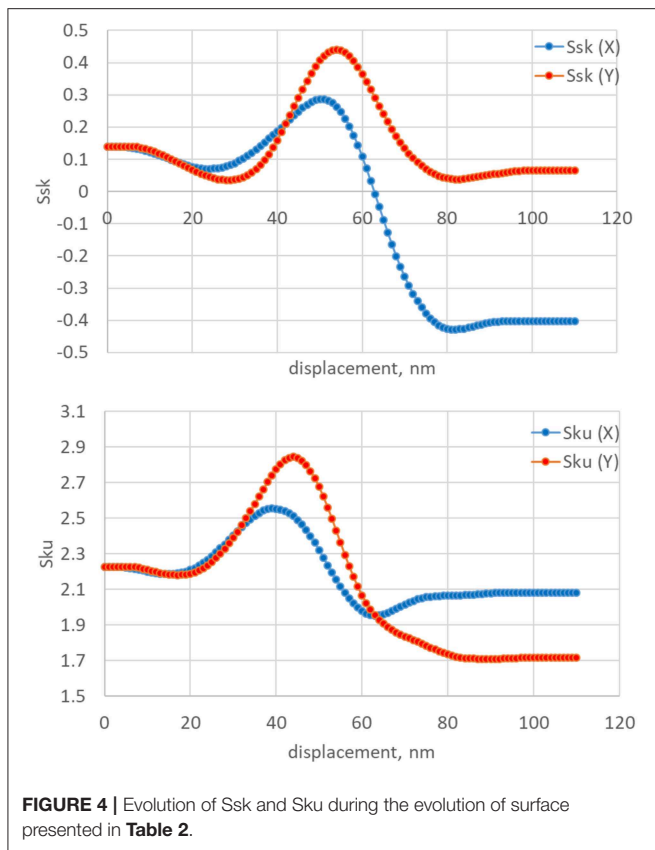
FIGURE 3 | Evolution of (A) Sa and (B) Sq during the surface transformation occurred due to wear.

friction process can be easily identified on the ESP graph in the selected direction of sliding.

Evolution of Roughness Parameters During the Simulated Abrasive Wear

To investigate, how the roughness parameters vary due to the transition of surface texture, a series of numerical calculations were performed by using the simulated worn surfaces described in previous section. All the calculations of roughness parameters were performed under the stepwise displacement control. A displacement Δz is set in the normal direction to the nominal plane of rough surface. The maximum value of Δz was set to 110 nm based on estimation result presented in previous section and was subdivided into 110 steps. The evolution of Sa and Sq of surface was investigated for a series of increasing displacement Δz and it is shown in **Figure 4**.

Several important observations can be done from Sa and Sq graphs (see **Figure 3**). Both of them begins from the corresponding values of surface $Sa = 37.94$ and $Sq = 14.31$, respectively. Graph of Sa consist of two parts. First part is characterized by gradual decreasing because the areas undergoing wear contribute to the overall decreasing of surface heights. However, at the vertical displacement Δz about 70 nm, Sa becomes to increase gradually and reach constant value of 22.25 and 18.76 in X and Y directions, respectively. It can be explained as following. At this displacement, the height magnitude of grooved structure becomes to dominate upon the initial granular structure, and stabilizes as a constant value



when a worn grooved surface has finally formed. The drop on both graphs can be represented as a delimiter for an amplitude transition between virgin and worn surfaces.

In contrast to Sa , a graph of Sq has no sharp drop (see Figure 3B). Sq graph depicts as an inverted smoothed bell-like function with a minimum of Δz about 60 nm. Comparing to the transition behavior of Sa , Sq has reached the minimum value of Δz earlier than Sa . It means that Sq is more sensitive to the surface structure changes due to wear. Simulation result also shows that Sq tends to decrease at the initial stage of wear, where the upper parts of asperities underwent a minor material loss. The formation of grooved surface began to dominate, as the main surface texture, approximately at the minimum of Sq (see Table 1). Obtained results are in agreement with results of Jeng and co-authors (Jeng and Gao, 2000; Jeng et al., 2004), but represent more complicated transition behavior of Sa and Sq when the virgin surface is transformed to the grooved worn surface.

Figure 4 shows the evolution of Ssk and Sku during the transition of surface structures. The shape of curves has more complex behavior than shape of Sa and Sq . The results show that both skewness and kurtosis curves have peaks at Δz about 50 and 40 nm, respectively. Comparing the extreme points on the graphs of Sa , Sq , Ssk , Sku , one can conclude that a kurtosis (Sku) is more sensitive to the surface transformation due to wear.

Comparison between the roughness parameters of surface and its ESP profiles allows concluding that there are no evident

TABLE 2 | The roughness parameters of the effective surface profiles along axis X and Y, and corresponding worn surfaces.

	Sa	Sq	Ssk	Sku
ESP along X	10.15	12.26	0.40	2.05
ESP along Y	10.55	11.89	0.07	1.69
Worn surface along X	10.15	12.21	−0.40	2.08
Worn surface along Y	10.55	11.84	−0.07	1.72

matches. The values of Sa and Sq of the ESP are lower than those of Sa and Sq of the surface listed in Table 1. It is reasonable because the height range of ESP is up to twice lower than the average height range of surface profiles. Skewness and kurtosis (Ssk and Sku) cannot be qualitatively compared because the ESP profiles have the positive value of Ssk and Sku lower than 3 due to their origin always. The roughness parameters of ESPs and simulated worn surfaces are listed in Table 2.

Also, it should be noted, that presented graphs demonstrate a transition process occurring between two different surface structures, but final surface structure and its surface parameters could be predicted by the ESP in the selected direction.

As one would expect, the roughness parameters are similar for an effective surface profile and corresponding worn surfaces. The similarity presents because the ESP and corresponding worn surface are inverted in origin and the amplitude (height) roughness parameters are considered. The negative value of skewness is easily explained. The effective surface profile in most of cases will have the positive Ssk because it consists of rounded top asperities and sharp thin pits formed due to the overlapping of neighboring ones. The worn surface has an inverted structure: the thin sharp peaks and big curved valleys that characterizes by the negative skewness. A small variation in the values of Sq and Sku are probably caused by the digitizing collapsing error in calculation procedure implemented, which is different for an inverted data profiles.

Thus, the main feature of the roughness parameters of ESP and worn surfaces, listed in Table 2, is that these parameters were evaluated based on the height data of real surface with implementation of concept of the effective surface profile, presented in Figure 2, and allow qualitative prediction of the structure of worn surface and its roughness parameters.

CONCLUSIONS

A new consideration of conventional surface data has been presented to predict the structure of worn profile that could be formed during abrasive wear process. Such consideration allows us to introduce the concept of an effective surface profile as a powerful phenomenological tool for surface characterization based on the height data of initial rough surface. The wear process, discussed in this paper, is considered as the degradation of the soft rough surface by the interlocking hard irregularities, plowing, and abrasion of material by means of the hard asperities of counterface rather than adhesion of asperities in friction and

without consideration of cases in which wear debris are trapped onto the contact area.

- 1 The results of roughness analysis of profiles, which were derived from rough surface, have clearly shown that, in the present case, there is no good correlation of the height roughness parameters S_a , S_q , S_{ku} , S_{sk} of the surface topography with the corresponding parameters of surface profiles. It was deduced that this approach is not effective for the prediction of worn surface structure formed during sliding friction.
- 2 The concept of effective surface profile has been proposed to construct the front profile of surface consisting of asperities involved in the contact during sliding friction.
- 3 In the frame of idealized model of sliding of a hard rough surface upon a soft rough one, the contact area A_s and contact pressure P_s , under the shakedown pressure p_s , were theoretically estimated.
- 4 A simulation procedure is proposed for topographical representation of worn surfaces produced by the rough surface in both perpendicular directions. The effective surface profiles as a template of possible transformation of soft surface are

used in selected directions. The roughness parameters of worn surfaces are estimated and compared. It has been revealed that the prediction of worn surface structure and its roughness parameters are possible by using effective surface profile with respect to the selected direction of sliding.

The results above widen the understanding of friction and will advance the ability to predict the wear pattern on a surface that has not been attended before in the surface analysis in tribology.

AUTHOR CONTRIBUTIONS

AK proposed the concept of effective surface profile and done calculations. ZY and CH conducted measurements. YM involved in the preparation of the manuscript.

ACKNOWLEDGMENTS

This work was supported by the National Natural Science Foundation of China (NSFC) with grant No. 51635009 and the Tsinghua University Initiative Scientific Research Program No.2015THZ0.

REFERENCES

- Adams, G. G., and Nosonovsky, M. (2000). Contact modeling — forces. *Tribol. Int.* 33, 431–442. doi: 10.1016/S0301-679X(00)00063-3
- Ao, Y., Wang, Q. J., and Chen, P. (2002). Simulating the worn surface in a wear process. *Wear* 252, 37–47. doi: 10.1016/S0043-1648(01)00841-9
- Archard, J. F. (1953). Contact and rubbing of flat surfaces. *J. Appl. Phys.* 24, 981–988. doi: 10.1063/1.1721448
- Aslan, D., and Budak, E. (2015). Surface roughness and thermo-mechanical force modeling for grinding operations with regular and circumferentially grooved wheels. *J. Mater. Process. Technol.* 223, 75–90. doi: 10.1016/j.jmatprotec.2015.03.023
- Bhushan, B. (1998). Contact mechanics of rough surfaces in tribology: multiple asperity contact. *Tribol. Lett.* 4, 1–35. doi: 10.1023/A:1019186601445
- Bhushan, B. (2001). “Chapter 2: Surface roughness analysis and measurement techniques,” in *Modern tribology handbook. Vol. 1*, ed B. Bhushan (Boca Raton, FL: CRC Press), 49–119. doi: 10.1201/9780849377877.ch2
- Borodich, F. M., and Bianchi, D. “Surface synthesis based on surface statistics,” in *Encyclopedia of Tribology*, eds Q. J. Wang and Y.-W. Chung (Boston, MA: Springer), 3472–3478. doi: 10.1007/978-0-387-92897-5_309
- Borodich, F. M., Pepelyshev, A., and Savencu, O. (2016). Statistical approaches to description of rough engineering surfaces at nano and microscales. *Tribol. Int.* 103, 197–207. doi: 10.1016/j.triboint.2016.06.043
- Borodich, F. M., and Savencu, O. (2017). “Hierarchical models of engineering rough surfaces and bio-inspired adhesives,” in *Bio-Inspired Structured Adhesives*, eds L. Heepe, L. Xue, and S. N. Gorb (Cham: Springer), 179–219. doi: 10.1007/978-3-319-59114-8_10
- Bowden, F. P., and Tabor, D. (1964). *Friction and Lubrication of Solids*. Oxford: Clarendon Press.
- Cabanettes, F., and Rosén, B.-G. (2014). Topography changes observation during running-in of rolling contacts. *Wear* 315, 78–86. doi: 10.1016/j.wear.2014.04.009
- Cao, Y., Guan, J., Li, B., Chen, X., Yang, J., and Gan, C. (2013). Modeling and simulation of grinding surface topography considering wheel vibration. *Int. J. Adv. Manuf. Technol.* 66, 937–945. doi: 10.1007/s00170-012-4378-7
- Challen, J. M., McLean, L. J., and Oxley, P. L. B. (1984). Plastic deformation of a metal surface in sliding contact with a hard wedge: its relation to friction and wear. *Proc. R. Soc. London A Math. Phys. Eng. Sci.* 394, 161–181. doi: 10.1098/rspa.1984.0074
- da Silva, W. M., and de Mello, J. D. B. (2009). Using parallel scratches to simulate abrasive wear. *Wear* 267, 1987–1997. doi: 10.1016/j.wear.2009.06.005
- Darafon, A., Warkentin, A., and Bauer, R. (2013). 3D metal removal simulation to determine uncut chip thickness, contact length, and surface finish in grinding. *Int. J. Adv. Manuf. Technol.* 66, 1715–1724. doi: 10.1007/s00170-012-4452-1
- Dong, W., Sullivan, P., and Stout, K. (1992). Comprehensive study of parameters for characterizing three-dimensional surface topography I: some inherent properties of parameter variation. *Wear* 159, 161–171. doi: 10.1016/0043-1648(92)90299-N
- Dong, W., Sullivan, P., and Stout, K. (1993). Comprehensive study of parameters for characterizing three-dimensional surface topography II: statistical properties of parameter variation. *Wear* 167, 9–21. doi: 10.1016/0043-1648(93)90050-V
- Dong, W., Sullivan, P., and Stout, K. (1994a). Comprehensive study of parameters for characterising three-dimensional surface topography III: parameters for characterising amplitude and some functional properties. *Wear* 178, 29–43. doi: 10.1016/0043-1648(94)90127-9
- Dong, W., Sullivan, P., and Stout, K. (1994b). Comprehensive study of parameters for characterising three-dimensional surface topography IV: parameters for characterising spatial and hybrid properties. *Wear* 178, 45–60. doi: 10.1016/0043-1648(94)90128-7
- Eldredge, K. R., and Tabor, D. (1955). The mechanism of rolling friction. I. The plastic range. *Proc. R. Soc. A Math. Phys. Eng. Sci.* 229, 181–198. doi: 10.1098/rspa.1955.0081
- Etsion, I. (2012). Discussion of the paper: optical *in situ* micro tribometer for analysis of real contact area for contact mechanics, adhesion, and sliding experiments. *Tribol. Lett.* 46, 205–205. doi: 10.1007/s11249-012-9930-y
- Gadelmawla, E. S., Koura, M. M., Maksoud, T. M. A., Elewa, I. M., and Soliman, H. H. (2002). Roughness parameters. *J. Mater. Process. Technol.* 123, 133–145. doi: 10.1016/S0924-0136(02)00060-2
- Glaeser, W. A. (1992). *Materials for Tribology*. Amsterdam: Elsevier Science.
- Gong, Y., Wang, B., and Wang, W. (2002). The simulation of grinding wheels and ground surface roughness based on virtual reality technology. *J. Mater. Process. Technol.* 129, 123–126. doi: 10.1016/S0924-0136(02)00589-7
- Goryacheva, I. G. (1998). *Contact Mechanics in Tribology*. Dordrecht: Kluwer Academic Publishers.
- Greenwood, J. A. (1997). Analysis of elliptical Hertzian contacts. *Tribol. Int.* 30, 235–237. doi: 10.1016/S0301-679X(96)00051-5

- Greenwood, J. A., and Williamson, J. B. P. (1966). Contact of nominally flat surfaces. *Proc. R. Soc. Lond. A. Math. Phys. Sci.* 295, 300–319. doi: 10.1098/rspa.1966.0242
- Greenwood, J. A., and Wu, J. J. (2001). Surface roughness and contact: an apology. *Meccanica*. 36, 617–630. doi: 10.1023/A:1016340601964
- Hao, L., and Meng, Y. (2015). Numerical prediction of wear process of an initial line contact in mixed lubrication conditions. *Tribol. Lett.* 60:31. doi: 10.1007/s11249-015-0609-z
- Hayward, I. P., Singer, I. L., and Seitzman, L. E. (1992). Effect of roughness on the friction of diamond on cvd diamond coatings. *Wear* 157, 215–227. doi: 10.1016/0043-1648(92)90063-E
- Hsu, S. M., Shen, M. C., and Ruff, A. W. (1997). Wear prediction for metals. *Tribol. Int.* 30, 377–383. doi: 10.1016/S0301-679X(96)00067-9
- Jeng, Y.-R., and Gao, C.-C. (2000). Changes of surface topography during wear for surfaces with different height distributions. *Tribol. Trans.* 43, 749–757. doi: 10.1080/10402000008982404
- Jeng, Y.-R., Lin, Z.-W., and Shyu, S.-H. (2004). Changes of surface topography during running-in process. *J. Tribol.* 126, 620–625. doi: 10.1115/1.1759344
- Jiang, X., Scott, P. J., Whitehouse, D. J., and Blunt, L. (2007a). Paradigm shifts in surface metrology. Part I. Historical philosophy. *Proc. R. Soc. A Math. Phys. Eng. Sci.* 463, 2049–2070. doi: 10.1098/rspa.2007.1874
- Jiang, X., Scott, P. J., Whitehouse, D. J., and Blunt, L. (2007b). Paradigm shifts in surface metrology. Part II. The current shift. *Proc. R. Soc. A Math. Phys. Eng. Sci.* 463, 2071–2099. doi: 10.1098/rspa.2007.1873
- Kapoor, A., and Johnson, K. L. (1992). Effect of changes in contact geometry on shakedown of surfaces in rolling/sliding contact. *Int. J. Mech. Sci.* 34, 223–239. doi: 10.1016/0020-7403(92)90073-P
- Kapoor, A., and Johnson, K. L. (1994). Plastic ratchetting as a mechanism of metallic wear. *Proc. R. Soc. A Math. Phys. Eng. Sci.* 445, 367–384. doi: 10.1098/rspa.1994.0066
- Kapoor, A., Williams, J. A., and Johnson, K. L. (1994). The steady state sliding of rough surfaces. *Wear* 175, 81–92. doi: 10.1016/0043-1648(94)90171-6
- Kato, K. (2002). Classification of wear mechanisms/models. *Proc. Inst. Mech. Eng. Part J J. Eng. Tribol.* 216, 349–355. doi: 10.1243/09544110260216649
- Lu, W., Zhang, G., Liu, X., Zhou, L., Chen, L., and Jiang, X. (2014). Prediction of surface topography at the end of sliding running-in wear based on areal surface parameters. *Tribol. Trans.* 57, 553–560. doi: 10.1080/10402004.2014.87165
- Manier, C.-A., Spaltmann, D., Theiler, G., and Woydt, M. (2008). Carbonaceous coatings by rolling with 10% slip under mixed/boundary lubrication and high initial Hertzian contact pressures. *Diam. Relat. Mater.* 17, 1751–1754. doi: 10.1016/j.diamond.2008.01.066
- Meng, H. C., and Ludema, K. C. (1995). Wear models and predictive equations: their form and content. *Wear* 181–183, 443–457. doi: 10.1016/0043-1648(95)90158-2
- Popov, V. (2010). *Contact Mechanics and Friction - Physical Principles and Applications*. Berlin: Springer-Verlag. doi: 10.1007/978-3-642-10803-7
- Popov, V. L., and Pohrt, R. (2018). Adhesive wear and particle emission: numerical approach based on asperity-free formulation of Rabinowicz criterion. *Friction* 6, 260–273. doi: 10.1007/s40544-018-0236-4
- Reizer, R., Pawlus, P., Galda, L., Grabon, W., and Dzierwa, A. (2012). Modeling of worn surface topography formed in a low wear process. *Wear* 278–279, 94–100. doi: 10.1016/j.wear.2011.12.012
- Sep, J., Tomczewski, L., Galda, L., and Dzierwa, A. (2017). The study on abrasive wear of grooved journal bearings. *Wear* 376–377, 54–62. doi: 10.1016/j.wear.2017.02.034
- Shahabi, H. H., and Ratnam, M. M. (2016). Simulation and measurement of surface roughness via grey scale image of tool in finish turning. *Precis. Eng.* 43, 146–153. doi: 10.1016/j.precisioneng.2015.07.004
- Stout, K. J., et al. (1993). *The Development of Methods for the Characterisation of Roughness in Three Dimensions, 1st Edn.* Birmingham: University of Birmingham Edgbaston.
- Xie, Y., and Williams, J. A. (1996). The prediction of friction and wear when a soft surface slides against a harder rough surface. *Wear* 196, 21–34. doi: 10.1016/0043-1648(95)06830-9
- Yu, C., and Wang, Q. J. (2012). Friction anisotropy with respect to topographic orientation. *Sci. Rep.* 2:988. doi: 10.1038/srep00988
- Yuan, C. Q., Peng, Z., Yan, X. P., and Zhou, X. C. (2008). Surface roughness evolutions in sliding wear process. *Wear* 265, 341–348. doi: 10.1016/j.wear.2007.11.002
- Yuan, C. Q., Yan, X. P., and Peng, Z. (2007). Prediction of surface features of wear components based on surface characteristics of wear debris. *Wear* 263, 1513–1517. doi: 10.1016/j.wear.2006.11.029
- Zhuravlev, V. A. (2007). On the question of theoretical justification of the Amontons—Coulomb law for friction of unlubricated surfaces. *Proc. Inst. Mech. Eng. Part J J. Eng. Tribol.* 221, 893–898. doi: 10.1243/13506501JET176
- Zmitrowicz, A. (2006). Wear patterns and laws of wear – a review. *J. Theor. Appl. Mech.* 44, 219–253. Available online at: <http://www.ptmts.org.pl/jtam/index.php/jtam/article/view/v44n2p219/469>

Conflict of Interest Statement: The authors declare that the research was conducted in the absence of any commercial or financial relationships that could be construed as a potential conflict of interest.

Copyright © 2019 Kovalev, Yazhao, Hui and Meng. This is an open-access article distributed under the terms of the Creative Commons Attribution License (CC BY). The use, distribution or reproduction in other forums is permitted, provided the original author(s) and the copyright owner(s) are credited and that the original publication in this journal is cited, in accordance with accepted academic practice. No use, distribution or reproduction is permitted which does not comply with these terms.



Atomistic Insights Into Lubricated Tungsten/Diamond Sliding Contacts

Pedro A. Romero¹, Leonhard Mayrhofer¹, Pantcho Stoyanov^{1,2}, Rolf Merz³, Michael Kopnarski³, Martin Dienwiebel^{1,2} and Michael Moseler^{1,4,5*}

¹ Fraunhofer-Institute for Mechanics of Materials IWM–MicroTribology Center, Freiburg, Germany, ² Karlsruhe Institute of Technology, Institute for Applied Materials, Karlsruhe, Germany, ³ Institut für Oberflächen- und Schichtanalytik (IFOS), University of Kaiserslautern, Kaiserslautern, Germany, ⁴ Physics Department, University of Freiburg, Freiburg, Germany, ⁵ Freiburg Materials Research Center, University of Freiburg, Freiburg, Germany

OPEN ACCESS

Edited by:

Roman Pohrt,
Technische Universität Berlin,
Germany

Reviewed by:

Martin H. Müser,
Saarland University, Germany
Liran Ma,
Tsinghua University, China

*Correspondence:

Michael Moseler
mos@iwmm.fhg.de

Specialty section:

This article was submitted to
Tribology,
a section of the journal
Frontiers in Mechanical Engineering

Received: 05 December 2018

Accepted: 01 March 2019

Published: 02 April 2019

Citation:

Romero PA, Mayrhofer L, Stoyanov P,
Merz R, Kopnarski M, Dienwiebel M
and Moseler M (2019) Atomistic
Insights Into Lubricated
Tungsten/Diamond Sliding Contacts.
Front. Mech. Eng. 5:6.
doi: 10.3389/fmech.2019.00006

The reinforcement of coatings with diamond particles results in superior tribological performance in automotive applications. In addition to improving the coating's bulk properties, sliding of diamond on metallic counter bodies contributes to improved tribological performance. Therefore, in order to design better diamond-reinforced coatings, it is imperative to understand the atomistic mechanisms at sliding metal/diamond interfaces. Here, we investigate the interfacial tribochemical mechanisms leading to low friction in lubricated tungsten/diamond sliding contacts by combining reactive atomistic simulations with on-line tribometry experiments linked to chemical analysis. Reactive classical molecular dynamics simulations reveal the dehydrogenation of hexadecane lubricant molecules between tungsten/diamond contacts by proton transfer from the hexadecane to octahedral sites of the tungsten surface. Subsequent chemisorption of the radicalized hexadecane on dangling C-bond sites of the diamond surface leads to the formation of low-density hydrocarbon films, which significantly lower frictional resistance in the tribo-contact. Quasi-static density functional theory calculations confirm the classical molecular dynamics results and reveal that radicalized hydrocarbon molecules can also bond *via* C–O bonds on a WO₃ layer covering the tungsten counter surface. The on-line tribometry experiments confirm the reduction of friction under hexadecane lubrication, and *ex situ* chemical analysis by means of X-ray photoelectron spectroscopy (XPS), Auger electron spectroscopy (AES), and electron energy loss spectroscopy (EELS) provides evidence of the formation of a carbon-rich tribofilm on the diamond and tungsten-oxide surfaces as predicted by the atomistic simulations.

Keywords: molecular dynamics (MD), DFT, tribochemistry, hydrocarbon, diamond/tungsten, tribometry, XPS, AES

INTRODUCTION

Lubricated diamond/steel tribocouples exhibit amazingly small friction coefficients and wear under boundary lubrication conditions (Mehan and Hayden, 1981). Indeed, diamond particles are added to tribological coatings sliding against steel in order to reduce friction and improve wear resistance (Wang et al., 2005; Venkateswarlu et al., 2009; Kim et al., 2011; Yin et al., 2017). For instance, piston rings used in diesel engines showing superior tribological performance employ galvanic chromium

coatings that are filled with microscale diamond particles (Kennedy et al., 2014; Linsler et al., 2017). Therefore, since piston rings slide against metallic cylinder liners, the fundamental tribological mechanisms governing friction and wear in lubricated metal/diamond contacts are not only of academic (Mehan and Hayden, 1981) but also of industrial interest (Esser et al., 2004).

Although already used in technical applications, the mechanisms leading to ultralow friction in lubricated metal/diamond contacts are not well-understood. It is unclear whether diamond undergoes a crystalline/amorphous phase transition (Pastewka et al., 2011) or whether chemical mixing leads to the formation of carbides. Furthermore, the role of the lubricant is still elusive. It certainly plays an important role for friction reduction under boundary lubrication. Is it chemically inert and does it strongly physisorb to the surface? Or is it susceptible to tribochemical reactions and chemisorbs on one of the tribopartners? These questions cannot be answered by macroscopic tribological experiments.

In this article, a hexadecane lubricated tungsten/diamond contact is studied as a simple model system for industrial metal/diamond combinations lubricated by complex engine oils. By combining atomic-scale simulations with on-line tribometry experiments, the interfacial chemical mechanisms leading to low friction between hexadecane-lubricated tungsten/diamond sliding contacts are elucidated. We perform classical molecular dynamics and *ab initio* density functional theory (DFT) molecular static simulations to understand the surface chemistry leading to the formation of carbon reaction layers that reduce friction in tungsten/diamond tribological contacts. The accompanying experiments employing an on-line tribometer as well as X-ray photoelectron spectroscopy (XPS), Auger electron spectroscopy (AES), and electron energy loss spectroscopy (EELS) *ex situ* analysis of the counter surfaces, corroborate these findings.

METHODS

Classical Molecular Dynamics Simulations

Reactive classical molecular dynamics (MD) simulations of tribologically sheared hexadecane ($C_{16}H_{34}$) lubricant molecules confined between a tungsten (100) and reconstructed diamond (100) surface are performed. Two different surface terminations of the diamond are considered. A reconstructed diamond (100) surface with complete surface H termination [dia(100)H] provides a lower limit of reactivity for an initially non-reactive diamond surface, while the unreconstructed diamond (100) without H passivation [dia(100)] provides an upper limit of reactivity—representing a fully reactive diamond surface as it occurs for instance after a wear event that removes passivation. The dimensions of the diamond substrate are $5.00 \times 2.50 \times 5.71 \text{ nm}^3$, while the dimensions of the monocrystalline tungsten substrate are $5.06 \times 2.53 \times 5.70 \text{ nm}^3$. For both counter bodies, contact occurs on their (100) surfaces while being sheared at 30 m/s under a contact pressure of 10 GPa. The tribocouple is thermostated at 300 K using a dissipative particle dynamics (DPD) thermostat (Groot and Warren, 1997) at the outer faces

of the counter bodies with a dissipation constant of 5 eV ps nm^{-2} and a cutoff of 0.5 nm.

A 10-GPa pressure in the contact is established by applying the Pastewka–Moser–Moseler tribo-barostat (Pastewka et al., 2008). The simulations are performed using a screened version (Stoyanov et al., 2013a) of the bond-order potential for W-C-H material systems developed by Juslin et al. (2005) and applied by us for various tribological simulations of W-C-H systems (Stoyanov et al., 2013a,b, 2014, 2015).

Density Functional Theory Quasi-Static Calculations

In order to verify the surface chemistry observed in the classical molecular dynamics simulations and to extend the numerical investigations to oxide surfaces, electronic structure calculations are performed employing the DFT (Hohenberg and Kohn, 1964; Kohn and Sham, 1965) as implemented in the VASP software suite (Kresse and Hafner, 1993, 1994) along with projector augmented-wave (PAW) potentials (Blöchl, 1994; Kresse and Joubert, 1999) for the simulated elements (i.e., W, C, O, H) and the PBE (Perdew et al., 1996) generalized gradient approximation to the XC potential. Structural relaxations are performed until the convergence criterion of a maximal force of 0.2 eV/nm acting on a single atom is reached. The Kohn–Sham wave functions are expanded in a plane wave basis using an energy cutoff of 400 eV. Periodic boundary conditions are applied along all directions. Chemical reaction energies are calculated as $\Delta E = E_{Ret} - E_{Prod}$, where E_{Ret} and E_{Prod} are the DFT ground state energies of the reactant and product states, respectively. With this definition, positive reaction energies indicate exothermic processes.

First, in order to verify the stability of hydrocarbon molecules in tungsten/diamond contacts, butane (C_4H_{10}) molecules confined between tungsten (100), reconstructed H-passivated diamond (100), and WO_3 (001) surfaces are relaxed quasi-statically under increasing normal pressures up to ~ 70 GPa. For these simulations, in order to successively increase the normal pressure, the simulation box is reduced step by step along the surface normal, and the system is quasi-statically relaxed at each step. Additionally, radicalized butane (i.e., C_4H_9) molecules are relaxed on fully and partially passivated (100) diamond surfaces in order to study the removal of H passivation from the diamond surface by hydrocarbon radicals. Furthermore, the chemical adsorption energies of hydrocarbon molecules and radicals on diamond, tungsten, and tungsten oxide surfaces with reactive sites are determined.

Tribometry Experiments and Characterization

Friction and wear measurements are conducted using an “on-line” tribometer, equipped with a force sensor, a holographic microscope, and an atomic force microscope, permitting the monitoring of topographical changes after each cycle. The instrument is described in detail elsewhere (Korres and Dienwiebel, 2010). The experiments are performed on a 99.9 wt.% tungsten plate in the “as-rolled” condition and polished down to an rms roughness of $34 \pm 4 \text{ nm}$ with no significant

influence on the near surface structure or the chemical composition (as verified by SEM and XPS analyses). A diamond sphere with a radius of 1.5 mm and a roughness of 1.2 nm was used as the counter surface. The experiments are performed with a sliding velocity of 5 mm/s and an initial normal load of 2 N in reciprocating slide mode. The worn surfaces (i.e., plates, tips, and wear material) are characterized by *ex situ* chemical and structural analyses using XPS, AES, and EELS. Lateral elemental concentration distributions are also obtained by parallel imaging XPS.

RESULTS AND DISCUSSION

Reactive Classical Molecular Dynamics Study of Hydrocarbon-Lubricated Tungsten/Diamond Systems

We used reactive classical molecular dynamics to investigate hexadecane-lubricated tungsten/diamond tribocouples. Since the typically experiments are performed under ambient conditions, contact is expected to mainly occur between passivated diamond surfaces and tungsten oxide counter surfaces. Unfortunately, current classical MD simulations are restricted to systems containing W-C-H (Juslin et al., 2005), since an accurate force field for W-C-O-H is not available yet. Therefore, in this section, simulations of hexadecane-lubricated tungsten/diamond tribopairs are presented with the intention of providing atomistic insights into the generic chemistry between hydrocarbon molecules in a sliding metal/diamond contact. In the next section, these results will be verified and extended to W-C-O-H systems using DFT simulations.

Figure 1 presents the results of our classical reactive MD simulations. Snapshots of the hydrocarbon-lubricated simulations with a bare W(100) surface and an H-terminated reconstructed diamond (100) surface are shown in **Figure 1A** at time instances during the initial pressurization phase ($t = 0.04$ ns), the subsequent shearing phase ($t = 4.5$ ns), and after the final separation ($t > 4.7$ ns) of the counter surfaces. The same instances for the case without H termination of the reconstructed diamond surface are shown in **Figure 1B**. Interestingly, in both cases—W(100)/C₁₆H₃₄/dia(100)H and W(100)/C₁₆H₃₄/dia(100)—a thin hydrocarbon film has formed on the diamond surface (see **Figures 1A,B** for $t > 4.7$ ns). We note that this film has a lower density for W(100)/C₁₆H₃₄/dia(100)H and that in this case, also the tungsten surface carries a chemisorbed hydrocarbon fragment.

The chemical reactions leading to the formation of these films can be described as follows. Upon pressurization and shearing of hydrocarbon molecules (such as C₁₆H₃₄) between a bare W(100) surface and a fully passivated diamond (100) surface, hydrogen atoms dissociate from the C₁₆H₃₄ chains and diffuse mainly into the uppermost layers of the tungsten [see the second snapshot at ($t = 4.5$ ns) in **Figures 1A,B**]. The sliding motion then occurs between the H-enriched uppermost W layers and the degraded hydrocarbon molecules. As shearing under high pressure continues, radical sites on the hydrocarbon chains are pushed against the diamond surfaces and react with

surface hydrogen atoms. This leads to partial dehydrogenation of the H-passivated diamond counter surface and results in the creation of dangling C bonds on the diamond. Eventually, radicalized hydrocarbon molecules bind to the diamond surface on these dangling C bonds *via* C–C covalent bonds. This can be clearly seen in **Figures 1C,D**, where the hydrocarbon molecules remain attached to the diamond surface after retraction of the counter surfaces. **Figure 1F** presents a close-up view of **Figure 1A**, highlighting the first H atoms that are dissociated from the C₁₆H₃₄ molecules and adsorbed on octahedral sites of the bcc tungsten surface. The first anchoring of a radicalized hydrocarbon on the partially dehydrogenated diamond (100) surface is displayed in **Figure 1G**. Interestingly, a large amount of lubricant H atoms has entered the tungsten lattice before the first hydrocarbon anchoring occurred. This indicates that many hydrocarbon molecules have already been radicalized before the anchoring reactions start.

The accumulation of hydrogen atoms within the tungsten lattice is a very clear sign that the original C₁₆H₃₄ molecules are significantly degraded under high-pressure shearing between bare tungsten and fully passivated diamond surfaces. Upon retraction of the sliding counterbodies, as shown in **Figure 1C**, the hexadecane chains remain bonded to the diamond surface, and most of the hydrogen atoms are located within the tungsten specimen. As expected, this phenomenon is more evident in the case of a non-hydrogen-terminated (and thus more reactive) diamond surface sliding against tungsten, where a higher number of dangling C bonds on the radicalized C₁₆H₃₄ chains can bond to dangling C bonds on the diamond surface (compare close-up image of the sliding interface in **Figure 1C** with that in **Figure 1D** where the diamond surface was not H terminated). These simulations show that during hydrocarbon-lubricated sliding between diamond and tungsten, the carbon-rich layer stemming from the lubricant attaches preferentially to the diamond counter surface with only very minor bonding onto the H-enriched tungsten surface.

The evolution of the shear stress τ and friction coefficient μ of the tungsten/diamond contacts is displayed in **Figure 1E**. For both the W(100)/C₁₆H₃₄/dia(100) and the W(100)/C₁₆H₃₄/dia(100)H sliding systems, the local friction coefficient $\mu = \frac{\tau}{p}$ exhibits an ultralow value of $\mu \approx 0.05$. Interestingly, in our classical MD simulations, the tungsten surface does not form any mixed WC phase in the presence of a hydrocarbon lubricant. If this were to happen, the hydrocarbon lubricant molecules would be consumed by the W surface and cold welding would lead to much higher friction coefficients.

Before we turn to the experimental investigation of a hexadecane-lubricated tungsten/diamond contact, a critical assessment of our classical simulations is in order. Since these experiments are performed under ambient conditions, oxygen atoms from atmospheric O₂ and H₂O are expected to play an important role. Unfortunately, we are currently not able to reliably model oxygen with classical reactive molecular dynamics, and therefore, more advanced simulation tools are needed to elucidate the degree of hydrocarbon radicalization and bonding between hydrocarbon radicals and reactive sites on tungsten oxide surfaces.

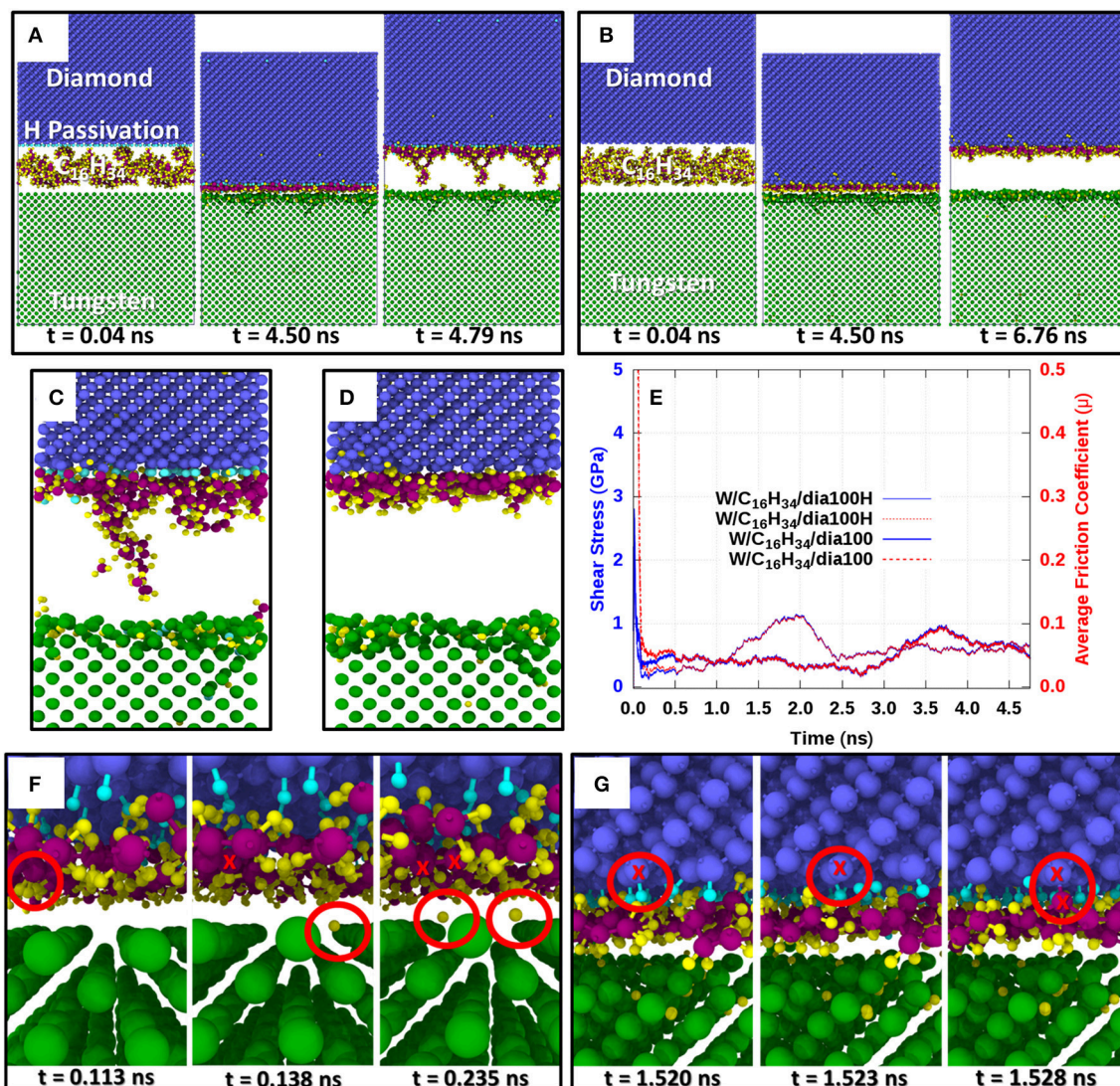


FIGURE 1 | Classical molecular dynamics simulations of hexadecane-lubricated tungsten/diamond tribocouples. Diamond carbon atoms are colored in blue, W atoms in green, H atoms in yellow, hexadecane C atoms in purple, and H atoms terminating the diamond surface in cyan. The lower surface is always a bare tungsten (100) surface. **(A)** Evolution of the lubricated tribocouple with H termination of the reconstructed diamond (100) surface $W(100)/C_{16}H_{34}/dia(100)H$. **(B)** Evolution of the lubricated tribocouple without H termination of the reconstructed diamond (100) surface $W(100)/C_{16}H_{34}/dia(100)$. **(C,D)** Close-up views of the contact interface after retraction for the cases in **(A)** and **(B)**, respectively. The plot in **(E)** shows the evolution of shear stress (solid blue lines) and coefficient of friction (dotted red lines) for $W(100)/C_{16}H_{34}/dia(100)H$ and $W(100)/C_{16}H_{34}/dia(100)$. Close-up views of the initial chemical reactions observed for $W(100)/C_{16}H_{34}/dia(100)H$ are depicted in **(F)** and **(G)**. **(F)** Initial radicalization of $C_{16}H_{34}$ hydrocarbons after dissociation of H atoms while in sliding contact under high pressure (~ 10 GPa). **(G)** First bonding of radicalized hydrocarbons on the diamond surface after the dehydrogenation of the initially fully H-passivated diamond (100) surface.

Density Functional Theory Investigations of the Reactivity of Lubricated W and Diamond Surfaces

DFT electronic structure calculations were performed to verify the hydrocarbon radicalization, hydrogen diffusion, and subsequent bonding of hydrocarbon radicals to the diamond observed in our classical MD simulations. Of course, DFT MD sliding simulations with system sizes and simulation times similar to those in the classical MD simulations are impossible with current computer resources. However, we can

perform quasi-static pressure relaxation DFT simulations with chemically similar but smaller hydrocarbon molecules confined between diamond and W surfaces at different normal pressures. Under these conditions, the radicalization of hydrocarbons under high pressure and the subsequent bonding of the radicalized molecules on the counter surfaces can be studied. It is already expected that compressing hydrocarbon molecules between non-passivated diamond surfaces will result in a high reactivity between the molecules and the surface, which would include generation of radicals and bonding of these

radicals on the dangling bonds of the diamond surface. This uninteresting case was not simulated here. Instead, the lower limit of surface reactivity was considered by studying hydrogen-passivated diamond (100) surface as well as a bare tungsten (100) surface.

First, **Figure 2A** shows the DFT relaxation of butane molecules (C_4H_{10}) between reconstructed and fully H-passivated diamond (100) surfaces. In this case, it is impossible to generate hydrocarbon radicals by increasing the contact pressure up to ~ 69 GPa, where the simulations are stopped. Conversely, as shown in **Figure 2B**, successively compressing butane between bare W(100) surfaces results in the generation of hydrocarbon radicals and in the adsorption of the dissociated H atoms on the tungsten surfaces for pressures below 10 GPa. We note that the radical formation is observed in the DFT simulations without thermal activation, such that the critical pressure for radical formation obtained in the quasi-static calculations is an upper limit for the critical pressure at finite temperature. Recall that the classical MD simulations presented in **Figure 1** show that once H atoms are dissociated from the hydrocarbon chains, the majority of these freed H atoms preferentially occupy interstitial sites close to the tungsten surface. Hence, a bare tungsten surface is able to radicalize hydrocarbon molecules and absorb and retain dissociated H atoms within its lattice. This verifies the hydrocarbon radicalization and H absorption predicted by the classical MD simulations in **Figure 1**.

In addition, the classical simulations in **Figure 1** predict that once hydrogen atoms are dissociated from the lubricant, the radicalized hydrocarbon molecules bond onto dangling C bonds of the diamond surface. These predictions are also verified by the formation energies presented in **Figures 2C–F**. Even in the extreme case of a fully reconstructed and H-passivated (100) diamond surface, the radicalized molecules can remove H atoms from the diamond surface as indicated by the 0.11-eV formation energy shown in **Figure 2C**. Here, a positive formation energy indicates an exothermic reaction. If there are dangling C bonds on the diamond (100) surface, the radicalized hydrocarbons can bond to the diamond surface through C–C covalent bonds with significant gains in energy. As shown in **Figure 2D**, if the hydrocarbon molecule is radicalized due to an H atom vacancy at the end of the molecule, there is an exothermic energy gain of 4.16 eV, while as shown in **Figure 2E**, if the radical site is in the middle of the hydrocarbon molecule, the exothermic energy gain is slightly reduced to 3.33 eV. Both of these energy values are significantly higher than the highest exothermic energy gain of 1.44 eV obtained by bonding a radical hydrocarbon (with an H missing at the tail of the molecule) on a hydrogen-saturated W(100) surface, as shown in **Figure 2E**. Even in the case of a W surface without any adsorbed H, the exothermic formation energy gain of 2.64 eV is still significantly lower than that of the diamond surface. These energy values indicate that radical hydrocarbons are preferentially bonded onto the diamond surface when the other counter surface is a bare W surface as in the classical MD simulations presented in **Figure 1**.

Density Functional Theory Investigations of the Reactivity of Lubricated WO_3

In experiments under ambient conditions, most of the tungsten surface is covered by tungsten oxide (WO_3), which means that hydrocarbon molecules would be compressed between a WO_3 and a diamond surface. This situation could not be modeled with classical MD; however, it can be investigated quasi-statically with DFT. If hydrocarbon molecules are compressed between (100) WO_3 surfaces with an oxygen-deficient pure W termination or a stoichiometric $\frac{1}{2}$ ML coverage with additional oxygen ions, no hydrocarbon radicalization was observed with pressures up to 12 GPa (i.e., the yield stress of pure crystalline WO_3), where plastic deformation starts to occur within WO_3 (not shown here). However, as displayed in **Figure 3A**, as soon as an oxygen coverage beyond $\frac{1}{2}$ ML is simulated, hydrocarbon radicalization evolves quickly at relatively low pressures of approximately 1.5 GPa (metallic W required 10 GPa before hydrocarbon radicalization). Therefore, on the tungsten/tungsten oxide side of the tribocouple, the most likely sources of hydrocarbon radicalization are the highest tungsten oxide asperities, followed by exposed patches of pure tungsten (presumably generated by wear events). Hydrocarbon radicalization on the diamond side of the tribocouple could also occur at exposed patches of non-passivated diamond at asperity peaks. However, since diamond is the harder material in the tribocouple and if the system is in a humid environment, the diamond surface is expected to remain mostly passivated with only a few sites with dangling C bonds where hydrocarbon radicals or free H atoms could quickly bond. Therefore, we expect the tungsten/tungsten oxide side of the tribocouple to be the main driver of hydrocarbon radicalization.

It is also important to look into the ability of WO_3 surfaces to adsorb hydrocarbon radicals. **Figures 3B–D** shows the energies for the adsorption of a C_4H_9 radical (with an H missing on a tail) on an oxygen-deficient, a stoichiometric oxygen-saturated, and a fully oxygen-saturated WO_3 (100) surface with exothermic energy gains of 1.32, 2.02, and 1.82 eV, respectively. Comparing these formation energies with those in **Figure 2**, it can be concluded that in a hydrocarbon-lubricated tungsten/diamond contact, radicalized hydrocarbon molecules are more strongly adsorbed on dangling carbon bonds of the diamond surface, but these radicals can also react with the tungsten side by bonding directly to the tungsten oxide surface. In case of a stoichiometrically O-terminated WO_3 (100) surface, the radicalization and subsequent adsorption of a butane molecule *via* a C–O bond is slightly exothermic with a reaction energy of 0.27 eV (see **Figure 3E**). Interestingly, as shown in **Figure 3F**, the radicalization and bonding of the radical *via* a C–OH group on a WO_3 surface with slightly overstoichiometric O coverage (i.e., $\frac{1}{2}$ ML + 1 O-ion coverage; see **Figure 3F**) result in a significant exothermic energy gain of 4.40 eV. However, as shown in **Figure 3G**, this molecule can be easily desorbed as a C_4H_9OH molecule with a modest energy cost of 0.67 eV. Hence, the presence of tungsten oxide surfaces can lead to the addition of oxygen-containing functional groups to the hydrocarbon lubricant molecules, which after a subsequent radicalization could be transferred to the diamond surface. This

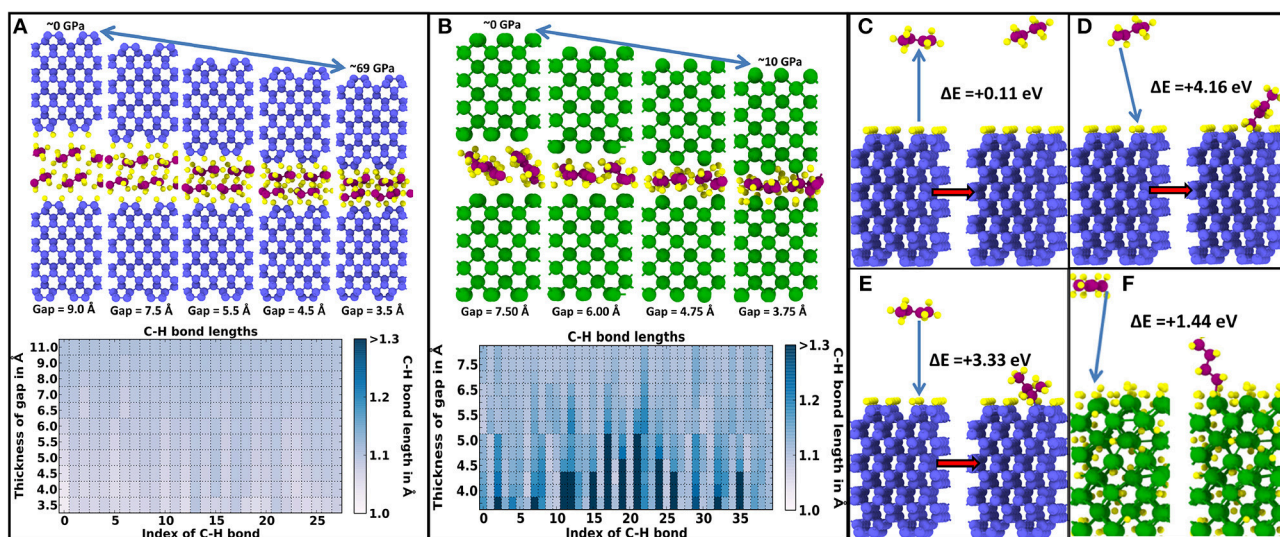


FIGURE 2 | Density functional theory (DFT) quasi-static pressure relaxation simulations showing the activation and sometimes radicalization of butane (C_4H_{10}) molecules confined between diamond (100) and W (100) surfaces. Coloring of atoms is as follows: diamond C atoms are blue, H atoms yellow, butane C atoms purple, and W atoms green. **(A)** Stability of hydrocarbon C_4H_{10} molecules indicated by an almost constant C–H bond length between molecules confined between reconstructed H-passivated (100) diamond surfaces. **(B)** Progressive elongation and eventual breaking of some C–H bonds in the C_4H_{10} molecules with decreasing gap separation between bare W(100) surfaces. In **(A)** and **(B)**, the top panel shows selected snapshots with decreasing interface gap (i.e., increasing pressure), while the bottom panel shows the elongation of each C–H bond with decreasing interface gap. **(C)** Energy gain during proton transfer from a diamond (100) surface to a C_4H_9 radical. **(D)** Adsorption of a $CH_2C_3H_7$ radical (with an H missing on a tail group) on a diamond (100) surface with one dangling C bond. **(E)** Adsorption of a $CH_3-CH-C_2H_5$ radical (with one H missing on an inner C group) on a diamond (100) surface with one dangling C bond. **(F)** Adsorption of a $CH_2C_3H_7$ radical (with an H missing on a tail group) on a hydrogen-saturated tungsten (100) surface.

would result in a hydrocarbon film on the diamond tribopartner that contains oxygen.

Friction and Wear Experiments

Tribological experiments with hexadecane-lubricated tungsten/diamond interfaces were conducted to compare with the atomistic simulations presented above. The evolution of the friction coefficient and wear rate during hexadecane-lubricated sliding of diamond against tungsten is presented in **Figure 4A**. In the experiments, the coefficient of friction remains relatively low and constant with an average value of $\mu \sim 0.05$ despite the fact—as we know from earlier studies—that the experiments are conducted in the mixed or boundary lubrication regime (Stoyanov et al., 2013b). Interestingly, nearly no running-in phase was observed, which could be attributed to the low initial roughness and/or the filling-in of the contact interface by lubricant molecules. This hydrocarbon-induced reduction in friction is typical for lubricated metal/diamond contacts (Mehan and Hayden, 1981). The initial wear rate of ~ 23 nm/m as measured through topography maps quickly decreased to a value of < 0.7 nm/m at the 1,000th cycle. Inset images of the wear track after 50 and 1,000 cycles are shown in **Figure 4A**.

XPS *ex situ* analysis of the worn diamond surface after the test in **Figure 4A** is presented in **Figure 4B**. The XPS depth profile in **Figure 4B** indicates predominately carbon with some small traces of oxygen. The SEM inset image of the diamond tip displayed in **Figure 4B** clearly indicates a certain degree of material transfer. To further investigate this material transfer, EELS analysis is

performed on the transferred material on the worn diamond tip. **Figure 4C** presents the cross section of a particle as well as EELS elemental mapping that indicates a high carbon content, some traces of oxygen, and a small amount of tungsten. The transfer of oxygen and tungsten provides evidence that there is material transfer from the tungsten surface to the diamond tip. The high carbon content observed as transfer material on the diamond tip most likely originates from the hydrocarbon molecules that degrade and bond to the diamond tip. However, the possibility of formation of an amorphous carbon layer emerging from the diamond itself cannot be excluded by *ex situ* XPS and EELS analysis of the diamond tip alone. Nevertheless, as indicated by the atomistic simulations above, the hydrocarbon molecules can be easily degraded when in contact with bare tungsten and tungsten oxide surfaces under high pressure, and these radicalized molecules can then bond most favorably on reactive sites on the diamond surface. The apparent pressure in the experiments was on the order of MPas. However, the local pressures at asperity level are expected to be on the order of GPas. A g_{rms} of 0.004 was measured for the polished tungsten plate, which, based on Persson's theory (Persson, 2006), predicts an average pressure of 1 GPa at the asperity level. Keeping in mind that there is a distribution of asperity pressure around an average value of 1 GPa, we also expect pressure at the asperity level well above 1 GPa (i.e., up to 10 GPa).

Next, we report the chemical analysis of the tungsten surface. **Figure 5A** presents an SEM image of the wear track on the tungsten plate after hexadecane-lubricated sliding against

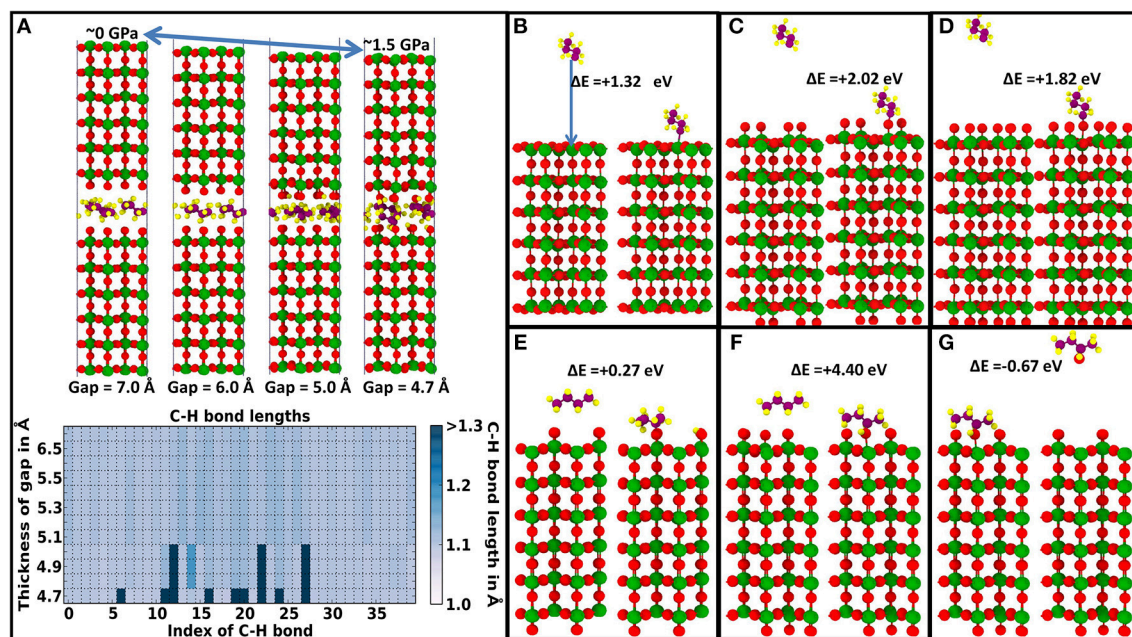


FIGURE 3 | Radicalization and adsorption of hydrocarbon molecules on WO_3 surfaces. Coloring of atoms is as follows: W atoms are green, O atoms red, H atoms yellow, and hydrocarbon C purple. **(A)** DFT quasi-static pressure relaxation showing the sudden elongation and breaking of some C–H bonds in butane (C_4H_{10}) molecules with increasing pressure between reactive WO_3 surfaces. In **(A)**, the top panel shows selected snapshots with decreasing interface gap (i.e., increasing pressure), while the bottom panel depicts the elongation of each C–H bond with decreasing interface gap. Adsorption of a $\text{CH}_2\text{--C}_3\text{H}_7$ radical (an H missing at the tail) on **(B)** an oxygen-deficient purely W-terminated WO_3 (100) surface, **(C)** a stoichiometrically (i.e., $\frac{1}{2}$ ML O-ion coverage) oxygen-saturated WO_3 (100) surface, and **(D)** a fully oxygen-saturated WO_3 (100) surface. Generation of a $\text{C}_2\text{H}_5\text{CHCH}_3$ radical (a missing H atom in the interior) and its adsorption after dissociation of an H atom from a C_4H_{10} molecule on **(E)** a stoichiometrically O-terminated (i.e., $\frac{1}{2}$ ML O-ion coverage) WO_3 (100) surface and **(F)** a WO_3 (100) surface with one more O-ion than stoichiometrically necessary (i.e., $\frac{1}{2}$ ML + 1 O-ion coverage). **(G)** Desorption energy of a $\text{C}_4\text{H}_9\text{OH}$ molecule from a WO_3 surface with $\frac{1}{2}$ ML + 1 O oxygen [after the adsorption event shown in **(F)**].

diamond. The AES analysis maps in **Figure 5B** clearly show an increase in the oxide content on the worn surface compared to the unworn surface, which is typical for metallic sliding contacts and has been reported numerous times (Rigney, 2000; Fu et al., 2003; Scherge et al., 2003; Stoyanov et al., 2013a). Interestingly, the carbon content is noticeably higher in the worn regions compared to the unworn ones. To provide a better understanding of this carbon-based layer (i.e., increased carbon concentration) in the case of the lubricant, we looked at the bonding behavior of the carbon on the tungsten surface using XPS detail analysis as shown in **Figure 5C**. The analysis suggests that all carbon atoms, not bound inside aliphatic hydrocarbon chains, are predominantly bonded to oxygen without any evidence of carbon bonding with tungsten *via* C–W bonds as in tungsten carbide. Conversely, the oxygen is also bonded with tungsten in the form of WO_3 on the surface of the tungsten specimen. It is likely that the increased oxide content on the worn surface promotes the formation of the carbon-based layer on the worn surface. The carbon-based layer found on the W surface after lubricated sliding most likely stems from the hydrocarbon molecules rather than the diamond tip as suggested by our DFT simulations.

The DFT simulations verified the formation of a hydrocarbon film on the diamond counter surface and additionally showed

that hydrocarbon molecules can radicalize and chemisorb *via* C–O bonds on WO_3 surfaces, suggesting that the lubricant-derived hydrocarbon films also form on tungsten counter surfaces with WO_3 passivation. These processes are summarized in graphical form in **Figure 6** by presenting one possible reaction path starting from a worn W/ WO_3 surface, a passivated diamond surface, and pristine hydrocarbon lubricant molecules between the tungsten/diamond interface (**Figure 6A**). Next, as sketched in **Figure 6B**, the hydrocarbon molecules are radicalized as they are sheared under high pressures against patches of WO_3 and W on the worn tungsten surface. Once several hydrocarbon molecules have been radicalized and as shearing under high pressure continues (**Figure 6C**), these hydrocarbon radicals can remove some of the H atoms or OH groups from the passivated diamond surface. Subsequently, the other radicals can covalently bond to the diamond surface at sites with dangling C bonds (**Figure 6D**).

Finally, we note that we could not perform the DFT simulations with hexadecane $\text{C}_{16}\text{H}_{34}$ molecules because DFT simulations are computationally very expensive and typically limited to a few 100 atoms. However, we also note that even though the DFT simulations were performed with short hydrocarbon molecules (i.e., butane C_4H_{10}), we expect a very similar reaction process for longer hydrocarbon molecules (i.e.,

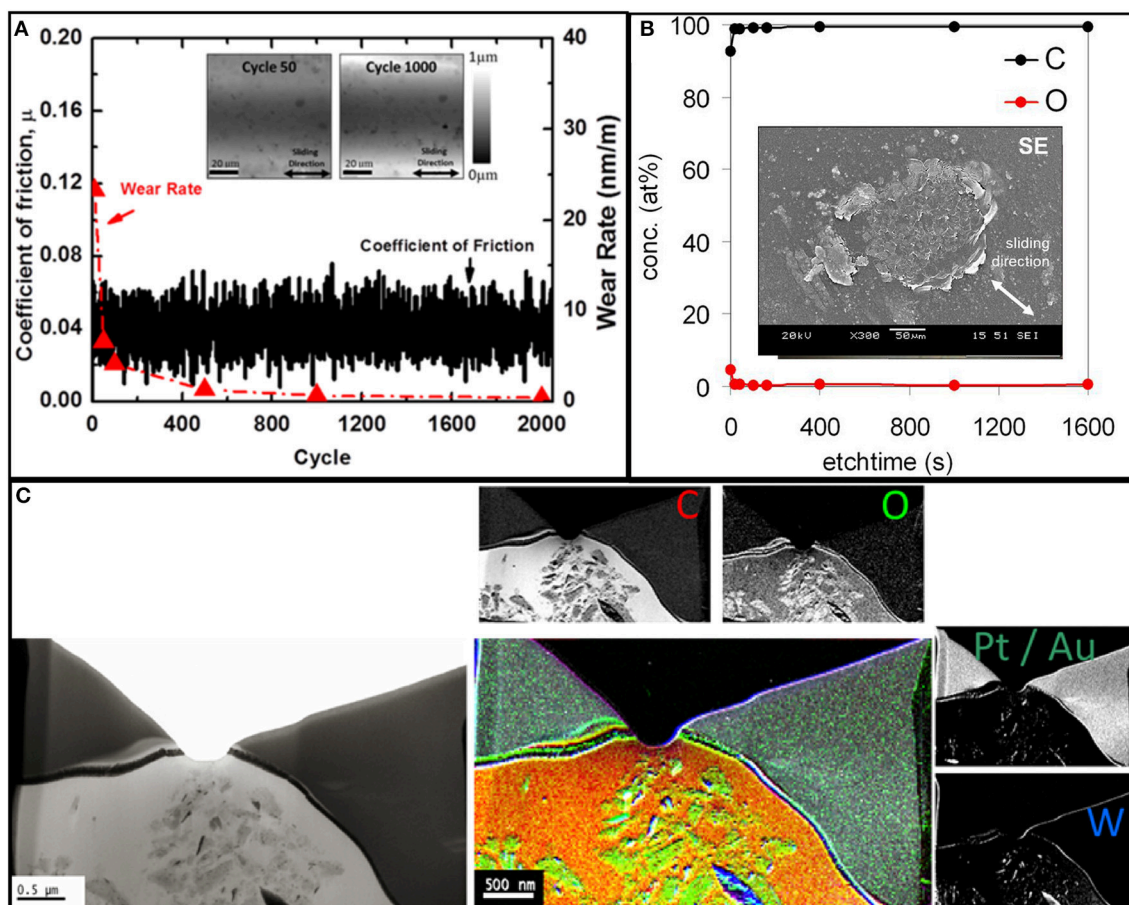


FIGURE 4 | (A) Coefficient of friction and wear rate vs. cycle for diamond sliding against tungsten under hexadecane-lubricated conditions. The inserts show images of the wear track after 50 and 1,000 cycles obtained using the on-line tribometer. Chemical analysis of the worn diamond surface with **(B)** showing an X-ray photoelectron spectroscopy (XPS) depth profile of the worn diamond surface with an SEM inset of the diamond surface after sliding. **(C)** Electron energy loss spectroscopy (EELS) analysis of a wear material particle on the diamond counter surface generated during sliding.

hexadecane $C_{16}H_{34}$). To provide some evidence for this, we calculated the radical formation energy for both C_4H_{10} and $C_{16}H_{34}$ molecules. An endothermic radical formation energy value of 2.07 eV was obtained for both C_4H_{10} and $C_{16}H_{34}$ for dehydrogenation in the middle of the molecular chain. For dehydrogenation at the tail end of the molecular chain, endothermic radical formation energy values of 2.26 and 2.25 eV were obtained for C_4H_{10} and $C_{16}H_{34}$, respectively. This is a good indication that C_4H_{10} and $C_{16}H_{34}$ will undergo a very similar radicalization process when sheared under high pressure between diamond/W/ WO_3 sliding interfaces. Additionally, in a different study (Kuwahara et al., 2019), short $C_7H_{12}O_2$ and long $C_{18}H_{34}O_2$ acid molecules, which have different molecular lengths but the same reactive centers, were investigated using tight binding, which is computationally less expensive than DFT. In that study, it was shown that short cis-heptanoic acid ($C_7H_{12}O_2$) molecules undergo very similar tribochemical reactions as the longer oleic acid ($C_{18}H_{34}O_2$) molecules during shearing under high pressure between sliding ta-C counter surfaces. Therefore, we expect C_4H_{10} and $C_{16}H_{34}$ confined between diamond/W/ WO_3 surfaces

to follow very similar reaction paths with only minor differences in the pressure and energy required for the reactions.

CONCLUSION

Lubricated metal/diamond contacts exhibit noticeably low friction (Mehan and Hayden, 1981); however, the atomistic mechanisms for this phenomenon are still unclear. Here, we investigated the interfacial tribochemical mechanisms leading to low friction in lubricated tungsten/diamond sliding contacts using reactive atomistic simulations and an on-line tribometer linked to chemical analysis. First, reactive classical molecular dynamics simulations of tungsten (100) sliding against diamond (100) under high pressure revealed the radicalization of hydrocarbon molecules by proton transfer to the tungsten surface and their subsequent chemisorption onto dangling C bonds on the diamond surface. This results in the formation of hydrocarbon films that chemisorb on the diamond surface. Despite the small number of lubricant molecules between the tungsten and the diamond surface, an ultralow friction of $\mu =$

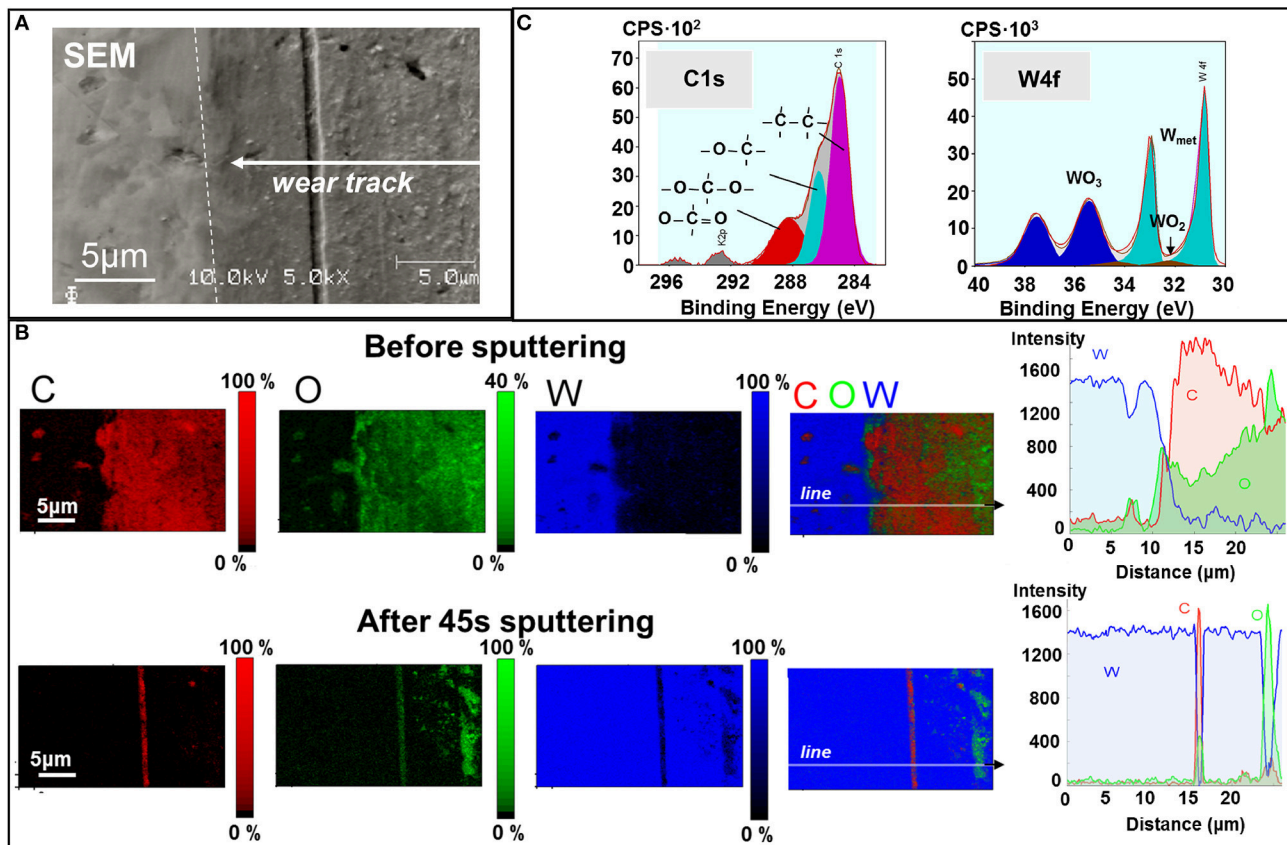


FIGURE 5 | Chemical analysis of the worn tungsten surface after hexadecane-lubricated sliding. **(A)** SEM image of the wear track on the tungsten counter surface. **(B)** Auger electron spectroscopy (AES) mapping and XPS of the wear track before and after 45 s of sputtering. **(C)** XPS detail spectra and binding states on the wear track.

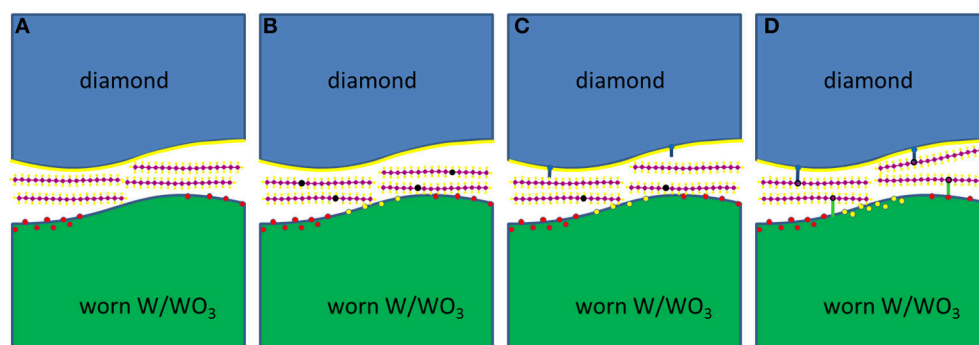


FIGURE 6 | Schematic of a probable reaction path for the radicalization and chemical adsorption of hydrocarbon molecules between W/diamond and WO_3 /diamond sliding interfaces. **(A)** Sliding of diamond against the tungsten counterbody under high loads results in wear of the WO_3 material that passivates the tungsten surface. This creates reactive patches of worn W and/or WO_3 . **(B)** These reactive sites can then easily radicalize the initially saturated hydrocarbon molecules. **(C)** The radicalized molecules can then remove passivating H atoms (or OH groups) from the diamond surface, resulting in the creation of reactive sites on the diamond surface. **(D)** The remaining radical molecules can then bond onto reactive sites on the diamond surface or on the worn W/ WO_3 surface. The preferential bonding of the radicals on the diamond and WO_3 surfaces can eventually result in the formation of hydrocarbon layers attached to the diamond and WO_3 surfaces, while desorption of the absorbed molecules on WO_3 sites can result in the formation of molecules with O and/or OH groups, which can eventually also be adsorbed onto the diamond surface.

0.05 was recorded in the classical MD simulations. This very low friction resistance is a direct result of the hydrocarbon film, since both the absence of lubricant reactions and the

formation of a WC film would result in cold welding and high friction. Quasi-static DFT calculations confirmed the classical MD results. Additional DFT calculations demonstrate that

hydrocarbon molecules can radicalize and chemisorb *via* C–O bonds on WO₃ surfaces, suggesting that the lubricant-derived hydrocarbon films also form on tungsten counter surfaces with WO₃ passivation. Our on-line tribometer experiments confirm the scenario derived from the classical and DFT simulations. In the simulation as well as in the experiment, ultralow friction of tungsten/diamond sliding contacts under C₁₆H₃₄ lubrication was observed. Furthermore, *ex situ* chemical analysis by means of XPS, EELS, and AES reveals evidence of the formation of a carbon-rich tribofilm on the diamond and tungsten oxide surfaces as predicted by the atomistic simulations. That no signs of the formation of WC phases were found is also in agreement with our classical MD results.

We believe that the tribochemical mechanisms reported in this article are transferable to other lubricated metal/diamond pairings such as, e.g., steel/diamond combinations. There is experimental evidence in the context of *white etching crack* research that steel is also able to abstract hydrogen from mineral oils (Kuerten et al., 2016). Therefore, it is likely that the ultralow friction coefficients recorded by Mehan and Hayden (1981) for steel/diamond pairings originate from *in situ* tribochemical formation of low-friction hydrocarbon films. These films should be extremely effective under boundary lubrication conditions: while free lubricant molecules can be squeezed out of asperity contacts, chemisorbed films stay in the contact and prevent cold welding and high friction. Of course, further research for other

metal/diamond combinations is now in order. The methodology and the results in this article will prove a useful guide for such future investigations.

DATA AVAILABILITY

The datasets generated for this study are available on request to the corresponding author.

AUTHOR CONTRIBUTIONS

All authors listed have made a substantial, direct and intellectual contribution to the work, and approved it for publication.

ACKNOWLEDGMENTS

We thank the Deutsche Forschungsgemeinschaft for financial support under contracts FI451, MO879, SCH425, and KO 120/12-1, as well as CRC 926 (MICOS) and DI1494. The authors would also like to thank Dr. Alfons Fischer and Dr. Alexander Brodyanski for the helpful discussions. Finally, we gratefully acknowledge the computing time granted under project-aticsi at KIT HLRII and under project No. hfr09 on the supercomputer JUROPA for some of the classical MD simulations, and under project no. hfr04 on the supercomputer JURECA for the DFT calculations at NIC Jülich Supercomputing Center.

REFERENCES

- Blöchl, P. E. (1994). Projector augmented-wave method. *Phys. Rev. B* 50, 17953–17979. doi: 10.1103/PhysRevB.50.17953
- Esser, J., Linde, R., and Münchow, F. (2004). Diamond-reinforced running surface for combustion rings. *MTZ Worldw.* 65, 27–28. doi: 10.1007/BF03227689
- Fu, X. Y., Rigney, D. A., and Falk, M. L. (2003). Sliding and deformation of metallic glass: experiments and MD simulations. *J. Non Cryst. Solids* 317, 206–214. doi: 10.1016/S0022-3093(02)01999-3
- Groot, R. D., and Warren, P. B. (1997). Dissipative particle dynamics: bridging the gap between atomistic and mesoscopic simulation. *J. Chem. Phys.* 107, 4423–4435. doi: 10.1063/1.474784
- Hohenberg, P., and Kohn, W. (1964). The inhomogeneous electron gas. *Phys. Rev.* 136, B864. doi: 10.1103/PhysRev.136.B864
- Juslin, N., Erhart, P., Träskelin, P., Nord, J., Henriksson, K., Salonen, E., et al. (2005). Analytical interatomic potential for modeling nonequilibrium processes in the W–C–H system. *J. Appl. Phys.* 98:123520. doi: 10.1063/1.2149492
- Kennedy, M., Hoppe, S., and Esser, J. (2014). Lower friction losses with new piston ring coating. *MTZ Worldw.* 75, 24–29. doi: 10.1007/s38313-014-0135-7
- Kim, Y., Park, H., An, J. U., Kan, T.-S., and Park, J. (2011). Development of nano diamond polymer coating on piston skirt for fuel efficiency. *SAE Int. J. Engines* 4, 2080–2086. doi: 10.4271/2011-01-1401
- Kohn, W., and Sham, L. J. (1965). Multiple pilomatricoma with perforation. *Phys. Rev.* 140, A1133–A1138. doi: 10.1103/PhysRev.140.A1133
- Korres, S., and Dienwiebel, M. (2010). Design and construction of a novel tribometer with online topography and wear measurement. *Rev. Sci. Instrum.* 81:063904. doi: 10.1063/1.3449334
- Kresse, G., and Hafner, J. (1993). *Ab initio* molecular dynamics for liquid metals. *Phys. Rev. B* 47, 558–561. doi: 10.1103/PhysRevB.47.558
- Kresse, G., and Hafner, J. (1994). *Ab initio* molecular-dynamics simulation of the liquid–metal–amorphous–semiconductor transition in germanium. *Phys. Rev. B* 49, 14251–14269. doi: 10.1103/PhysRevB.49.14251
- Kresse, G., and Joubert, D. (1999). From ultrasoft pseudopotentials to the projector augmented-wave method. *Phys. Rev. B* 59, 1758–1775. doi: 10.1103/PhysRevB.59.1758
- Kuerten, D., Winzer, N., Kailer, A., Pfeiffer, W., Spallek, R., and Scherge, M. (2016). *In-situ* detection of hydrogen evolution in a lubricated sliding pin on disk test under high vacuum. *Tribol. Int.* 93, 324–331. doi: 10.1016/j.triboint.2015.07.028
- Kuwahara, T., Romero, P. A., Makowski, S., Weihnacht, V., Moras, G., and Moseler, M. (2019). Mechano-chemical decomposition of organic friction modifiers with multiple reactive centres induces superlubricity of ta-C. *Nat. Commun.* 10:151. doi: 10.1038/s41467-018-08042-8
- Linsler, D., Kümmel, D., Nold, E., and Dienwiebel, M. (2017). Analysis of the running-in of thermal spray coatings by time-dependent stribeck maps. *Wear* 376–377, 1467–1474. doi: 10.1016/j.wear.2017.02.026
- Mehan, R. L., and Hayden, S. C. (1981). Friction and wear of diamond materials and other ceramics against metal. *Wear* 74, 195–212. doi: 10.1016/0043-1648(81)90163-0
- Pastewka, L., Moser, S., Gumbsch, P., and Moseler, M. (2011). Anisotropic mechanical amorphization drives wear in diamond. *Nat. Mater.* 10, 34–38. doi: 10.1038/nmat2902
- Pastewka, L., Moser, S., Moseler, M., Blug, B., Meier, S., Hollstein, T., et al. (2008). The running-in of amorphous hydrocarbon tribocoatings: a comparison between experiment and molecular dynamics simulations. *Zeitschrift Fuer Met. Res. Adv. Tech.* 99, 1136–1143. doi: 10.3139/146.101747
- Perdew, J. P., Burke, K., and Ernzerhof, M. (1996). Generalized gradient approximation made simple. *Phys. Rev. Lett.* 77, 3865–3868. doi: 10.1103/PhysRevLett.77.3865
- Persson, B. N. J. (2006). Contact mechanics for randomly rough surfaces. *Surf. Sci. Rep.* 61, 201–227. doi: 10.1016/j.surfrep.2006.04.001
- Rigney, D. A. (2000). Transfer, mixing and associated chemical and mechanical processes during the sliding of ductile materials. *Wear* 245, 1–9. doi: 10.1016/S0043-1648(00)00460-9

- Scherge, M., Shakhvorostov, D., and Pöhlmann, K. (2003). Fundamental wear mechanism of metals. *Wear* 255, 395–400. doi: 10.1016/S0043-1648(03)00273-4
- Stoyanov, P., Merz, R., Romero, P. A., Wählich, F. C., Abad, O. T., Gralla, R., et al. et al. (2015). Surface softening in metal-ceramic sliding contacts: an experimental and numerical investigation. *ACS Nano* 9, 1478–1491. doi: 10.1021/nn505968m
- Stoyanov, P., Romero, P. A., Järv, T. T., Pastewka, L., Scherge, M., Stemme, P., et al. (2013a). Experimental and numerical atomistic investigation of the third body formation process in dry tungsten/tungsten-carbide tribo couples. *Tribol. Lett.* 50, 67–80. doi: 10.1007/s11249-012-0085-7
- Stoyanov, P., Stemmer, P., Järvi, T. T., Merz, R., Romero, P. A., Scherge, M., et al. (2013b). Friction and wear mechanisms of tungsten-carbon systems: a comparison of dry and lubricated conditions. *ACS Appl. Mater. Interfaces* 5, 6123–6135. doi: 10.1021/am4010094
- Stoyanov, P., Stemmer, P., Järvi, T. T., Merz, R., Romero, P. A., Scherge, M., et al., et al. (2014). Nanoscale sliding friction phenomena at the interface of diamond-like carbon and tungsten. *Acta Mater.* 67, 395–408. doi: 10.1016/j.actamat.2013.12.029
- Venkateswarlu, K., Rajinikanth, V., Naveen, T., Sinha, D. P., Atiquzzaman, S., and Ray, A. K. (2009). Abrasive wear behavior of thermally sprayed diamond reinforced composite coating deposited with both oxy-acetylene and HVOF techniques. *Wear* 266, 995–1002. doi: 10.1016/j.wear.2009.02.001
- Wang, L., Gao, Y., Xue, Q., Liu, H., and Xu, T. (2005). Effects of nano-diamond particles on the structure and tribological property of Ni-matrix nanocomposite coatings. *Mater. Sci. Eng. A* 390, 313–318. doi: 10.1016/j.msea.2004.08.033
- Yin, S., Xie, Y., Cizec, J., Ekoi, E. J., Hussain, T., Dowling, D. P., et al. (2017). Advanced diamond-reinforced metal matrix composites via cold spray: properties and deposition mechanism. *Compos. Part B Eng.* 113, 44–54. doi: 10.1016/j.compositesb.2017.01.009

Conflict of Interest Statement: The authors declare that the research was conducted in the absence of any commercial or financial relationships that could be construed as a potential conflict of interest.

Copyright © 2019 Romero, Mayrhofer, Stoyanov, Merz, Kopnarski, Dienwiebel and Moseler. This is an open-access article distributed under the terms of the Creative Commons Attribution License (CC BY). The use, distribution or reproduction in other forums is permitted, provided the original author(s) and the copyright owner(s) are credited and that the original publication in this journal is cited, in accordance with accepted academic practice. No use, distribution or reproduction is permitted which does not comply with these terms.



Role of Interfacial Water and Applied Potential on Friction at Au(111) Surfaces

Leila Pashazanusi¹, Kai Kristiansen², Shaowei Li³, Yu Tian³ and Noshir S. Pesika^{1*}

¹ Department of Chemical and Biomolecular Engineering, Tulane University, New Orleans, LA, United States, ² Department of Chemical Engineering, University of California, Santa Barbara, Santa Barbara, CA, United States, ³ State Key Laboratory of Tribology, Tsinghua University, Beijing, China

OPEN ACCESS

Edited by:

Jacqueline Krim,
North Carolina State University,
United States

Reviewed by:

Hyun-Joon Kim,
Kyungpook National University,
South Korea
Martin H. Müser,
Saarland University, Germany

*Correspondence:

Noshir S. Pesika
npesika@tulane.edu

Specialty section:

This article was submitted to
Tribology,
a section of the journal
Frontiers in Mechanical Engineering

Received: 13 March 2019

Accepted: 06 June 2019

Published: 21 June 2019

Citation:

Pashazanusi L, Kristiansen K, Li S,
Tian Y and Pesika NS (2019) Role of
Interfacial Water and Applied Potential
on Friction at Au(111) Surfaces.
Front. Mech. Eng. 5:39.
doi: 10.3389/fmech.2019.00039

The tribological properties between an AFM tip and a Au(111) surface in an aqueous environment is influenced by an applied electrical potential. Using lateral force microscopy, we measure the resulting friction force, while simultaneously applying a pre-determined electrical potential on the Au surface via a three-electrode setup. Applying a positive potential to the Au surface forms an interfacial water layer at the Au/electrolyte interface, which sharply increases friction. However, when an anodic potential is applied, lower friction forces are measured. The potential dependent friction is observed on ultra-smooth gold surfaces as well as Au surfaces with larger roughness. An increase in the ionic strength of the electrolyte is found to lower friction. The use of an aqueous NaOH solution is found to lower the critical potential at which the friction sharply increases. Normal force curves are also measured as a function of approach velocity. The normal force linearly increases as the approach velocity increases in agreement with a drainage model. These results provide valuable insight into the effect of applied electrical potentials on the properties of water at charged surfaces and can potentially impact a wide range of fields including tribology, micro-electro-mechanical systems (MEMS), energy storage devices, fuel cells, and catalysis.

Keywords: nanotribology, interfacial (bound) water, electric field, hydrogen bonding, solid electrolyte interface (SEI)

INTRODUCTION

The study of molecular interactions between surfaces and colloids has been of great interest (Hugel and Seitz, 2001; Israelachvili, 2011; Balzer et al., 2013; Pashazanusi et al., 2017a) for several decades. A significant number of studies have been conducted aiming to better understand the tribological behavior of interfaces at the molecular scale (Mo et al., 2009; Schirmeisen and Schwarz, 2009; Balzer et al., 2013; Pérez, 2014; Weymouth et al., 2014). However, there are still unexplained phenomena and a clear understanding of nanoscale friction is yet to be achieved (Kim and Kim, 2009). AFM is a promising tool for acquiring diverse tribological information and understanding underlying mechanisms (Meyer et al., 1989; Overney and Meyer, 1993; Carpick and Salmeron, 1997). The ability to control and manipulate the frictional properties of a system at the nanoscale has resulted in numerous tribological studies (Park, 2011; Greiner et al., 2012; Gallagher et al., 2016). Controlling small-scale friction during sliding has potential application in a variety of areas

including nano/micro-electro-mechanical systems (NEMS/MEMS) (Kim et al., 2007; Achanta and Celis, 2015). The application of external stimuli, which enables reversible modification of interfacial properties, is an effective strategy to control and tune friction (Binggeli et al., 1993; Park et al., 2006; Karuppiyah et al., 2009). Particularly, application of the electrical potential has been shown to influence the tribological behavior at interfaces in various solutions (Labuda et al., 2011; Sweeney et al., 2012; Strelcov et al., 2015).

Within a few nanometers away from an electrode surface, water rearranges into a highly confined structure (Kim et al., 2003; Khan et al., 2010; Velasco-Velez et al., 2014), showing unique physical properties different from those of bulk water (Lee and Rossky, 1994; Toney et al., 1994; Dhinojwala and Granick, 1997; Raviv and Klein, 2002). For instance, the effective viscosity of water layers extended up to 5 nm away from an electrode surface has been found to increase dramatically upon applying a positive potential (Antognozzi et al., 2001; Xie et al., 2009; Guriyanova et al., 2011; Plausinaitis et al., 2014). Guriyanova et al. (2011) reported that the effective viscosity of water layers at positively charged electrode surfaces can be on the order of 10^6 – 10^7 larger compared to bulk water. The influence of the highly ordered and confined water molecules on frictional properties of an electrode in the presence of an applied electrical potential have been the subject of several studies (Valtiner et al., 2012; Dhopatkar et al., 2016; Pashazanusi et al., 2017b). Dhopatkar et al. (2016) investigated the effect of a highly confined “ice-like” water layer on the friction of two surfactant coated surfaces sliding against each other. They found that increasing the concentration of a cationic surfactant, which absorbs as a monolayer on the shearing surfaces, lowered the coefficient of friction (CoF). Valtiner et al. (2012) investigated the potential dependent friction forces between a mica surface and a gold electrode. They performed experiments measuring the friction on a gold surface maintained at 0 V vs. Ag/AgCl and a positively charged gold surface (+0.4 V vs. Ag/AgCl). The latter surface exhibited higher kinetic friction compared to the neutral gold surface. They attributed the increase in friction to the formation of a viscous water layer at the positively charged electrode. However, the increase in the friction was relatively small because of the limited range of applied positive potential. Based on these previous studies, it has been inferred that water molecules can reorient in the presence of an applied electric field which in turn can influence interfacial normal and friction forces.

In our previous work, we presented an exploratory study on the effect of an applied potential on the friction force between an AFM tip and a gold electrode surface over a wider range of applied potentials (i.e., -0.6 to $+0.6$ V vs. Ag) (Pashazanusi et al., 2017b). We observed a reversible potential-dependent friction behavior on a gold electrode surface as the surface potential was increased. At $\sim +0.4$ V, a sharp increase in the friction forces was observed. The CoF between an AFM tip and a gold surface (see **Figure 1**) at the applied potential of $+0.6$ V was reported to be 26 times higher than that at the applied potential of -0.6 V. The drastic change in the CoF was attributed to the formation of an interfacial water layer (IWL) on a positively charged

electrode surface. However, there are several parameters in such electrochemical systems including the electrolyte concentration and composition that can possibly impact the properties and formation of the IWL.

This work is an extension of our previous work and provides a deeper understanding of how several experimental parameters (i.e., surface roughness, salt composition, and concentration) affect the tribological properties of a gold surface exposed to an applied electrical potential in an aqueous electrolyte solution. In addition, normal force measurements conducted at various approach velocities further support our hypothesis of the formation of a highly viscous water layer and are consistent with hydrodynamic drainage theory. These results provide a better understanding of the interactions between surfaces in the presence of an applied potential and can have a transformative impact in several areas of science including tribology, MEMs, energy storage devices, fuel cells, and catalysis.

EXPERIMENTAL

Preparation of Gold Electrode

Fifteen millimeter mica disks (Highest Grade V1 AFM Mica Disc) were purchased from Ted Pella, Inc. and utilized upon cleaving by a fresh sharp blade. Using thermal evaporation deposition (ATC Orion Sputtering System, AJA International, Inc.), the freshly cleaved mica was coated with a 5 nm Cr film, acting as an adhesion layer, topped with a 100 nm gold film. A uniform smooth gold film was obtained by maintaining a slow deposition rate (1 \AA/s) and a high vacuum ($\sim 10^{-6}$). The substrate was allowed to cool down in the chamber before rinsing with distilled water and drying in air. AFM was used to characterize the surface roughness of the gold substrate (rms ~ 3.5 nm) based on AFM images (**Figure 2A**).

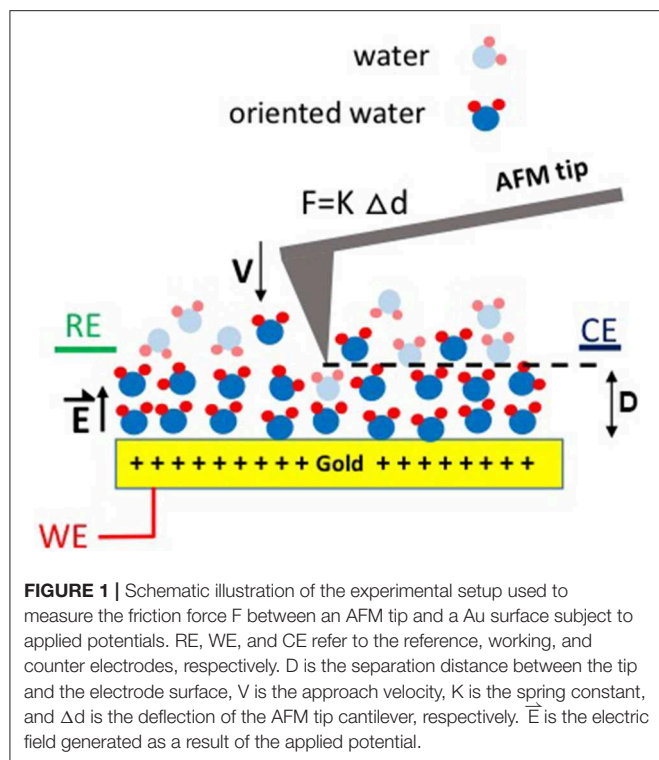
Preparation of Ultra-Smooth Gold Electrode

Atomically smooth gold surfaces were prepared using the mica templating method (Chai and Klein, 2007). First, a 42 nm gold film on mica was deposited in an electron-beam evaporation system. A muscovite mica sheet of 10 cm in diameter and a few 100 μm thick were freshly cleaved before the deposition to avoid any contamination. Second, pieces of $1.5 \times 1.5 \text{ cm}^2$ step-free regions of the gold-coated mica sheet were cut and silicon wafer pieces were cut in squares of $1 \times 1 \text{ cm}^2$. A few 100 μm thick layer of UV-curing glue (Norland 81) was applied on top of each clean silicon wafers piece in a laminar flood hood environment before carefully place the gold-coated mica pieces with the gold side facing down on the glue. The UV glue was cured for at least 2 h. Lastly, right before using the gold surface, the mica was peeled off the gold.

In both thermal evaporation and E-beam evaporation devices, a quartz crystal was used to calibrate, and control the deposition rate and the film thickness.

In situ Electrochemistry-AFM

A 3-electrode electrochemical cell was used to track changes in friction as a function of applied potential between the



AFM tip and the gold surface. The potential range was limited so as to prevent the oxidation of gold. A Au substrate, Pt mesh, and Ag wire served as the working, counter, and reference electrode, respectively. Electrochemical experiments were performed in different concentrations of aqueous NaCl (i.e., 1, 10mM, 0.1, and 1 M) to investigate the effect of salt concentration on friction forces. To explore the influence of ions on the potential-dependent friction, 0.1 M aqueous NaOH was used as an alternative electrolyte. In order to confirm that the electrochemical setup in the AFM experiments was reliable, similar electrochemical experiments were performed using a conventional PTFE electrochemical cell (Oguntoye et al., 2017).

Friction Measurements Using AFM

Friction forces were measured using atomic force microscopy (AFM) (Dimension Icon, Bruker) in lateral force friction (LFM) mode. An AFM probe (NTESP, Bruker) with a sharp tip (estimated radius 10 nm, height 15 μm , spring constant $K_c = 34 \text{ N/m}$) was used for the friction measurements on the gold substrates. Additionally, an AFM colloidal probe (CP-NCH-SiO₂, sQube, estimated diameter 10 μm , spring constant $K_c = 37 \text{ N/m}$) was used to measure force curves (i.e., normal forces as a function of separation distance between the colloidal probe and the gold surface).

The normal spring constant of the cantilever was calibrated by using the thermal tune technique in air and liquid. The lateral (or torsional) spring constant k_T of the cantilever was obtained by using the following equation: $k_T = Gwt^3/(3h^2l)$ where G , w , t , l

are the shear modulus, width, thickness, length of the cantilever, respectively, and h is tip height (Cannara et al., 2006). The normal sensitivity of the cantilever was obtained via measuring the slope of the vertical voltage signal vs. distance curve (Palacio and Bhushan, 2010). The lateral sensitivity of the cantilever was calculated by averaging the initial slope of the friction loop, in which the lateral voltage signal is plotted vs. lateral distance, in both forward and backward scan directions (Liu et al., 1996; Cain et al., 2000).

Friction was measured by recording the lateral deflection of the cantilever as the tip scanned the surface perpendicular to long axis of the cantilever (scan size of 500 nm and speed of 1 $\mu\text{m s}^{-1}$) while the electrical potential of the gold surface was varied. A method previously proposed in the literature (Schwarz et al., 1996) was used to convert the lateral voltage signal into quantitative friction forces. Friction loops were recorded from the same location.

Normal Force Measurement Using AFM

Atomic force microscopy Ramp mode was used to record normal forces vs. separation distance as a tip approaches the gold substrate followed by jumping into contact and then separates and retracts from the surface. To study the effect of the approach velocity on the normal force interactions, force-distance curves were obtained for approaching velocities of 50, 100, 200, 500, and 900 nm/s. A 200 nm ramp scan size was used in these experiments. The “Ramp mode” consists of the tip moving toward the surface at a pre-determined velocity until contact is achieved followed by separation at the same velocity. The total displacement, i.e., ramp size (which is correlated to the separation distance between the tip and the surface) can also be varied.

RESULTS AND DISCUSSION

Based on prior literature presented in the introduction and our past work (Pashazanusi et al., 2017b), we hypothesize that the underlying and dominant mechanism that modulates the friction force is hydrogen bonding between oriented IWLs and also between the IWLs and the AFM tip (and/or the hydration layer on the AFM tip). The results we present do not provide a direct evidence of the formation of IWLs, however they do support our hypothesis. Below we present our results and provide a discussion of the results with the assumption that hydrogen bonding is the underlying interaction that dominates this phenomenon. Our assumption is further supported by recent work which reproduced our results and further demonstrated that the ability of the tip to experience hydrogen bonding (i.e., a hydrophilic silicon oxide tip capable of hydrogen bonding showed a change in friction as a function of applied potential while a hydrophobic polystyrene tip not capable of hydrogen bonding did not experience any change in friction as a function of the applied potential) affected the friction forces (Li et al., 2018). **Figure 2A** shows the friction force between a sharp AFM tip and a gold surface as a function of the applied normal load under four different conditions: (i) on dry gold, (ii) on gold under aqueous conditions with no applied potential [i.e., open circuit potential (OCP)], (iii) on gold under aqueous conditions

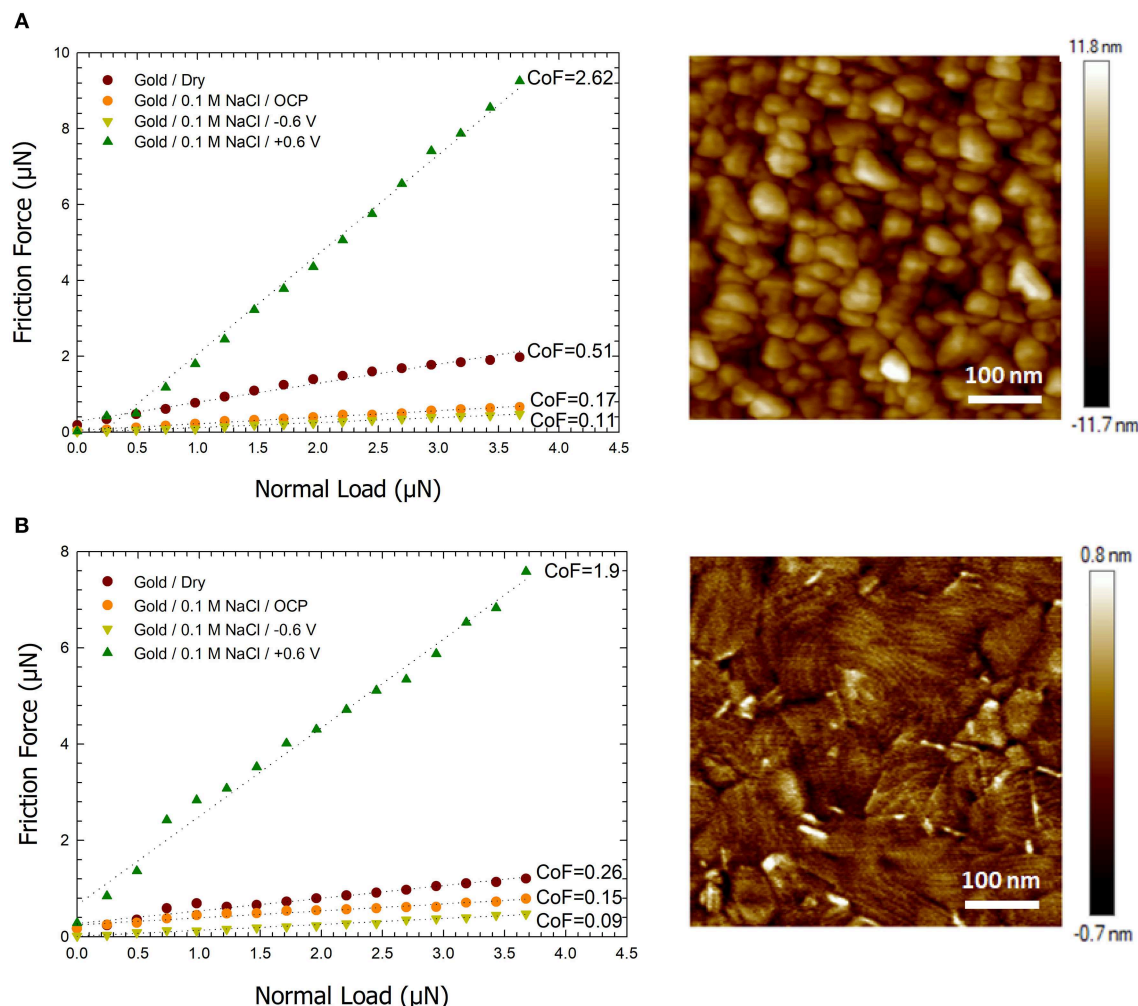
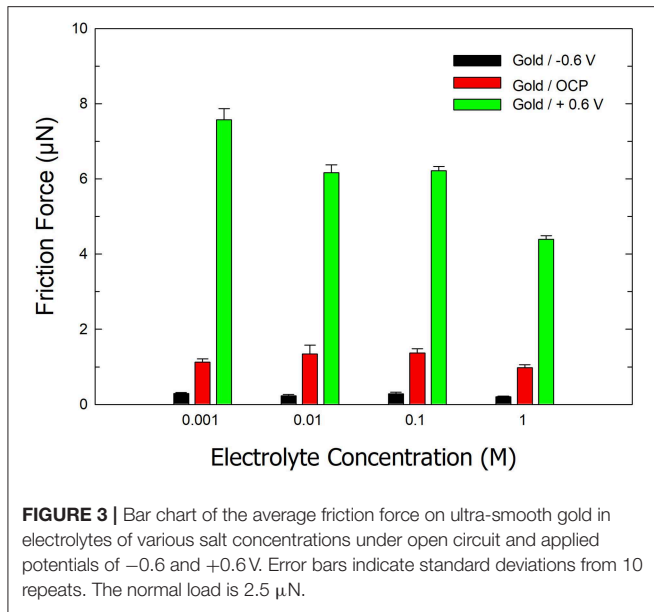


FIGURE 2 | Plots of the friction force vs. normal load for dry, open circuit, and applied potentials of -0.6 and $+0.6$ V between a sharp AFM tip and **(A)** a gold surface formed by sputtering **(B)** an ultra-smooth Au surface formed by e-beam deposition. The images to the right are AFM height images of the corresponding gold surfaces. A scan size of 500 nm and scan speed of $1 \mu\text{m} \cdot \text{s}^{-1}$ was used for friction measurements.

with a -0.6 V vs. Ag potential, and (iv) on gold under aqueous conditions with a $+0.6$ V vs. Ag potential. The friction force increases linearly with load in agreement with Amontons' law for all conditions. The CoF between the AFM tip and the gold surface under dry conditions is found to be ~ 0.51 which is in a similar range to previously reported values in the literatures (Antler, 1963). Under aqueous NaCl solution conditions and without applying a potential, the gold surface inherently gains a slight negative charge of -0.12 V (Pashazanusi et al., 2017b) and the CoF is lowered to 0.17. Under these conditions, the aqueous salt solution serves as a boundary lubricant thereby reducing the interaction between the AFM tip and the Au surface. Hydrogen bonding between the AFM tip and the IWL is still present. By applying a negative potential on the Au surface, the number of broken hydrogen bonds increases (Velasco-Velez et al., 2014; Pashazanusi et al., 2017b), which in turn decreases the attractive interaction between the tip and the IWLs. Thus, under aqueous conditions with a -0.6 V applied

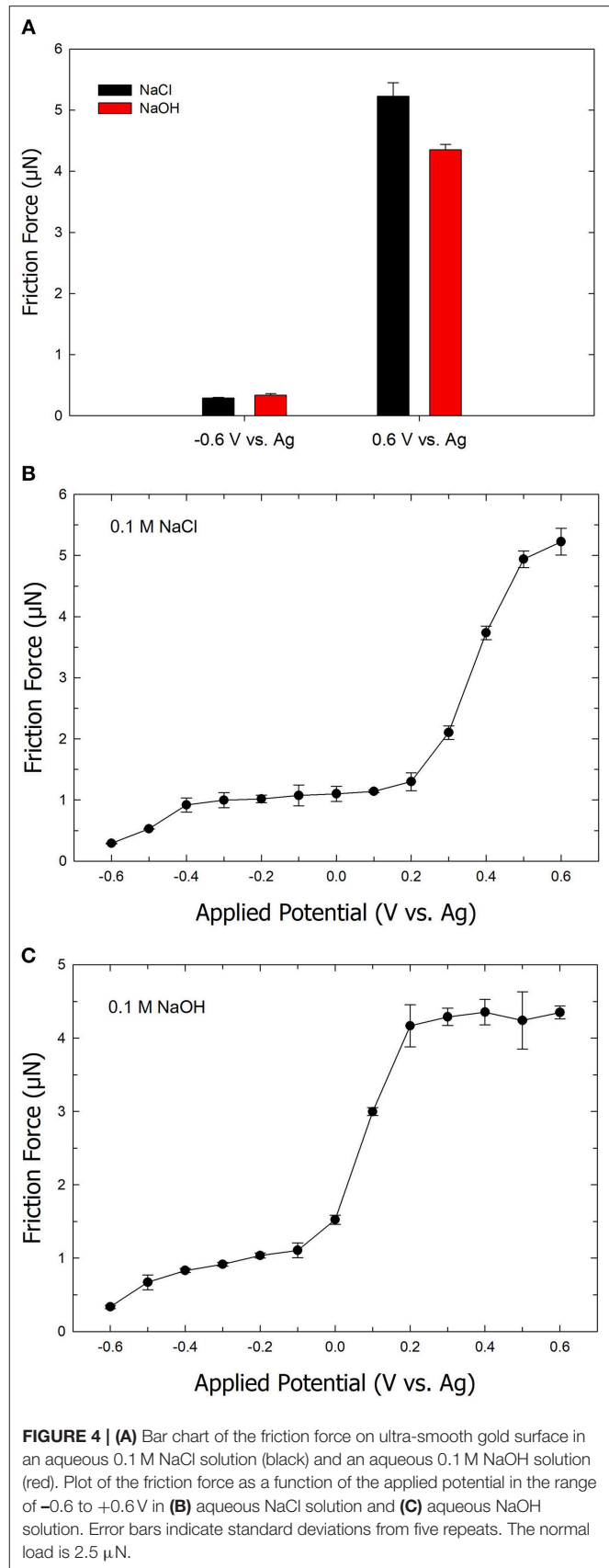
potential, water behaves as a more effective boundary lubricant and lowers the friction further, resulting in a CoF of 0.11. Upon applying a positive potential, e.g., $+0.6$ V, hydrogen bonding becomes more effective, resulting in water molecules next to the Au surface reorganizing into a nanostructured fluid and interacting strongly, again through hydrogen bonding, with the AFM tip. The formation of highly oriented water molecules is also expected to increase the IWL thickness, which will be discussed later. Under these conditions, the IWL no longer acts as an effective boundary lubricant, and results in a high CoF of 2.62.

The same experiment was conducted on an ultra-smooth gold surface to verify if the roughness of the gold surface affected the formation of the IWL. The ultra-smooth gold surface had an rms value of 0.2 nm (see Figure 2B) compared to the gold surfaces formed by sputtering with an rms of 3.3 nm. Figure 2B shows a plot of friction force on the ultra-smooth gold surface vs. applied normal load under the same aforementioned



conditions. Under dry conditions, the CoF on the ultra-smooth gold surface was 0.26. Ultra-smooth gold contains smaller and fewer asperities thereby resulting in lower friction forces. Under aqueous conditions and an OCP, the CoF is measured as 0.15. At the potential of -0.6 V, the coefficient the friction decreases to 0.09. At the potential of the $+0.6$ V, the CoF is again observed to be high (CoF = 1.9). Although the value of coefficient of the friction on the ultra-smooth gold surface is smaller than that observed on the gold sputtered surface, the trend of the change in friction as a function of the applied load and potential is similar. Both gold substrates exhibit high CoF values when a positive potential is applied but low CoF values when a negative potential is applied. Based on these results, and to avoid any influence of surface roughness, all future experiments described below were conducted on ultra-smooth Au surfaces. Based on our previous work (Pashazanusi et al., 2017b), we do not expect any damage to the gold surface under the normal loads used in this study.

Figure 3 displays the effect of electrolyte concentration on the friction forces on ultra-smooth gold under aqueous conditions and an (i) OCP, (ii) applied potential of -0.6 V, and (iii) applied potential of $+0.6$ V. The friction experiments were performed in electrolytes with concentrations of 1, 10 mM, 0.1, and 1 M. At a potential of -0.6 V, low friction values were obtained for all concentrations. Similarly, under aqueous conditions and no applied potential, the friction forces were similar for all concentrations. However, a decrease in friction was observed with an increase in electrolyte ionic strength at positive potentials. At an applied potential of $+0.6$ V, the friction force is $\sim 7.56 \pm 0.3 \mu\text{N}$ in a 1 mM electrolyte compared to $4.38 \pm 0.1 \mu\text{N}$ in a 1 M electrolyte. We attribute this decrease in friction to a similar mechanism that is involved in the freezing point depression of water in the presence of salt. In the latter case, salt ions disrupt the equilibrium of water molecules entering



and leaving the solid state (i.e., ice). A similar mechanism is proposed to explain the decrease in friction forces with increasing salt concentration. The presence of salt disrupts the hydrogen bonding between the AFM tip surface and the IWLs thereby reducing friction.

To understand the effect of the electrolyte anion on the friction forces, friction experiments were performed using 0.1 M NaOH as an electrolyte instead of 0.1 M NaCl. **Figure 4A** shows the friction forces on positively and negatively charged Au surfaces using NaOH compared to NaCl. At a potential of -0.6 V, the friction force is similar for both NaOH (red column) and NaCl (black column) electrolytes. At the potential of $+0.6$ V, the friction is observed to be higher in a NaCl electrolyte solution compared to a NaOH electrolyte solution. **Figure 4B** exhibits a plot of friction forces as a function of applied potential on an ultra-smooth gold surface using NaCl as the electrolyte. At the applied potential of -0.6 V, the friction is at its lowest value. As the applied potential increases to $+0.2$ V, the friction gradually increases. Further increase in the applied potential (i.e., $> +0.2$ V) leads to a sharp increase in the friction force. In our previous work, we demonstrated that the potential range of -0.6 to $+0.6$ V, where main changes in friction forces occur, is free of any Faradaic process including gold oxidation (Pashazanusi et al., 2017b). The friction of the ultra-smooth gold drastically increases from a value of $0.2 \mu\text{N}$ (at -0.6 V) to $5.2 \mu\text{N}$ (at $+0.6$ V) corresponding to an increase in friction by a factor of 26. The sharp changes in the friction can be explained by the dependency of the shear viscosity of interfacial water (which is dependent on the number of hydrogen bonds) at the gold interface. These results suggest that the reorientation of water molecules at the interface forms a highly viscous IWL at the positively charged gold surface, which increases the shear viscosity, thereby increasing friction. However, at the negatively charged surface, the shear viscosity of water next to the gold surface becomes smaller due to lower number of hydrogen bonds, resulting in a decrease in friction.

Figure 4C shows data for the same experiment as above with the exception of substituting NaCl with NaOH as the electrolyte. The friction is again observed to be at the lowest at a potential of -0.6 V, followed by a gradual increase in friction as the potential increases. Similarly, a sharp rise in friction is found over the range of 0 to $+0.2$ V. The friction then levels off as the applied potential is increased to $+0.6$ V. The critical potential, where the drastic change in friction is observed, shifts to a lower value when NaOH is used as the electrolyte. The observed shift in the critical potential can be attributed to differences between the inhibition of the hydrogen bond formation by Cl^- ions compared to OH^- ions. Because of the self-ionization of water (i.e., $\text{H}_2\text{O} + \text{H}_2\text{O} \leftrightarrow \text{H}_3\text{O}^+ + \text{OH}^-$), the addition of OH^- (i.e., the increase in pH as a result of using NaOH) is not expected to significantly disrupt hydrogen bonding or the formation of a viscous IWL. However, Cl^- ions disrupt hydrogen bond formation, which manifests as requiring a higher positive potential (or driving force) to form the viscous IWL. The difference in the equilibrium potential between a Ag wire in 0.1 M NaOH compared to 0.1 M NaCl was measured and found to be negligible. Therefore, the difference in tribological behavior between the two different electrolyte

systems cannot be attributed to the reference electrode. Another feature that is apparent when comparing **Figures 4B,C** is the fact the friction force levels at a value of $4.3 \mu\text{N}$ in the case of using NaOH compared to a still increasing value beyond $5 \mu\text{N}$ in the case of using NaCl, at high positive potentials. The latter would

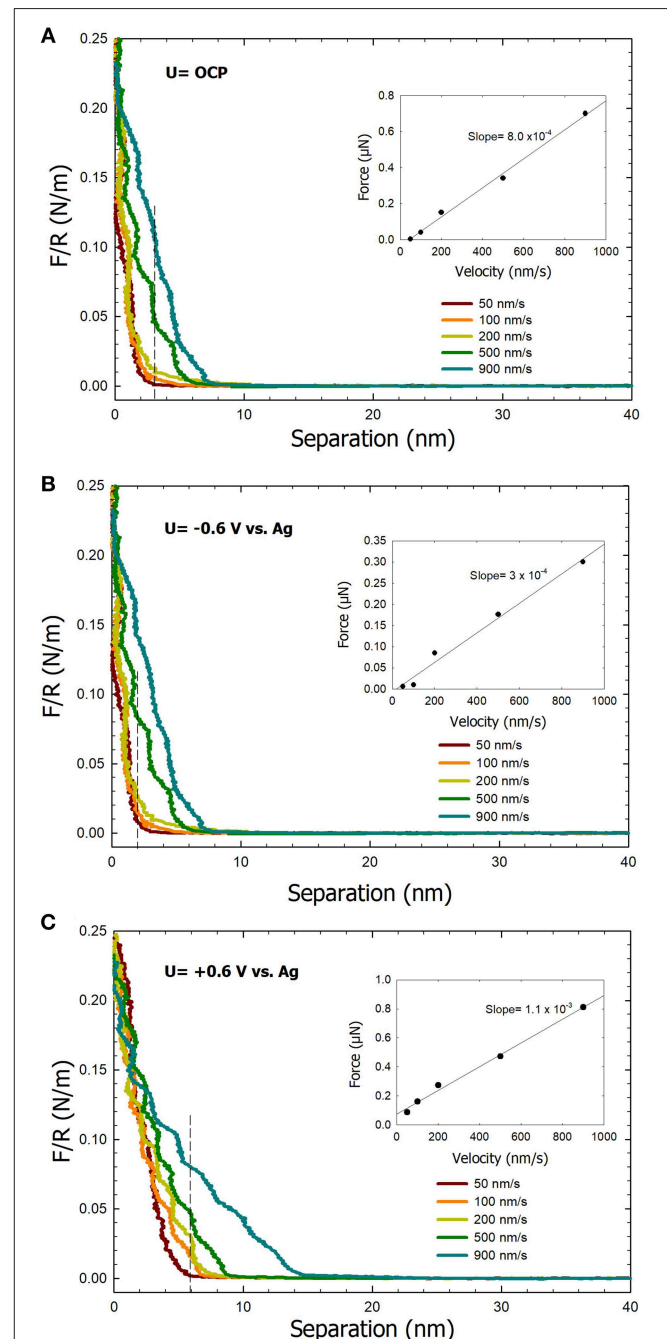


FIGURE 5 | Normal force curves recorded between a colloidal AFM probe and an ultra-smooth gold electrode surface at the various tip approach velocities in 0.1 M NaCl as the electrolyte at (A) open circuit potential, (B) -0.6 V, and (C) $+0.6$ V. The inset plots correspond to force vs. velocity data at a specific separation distance (denoted by the dashed lines).

imply that the AFM tip experiences stronger interactions with the IWL in the presence of NaCl compared to NaOH. We attribute this difference to the fact that at a high pH (i.e., in the presence of 0.1 M NaOH), the hydroxyl groups present on the AFM tip are de-protonated, thereby yielding a larger negative charge on the AFM tip (Tourinho et al., 2002). As a result, hydrogen bonding is disrupted (similar to when a negative potential is applied to a gold surface) at the IWL/AFM tip interface, which results in a decrease in the magnitude of the friction force.

Figure 5 shows the effect of the approach velocity on the normal force between a colloidal AFM tip probe and an ultra-smooth gold substrate. Experiments were performed under open circuit, an applied potential of -0.6 V, and an applied potential of $+0.6$ V, using approach velocities of 50, 100, 200, 500, and 900 nm/s in 0.1 M NaCl. A repulsive force regime is observed in the force curves under both open circuit and the applied potential of $+0.6$ V conditions (**Figures 5A,C**, respectively) that can be attributed to the presence of a highly viscous IWL. Under these conditions, a noticeable difference in the forces curves is observed specifically with the onset of the repulsive force. Under the applied potential of -0.6 V, the repulsive force is negligible at the small velocities, which is consistent with our previous work (Pashazanusi et al., 2017b). However, upon increasing the velocity to 900 nm/s, a small repulsive force regime appears in the force curves (**Figure 5B**). The classical hydrodynamic drainage model $F = 6\pi\eta R^2V/D$, where η is the effective viscosity, R is the tip radius, V is the approach velocity, and D is the separation distance between the tip and surface (Feibelman, 2004) predicts a linear dependence of the force F with increasing velocity. The insets in **Figure 5** show plots of the normal force as a function of the approach velocity. The forces are reported at separation distances of 2, 4, and 5.5 (dotted lines) and obtained from the force curves in **Figure 5**. These specific separation distances were chosen for our analysis based on when a repulsive force became significant in the force curves. In all three cases, a linear dependence between the normal force and the approach velocity was obtained which further supports the formation of a highly viscous IWL. Electrical double layer forces are negligible in our system due to the high ionic strength of the electrolyte (i.e., 0.1 M NaCl resulting in a Debye length of ~ 1 nm) (Israelachvili, 2011). A linear regression of the normal force vs. approach velocity data yields a slope that correlates with the viscosity at a constant separation distance. The linear plotted graph under applied potential of $+0.6$ V condition exhibits the highest slope, thereby the highest viscosity. We note that the approach velocity in the hydrodynamic drainage model is the instantaneous velocity which cannot be directly measured with AFM (due to the deflection of the cantilever), however, we assume that the instantaneous velocity is close to

the applied approach velocities. The observed step-like behavior in the force curves is reminiscent of the oscillatory forces first observed by Israelachvili and Pashley (1983) because of the molecular ordering of water at surfaces resulting in repulsive hydration forces. Previously, it has been shown that the viscosity of interfacial water next to the gold with the surface potential of $+0.6$ V is ~ 5 orders of magnitude higher than for bulk water (Guriyanova et al., 2011). At a surface potential of -0.6 V, the viscosity of the IWL next to the gold surface decreases to lower values (Park, 2011; Pashazanusi et al., 2017b), even lower compared to the OCP case. The latter is again consistent with the fact that in the OCP case, water still orients to a certain extent with relatively more effective hydrogen bonding compared to bulk water.

CONCLUSIONS

In this study, the effect of several system parameters (i.e., surface roughness, salt concentration, and composition) on the friction force between an AFM tip and a gold surface was investigated. Applying a positive potential to a gold surface, irrespective of surface roughness, resulted in high friction forces between an AFM tip and the gold surface. We attribute the increase in friction to the effective hydrogen bonding between the viscous IWL and the AFM tip. However, interfacial water next to a gold surface with an anodic applied potential has properties closer to bulk water, which resulted in lower friction. Higher friction forces were observed when using electrolyte solutions of lower ionic strength when a potential of $+0.6$ V was applied on the Au surface. Additionally, it was found the sharp rise in friction was still present when using NaOH instead of NaCl as the aqueous electrolyte albeit the sharp rise occurred at a different critical applied potential. Force curve measurements performed at different approach velocities yielded a linear dependence, which is consistent with the hydrodynamic drainage model, and supported the formation of a highly viscous IWL at positive applied potential.

DATA AVAILABILITY

All datasets generated for this study are included in the manuscript and/or the supplementary files.

AUTHOR CONTRIBUTIONS

LP and SL designed and performed the experiments. KK provided samples and offered valuable suggestions for the experimental section. NP and YT designed the experiments and provided guidance for the project.

REFERENCES

- Achanta, S., and Celis, J. P. (2015). "Nanotribology of mems/nems," in *Fundamentals of Friction and Wear on the Nanoscale* (New York, NY: Springer), 631–656. doi: 10.1007/978-3-319-10560-4_27
- Antler, M. (1963). The lubrication of gold. *Wear* 6, 44–65. doi: 10.1016/0043-1648(63)90006-1
- Antognozzi, M., Humphris, A., and Miles, M. (2001). Observation of molecular layering in a confined water film and study of the layers viscoelastic properties. *Appl. Phys. Lett.* 78, 300–302. doi: 10.1063/1.1339997

- Balzer, B. N., Gallei, M., Hauf, M. V., Stallhofer, M., Wiegler, L., Holleitner, A., et al. (2013). Nanoscale friction mechanisms at solid-liquid interfaces. *Angewandte Chemie*, 52, 6541–6544. doi: 10.1002/anie.201301255
- Binggeli, M., Christoph, R., Hintermann, H.-E., Colchero, J., and Marti, O. (1993). Friction force measurements on potential controlled graphite in an electrolytic environment. *Nanotechnology* 4, 59–63. doi: 10.1088/0957-4484/4/2/001
- Cain, R. G., Biggs, S., and Page, N. W. (2000). Force calibration in lateral force microscopy. *J. Colloid Interface Sci.* 227, 55–65. doi: 10.1006/jcis.2000.6840
- Cannara, R. J., Eglin, M., and Carpick, R. W. (2006). Lateral force calibration in atomic force microscopy: a new lateral force calibration method and general guidelines for optimization. *Rev. Sci. Instr.* 77:053701. doi: 10.1063/1.2198768
- Carpick, R. W., and Salmeron, M. (1997). Scratching the surface: fundamental investigations of tribology with atomic force microscopy. *Chem. Rev.* 97, 1163–1194. doi: 10.1021/cr960068q
- Chai, L., and Klein, J. (2007). Large area, molecularly smooth (0.2 nm rms) gold films for surface forces and other studies. *Langmuir* 23, 7777–7783. doi: 10.1021/la063738o
- Dhinojwala, A., and Granick, S. (1997). Relaxation time of confined aqueous films under shear. *J. Am. Chem. Soc.* 119, 241–242. doi: 10.1021/ja9632318
- Dhopatkar, N., Defante, A. P., and Dhinojwala, A. (2016). Ice-like water supports hydration forces and eases sliding friction. *Sci. Adv.* 2:e1600763. doi: 10.1126/sciadv.1600763
- Feibelman, P. J. (2004). Effect of high-viscosity interphases on drainage between hydrophilic surfaces. *Langmuir* 20, 1239–1244. doi: 10.1021/la035430s
- Gallagher, P., Lee, M., Amet, F., Maksymovych, P., Wang, J., Wang, S., et al. (2016). Switchable friction enabled by nanoscale self-assembly on graphene. *Nat. Commun.* 7:10745. doi: 10.1038/ncomms10745
- Greiner, C., Felts, J. R., Dai, Z., King, W. P., and Carpick, R. W. (2012). Controlling nanoscale friction through the competition between capillary adsorption and thermally activated sliding. *ACS Nano*, 6, 4305–4313. doi: 10.1021/nn300869w
- Guriyanova, S., Mairanovsky, V. G., and Bonaccorso, E. (2011). Superviscosity and electroviscous effects at an electrode/aqueous electrolyte interface: An atomic force microscope study. *J. Colloid Interface Sci.* 360, 800–804. doi: 10.1016/j.jcis.2011.04.072
- Hugel, T., and Seitz, M. (2001). The study of molecular interactions by AFM force spectroscopy. *Macromol. Rapid Commun.* 22, 989–1016. doi: 10.1002/1521-3927(20010901)22:13<989::AID-MARC989>3.0.CO;2-D
- Israelachvili, J. N. (2011). *Intermolecular and Surface Forces*. Amsterdam: Academic press.
- Israelachvili, J. N., and Pashley, R. M. (1983). Molecular layering of water at surfaces and origin of repulsive hydration forces. *Nature* 306, 249–250. doi: 10.1038/306249a0
- Karuppiiah, K. S., Zhou, Y., Woo, L. K., and Sundararajan, S. (2009). Nanoscale friction switches: friction modulation of monomolecular assemblies using external electric fields. *Langmuir* 25, 12114–12119. doi: 10.1021/la901221g
- Khan, S. H., Matei, G., Patil, S., and Hoffmann, P. M. (2010). Dynamic solidification in nanoconfined water films. *Phys. Rev. Lett.* 105:106101. doi: 10.1103/PhysRevLett.105.106101
- Kim, H.-J., and Kim, D.-E. (2009). Nano-scale friction: a review. *Int. J. Prec. Eng. Manufact.* 10, 141–151. doi: 10.1007/s12541-009-0039-7
- Kim, H. I., Kushmerick, J. G., Houston, J. E., and Bunker, B. C. (2003). Viscous “interphase” water adjacent to oligo (ethylene glycol)-terminated monolayers. *Langmuir* 19, 9271–9275. doi: 10.1021/la034585x
- Kim, S. H., Asay, D. B., and Dugger, M. T. (2007). Nanotribology and MEMS. *Nano Today* 2, 22–29. doi: 10.1016/S1748-0132(07)70140-8
- Labuda, A., Hausen, F., Gosvami, N. N., Grütter, P. H., Lennox, R. B., and Bennewitz, R. (2011). Switching atomic friction by electrochemical oxidation. *Langmuir* 27, 2561–2566. doi: 10.1021/la104497t
- Lee, S. H., and Rossky, P. J. (1994). A comparison of the structure and dynamics of liquid water at hydrophobic and hydrophilic surfaces—a molecular dynamics simulation study. *J. Chem. Phys.* 100, 3334–3345. doi: 10.1063/1.466425
- Li, S. W., Bai, P. P., Li, Y. Z., Chen, C. F., Meng, Y. G., and Tian, Y. (2018). Electric potential-controlled interfacial interaction between gold and hydrophilic/hydrophobic surfaces in aqueous solutions. *J. Phys. Chem. C* 122, 22549–22555. doi: 10.1021/acs.jpcc.8b06755
- Liu, E., Blanpain, B., and Celis, J.-P. (1996). Calibration procedures for frictional measurements with a lateral force microscope. *Wear* 192, 141–150. doi: 10.1016/0043-1648(95)06784-1
- Meyer, E., Heinzelmann, H., Grütter, P., Jung, T., Hidber, H.-R., Rudin, H., and Güntherodt, H.-J. (1989). Atomic force microscopy for the study of tribology and adhesion. *Thin Solid Films* 181, 527–544. doi: 10.1016/0040-6090(89)90522-1
- Mo, Y., Turner, K. T., and Szlufarska, I. (2009). Friction laws at the nanoscale. *Nature* 457, 1116–1119. doi: 10.1038/nature07748
- Oguntoye, M., Oak, S., Pashazanusi, L., Pratt, L., and Pesika, N. S. (2017). Vertically-aligned carbon nanotube arrays as binder-free supports for nickel cobaltite based faradaic supercapacitor electrodes. *Electrochim. Acta* 236, 408–416. doi: 10.1016/j.electacta.2017.03.172
- Overney, R., and Meyer, E. (1993). Tribological investigations using friction force microscopy. *MRS Bull.* 18, 26–34. doi: 10.1557/S0883769400047096
- Palacio, M. L., and Bhushan, B. (2010). Normal and lateral force calibration techniques for AFM cantilevers. *Crit. Rev. Solid State Mater. Sci.* 35, 73–104. doi: 10.1080/10408430903546691
- Park, J. Y. (2011). Tuning nanoscale friction on Pt nanoparticles with engineering of organic capping layer. *Langmuir* 27, 2509–2513. doi: 10.1021/la104353f
- Park, J. Y., Ogletree, D. E., Thiel, P. A., and Salmeron, M. (2006). Electronic control of friction in silicon pn junctions. *Science* 313, 186–186. doi: 10.1126/science.1125017
- Pashazanusi, L., Lwoya, B., Oak, S., Khosla, T., Albert, J. N. L., Tian, Y., et al. (2017a). Enhanced Adhesion of mosquitoes to rough surfaces. *ACS Appl. Mater. Interfaces* 9, 24373–24380. doi: 10.1021/acsami.7b06659
- Pashazanusi, L., Oguntoye, M., Oak, S., Albert, J. N. L., Pratt, L. R., and Pesika, N. S. (2017b). Anomalous potential-dependent friction on Au (111) measured by AFM. *Langmuir* 34, 801–806. doi: 10.1021/acs.langmuir.7b03023
- Pérez, R. (2014). Nanoscale friction: distorted by the tip. *Nat. Mater.* 13, 118–119. doi: 10.1038/nmat3875
- Plausinaitis, D., Pulmanas, A., Kubilius, V., Raudonis, R., and Daujotis, V. (2014). Properties of an interfacial solution layer at gold electrode surface in perchlorate and chloride solutions: piezoelectric resonator and drag force study. *Electrochim. Acta* 121, 278–284. doi: 10.1016/j.electacta.2014.01.007
- Raviv, U., and Klein, J. (2002). Fluidity of bound hydration layers. *Science* 297, 1540–1543. doi: 10.1126/science.1074481
- Schirmeisen, A., and Schwarz, U. D. (2009). Measuring the friction of nanoparticles: a new route towards a better understanding of nanoscale friction. *ChemPhysChem* 10, 2373–2382. doi: 10.1002/cphc.200900378
- Schwarz, U., Köster, P., and Wiesendanger, R. (1996). Quantitative analysis of lateral force microscopy experiments. *Rev. Sci. Instr.* 67, 2560–2567. doi: 10.1063/1.1147214
- Strelcov, E., Kumar, R., Bocharova, V., Sumpter, B. G., Tselev, A., and Kalinin, S. V. (2015). Nanoscale lubrication of ionic surfaces controlled via a strong electric field. *Sci. Rep.* 5:8049. doi: 10.1038/srep08049
- Sweeney, J., Hausen, F., Hayes, R., Webber, G. B., Endres, F., Rutland, M. W., et al. (2012). Control of nanoscale friction on gold in an ionic liquid by a potential-dependent ionic lubricant layer. *Phys. Rev. Lett.* 109:155502. doi: 10.1103/PhysRevLett.109.155502
- Toney, M. F., Howard, J. N., Richer, J., Borges, G. L., Gordon, J. G., Melroy, O. R., et al. (1994). Voltage-dependent ordering of water molecules at an electrode-electrolyte interface. *Nature* 368:444. doi: 10.1038/368444a0
- Tourinho, F. A., Campos, A. F. C., Aquino, R., Lara, M. C. F. L., da Silva, G., and Depeyrot, J. (2002). Surface charge density determination in electric double layered magnetic fluids. *Braz. J. Phys.* 32, 501–508. doi: 10.1590/S0103-97332002000300008
- Valtiner, M., Banquy, X., Kristiansen, K., Greene, G. W., and Israelachvili, J. N. (2012). The electrochemical surface forces apparatus: the effect of surface roughness, electrostatic surface potentials, and anodic oxide growth on interaction forces, and friction between dissimilar surfaces

- in aqueous solutions. *Langmuir* 28, 13080–13093. doi: 10.1021/la3018216
- Velasco-Velez, J.-J., Wu, C. H., Pascal, T. A., Wan, L. F., Guo, J., Prendergast, D., (2014). The structure of interfacial water on gold electrodes studied by x-ray absorption spectroscopy. *Science* 346, 831–834. doi: 10.1126/science.1259437
- Weymouth, A. J., Hofmann, T., and Giessibl, F. J. (2014). Quantifying molecular stiffness and interaction with lateral force microscopy. *Science* 343, 1120–1122. doi: 10.1126/science.1249502
- Xie, G., Luo, J., Liu, S., Guo, D., and Zhang, C. (2009). “Freezing” of nanoconfined fluids under an electric field. *Langmuir* 26, 1445–1448. doi: 10.1021/la903419v

Conflict of Interest Statement: The authors declare that the research was conducted in the absence of any commercial or financial relationships that could be construed as a potential conflict of interest.

Copyright © 2019 Pashazanusi, Kristiansen, Li, Tian and Pesika. This is an open-access article distributed under the terms of the Creative Commons Attribution License (CC BY). The use, distribution or reproduction in other forums is permitted, provided the original author(s) and the copyright owner(s) are credited and that the original publication in this journal is cited, in accordance with accepted academic practice. No use, distribution or reproduction is permitted which does not comply with these terms.



Investigation on Dynamic Response of Rubber in Frictional Contact

Ken Nakano^{1*}, Kai Kawaguchi¹, Kazuho Takeshima¹, Yu Shiraishi¹, Fabian Forsbach², Justus Benad², Mikhail Popov² and Valentin L. Popov^{2*}

¹ Faculty of Environment and Information Sciences, Yokohama National University, Yokohama, Japan, ² Department of System Dynamics and Friction Physics, Technische Universität Berlin, Berlin, Germany

OPEN ACCESS

Edited by:

Irina Georgievna Goryacheva,
Institute for Problems in Mechanics
(RAS), Russia

Reviewed by:

Luciano Afferrante,
Politecnico di Bari, Italy
Erik Kuhn,
Hamburg University of Applied
Sciences, Germany
Fedor Stepanov,
Institute for Problems in Mechanics
(RAS), Russia

*Correspondence:

Ken Nakano
nakano@ynu.ac.jp
Valentin L. Popov
v.popov@tu-berlin.de

Specialty section:

This article was submitted to
Tribology,
a section of the journal
Frontiers in Mechanical Engineering

Received: 21 December 2018

Accepted: 04 March 2019

Published: 26 March 2019

Citation:

Nakano K, Kawaguchi K,
Takeshima K, Shiraishi Y, Forsbach F,
Benad J, Popov M and Popov VL
(2019) Investigation on Dynamic
Response of Rubber in Frictional
Contact. *Front. Mech. Eng.* 5:9.
doi: 10.3389/fmech.2019.00009

In the present work, we analyze a device for measuring the dynamic response of rubber in sliding contact. The principle of the device is to measure excited oscillations of a mechanical system with a sliding contact between a rubber roller and a rigid surface. Depending on the contact properties, varying oscillation amplitudes are measured. The goal is to determine dynamic response properties of rubber from oscillating tests. For this sake, an analytical model is introduced in which the contact problem and system dynamics are considered in detail. Analytical and numerical results obtained for this model are compared with some experimental data and discussed both on a qualitative and quantitative level.

Keywords: rubber, contact, sliding friction, viscoelasticity, contact stiffness, contact damping

INTRODUCTION

Elastomers such as rubber are of great importance in many technical applications, particularly where large frictional forces occur (Saccomandi and Ogden, 2004; Popov, 2017). Tires, transportation rollers, shoe soles, seals, contact materials of buttons and keys on small electronic devices, or viscoelastic vibration dampers in structures and machines (Jones, 2001; Rao, 2003) are only a few examples. High industrial demands require a profound knowledge of the material properties of elastomers used in these components. An accurate, yet rapid and simple acquisition of these material parameters is often desired. Especially difficult is accurate determination of dynamic response in frictional contacts, which is important for analyzing stability of sliding contacts (Braun et al., 2009; Nakano and Maegawa, 2009; Amundsen et al., 2012). An efficient acquisition of material properties and determination of dynamic response of rubber is the goal of the measuring device we study in this paper.

The principle of the device is to measure excited oscillations of a mechanical system with a sliding contact between a rubber roller and a rigid surface. Depending on the contact properties, varying oscillation amplitudes are measured. By introducing an analytical model for the contact between the rubber roller and the rigid oscillator, material and dynamic response properties that we seek can be extracted from the experimental data. With such a procedure, the quality of the results will depend to a large extent on how efficiently and accurately one can model the contact.

Elastomers exhibit a time-dependent behavior generally characterized by a large spectrum of relaxation times, which adds complexity to the already multi-scalar properties of the contacting surfaces, which makes the numerical modeling a challenge (Kürschner et al., 2015). Many of these difficulties can be overcome with the application of the method of dimensionality reduction (Popov and Heß, 2015) with which we can map the given three-dimensional contact problem to an equivalent contact problem of a transformed indentation profile with a one-dimensional viscoelastic foundation of independent rheological elements, for details see Benad (2018); Popov et al. (2018). In order

to obtain a first qualitative and quantitative understanding of the measuring device, we begin in the present investigation with a simplified model of only one of these rheological elements consisting of a single spring and a single damper to model the contact. In this approach, we follow the recent works of Popov (2016), Mao et al. (2017) and Benad et al. (2018) in which the influence of oscillations on friction is investigated. It will be shown that many characteristic features of the system studied in the present paper show already with such a simplified one-element model. This paves the way for more detailed studies in the future.

The parts of this work are organized as follows: First, we describe the chosen analytical model of the system. We then discuss two limiting cases for the motion of the system and present the analytical solutions for these cases. Afterwards, we turn from the limiting cases to the arbitrary motion of the system which is investigated numerically. The results are first discussed on a qualitative level and then compared with the data obtained from a measuring device. We conclude with a summary and a brief outlook in which we address open questions, which are recommended for investigation in future works using more detailed models.

INVESTIGATED SYSTEM

Analytical Model

Figure 1 is the analytical model showing a mechanism for measuring dynamic response of rubber in sliding contact. The rubber roller with the radius R contacts with the arc-shaped rigid surface of a rigid arm at the normal load W and rotates about the “rotational axis” with the peripheral velocity V . The rigid arm is supported by a torsional spring (torsional spring constant: K_0 and torsional damping coefficient: C_0), which allows the rigid arm to oscillate about the “torsional axis.” The moment of inertia of the rigid arm about the torsional axis is J . The distance between the torsional axis and the contact point is b , which is identical to the curvature radius of the rigid surface. The rigid arm is pinched by two translational springs (translational spring constant: k_0 and translational damping coefficient: c_0) at the distance a from the torsional shaft. One of the translational springs is supported by an actuator (denoted by PZT) mounted to the base, while the other is supported directly by the base under a certain preload. When the actuator provides the harmonic displacement excitation

$$u(t) = u_0 \sin \omega t \quad (1)$$

we measure the steady-state response of the angular displacement of the rigid arm

$$\theta(t) = \alpha \sin(\omega t + \varphi) + \theta_0 \quad (2)$$

where t is the time, u_0 is the amplitude, ω is the angular frequency, α is the angular amplitude, φ is the phase shift, and θ_0 is the static angular displacement.

Equation of Motion

The equation of motion of the rigid arm is written as

$$J\ddot{\theta} + (C_0 + 2a^2c_0)\dot{\theta} + (K_0 + 2a^2k_0)\theta = ak_0u + ac_0\dot{u} + bF \quad (3)$$

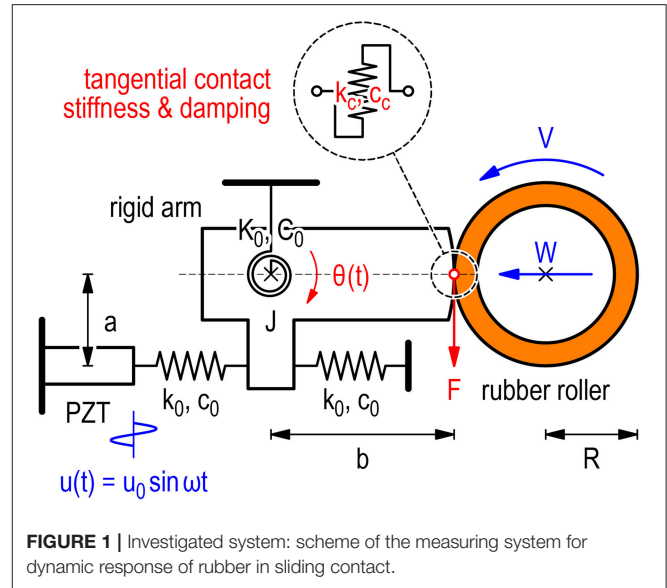


FIGURE 1 | Investigated system: scheme of the measuring system for dynamic response of rubber in sliding contact.

where $(\dot{})$ is the time derivative and F is the tangential force acting on the rigid arm due to the rubber roller. By using the following notations

$$K = K_0 + 2a^2k_0 \quad (4)$$

$$C = C_0 + 2a^2c_0 \quad (5)$$

$$\Gamma = au_0\sqrt{k_0^2 + (c_0\omega)^2} \quad (6)$$

$$\varphi_0 = \tan^{-1}\left(\frac{c_0\omega}{k_0}\right) \quad (7)$$

the equation of motion can be rewritten as

$$J\ddot{\theta} + C\dot{\theta} + K\theta = \Gamma \sin(\omega t + \varphi_0) + bF \quad (8)$$

Note that the phase shift φ_0 is coming from the viscoelastic properties of the two translational springs (i.e., k_0 and c_0), not from the viscoelastic properties of the contact.

Limiting Cases

Case I: No Contact

First, let us consider the situation of “no contact” (i.e., $W = 0$ and $V = 0$). Since the rubber roller does not contact with the rigid surface, the tangential force vanishes (i.e., $F = 0$). Then we obtain the steady-state response Equation (2) with α and φ

$$\alpha = \frac{\left(\frac{\Gamma}{K}\right)}{\sqrt{(1 - \Omega^2)^2 + (2\zeta\Omega)^2}} \quad (9)$$

$$\varphi = -\tan^{-1}\left(\frac{2\zeta\Omega}{(1 - \Omega^2)}\right) + \varphi_0 \quad (10)$$

respectively, where the dimensionless excitation frequency Ω and the dimensionless damping ratio ζ are given by

$$\Omega = \frac{\omega}{\sqrt{\frac{K}{J}}} \quad (11)$$

$$\zeta = \frac{C}{(2\sqrt{JK})} \quad (12)$$

respectively.

Case II: Static Contact

Secondly, let us consider the situation of “stationary contact” (i.e., $W > 0$ and $V = 0$). With no slippage at the contact, the tangential force is given by

$$F = -bk_c\theta - bc_c\dot{\theta} \quad (13)$$

where k_c and c_c are the tangential contact stiffness and the tangential contact damping, respectively. Then we obtain the angular amplitude and the phase shift in the same forms as Equations (9), (10), where Ω and ζ are given by

$$\Omega = \frac{\omega}{\sqrt{\frac{(K+b^2k_c)}{J}}} \quad (14)$$

$$\zeta = \frac{(C+b^2c_c)}{(2\sqrt{J(K+b^2k_c)})} \quad (15)$$

respectively.

Case III: Fully Slipping Contact

Thirdly, let us consider the situation of “fully slipping contact” (i.e., $W > 0$ and $V > 0$). With considering the frictional force with the constant friction coefficient μ , the tangential force at the contact is given by

$$|F| = \mu W \quad (16)$$

This merely shifts the equilibrium position of the oscillator, but does not influence its frequency and damping (Nakano, 2006). Thus, both remain the same as the case of “no contact” and are given by Equations (11, 12).

Arbitrary Case

To examine the arbitrary motion of the system, the equation of motion Equation (8) can be easily solved numerically using the Euler time integration procedure. Therein, the calculation scheme for the contact force is the following: In each time step of the dynamic simulation, it is first assumed that the immediate contact between the contact spring and the oscillator is sticking. Thus, the change of the tangential contact force is equal to

$$\Delta F = (k_c(V - b\dot{\theta}) - c_cb\ddot{\theta}) \Delta t \text{ if } |F| < \mu W \text{ (stick)} \quad (17)$$

This is valid as long as the absolute value of the tangential force remains smaller than the normal force multiplied with the coefficient of friction. If this condition is violated in the given

time step, then the tangential force is set to the normal force times the coefficient of friction with the appropriate sign:

$$F = \text{sign}(V - b\dot{\theta}) \mu W \text{ (slip)} \quad (18)$$

The above equations describe unambiguously the procedure for determining the tangential force in each time step. We will now turn to a qualitative discussion of the simulation results. Thereafter, the simulation results will be compared to some experimental data.

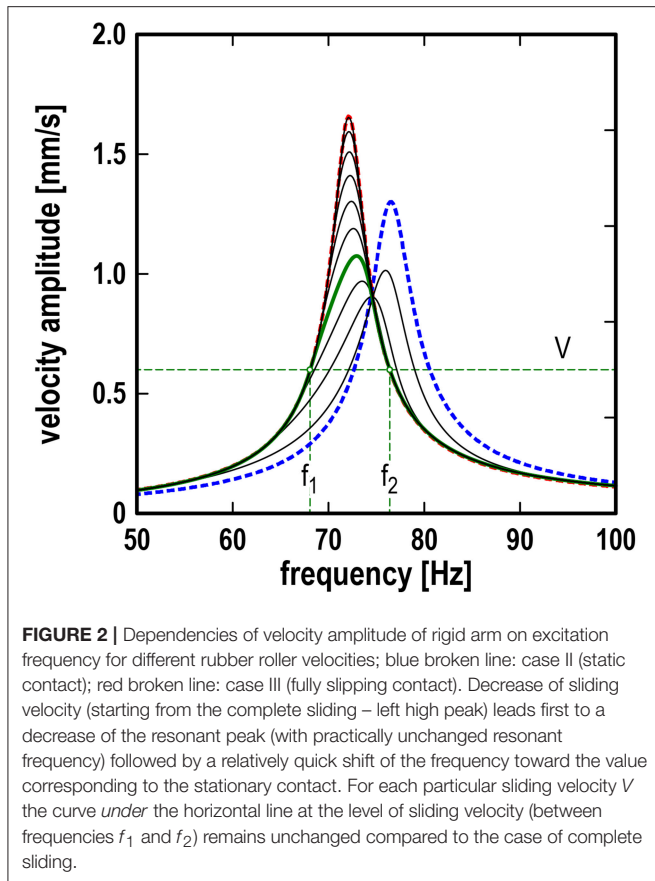
TRANSITION BETWEEN STICKING AND SLIPPING REGIMES

In the previous section, we identified essentially two limiting cases for the motion of the system. For one of them, the velocity of the roller V is zero (Case II: static contact), while for the other, it is very high (Case III: fully slipping contact). It is clear that when the roller starts rotating, there will be some transition between the two regimes. Some features of this transition are relatively simple and robust, which can be discussed on the qualitative level. We will now illustrate these qualitative features with the numerical results.

Consider first the dependency of the velocity amplitude of the rigid arm on the excitation frequency. This is shown in **Figure 2** for both the case of static contact with no slip (right resonance curve, displayed with a blue broken line) and the case of sliding contact with no stick (upper left resonance curve, displayed with a red broken line). If the peripheral velocity of the roller is larger than the velocity amplitude of the rigid arm, then the roller will continuously slide on the rigid arm surface with a relative velocity, which keeps changing its absolute value but not the sign. Therefore, the force of friction will remain constant at any time. This will introduce some static displacement but will not affect the resonance curve. Thus, if the rotation velocity of the roller is larger than the maximum velocity amplitude, the roller does not influence the oscillations and they occur exactly as in the non-contact mode. This is similar to the effects which are seen in the active control of friction by oscillations, where there is also a critical velocity, after which there is no influence of oscillations by the force of friction (Popov, 2016).

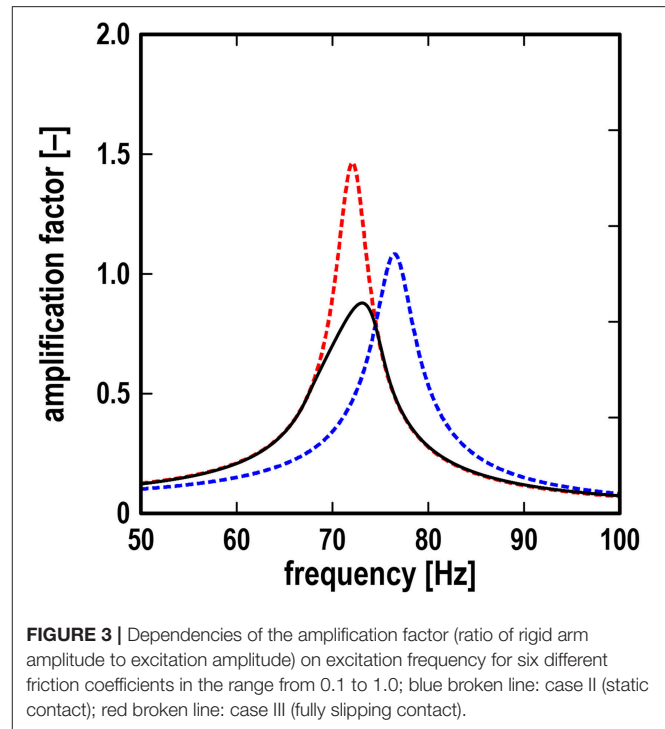
Let us now consider the case when the roller velocity is smaller than the maximum oscillation velocity. Consider some particular roller velocity, as shown for instance with the horizontal green broken line in **Figure 2** and denoted by V . This line has two intersection points with the resonance curve for the velocity amplitude at the frequencies f_1 and f_2 . For all frequencies smaller than f_1 or larger than f_2 the roller velocity is larger than the velocity amplitude. This means that in these two regions, the contact with the roller does not influence the resonance curve. Between f_1 and f_2 , partial stick occurs, and the resonance curve differs from that without the contact. For the chosen roller velocity, the corresponding dependency is shown with the green bold curve.

Accordingly, we can identify three stages during the decrease of the roller velocity: (1) At very high sliding velocities, the contact with the roller does not influence the resonance curve. (2)



When the roller velocity touches the maximum of the resonance curve, first only the top of the curve becomes “cut”—without significantly changing the resonance frequency. (3) Further decrease of the roller velocity leads to a shift of the maximum of the resonance curve to the right; finally, it tends toward the case of static contact.

Note that in **Figure 2**, the shape of the resonance curve below the level of the roller velocity V remains unchanged compared with the limiting case III (fully slipping contact). Therefore, the resonance curve below the roller velocity level does not depend on the friction coefficient, which only determines the static shift of the oscillator. Between the frequencies f_1 and f_2 , the shape of the resonance curve is changed, and it could depend on the friction coefficient. However, most surprisingly, the results of the numerical simulation of the investigated model show that there is no such dependence. **Figure 3** illustrates this somewhat counter-intuitive feature. In addition to the resonance curves for the two limiting cases (broken lines), it shows six additional resonance curves (black solid lines), all obtained for the same exemplary sliding velocity of the roller, which is low enough so as to allow an excitation frequency band in which partial stick occurs. Different finite values for the friction coefficient were used to obtain these six additional resonance curves. Not only do all six curves coincide in the frequency region of continuous sliding, but also in the middle frequency band, in which the resonance curves differ from the continuous sliding case due to the periods of stick.



COMPARISON WITH EXPERIMENTAL DATA

Figure 4 is a photograph of the apparatus developed for measuring dynamic response of rubber in sliding contact, which embodies the model shown in **Figure 1**. The rubber roller was made of styrene-butadiene rubber with Young's modulus of 15 MPa. As the counter surface of the rubber roller, an abrasive paper with an arithmetic roughness of $4.3 \mu\text{m}$ was affixed to the curved surface of the rigid arm. The specifications of the system were as follows: the moment of inertia $J = 5.0 \times 10^{-3} \text{ kgm}^2$, the torsional spring constant $K_0 = 9.9 \times 10^2 \text{ Nm}$, the torsional damping coefficient $C_0 = 4.3 \times 10^{-1} \text{ Nms}$, the translational spring constant $k_0 = 1.6 \times 10^4 \text{ N/m}$, the translational damping coefficient $c_0 = 1.2 \times 10^1 \text{ Ns/m}$, the length $a = 30 \text{ mm}$, and the length $b = 60 \text{ mm}$. The amplitude and frequency of the PZT actuator were $u_0 = 2.5 \mu\text{m}$, and $\omega/2\pi = 50$ to 100 Hz , respectively. The normal load was $W = 20 \text{ N}$ and the peripheral velocity of the rubber roller was $V = 20 \text{ mm/s}$. Note that the normal load was applied by pulling a coil spring with a low stiffness to minimize the variation of its value.

Let us now compare the analytical and numerical results with some experimental data on resonance curves. As in the previous sections, we first examine the limiting cases (i.e., case I: no contact, case II: static contact, and case III: fully slipping contact). It is shown in **Figure 5** that the theoretical results for cases I and II are in very good agreement with the experimental data for no contact ($W = 0 \text{ N}$ and $V = 0 \text{ mm/s}$) and the static contact ($W = 20 \text{ N}$ and $V = 0 \text{ mm/s}$), respectively, where the contact stiffness and contact damping are $k_c = 8.9 \times 10^4 \text{ N/m}$ and $c_c = 26 \text{ Ns/m}$,

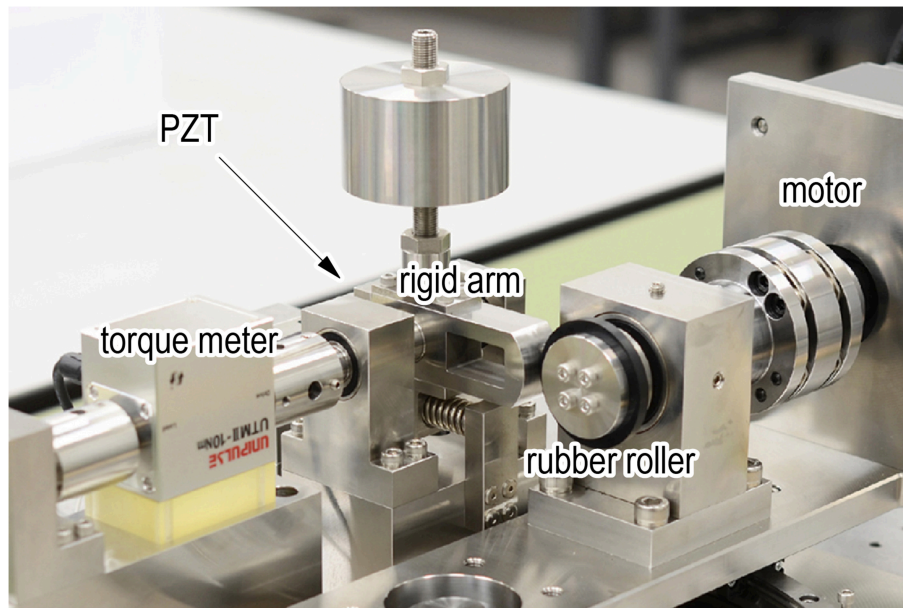


FIGURE 4 | Apparatus developed for measuring dynamic response of rubber in sliding contact.

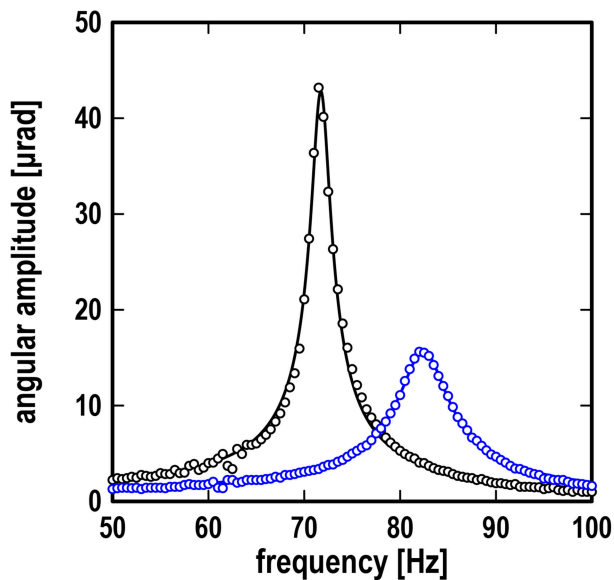


FIGURE 5 | Resonance curves showing frequency response of angular amplitude; black line: theoretical results for case I (no contact) and case III (fully slipping contact); blue line: theoretical result for case II (static contact) at $W = 20$ N; the blue line is barely visible due to excellent fitting; black symbols: experimental data at $W = 0$ N and $V = 0$ mm/s; blue symbols: experimental data at $W = 20$ N and $V = 0$ mm/s.

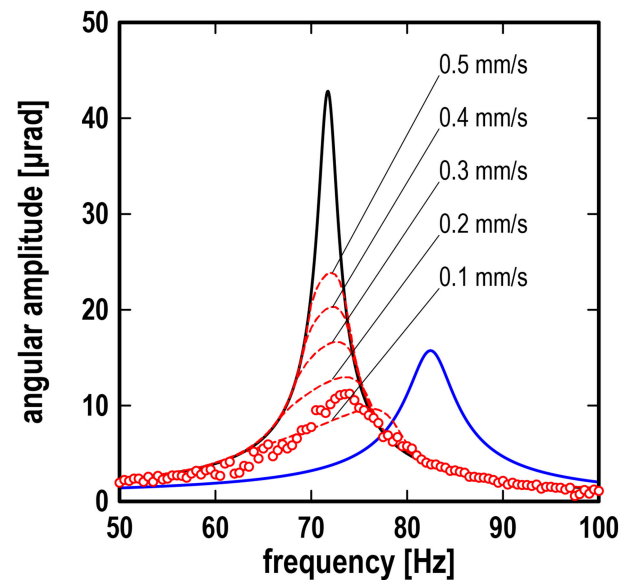


FIGURE 6 | Resonance curves showing frequency response of angular amplitude; black line: theoretical results for case I (no contact) or case III (fully slipping contact); blue line: theoretical result for case II (static contact) at $W = 20$ N; red lines: numerical results for arbitrary case at $W = 20$ N and $V = 0.1$ to 0.5 mm/s; red symbols: experimental data at $W = 20$ N and $V = 20$ mm/s.

respectively, which were determined by fitting experimental data to the theoretical solution Equation (9) with Equations (14), (15). The above values of k_c and c_c have been used for all simulations in contact: static contact, intermittent slip and full slip.

We now turn again to the transition between the limiting cases. From our theoretical results, we expect the resonance

amplitude to be lowered and the resonance frequency to be shifted to the right for the case of partial stick, when compared to limiting case I/III (no contact/fully slipping contact). This is confirmed with the experimental data, as can be seen in **Figure 6**. One can further observe from the graph that the experimental resonance curve differs substantially from the

resonance curve for case I/III in a certain frequency range around its resonance frequency, while for higher or lower frequencies the resonance curves still coincide. This is a characteristic feature in the transition phase which was also observed and described in detail in the previous section. On a qualitative level, however, a significant discrepancy of the roller velocities is evident comparing the experimental data of the transition with the corresponding numerical results. In order to obtain a similar resonance frequency and maximum amplitude, the roller velocity in the numerical simulation would have to be smaller by an approximate factor of 0.01 than in the experimental setup. A velocity of $V = 20$ mm/s as it is shown in **Figure 6** would fully comply with the slipping case in the framework of the simplified model. And yet, in the experimental data, we clearly observe a tendency which we would expect only at much lower velocities. At this stage, this leaves an open question which will have to be investigated further in future works. It is expected that a more detailed model for the contact will yield more accurate simulation results and provide insight on why the simplified model chosen in this work leads to the discrepancies in the transition curve.

CONCLUSION

In this work, we analyzed a measuring device whose basic principle lies in measuring excited oscillations of a mechanical system with a sliding contact between a rubber roller and a rigid surface, which is expected to lead to the extraction of material properties of rubber. In order to obtain a first qualitative and quantitative understanding of the device, we introduced a simple model of the system. Therein, the contact between the rubber roller and the rigid oscillator was modeled with one rheological element consisting of a single spring and a single damper. It was shown that many characteristic features of the system show already with such a simplified one-element model.

Essentially two limiting cases of the system were identified: The static contact, where the rotation velocity of the roller is zero, and the case of continuous sliding, where the velocity of the roller is so high as to never allow phases of stick between the rubber roller and the oscillator. It was shown that the latter coincides with the no contact case. The analytical and numerical results for the limiting cases obtained with the simplified model are in very good agreement with the experimental data.

When the roller starts rotation, there is a transition between the limiting cases. This was also confirmed experimentally. Some features of this transition are relatively simple and robust and were discussed on a qualitative level: At very high sliding velocities, the contact with the roller does not influence the resonance curve. When the roller velocity touches the maximum of the resonance curve of the velocity oscillations, first only the upper portion of the curve is slightly altered, without significantly changing the resonance frequency. A further decrease of the roller velocity leads to a shift of the maximum of the resonance

curve to the right before finally it tends toward the static contact case.

The qualitative features of the transition between the limiting cases upon decreasing the roller velocity which were obtained with the simplified model could also be observed in the available experimental data of the transition. On a quantitative level, however, a significant discrepancy of the roller velocities became evident when comparing the experimental data of the transition with the corresponding numerical results. In order to obtain a system response similar to the experimental data, the roller velocity in the numerical simulation had to be smaller than in the experiment by an approximate factor of 0.01. This leaves an open question which will have to be investigated further in future works.

It is expected that a more detailed model for the contact will yield more accurate simulation results and provide insight on why the simplified model chosen in this work leads to the discrepancies in the transition of the resonance curves. A first consideration in future works could be the friction law used in the model. As suggested and discussed in detail in Woodhouse et al. (2015), the Coulomb model in its simplest form (Coulomb, 1821), which we adopted in this work, may be too crude for predicting details of friction-driven vibration. More complex friction laws, for example as they are discussed in Barber (2018), may lead to better results. Therein, a critical component may be the dependence of the friction coefficient on the sliding velocity, see Grosch (1963). Another consideration should be the adoption of a more sophisticated contact model. Roller and oscillator of the apparatus are practically two wheels in contact. Such a rolling contact can be modeled more accurately than in the present paper using more than one rheological element with the method of dimensionality reduction, see Popov et al. (2015); Li and Popov (2017).

AUTHOR CONTRIBUTIONS

KN and VP conceived the study. KN designed the apparatus. YS, KT, and KK conducted experiments. MP, JB, and FF conducted numerical simulations. All authors contributed to writing the manuscript and approved it.

FUNDING

The authors are grateful for financial support of the Japan Society for the Promotion of Science (VP) and the Deutsche Forschungsgemeinschaft (MP).

ACKNOWLEDGMENTS

The authors thank Dr. Y. Osawa, Dr. K. Hagiwara, Mr. S. Hatanaka, and Ms. L. Zimmermann for valuable discussions.

REFERENCES

- Amundsen, D. S., Scheibert, J., Thøgersen, K., Trømborg, J., and Malthe-Sørensen, A. (2012). 1D model of precursors to frictional stick-slip motion allowing for robust comparison with experiments. *Tribol. Lett.* 45, 377–369. doi: 10.1007/s11249-011-9894-3
- Barber, J. (2018). *Contact Mechanics*. New York, NY: Springer. doi: 10.1007/978-3-319-70939-0

- Benad, J. (2018). Fast numerical implementation of the MDR transformations. *Fact. Univ. Mech. Eng.* 16, 127–138. doi: 10.22190/FUME180526023B
- Benad, J., Popov, M., Nakano, K., and Popov, V. L. (2018). Stiff and soft active control of friction by vibrations and their energy efficiency. *Forschung Ingenieur.* 82, 331–339. doi: 10.1007/s10010-018-0281-1
- Braun, O. M., Barel, I., and Urbakh, M. (2009). Dynamics of transition from static to kinetic friction. *Phys. Rev. Lett.* 103:194301. doi: 10.1103/PhysRevLett.103.194301
- Coulomb, C. (1821). *Theorie des Machines Simple (Theory of Simple Machines)*. Paris: Bachelier.
- Grosch, K. (1963). The relation between the friction and visco-elastic properties of rubber. *Proc. R. Soc. Lond. A Math. Phys. Sci.* 274, 21–39. doi: 10.1098/rspa.1963.0112
- Jones, D. (2001). *Handbook of Viscoelastic Vibration Damping*. New York, NY: John Wiley & Sons
- Kürschner, S., Popov, V. L., and Heß, M. (2015). “Contacts with elastomers,” in *Method of Dimensionality Reduction in Contact Mechanics and Friction*. (Berlin, Heidelberg: Springer Berlin Heidelberg), 99–113. doi: 10.1007/978-3-642-53876-6_7
- Li, Q., and Popov, V. L. (2017). Normal line contact of finite length cylinders. *Fact. Univ. Series Mech. Eng.* 15, 63–71. doi: 10.22190/FUME170222003L
- Mao, X., Popov, V. L., Starcevic, J., and Popov, M. (2017). Reduction of friction by normal oscillations. II. In-plane system dynamics. *Friction* 5, 194–206. doi: 10.1007/s40544-017-0146-x
- Nakano, K. (2006). Two dimensionless parameters controlling the occurrence of stick-slip motion in a 1-DOF system with Coulomb friction. *Tribol. Lett.* 24, 91–98. doi: 10.1007/s11249-006-9107-7
- Nakano, K., and Maegawa, S. (2009). Stick-slip in sliding systems with tangential contact compliance. *Tribol. Int.* 42, 1771–1780. doi: 10.1016/j.triboint.2009.04.039
- Popov, M. (2016). Critical velocity of controllability of sliding friction by normal oscillations in viscoelastic contacts. *Fact. Univ. Mech. Eng.* 14, 335–341. doi: 10.22190/FUME1603335P
- Popov, M., Benad, J., Popov, V. L., and Heß, M. (2015). “Acoustic emission in rolling contacts,” in *Method of Dimensionality Reduction in Contact Mechanics and Friction* (Berlin: Springer), 207–214. doi: 10.1007/978-3-642-53876-6_14
- Popov, V. L. (2017). *Contact Mechanics and Friction*. Berlin: Springer. doi: 10.1007/978-3-662-53081-8
- Popov, V. L., and Heß, M. (2015). *Method of Dimensionality Reduction in Contact Mechanics and Friction*. Berlin: Springer. doi: 10.1007/978-3-642-53876-6
- Popov, V. L., Willert, E., and Heß, M. (2018). Method of dimensionality reduction in contact mechanics and friction: a user's handbook III. Viscoelastic contacts. *Fact. Univ. Mech. Eng.* 16, 99–113. doi: 10.22190/FUME180511013P
- Rao, M. (2003). Recent applications of viscoelastic damping for noise control in automobiles and commercial airplanes. *J. Sound Vibration* 262, 457–474. doi: 10.1016/S0022-460X(03)00106-8
- Saccomandi, G., and Ogden, R. (2004). *Mechanics and Thermomechanics of Rubberlike Solids*. Wien: Springer. doi: 10.1007/978-3-7091-2540-3
- Woodhouse, J., Putelat, T., and McKay, A. (2015). Are there reliable constitutive laws for dynamic friction? *Philos. Transact. A* 373, 1–21. doi: 10.1098/rsta.2014.0401

Conflict of Interest Statement: The authors declare that the research was conducted in the absence of any commercial or financial relationships that could be construed as a potential conflict of interest.

Copyright © 2019 Nakano, Kawaguchi, Takeshima, Shiraishi, Forsbach, Benad, Popov and Popov. This is an open-access article distributed under the terms of the Creative Commons Attribution License (CC BY). The use, distribution or reproduction in other forums is permitted, provided the original author(s) and the copyright owner(s) are credited and that the original publication in this journal is cited, in accordance with accepted academic practice. No use, distribution or reproduction is permitted which does not comply with these terms.



Hydrated Seal Lip for Live Center in Machine Tools

Tetsuya Akiyama¹, Yuki Yoshioka¹, Takuro Honda¹, Yuta Nakashima² and Yoshitaka Nakanishi^{2*}

¹ Graduate School of Science and Technology, Kumamoto University, Kumamoto, Japan, ² Faculty of Science and Engineering, Kumamoto University, Kumamoto, Japan

OPEN ACCESS

Edited by:

Martin Hartl,
Brno University of Technology,
Czechia

Reviewed by:

Wenling Zhang,
University of Alberta, Canada
Liran Ma,
Tsinghua University, China

*Correspondence:

Yoshitaka Nakanishi
y-naka@mech.kumamoto-u.ac.jp

Specialty section:

This article was submitted to
Tribology,
a section of the journal
Frontiers in Mechanical Engineering

Received: 20 July 2018

Accepted: 12 September 2018

Published: 02 October 2018

Citation:

Akiyama T, Yoshioka Y, Honda T,
Nakashima Y and Nakanishi Y (2018)
Hydrated Seal Lip for Live Center in
Machine Tools.
Front. Mech. Eng. 4:14.
doi: 10.3389/fmech.2018.00014

When performing a cutting operation, a water-soluble cutting fluid may be used for cooling. Labyrinth and oil seals are commonly used in the rotating centers of machine tools to prevent the cutting fluid and dust from entering the inner parts. However, these seals do not demonstrate adequate functionality in a water-based environment. Therefore, a new rotary shaft seal was devised to separate the water-soluble cutting fluid from interacting with air. The rotary shaft seal was made from polyvinyl formal (PVF). Because PVF is a hydrophilic material, it is expected to provide suitable functionality as a seal in a water-based environment. Performance evaluations of PVF and oil seals were experimentally obtained and compared from the point of view of frictional torque, water-soluble cutting fluid leakage volume, and service life as a seal.

Keywords: live center, waterproof, seal lip, hydrated material, polyvinyl formal

INTRODUCTION

Rotary shaft seals used to separate liquid and air are important mechanical components in machine tools. Advances in rotary shaft seals have improved the quality of many machine products. Oil seals and labyrinth seals are well-known as general rotary shaft seals (Bock et al., 2003; Kim and Cha, 2009; Flitney, 2014). An oil seal forms a sliding surface between the rubber seal lip and the rotating shaft and is a component that prevents liquid leakage. Labyrinth seals, on the other hand, have a complicated fluid passage and rotate with the shaft, preventing leakage. Labyrinth seals are also mainly made of metals and are used in oil-based environments to prevent dust from entering the bearing housing or similar critical areas of machines. In addition, while the oil seal is a contact seal, one of the salient features of a labyrinth seal is that it is a non-contact seal. In general, the rotary shaft seal demonstrates excellent functionality in preventing the leakage of liquid when the speed of the rotating shaft is high or in oil-based environments. However, there are very few types of rotary shaft seals that can be used in a water-based environment. As a consequence of rapid technical innovation, there are increasingly more conditions under which shaft seals are required to operate these days. For example, when performing a cutting operation with a machine tool, water may be used for cooling the workpiece or turning tool (El Baradie, 1996a,b; Debnath et al., 2014). In a rotation center attached to a lathe or similar machine, an oil or a labyrinth seal is incorporated to prevent the liquid from entering the rotation center (Malleswara Rao et al., 2011).

However, these seals do not demonstrate excellent functionality in a water-based environment. A rotary shaft seal is needed to protect the mechanical elements from water-based liquid ingress in such a situation. In addition, the energy loss caused by the shaft seal should be minimized. Therefore, a rotary shaft seal that is suitable for such an environment is required in place of conventional seals. Accordingly, a new type of rotary shaft seal was specially designed to prevent water-based liquid leakage at a low frictional torque. A contact-type rotary shaft seal made of the hydrophilic material polyvinyl formal (PVF) was devised because such a seal using a hydrophilic material could show good performance just as an oil seal using a hydrophobic material shows an excellent function (Nakanishi et al., 2009). In a previous study, a shaft seal used an aqueous solution of polyethylene glycol (PEG), which is a non-Newtonian fluid; this solution was injected between the PVF seal rings to support the lubrication and sealing action at the sliding surface (Honda et al., 2018a). In another study, a new PVF seal with a simplified configuration that did not use a PEG solution was proposed (Honda et al., 2018b). While an oil seal demonstrates fluid lubrication on the sliding surface, a rotary shaft seal made of PVF is designed to provide boundary lubrication because oil films do not form easily in water-based environments (Bhate et al., 2004; Nakanishi et al., 2016, 2018; Honda et al., 2018a).

In this paper, we describe the development of a new rotary shaft seal for separating water and air using PVF as the sealant material under conditions where the rotary shaft operates at high speeds. This rotary shaft seal was experimentally evaluated from the perspective of frictional torque, water-soluble cutting fluid leakage volume, and service life.

MATERIALS AND METHODS

Sealing System

Figure 1 shows a schematic of the rotation center. The rotation center is mainly used to support the free end of the test piece in a machine tool, such as a lathe. Oil and labyrinth seals are generally used over the rotation centers in the sealing parts to prevent cutting fluids from entering bearing housings or similar areas. These seals prevent oil leaks and dust from entering these critical areas, and their functionality is fully demonstrated in an oil-based environment. However, when the oil-based environment is replaced with a water-based environment, these seals do not perform adequately. This is because oil seals are generally used to prevent leakage of oil and their seal lips are made of elastomer, which has hydrophobic characteristics. Therefore, oil seals sometimes suffer from inadequate lubrication of seal lips in water-based environments. Labyrinth seals have complex flow passages and they prevent leakage flow by operating at high shaft speed when fluids or gases enter into the flow passages. According to the seal structure, some leakage should be allowed when the shaft speed is low or shows zero. Furthermore, it is shown that the leakage amount of water is larger than that of oil because water has lower viscosity (Strmčnik and Majdič, 2017). Thus, PVF (PVA sponge D (D), SEIWA INDUSTRY Corp., Ltd., Japan), which is a hydrophilic material, was proposed as a sealing material because it is

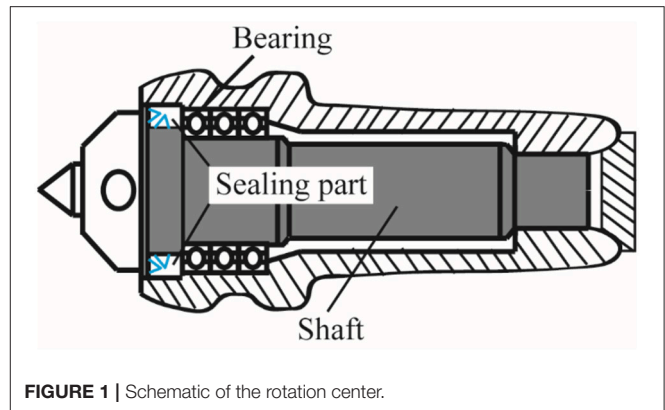


FIGURE 1 | Schematic of the rotation center.

thought that a seal performs better if the seal lip is made of hydrophilic or hydrated material when water is used as a subject fluid.

Figure 2 shows a schematic of the sealing system. A nitrile rubber oil seal (AC0678E0, NOK Corp., Japan) was also tested as a comparison to evaluate the PVF seal. The oil seal forms dynamic seal face between the seal lip and the shaft as shown in **Figure 2A**. Similarly, the PVF seal forms dynamic seal face between the inner surface of the seal and the shaft (**Figure 2B**). These two types of seals are assembled as shown in **Figure 2C**, and are designed to prevent leakage of the cutting fluid. The inner diameter of the PVF seal was 15.5 mm for a rotating shaft diameter of 16 mm (**Figure 3**). This mechanism prevents the cutting fluid leakage from between the inner surface of the PVF seal and the rotating shaft owing to the tightening action of the PVF seal on the rotating shaft. The dimensions of seal lips were decided considering practical applications such as easy replacement of a conventional seal with a new one. The thickness was fixed at 5 mm. It was adjusted by milling under dry conditions so that the swelled seal lip made proper contact against the shaft. The PVF seal was attached to the shaft under wet conditions. Furthermore, as listed in **Table 1**, the very porous structure of PVF may lead to the seepage of the cutting fluid through the PVF pores. Therefore, a silicone sealing material (PRO2020MJ, Kanpe Hapio Co., Ltd., Japan) was pasted on the side surfaces to prevent leakage, except from the dynamic seal face. Furthermore, as the PVF seal has a water retention property, the seal itself was expected to play the role of lubricant. The rotating shaft used for the test was made of stainless steel (SUS304, JIS). **Figure 4** shows the surface profile of the rotating shaft before the test (SE300-30, Kosaka Laboratory Ltd., Japan). In the test, a water-soluble cutting fluid prepared by diluting 200 mL of cutting oil (UNISOLUBLE-SG (N), JXTG Nippon Oil & Energy Corp., Japan) with 6,000 mL of tap water was used. The water-soluble cutting fluid has the primary advantage of excellent cooling capability.

Testing Device and Evaluated Methods

Figure 5 shows the test apparatus. The rotating shaft was continuously rotated at a constant speed of 5,000 rpm by AC

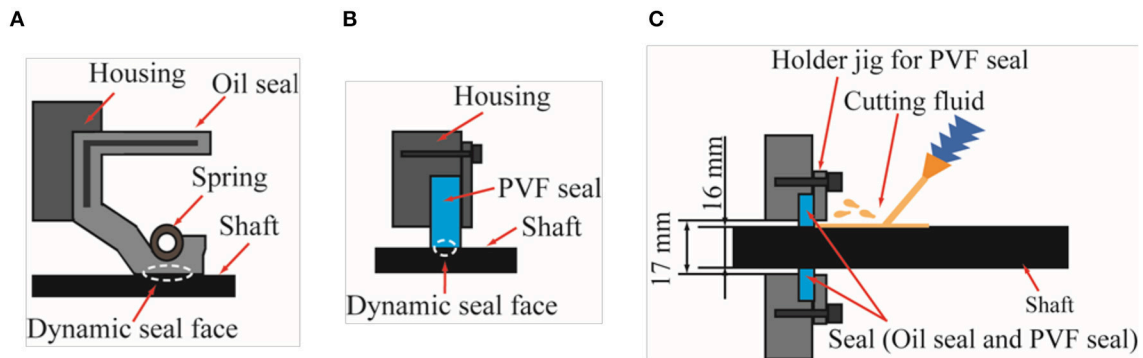


FIGURE 2 | (A) Schematic of dynamic seal face between an oil seal and the shaft. **(B)** Schematic of dynamic seal face between a PVF seal and the shaft. **(C)** Schematic of sealing system.

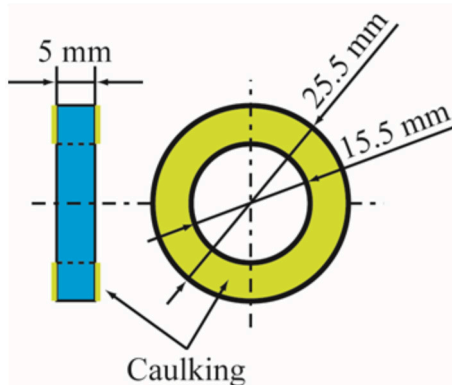


FIGURE 3 | Shape of the PVF seal.

servomotor (NXM620A, Oriental motor Corp., Ltd., Japan). In addition, the power consumed by this servomotor was measured using a voltage logger (LR5042, HIOKI E.E. Corp., Japan), and this was converted as a frictional torque generated by the rotary shaft seal. In this test, the total operating time was set for 5,000 h with a temporary suspension period of 720 h (30 days) occurring 2,500 h after the start. This was because, assuming that the seal is incorporated in the part of a factory machine tool for example, a situation in which the machine in the factory is stopped for 1 month is conceivable. The color of the cutting fluid changed when it was used for around 10 days. Therefore, the cutting fluid was replaced every 250 h. The limit value of the leakage volume of cutting fluid during the test was set to 0.1 mL/h. When this value was exceeded, it was considered that the rotary shaft seal had lost its leakage prevention functionality, and the test was terminated.

RESULTS AND DISCUSSION

Frictional Torque and Amount of Leakage

Figure 6 shows the frictional torque. In the graph of the oil seal, there are points where a negative value is given. This is probably because the long test caused a drift in the reference

TABLE 1 | Parameters of the PVF seal.

Parameter	Value
Pore diameter (μm)	80
Pore rate (%)	89
Water retention (%)	1,000
Elastic modulus (MPa)	0.087

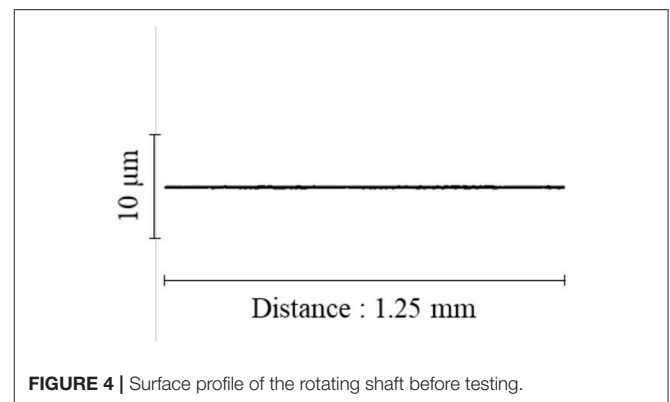


FIGURE 4 | Surface profile of the rotating shaft before testing.

point of 0 N·mm. In addition, the fluctuation of the torque value was large, with larger torque values shown for the initial torque and at other times. Furthermore, after the end of the stoppage period of 720 h (30 days), the oil seal leaked cutting fluid from immediately after the test was resumed and the leakage volume exceeded 0.1 mL/h; thus, the total operating time was 2,500 h. The average value of the frictional torque was 5.09 N·mm.

The PVF seal demonstrated low torque and a stable value. Furthermore, although the oil seal leaked cutting fluid immediately after the test was resumed after the end of the stoppage period, the PVF seal experienced no such leakage of cutting fluid and the test was continued up to 5,000 h. The average value of the frictional torque was 3.61 N·mm.

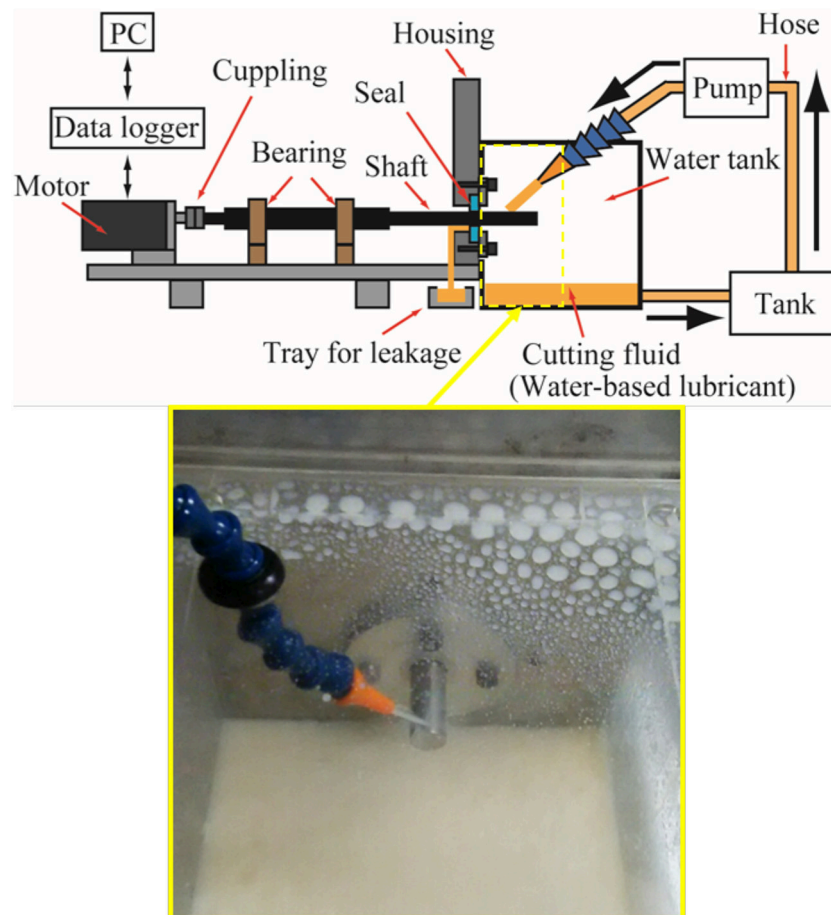


FIGURE 5 | Schematic and photograph of the testing device.

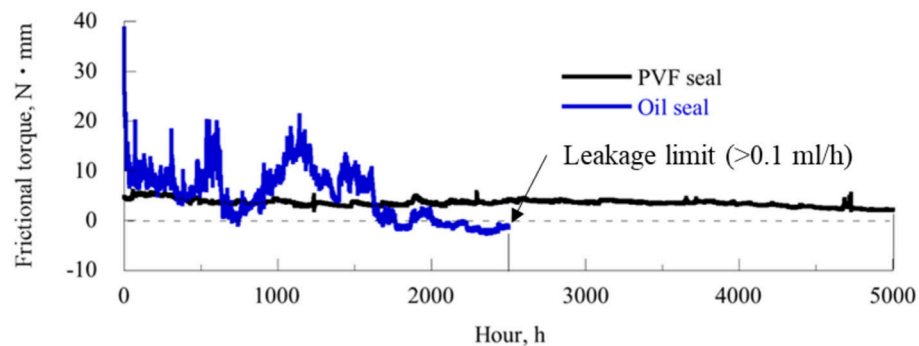


FIGURE 6 | Frictional torque.

The larger the frictional torque, the larger the energy loss caused by shaft seal. The PVF seal showed lower frictional torque than the oil seal, which meant that the PVF seal reduced the energy loss of the mechanical system. Consequently, the PVF seal had a longer service life. The PVF seal was superior because it beneficially reduced the frictional loss as much as possible. Cutting fluid leakage volumes in both tests were

below the measurement limit, excluding the end of the oil seal test.

Dynamic Seal Face

Figure 7 shows the microscopy (400-CAM052, SANWA SUPPLY INC., Japan) and SEM (TM3030, Hitachi High-Technologies Co. Ltd., Japan) images on the dynamic seal faces

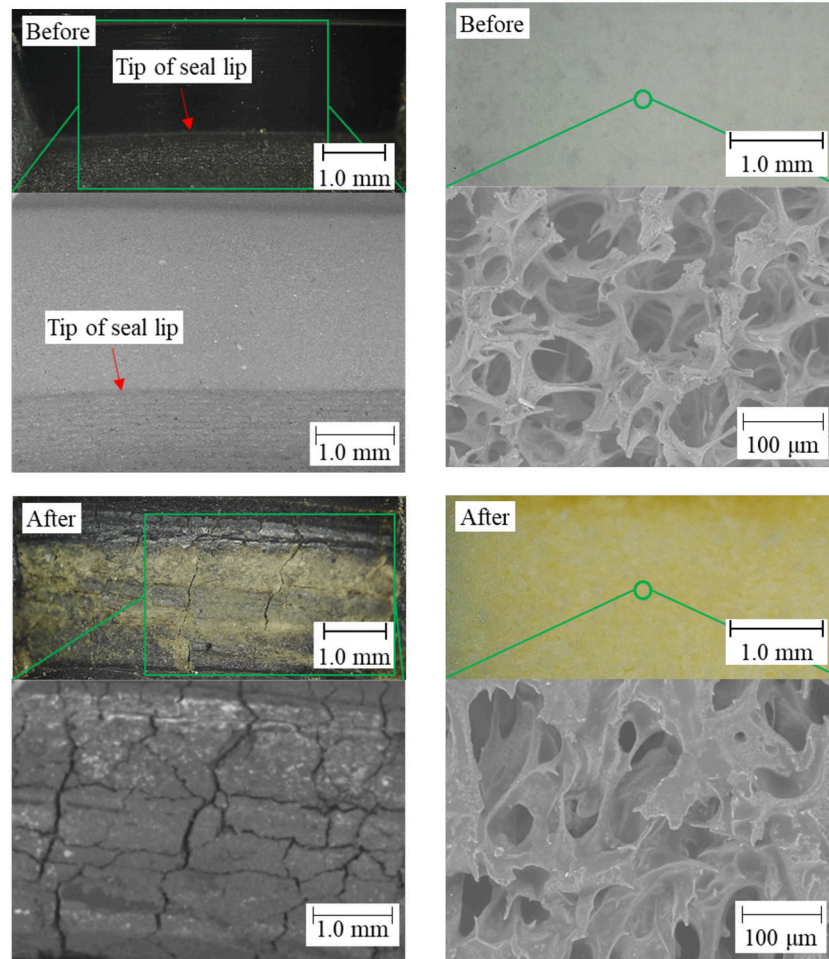


FIGURE 7 | Microscopy and SEM images of the dynamic seal face. Figures to the left are of the oil seal, and figures to the right are of the PVF seal.

of the two seals. The tip of the pre-test lip of the oil seal was observed to be worn and degraded after the test. This may be one cause of leakage. The oil seal should prevent liquid leakage owing to a fluid lubrication mechanism that forms a thin oil film on the dynamic seal face under an oil environment, thereby realizing low friction and wear. However, as a water-soluble cutting fluid was used in this experiment, a sufficient oil film was not formed in the dynamic seal face section, whereupon the seal lip and the rotating shaft were in direct contact with each other. This may be why the value of the torque was also high, and wear of the seal lip section was observed. The PVF seal was designed to operate by boundary lubrication. Namely, the PVF seal prevents leakage of water by being attached firmly to the rotating shaft to decrease clearance between the seal lip and the shaft regardless of its rotating condition. Moreover, PVF adsorbs water on the molecular level, so lubrication of the inner surface of the PVF seal is guaranteed even if the seal lip is tightly attached to the rotating shaft. The PVF seal showed less friction and smaller amounts of wear and leakage during the test.

After microscope observations after both tests, it was observed that the dynamic seal faces section is discolored. This was the color of the cutting fluid itself, and it can be concluded that this is due to the effect of the cutting fluid. Therefore, this discoloration is considered to not affect the functionality of the seal itself.

Roughness of the Rotating Shaft

Figure 8 shows the state of the shafts after the test and the surface profiles. From these figures, it was also confirmed that the shaft on which the oil seal was used had a rough surface and that a deep scratch was caused by the seal lip. This indicates that the rotating shaft and the seal lip are in direct contact with each other, and there probably was insufficient lubrication between them. On the contrary, in comparison with the rotating shaft on which the oil seal was used, deep scratches were not observed on the rotating shaft on which the PVF seal was used and the surface was also relatively smooth. From this, it can be said that the PVF seal has low friction and functions sufficiently as a seal under a water environment.

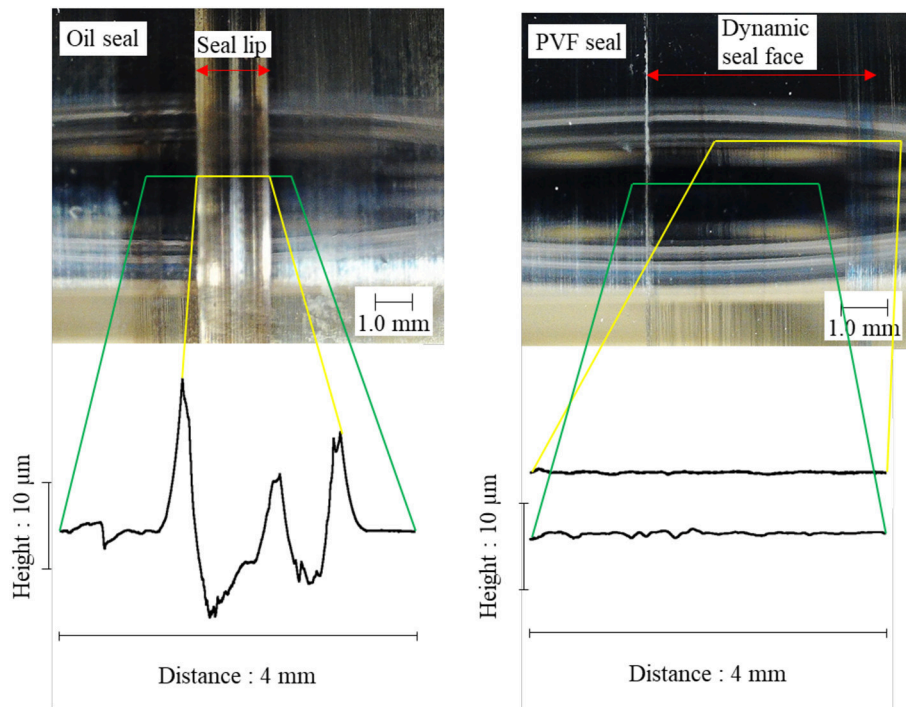


FIGURE 8 | Microscopy images and surface profiles of both rotating shafts.

CONCLUSION

A new PVF seal was developed as a rotary shaft seal for preventing leakage of water-soluble cutting fluid. The performance of the PVF seal and an oil seal were experimentally evaluated and compared. Under the condition that the rotational speed of the rotating shaft is 5,000 rpm under a water environment, the PVF seal is superior to the oil seal

in terms of frictional torque, leakage volume, and service life.

AUTHOR CONTRIBUTIONS

TA designed this research work and wrote the manuscript. YY and TH conducted the experiments. Both YuN and YoN managed and supervised all aspects of this work.

REFERENCES

- Bhate, N., Thermos, A. C., Aksit, M. F., Demiroglu, M., and Kizil, H. (2004). "Nom-metallic brush seals for gas turbine bearings," in *Proceedings of ASME Turbo Expo: Power for Land, Sea, and Air*. Vienna.
- Bock, E., Vogt, R., and Schreiner, P. (2003). New radial shaft seal concept for sealing hydraulic pumps and motors. *Seal. Technol.* 11, 6–10. doi: 10.1016/S1350-4789(03)11016-1
- Debnath, S., Reddy, M. M., and Yi, Q. S. (2014). Environmental friendly cutting fluids and cooling techniques in machining: a review. *J. Cleaner Prod.* 83, 33–47. doi: 10.1016/j.jclepro.2014.07.071
- El Baradie, M. A. (1996a). Cutting fluids: part I. Characterisation. *J. Mater. Process. Technol.* 56, 786–797.
- El Baradie, M. A. (1996b). Cutting fluids: part II. Recycling and clean machining. *J. Mater. Process. Technol.* 56, 798–806.
- Flitney, R. K. (2014). A description of the types of high speed rotary shaft seals in gas turbine engines and the implications for cabin air quality. *J. Biol. Phys. Chem.* 14, 85–89. doi: 10.4024/17FL14R.jbpc.14.04
- Honda, T., Kasamura, K., Nakashima, Y., Higaki, H., and Nakanishi, Y. (2018a). Low-friction shaft seal composed of bio-inspired materials covering low-speed range under water environment. *Proc. Inst. Mech. Eng. J J. Eng. Tribol.* 232, 36–42. doi: 10.1177/1350650117738702
- Honda, T., Nakashima, Y., Higaki, H., and Nakanishi, Y. (2018b). Fiber reinforcement of hydrophilic materials for a low-torque shaft seal in water environment. *Mech. Eng. Lett.* 4, 1–8. doi: 10.1299/mel.17-00590
- Kim, T. S., and Cha, K. S. (2009). Comparative analysis of the influence of labyrinth seal configuration on leakage behavior. *J. Mech. Sci. Technol.* 23, 2830–2838. doi: 10.1007/s12206-009-0733-5
- Malleswara Rao, J. N., Chenna Kesava Reddy, A., and Rama Rao, P. V. (2011). Evaluation of optimum values of surface roughness on aluminum work piece using roller burnishing. *Int. J. Eng. Res. Technol.* 4, 293–303.
- Nakanishi, Y., Honda, T., Kasamura, K., Nakashima, Y., and Higaki, H. (2018). Bio-inspired seal lip for application in electric vehicle coolant pumps. *Mech. Eng. Lett.* 4, 1–7. doi: 10.1299/mel.17-00654

- Nakanishi, Y., Honda, T., Nakashima, Y., and Higaki, H. (2016). Shaft seal for separation of water and air with low frictional torque. *Tribol. Int.* 94, 437–445. doi: 10.1016/j.triboint.2015.10.007
- Nakanishi, Y., Takashima, T., Higaki, H., Shimamoto, K., Ueno, T., Miura, H., et al. (2009). Development of biomimetic bearing with hydrated materials. *J. Biomech. Sci. Eng.* 4, 249–264. doi: 10.1299/jbse.4.249
- Strmčnik, E., and Majdič, F. (2017). Comparison of leakage level in water and oil hydraulics. *Adv. Mech. Eng.* 9, 1–12. doi: 10.1177/1687814017737723

Conflict of Interest Statement: The authors declare that the research was conducted in the absence of any commercial or financial relationships that could be construed as a potential conflict of interest.

Copyright © 2018 Akiyama, Yoshioka, Honda, Nakashima and Nakanishi. This is an open-access article distributed under the terms of the Creative Commons Attribution License (CC BY). The use, distribution or reproduction in other forums is permitted, provided the original author(s) and the copyright owner(s) are credited and that the original publication in this journal is cited, in accordance with accepted academic practice. No use, distribution or reproduction is permitted which does not comply with these terms.

Advantages of publishing in Frontiers



OPEN ACCESS

Articles are free to read
for greatest visibility
and readership



FAST PUBLICATION

Around 90 days
from submission
to decision



HIGH QUALITY PEER-REVIEW

Rigorous, collaborative,
and constructive
peer-review



TRANSPARENT PEER-REVIEW

Editors and reviewers
acknowledged by name
on published articles

Frontiers

Avenue du Tribunal-Fédéral 34
1005 Lausanne | Switzerland

Visit us: www.frontiersin.org

Contact us: info@frontiersin.org | +41 21 510 17 00



REPRODUCIBILITY OF RESEARCH

Support open data
and methods to enhance
research reproducibility



DIGITAL PUBLISHING

Articles designed
for optimal readership
across devices



FOLLOW US

@frontiersin



IMPACT METRICS

Advanced article metrics
track visibility across
digital media



EXTENSIVE PROMOTION

Marketing
and promotion
of impactful research



LOOP RESEARCH NETWORK

Our network
increases your
article's readership